Strongly-correlated one-dimensional bosons in continuous and quasiperiodic potentials

Hepeng Yao

INSTITUT POLYTECHNIQUE DE PARIS

NNT : 2020IPPAX057

Thèse de doctorat

Strongly-correlated one-dimensional bosons in continuous and quasiperiodic potentials

Thèse de doctorat de l'Institut Polytechnique de Paris
préparée à l'École polytechnique

École doctorale n°626 de l'Institut Polytechnique de Paris (IP Paris)
Spécialité de doctorat : Physique

Thèse présentée et soutenue à Palaiseau, le 20/10/2020, par

HEPENG YAO

Composition du Jury :

Thierry Giamarchi Professeur, University of Geneva (Department of Quantum Matter Physics)	Président
Guillaume Roux Maître de conférences, Université Paris-Saclay (Le Laboratoire de Physique Théorique et Modèles Statistiques)	Rapporteur
Ulrich Schneider Professeur, University of Cambridge (Cavendish Laboratory)	Rapporteur
Anna Minguzzi Directeur de recherche, Université Grenoble Alpes (Laboratoire de Physique et Modélisation des Milieux Condensés)	Examinateur
Hanns-Christoph Nägerl Professeur, University of Innsbruck (Institute for Experimental Physics)	Examinateur
Laurent Sanchez-Palencia Directeur de recherche, École polytechnique (Centre de Physique Théorique)	Directeur de thèse

Acknowledgements

The work reported in this manuscript was carried out in the **Centre de Physique Théorique (CPHT)** of **École Polytechnique**, located in Palaiseau, France. This thesis is funded by **DIM-SIRTEQ** via the **Centre National de la Recherche Scientifique (CNRS)**. The first two years of the thesis was done under the doctor school **École doctorale ondes et matière (EDOM)** and during the final year, I was transferred to the doctor school **École doctorale de l'Institut Polytechnique de Paris (ED IP Paris)**. I want to thank all of the above institutions for providing the framework of the thesis, as well as their staff for the valuable support on the administrative aspect.

First of all, I would like to express my deep gratitude to my supervisor **Laurent Sanchez-Palencia**. It is well-known how important the period of PhD is for those who wants to become a permanent researcher in the future, and I'm extremely lucky to have Laurent as my supervisor in this period. When guiding my thesis, he was always available to answer my questions, with great patience, kind, as well as enlightening ideas and explanations. I really learn a lot from him, not only for details about the certain projects we were studying, but also on how to perform a good research. His personality is a very good example for me which will shape me to be a good researcher in the future. Also, he was always trying his best to provide the best environment of research for me, on the aspects of computing resources, administrative issues, attending conferences and etc, which allows me to focus on research without additional worries.

Also, I would like to thank **Jean-René Chazottes**, the director of Centre de Physique Théorique. In spite of his busy schedule, he is always very kind, helpful and supportive for all the things which guarantees the PhDs to work under the best condition. Also, I would like to thank **Silke Biermann**, who is the coordinator of the condensed matter group, as well as the head of physics department now. On the one side, she was always providing us necessary informations and supports as a role of coordinator. On the other side, as a "colleague next door", it's a good memory to have those interesting discussions with her during those "long lunch", coffee break, barbecue and etc.

Then, I would like to thank the members of my PhD committee whom I have huge respect for. I would like to thank **Guillaume Roux** and **Ulrich Schneider** for kindly accepting to be the referees, and I want to thank them for their interest of reading the thesis. I would also like to thank **Thierry Giamarchi**, **Anna Minguzzi**, and **Hanns-Christophe Nägerl** for being the examinators.

During my PhD studies, numbers of collaborations have been carried out inside or outside the groups. I would like to thank **Anna Minguzzi** and **Patrizia Vignolo** for our collaborations on the Tan's contact project, especially for the beautiful analytical calculation of the contact formula they have provided. I would like to thank **Thierry Giamarchi** for our collaborations on the Bose glass project, where we have several waves of stimulating discussions in Leiden, Palaiseau and Geneva. I would like to thank **Ronan Gautier**, **Hakim Koudhli**, **Léa Bresque**, **Marco Biroli** and **Alessandro Pacco**, for our collaborations on different projects of quasiperiodic systems. It's interesting to work with master and bachelor students serving as a role of "quasi-supervisor" and I really benefit a lot from this experience for my future career. Special thanks should be dedicated

to Ronan, with whom we develop the QMC code to 2D and make the code much more efficient. Thanks to the talent of Ronan on numerics, we achieved huge progress on the code in 6 months which seems impossible for such a short period. The last and special thanks in this part should be delivered to **David Clément**, who has always been a strong support for us from the experimental aspect. I want to thank him not only for our collaboration on the Tan contact paper, but also for our further collaborations on the contact's measurement and suggestions on our quasiperiodic project as an experimentalist. I would also like to thank the members of him team, **Antoine Ténart**, **Gaétan Herce**, **Marco Mancini**, **Hugo Cayla**, **Cécile Carcy**.

The next wave of thanks should be given to my great colleagues in CPHT. I would like to firstly thank the members of our group, **Steven Thompson**, **Julien Despres**, **Louis Villa**, **Jan Schneider**. **Ronan Gautier**, **Hakim Koudhli**, **Léa Bresque**, **Marco Biroli** and **Alessandro Pacco**. Special thanks should be dedicated to Louis, not only for his strong support on analytical aspect of many problems and the French abstract of the thesis, but also for the tennis session we had each week. This provided us a good relax between research on physics (and probably also prepared us well for Roland Garros). Moreover, I would also like to thank Jan for the nice coffee you've made for us. And I would like to thank Zhaoxuan and Kim for the typos you found in the first version of the manuscript. Beyond our group, I would also like to thank some other members of the condensed matter group, **Steffen Backes**, **Alaska Subedi**, **Leonid Pourovskii**, **Michel Ferrero**, **Benjamin Lenz**, **Anna Galler**, **Sumanta Bhandary**, **Jakob Steinbauer**, **Benjamin Labrueil**, **James Bouse**, **Marcello Turtulici**. With all the names mentioned in this paragraph, we had so many nice discussions, lunches, coffee breaks and etc, which makes my stay in Palaiseau fruitful and enjoyable.

Furthermore, the administrative department and IT department are extremely powerful and helpful. I would like to thank the administrative department of CPHT, **Florence Auger**, **Malika Lang**, **Fadila Debbou**. Your high efficiency of work makes all the complicated administrative work easy for me. Also, I would also like to thank the IT department, **Jean-Luc Bellon**, **Danh Pham Kim**, **Yannick Fitamant** as well as **Aurélien Canou** as advisory support. With all your explanations and discussions of months, we finally install the QMC code and run it successfully on the cluster which seems like an impossible task at the very beginning. You also provided invaluable support for all kinds of numerical issues during my PhD.

During the three years of PhD, my family is always a strong support from my back. My father **Bingliang Yao** and mother **Aijun Liu** have always been supportive and helpful for me doing the PhD abroad. No matter whenever I need help from them, they are always trying their best to help me from seven thousands miles away. Also, I'm grateful to my father for his stimulating education, which makes me a physicists with strong ability on numerics, and to my mother for her strong ability on cooking which makes my vacation back in China enjoyable. Moreover, I want to thank my **grandparents**, my **aunts**, **uncles** and **cousins**, who always welcome me back to Beijing during summer or winter vacations. Finally, I want to thank my girlfriend **Wenwen Li**, who stays with me in Massy during the period of thesis writing. The process of writing thesis can be sometimes tortured mentally, and the confinement of COVID-19 pushes it to a harder situation. Thanks to her accompany, patience, kind and humor, I can keep calm and faithful during the writing period. The positive attitude you shared with me in this special period is an invaluable support for me which is decisive for the completion of this work.

Contents

Introduction **7**

Résumé **10**

1 Bosons in One Dimension **13**
1.1 The general interest of one dimensional bosons 14
1.2 One-dimensional bosons in the continuum 15
1.2.1 Lieb-Liniger bosons and delta-range interaction 15
1.2.2 One-dimensional bosons at zero temperature and Bethe ansatz . . . 16
1.2.3 One-dimensional bosons at finite temperature and Yang-Yang thermodynamics 20
1.2.4 The field description: Luttinger liquid theory 22
1.3 One-dimensional bosons in a lattice 23
1.3.1 One-dimensional Bose-Hubbard model 24
1.3.2 One-dimensional bosons in shallow periodic lattice 27
1.3.3 One-dimensional bosons in purely-disordered potentials 31

2 Continuous-space quantum Monte Carlo for bosons **33**
2.1 Path-integral Monte Carlo for interacting bosons 34
2.1.1 Feynman path integral for a single particle 34
2.1.2 Feynman path integral for many-body bosonic systems 36
2.1.3 The imaginary time propagator 38
2.1.4 Sampling the configurations using the Monte Carlo approach 40
2.1.5 Standard moves for path-integral Monte Carlo 43
2.2 Worm algorithm 45
2.2.1 The winding number 46
2.2.2 The extended partition function: Z-sector and G-sector 46
2.2.3 Monte Carlo moves in the worm algorithm 48
2.3 Computation of observables 51
2.3.1 Particle density and compressibility 51
2.3.2 Superfluid density 52
2.3.3 Green's function 53
2.3.4 Correlation function and momentum distribution 54

3 Tan's contact for trapped Lieb-Liniger bosons at finite temperature **56**
3.1 Two-parameter scaling function 58
3.1.1 The two-parameter scaling 58
3.1.2 Computing the scaling function using the Yang-Yang theory 61
3.1.3 Validation of the scaling function using quantum Monte Carlo 62
3.2 The behavior of the contact and regimes of degeneracy 65
3.2.1 The behavior of the contact in the homogeneous case 66
3.2.2 The scaling function in different regimes 66

3.2.3 The onset of maximum . . . 71
3.3 Experimental observability . . . 74
3.3.1 Accuracy of detection . . . 74
3.3.2 Validity condition of the quasi-1D regime . . . 74
3.3.3 Tube distributions . . . 75

4 Critical behavior in shallow 1D quasiperiodic potentials: localization and fractality 78
4.1 Localization, disorder and quasiperiodicity . . . 80
4.1.1 Basic concepts for localization . . . 80
4.1.2 Localization in different kinds of system . . . 81
4.2 Critical localization behavior in 1D shallow quasiperiodic lattices . . . 83
4.2.1 The localization properties of balanced bichromatic lattices . . . 83
4.2.2 Other quasi-periodic lattices and universality . . . 87
4.3 The fractality of the energy spectrum . . . 92
4.3.1 Fractals and fractal dimension . . . 92
4.3.2 Fractality of the energy spectrum for 1D quasiperiodic systems . . . 96
4.3.3 Properties of the spectrum fractal dimension . . . 100

5 Lieb-Liniger bosons in a shallow quasiperiodic potential 102
5.1 The Bose glass phase . . . 103
5.1.1 Bose glass phase in random potentials . . . 104
5.1.2 Bose glass phase in quasiperiodic Bose-Hubbard model . . . 106
5.2 The phase diagram for the shallow quasiperiodic systems . . . 112
5.2.1 Quantum Monte Carlo calculations for the determination of the phase 113
5.2.2 Analysis of the phase diagram . . . 116
5.3 Finite temperature effects . . . 117
5.3.1 The melting of the quantum phases . . . 117
5.3.2 Fractal Mott lobes . . . 121

6 Conclusion and perspectives 125

Appendix 128

List of publications 130

Bibliography 131

Introduction

"*Upward, not northward*", this is the famous sentence in the book "Flatland" by Edwin A. Abbott, where a two-dimensional (2D) square is given a glimpse of three-dimensional (3D) truth. This is the mantra he repeats, although he ends up dying without anyone in his world believing him. This book marks one of the first time that people perceives the power of dimensionality. In the nature, dimensionality plays a strong role. Although one of the main interest is to detect the existence of higher dimension in the context of high energy physics, understanding dimension lower than 3 is also valuable and interesting in many other fields.

In quantum physics, low dimensions are particularly rich. For instance, two-dimensional quantum systems appear to be extremely suitable for the study of topological effects, vortex physics and rotational ring structure [1]. Also, as pointed out by Refs. [1–3], the one-dimensional bosons have its special peculiarities such as the collective property of excitations, the power law decay of the correlation functions, as well as the fermionization of strongly-interacting bosons. More detailed discussion for the speciality of 1D bosons will be presented in the first chapter of this thesis.

From the experimental point of view, the achievement of Bose-Einstein condensates and ultracold Fermi seas since the second half of the 1990's have opened a new avenue to study three-dimensional quantum systems, but also in the lower dimensions [4–8]. With the development of quantum optics, people can change the dimensionality of the quantum systems and constrain one or two spatial dimensions with an attractive laser light, optical lattices and atom chips [9–12]. Various research has been carried out in low dimensional quantum systems [1, 9–39].

One-dimensional bosons is one of those low dimensional quantum systems which have attracted much attentions. In the continuum, they exhibit a special property called "fermionization" in the strongly-interacting limit, which is also known as the Tonks-Girardeau gases [40]. In 2004, these special gases have firstly been achieved experimentally, see Refs [9, 10]. Also, in the presence of periodic lattices or disorder, they show properties of quantum phase transition different from 3D, see examples in Refs. [13–16, 41]. It opens a new area of research where exists fruitful physics to be explored.

Understanding the quantum phase transitions as well as regime crossovers is one of the main topics in quantum statistical physics. In the field of ultracold atoms, the superfluid-Mott insulator transition in lattice systems is the most well-studied one, since this is a good quantum simulator for the conductance-insulator transition in condensed matter physics [13, 15, 42, 43]. However, it is also interesting to investigate other types of systems, for instance: (i) For continuous systems, the quantum gas can have different regimes of degeneracy depending on temperature, interactions and etc. (ii) In the presence of disorder or quasi-disorder, they can exhibit localization transitions.

In this manuscript, we theoretically study the properties of one-dimensional bosons in various types of systems, focusing on the phase transitions or crossovers between different quantum degeneracy regimes. Thanks to advanced quantum Monte Carlo simulations complemented by exact diagonalization and Yang-Yang thermodynamics, we can study

the properties of 1D bosons in various situations where the results are still lacking. The main results of the thesis constitute three parts. Firstly, focusing on the 1D harmonically trapped continuous bosons, we give a full characterization of the quantity called "Tan's contact" for arbitrary interactions and temperature. This is a experimentally measurable quantity which provides fruitful information about the system, such as the interaction energy and the variation of the grand potential. Our results turn out to show that this quantity gives a good characterization for different regimes. Especially, in the strongly-interacting regime, we find the Tan contact behaves non-monotonously versus temperature and exhibits a maximum which is the signature of the crossover to the fermionization at finite temperature, where other quantities always behave motononously. Secondly, we turn to the study of the localization properties of the 1D ideal gas in shallow quasiperiodic potentials. In the previous works, the localization problems in the tight-binding Aubry-André (AA) model have been extensively studied. The shallow lattice case is much less explored. However, it is interesting because it's different from the AA model and may cure the severe temperature problems in the ultracold atom systems. With the help of exact diagonalization, we find the universal critical behaviors for the critical potential, mobility edge as well as the critical exponent. Also, we study in detail the fractality of the energy spectrum and propose a method to calculate the fractal dimension. We find the fractal dimension is always smaller than one, which proves that the energy spectrum is nowhere dense and the mobility edge always stays in the band gap. Finally, we further study the quantum phase transition for the 1D interacting bosons in shallow quasiperiodic lattices. Similarly as the non-interacting case, the phase diagram has been widely studied in the deep lattice case in previous work where the temperature effect is not negligible. With the help of large scale QMC calculations, we determine the phase diagrams for shallow quasiperiodic lattices, where an incompressible insulator Bose glass phase appears in between the superfluid and Mott insulator. Then, we also investigate the thermal effects and find the stability of Bose glass against the finite temperature, which is strongly relevant for experimental observability. Moreover, by studying the melting of the Mott lobes, we find its structure is fractal-like and this property can be linked with the fractality of the single-particle spectrum.

The manuscript is organized as follows.

First of all, in Chapter 1 and 2, we give the introductions to the physics of 1D bosons and to the numerical approaches we shall extensively use in the remainder of the thesis, namely quantum Monte Carlo.

Chapter 1: We start with an introduction of bosons in one dimension. We first explain the general interest of 1D bosons. Then, we introduce the two main approaches for describing the 1D continuous bosons, i.e. the Lieb-Liniger model and the Luttinger liquid theory. Finally, we turn to the case of 1D bosons in a lattice. We focus on the case of tight-binding limit Bose-Hubbard model as well as the case of the shallow lattice, and explain the known results explored in the 2010's.

Chapter 2: We give an introductory presentation for the quantum Monte Carlo (QMC) approach we used in most of the following parts of the thesis. It is the path integral Monte Carlo approach in continuous space with worm algorithm implementations. We first present the basic path integral Monte Carlo with basic moves. Then, we present the worm algorithm which is an implementation that improves the computation efficiency. And we explain in the end the way of computing relevant observables.

Then, in the Chapters 3 to 5, we present the main results of this manuscript.

Chapter 3: We study a quantity called "Tan's contact" for 1D bosons which has be-

come pivotal in the description of quantum gases. We provide a full characterization of the Tan contact in harmonic traps with arbitrary temperatures and interactions. Combining the thermal Bethe ansatz, local-density approximation and quantum Monte Carlo calculations, we have shown the contact follows a universal two-parameters scaling and we determine the scaling function. We identify the behavior of the contact in various regime which characterizes the degeneracy for 1D bosons in continuum. Especially, we find the temperature dependence of the contact displays a maximum and it provides an unequivocal signature of the crossover to the fermionized regime, which is accessible in current experiments.

Chapter 4: We then study the critical behavior for 1D ideal gases in shallow quasiperiodic potentials. The quasiperiodic system provides an appealing intermediate between long-range ordered and genuine disordered systems with unusual critical properties. Here, we determine the critical localization properties of the single-particle problem in 1D shallow quasiperiodic potentials. On the one hand, we determine the properties of critical potential amplitude, mobility edge and inverse participation ratio (IPR) critical exponents which are universal. On the other hand, we calculate the fractal dimension of the energy spectrum and find it is non-universal but always smaller than unity, hence showing that the spectrum is nowhere dense and the mobility edge is always in a gap.

Chapter 5: We further study the case of 1D interacting bosons in shallow quasiperiodic lattices. The interplay of interaction and disorder in correlated Bose fluid leads to the emergence of a compressible insulator phase known as the Bose glass. While it has been widely studied in the tight-binding model, its observation remains elusive owing to the temperature effect. Here, with the large scale QMC calculations, we compute the full phase diagrams for the Lieb-Liniger bosons in shallow quasiperiodic lattices where the issue may be overcome. A Bose glass phase, surrounded by superfluid and Mott insulator, is found above a critical potential and for finite interactions. At finite temperature, we find the Bose glass phase is robust against thermal fluctuations up to temperatures accessible in current experiments of quantum gases. Also, we show that the melting of the Mott lobes is a characteristic of the fractal structure.

Chapter 6: We summarize the main results obtained in this work and give an outlook on it, from both theoretical and experimental points of view.

Résumé

"Vers le haut, pas vers le nord", telle est la célèbre phrase du livre "Flatland" d'Edwin A. Abbott, où un carré en deux dimensions (2D) laisse entrevoir une vérité en trois dimensions (3D). C'est le mantra qu'il répète, bien qu'il finisse par mourir sans que personne dans son monde ne le croit. Ce livre marque l'une des premières fois où les gens perçoivent le pouvoir de la dimensionnalité. Dans la nature, la dimensionnalité joue un rôle important. Bien que l'un des principaux intérêts soit de détecter l'existence d'une dimension supérieure dans le contexte de la physique des hautes énergies, la compréhension de la dimension inférieure à 3 est également précieuse et intéressante dans de nombreux autres domaines.

En physique quantique, les basses dimensions sont particulièrement riches. Par exemple, les systèmes quantiques bidimensionnels sont extrêmement adaptés à l'étude des effets topologiques, de la physique des tourbillons et de la structure des anneaux de rotation [1]. En outre, comme le soulignent les Réfs. [1–3], les bosons unidimensionnels ont leurs particularités telles que les propriétés collectives des excitations, la décroissance des fonctions de corrélation en loi de puissance, ainsi que la fermionisation des bosons à forte interaction. Une discussion plus détaillée de la spécificité des bosons 1D sera présentée dans le premier chapitre de cette thèse.

D'un point de vue expérimental, la réalisation de condensats de Bose-Einstein et de mers de Fermi ultra-froides depuis la seconde moitié des années 1990 a ouvert une nouvelle voie pour l'étude des systèmes quantiques tridimensionnels, mais aussi en dimensions inférieures [4–8]. Avec le développement de l'optique quantique, on peut changer la dimension des systèmes quantiques et contraindre une ou deux dimensions spatiales avec une lumière laser attractive, des réseaux optiques et des puces atomiques [9–12]. Diverses recherches ont été menées sur les systèmes quantiques de faible dimension [1, 9–39].

Les bosons unidimensionnels sont l'un de ces systèmes quantiques en basse dimension qui ont attiré beaucoup d'attention. Dans le continu, ils présentent une propriété spéciale appelée "fermionisation" dans la limite de forte interaction, qui est également connue sous le nom de gaz de Tonks-Girardeau [40]. En 2004, ces gaz particuliers ont été obtenus pour la première fois expérimentalement, voir les Réfs. [9, 10]. En outre, en présence de réseaux périodiques ou de désordre, ils présentent des propriétés de transition de phase quantique différentes de celles de la 3D, voir les exemples les Réfs. [13–16, 41]. Cela ouvre un nouveau domaine de recherche où il existe une physique fructueuse à explorer.

La compréhension des transitions de phase quantique et crossovers est l'un des principaux sujets de la physique statistique quantique. Dans le domaine des atomes ultra-froids, la transition superfluide-isolant de Mott dans les systèmes de réseaux est la plus étudiée, car c'est un bon simulateur quantique pour la transition conducteur-isolant en physique de la matière condensée [13, 15, 42, 43]. Cependant, il est également intéressant d'étudier d'autres types de systèmes, par exemple : (i) Pour les systèmes continus, le gaz quantique peut présenter différents régimes de dégénérescence en fonction de la température, des interactions, etc. (ii) En présence de désordre ou de quasi-désordre, ils peuvent présenter des transitions de localisation.

Dans ce manuscrit, nous étudions théoriquement les propriétés des bosons unidimensionnels dans différents types de systèmes, en nous concentrant sur les transitions de phase ou les crossovers entre différents régimes de dégénérescence quantique. Grâce à des simulations de Monte Carlo quantique avancées, complétées par des approches de diagonalisation exacte et la thermodynamique Yang-Yang, nous pouvons étudier les propriétés des bosons 1D dans diverses situations où les résultats font encore défaut. Les principaux résultats de la thèse consituent trois parties. Premièrement, en se concentrant sur les bosons continus 1D piégés de manière harmonique, nous donnons une caractérisation complète de la quantité appelée "contact de Tan" pour des interactions et des températures arbitraires. Il s'agit d'une quantité mesurable expérimentalement qui fournit des informations fructueuses sur le système, telles que l'énergie d'interaction et la variation du grand potentiel. Nos résultats montrent que cette quantité donne une bonne caractérisation pour différents régimes. En particulier, dans le régime d'interaction forte, nous constatons que le contact de Tan se comporte de manière non monotone en fonction de la température et présente un maximum qui est la signature de l'entre dans le régime de fermionisation à température finie, où d'autres quantités se comportent toujours de manière motonone. Ensuite, nous nous tournons vers l'étude des propriétés de localisation du gaz idéal 1D dans des potentiels quasi-périodiques peu profonds. Dans les travaux précédents, les problèmes de localisation dans le modèle Aubry- André (AA) de liaisons fortes ont été largement étudiés. Le cas du réseau peu profond est beaucoup moins exploré. Cependant, il est intéressant car il est différent du modèle AA et peut résoudre les sérieux problèmes de température dans les systèmes d'atomes ultrafroids. À l'aide d'une diagonalisation exacte, nous obtenons les comportements critiques universels pour le potentiel critique, le seuil de mobilité ainsi que l'exposant critique. Nous étudions également en détail la fractalité du spectre énergétique et proposons une méthode pour calculer la dimension fractale. Nous constatons que la dimension fractale est toujours inférieure à un, ce qui prouve que le spectre d'énergie n'est dense nulle part et que le seuil de mobilité reste toujours dans la bande interdite. Enfin, nous étudions plus en détail la transition de phase quantique pour les bosons 1D en interaction dans des réseaux quasi-périodiques peu profonds. De même que dans le cas des bosons idéaux, le diagramme de phase a été largement étudié dans des travaux précédents dans le cas des réseaux profonds où l'effet de la température n'est pas négligeable. À l'aide de calculs QMC à grande échelle, nous déterminons les diagrammes de phase pour les réseaux quasi-périodiques peu profonds, où une phase de verre de Bose, isolant incompressible, apparaît entre le superfluide et l'isolant de Mott. Ensuite, nous étudions également les effets thermiques et prouvons la stabilité du verre de Bose vis-à-vis de la température finie, ce qui est très important pour l'observabilité expérimentale. De plus, en étudiant la fusion des lobes de Mott, nous découvrons que sa structure est fractale et que cette propriété peut être reliée à la fractalité du spectre des particules individuelles.

Le manuscrit est organisé comme suit.

Tout d'abord, dans les chapitres 1 et 2, nous donnons des introductions à la physique des bosons 1D et aux approches numériques que nous utiliserons largement dans la suite de la thèse, à savoir le Monte Carlo quantique.

Chapitre 1 : Nous commençons par une introduction aux bosons en une dimension. Nous expliquons d'abord l'intérêt général des bosons 1D. Ensuite, nous introduisons les deux principales approches pour décrire les bosons 1D continus, c'est-à-dire le modèle de Lieb-Liniger et la théorie des liquides de Luttinger. Enfin, nous abordons le cas des bosons 1D dans un réseau. Nous nous concentrons sur le cas du modèle de Bose-Hubbard à liaisons fortes ainsi que sur le cas du réseau peu profond, et nous expliquons les résultats connus explorés dans les années 2010.

Chapitre 2 : Nous faisons une présentation introductive de l'approche de Monte Carlo quantique (QMC) que nous avons utilisée dans la plupart des parties suivantes de la thèse. Il s'agit de l'approche de Monte Carlo par intégrales de chemin dans l'espace continu avec des implémentations d'algorithmes de vers. Nous présentons tout d'abord la méthode de Monte Carlo par intégrales de chemin avec des mouvemetnts basiques. Ensuite, nous présentons l'algorithme du ver, est une implémentation qui améliore l'efficacité du calcul. Nous expliquons enfin la manière de calculer les observables pertinentes.

Ensuite, dans les chapitres 3 à 5, nous présentons les principaux résultats de ce manuscrit.

Chapitre 3 : Nous étudions une quantité appelée "contact de Tan" pour les bosons 1D, qui est devenue centrale dans la description des gaz quantiques. Nous fournissons une caractérisation complète du contact de Tan dans les pièges harmoniques pour des températures et des interactions arbitraires. En combinant l'ansatz de Bethe thermique, l'approximation de densité locale et les calculs de Monte Carlo quantique, nous avons montré que le contact suit une loi d'échelle universelle à deux paramètres et nous en déterminons la fonction d'échelle. Nous identifions le comportement du contact dans différents régimes de dégénérescence pour les bosons 1D dans le continu. En particulier, nous constatons que la dépendance du contact à la température présente un maximum et fournit une signature sans équivoque de l'entrée dans le régime fermionisé, accessible dans les expériences actuelles.

Chapitre 4 : Nous étudions ensuite le comportement critique des gaz idéaux 1D dans des potentiels quasi-périodiques peu profonds. Les systèmes quasi-périodiques constituent un intermédiaire intéressant entre les systèmes ordonnés à longue distance et les véritables systèmes désordonnés aux propriétés critiques inhabituelles. Ici, nous déterminons les propriétés critiques de localisation de particules uniques dans des potentiels quasi-périodiques 1D peu profonds. D'une part, nous déterminons les propriétés des exposants critiques, de l'amplitude du potentiel critique, du seuil de mobilité et du rapport de participation inverse (IPR) qui sont universels. D'autre part, nous calculons la dimension fractale du spectre d'énergie et constatons qu'elle est non universelle mais toujours inférieure à l'unité, montrant ainsi que le spectre n'est dense nulle part et que le seuil de mobilité est toujours dans une bande interdite.

Chapitre 5 : Nous étudions plus en détail le cas des bosons en interaction 1D dans des réseaux quasi-périodiques peu profonds. La compétition de l'interaction et du désordre dans le fluide de Bose corrélé conduit à l'émergence d'une phase isolante compressible connue sous le nom de verre de Bose. Bien qu'elle ait été largement étudiée dans le modèle de liaisons fortes, son observation reste insaisissable en raison de l'effet de la température. Ici, avec les calculs QMC à grande échelle, nous calculons les diagrammes de phase complets pour les bosons de Lieb-Liniger dans des réseaux quasi-périodiques peu profonds où le problème peut être surmonté. Une phase de verre de Bose, entourée de superfluide et d'isolants de Mott, se trouve au-dessus d'un potentiel critique et pour des interactions finies. À température finie, nous constatons que la phase de verre de Bose est robuste contre les fluctuations thermiques jusqu'à des températures accessibles dans les expériences actuelles sur les gaz quantiques. De plus, nous montrons que la fusion des lobes de Mott est une caractéristique de la structure fractale.

Chapitre 6 : Nous résumons les principaux résultats obtenus dans ce travail et donnons en discutons les perspectives, tant du point de vue théorique qu'expérimental.

Chapter 1

Bosons in One Dimension

Thanks to the development of the cooling techniques as well as quantum optics, people are able to generate ultracold quantum systems with the temperature scale from micro-Kelvin to nano-Kelvin [4–6]. At this temperature scale, it's possible to obtain Bose-Einstein condensates(BEC) for bosons and ultracold Fermi sea for fermions [7, 8], which opens a new domain to study quantum physics both in and out of equilibrium.

In the past decades, there are two main developments which enlarge the accessible range of physics for cold atom systems. On the one hand, various techniques for controlling the strength of interaction appeared, such as Feshbach resonances [44, 45]. It enables experimentalists to achieve ultracold gases where the interaction can be controlled. More importantly, even when the interactions are strong, they are still two-body interactions. On the other hand, using optical lattices or atom chips, it is possible to strongly confine the quantum gases in one or two directions and realise dimension of 1D and 2D [9–12]. For instance, as shown in Fig 1.1, with two pairs of laser with strong amplitudes, one can generate 2D optical lattices and cut the BEC systems into a bunch of 1D tubes. With these two developments, one can now generate low dimension strongly-interacting cold atom systems, which is an interesting system to study for both theoreticians and experimentalists. In one-dimension, the gases reach strongly-interacting regime in the dilute case, which is totally different from 3D. Also, thanks to the geometry confinement, the excitations can only be collective. In two-dimension, the system also has many special features. For instance, the superfluid transition is BKT type, it is an ideal structure to study vortex pair and rotational ring, and etc.

In this chapter, we start by discussing in detail the interests of studying the 1D interacting bosonic systems, which is the main subject we address in this manuscript. Then,

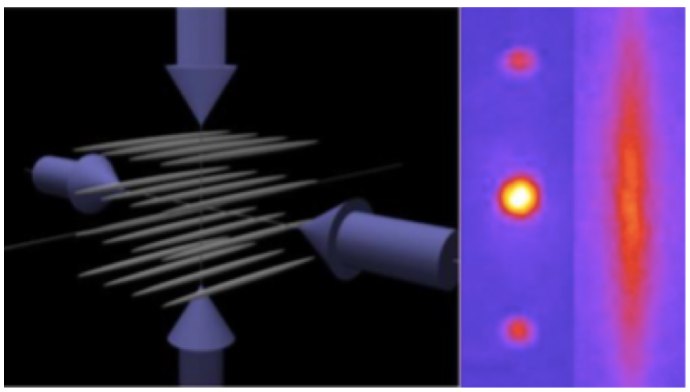

Figure 1.1: One-dimensional tubes of Bose gases in actual experiments, which is created by 2D optical lattices with strong amplitudes.

we give the two descriptions of 1D bosons in continuum, namely Lieb-Liniger Hamiltonian and Luttinger liquid. The first one is based on the picture of particle description and describe the physics by its kinetic movement and interactions. This is the Hamiltonian widely used in nowadays research, as well as most of the study in this thesis. The second one is based on the field operator description. It is useful when studying certain quantities such as phonon speed and correlation function. This description can also be generalized to fermionic systems. Finally, we introduce the basic properties of 1D bosons in a periodic optical lattice. We discuss the phase transitions in the deep and shallow periodic lattice cases, as well as the case in the presence of a disordered potential.

1.1 The general interest of one dimensional bosons

In this section , we present the general interests for performing research on one-dimensional strongly correlated bosonic systems. The interest of such kind of system can be separated into three main aspects.

Firstly, thanks to the two techniques mentioned above, we obtain atomic systems which interaction cannot be ignored. Comparing with ideal gases, the interacting systems present a flurry of new properties and phenomenons. For instance, loading the system into periodic lattices, the interacting system can realize a phase transition from superfluid to Mott insulator [13, 15, 42, 43]. Adding disorder into the system, one finds a variety of localization effects, such as collective Anderson localization [46–51], Bose glass physics [52–54], and many-body localization. Moreover, on the theoretical side, standard techniques for ideal bosons are not efficient any more. It calls for more advanced techniques, both analytical (such as Yang-Yang thermodynamics, Bethe ansatz and etc.) and numerical (such as quantum Monte Carlo, density matrix renormalization group, tensor network and etc.) [3, 55–59].

Secondly, the cold atom setup is one of the best choices serving for quantum simulators nowadays. Loading the atoms into optical lattices, one can simulate electrons in solid. There are two advantages for such a machine performing quantum simulation. On the one hand, the control of parameters is easy. For example, we can change the amplitude of the periodic potential by simply increasing the power of lasers or use Feshbach resonances to control the interactions. On the other hand, there are many simple and powerful measurement tools for such a system. For instance, by releasing the atoms and performing the so-called time of flight (TOF) detection, people can measure plenty of quantities, such as atom number, momentum distribution, temperature and etc.

Thirdly, low dimensional atomic gases exhibit totally new and interesting physical properties which are significantly different from 3D. This can be understood by an illustration based on Fig. 1.2. We depict here two extreme cases of interacting quantum gases. In Fig. 1.2(a), the system is fully delocalized and thus the dominant energy term is the

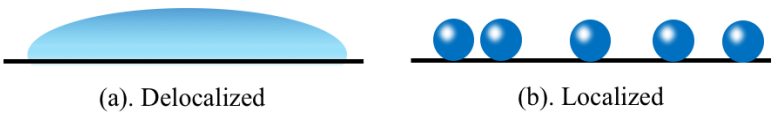

Figure 1.2: Two extreme cases for interacting quantum gases. (a). The delocalized system where the energy is dominant by the two-body interactions. (b). The localized system system where the kinetic energy is dominant.

interaction energy. So the average energy per particle e_1 could be estimated as

$$e_1 = \frac{E}{N} \simeq \frac{1}{2} gn \tag{1.1}$$

where E is the total energy, N the particle number, n the density of particle and g is the coupling constant which controls the interaction strength between two particles and will be introduced more carefully later. The opposite extreme case would be Fig. 1.2(b), where the system is fully localized. In this case, the particle can be treated as hard balls with radius a and the dominant term now is the kinetic energy. Therefore, the energy per particle can be written as

$$e_2 \simeq \frac{\hbar^2}{2ma^2} \simeq \frac{\hbar^2 n^{2/d}}{m} \tag{1.2}$$

where m is the mass of a single particle, $\hbar$ the Planck constant and d the dimension of the system. If the quantum system is in the strongly-interacting regime, we expect $e_1 \gg e_2$ and the particles tend to occupy different spaces. In three dimensions, it yields

$$n^{1/3} \gg \frac{\hbar^2}{mg} \tag{1.3}$$

Hence, the strong interaction regime corresponds to high densities. This conclusion seems natural with the common understanding. However, now if we turn to one dimension, we shall get

$$n^{-1} \gg \frac{\hbar^2}{mg} \tag{1.4}$$

and it indicates that the strongly-interacting regime is found for low density, which is counter-intuitive. Moreover, at low temperature, the strongly-interacting 1D bosons will be fermionized and this is the so called Tonks-Girardeau gases. The origin of this effect is that the interaction is repulsive and short range. Therefore, due to the confined structure in 1D, the atoms will avoid to be on top of each other and they also cannot meet the other atoms except the nearest neighbors. This creates a "Pauli blocking in position space" and thus part of the properties of the system will be the same as ideal fermions. All these properties are specific to 1D systems.

Here, it is also important to define a dimensionless interaction strength, namely the Lieb-Liniger parameter,

$$\gamma = \frac{mg}{\hbar^2 n}. \tag{1.5}$$

From Eq. (1.4), we can see that this quantity can help us easily verify the three interacting regimes for 1D bosons, namely strong interaction ($\gamma \gg 1$), intermediate interaction ($\gamma \sim 1$) and weak interaction ($\gamma \ll 1$). This quantity will be widely used in the following discussion.

1.2 One-dimensional bosons in the continuum

In this section, we discuss the basic of 1D Bosons in continuous systems. First, we start with the Lieb-Liniger model, which describes the system as individual particles with two-body interactions. Then, we introduce the Bethe ansatz and Yang-Yang thermodynamics which are efficient methods for solving this Hamiltonian. Finally, we discuss the Luttinger liquid theory which is the field operator description for 1D systems at low temperature.

1.2.1 Lieb-Liniger bosons and delta-range interaction

In this manuscript, we always consider 1D ultracold bosons with repulsive interactions in different kinds of external potentials. To describe such a kind of system, the widely-used

model is the one given by Lieb and Liniger in 1963 [55, 56],

$$\mathcal{H} = \sum_{1\leq j\leq N}\Big[-\frac{\hbar^2}{2m}\frac{\partial^2}{\partial x_j^2} + V(x_j)\Big] + g\sum_{j<\ell}\delta(x_j - x_\ell), \tag{1.6}$$

where m is the particle mass, x is the space coordinate and g the coupling constant for the two-body interactions. The three terms in the Hamiltonian are the kinetic term, external potential and two-body interactions, respectively. For the external potential $V(x)$, we take the form of a harmonic trap in the Tan's contact project (Chapter 3) and a quasiperiodic lattice in the localization project (Chapter 4 and 5).

Here, we consider a strictly 1D gas which is normally generated by an efficient transverse confinement,

$$\hbar\omega_\perp \gg k_{\rm B}T, \mu \tag{1.7}$$

with $\omega_\perp$ the trap frequency on the transverse direction, T the temperature of the system and μ the chemical potential. This condition simply implies that no excitations are created in the transverse direction and all the physics occurs only along the 1D tube. In the actual experiment, the interaction is normally controlled by the Feshbach resonant [60] or external lattices [61], which yields the relevant parameter named s-wave scattering length $a_{\rm sc}$. We can also write the effective 1D scattering length as [62]

$$a_{\rm 1D} = -l_\perp(\frac{l_\perp}{a_{\rm sc}} - C) \tag{1.8}$$

with $l_\perp = \sqrt{\hbar/m\omega_\perp}$ the oscillation length in the transverse direction, $C = |\zeta(1/2)|/\sqrt{2} = 1.0326$ and ζ the Riemann zeta function. Then, taking the pseudopotential form from the scattering problem [63], we can write the interaction term as the form of delta function in Eq. (1.6) and the parameter g writes

$$g = -\frac{2\hbar^2}{ma_{\rm 1D}}. \tag{1.9}$$

In the following, we only consider the case where the term $a_{\rm 1D}$ is always a negative number which leads to g always positive. This indicates that the interactions are repulsive and this is normally the case in nowadays' ultracold atom experiments. Also, different from the 3D case where g increases with a_{3D}, we find larger g when $a_{\rm 1D}$ is smaller. Moreover, when the condition Eq. (1.7) is not satisfied but the size on the longitude direction is much larger than the transverse one, we obtain the so called elongated gas (also named as cigar shaped gas). In this case, the Eqs (1.6) and (1.9) are not valid any more. One has to consider the 3D structure and establish another effective 1D Hamiltonian, see details for instance in Ref. [64–67]

Here, one may notice that the systems which satisfy Eq. (1.6) is known to be integrable in homogeneous case. It can be studied at zero temperature using the Bethe ansatz [56] and at finite temperature with Yang-Yang thermodynamics [57], which we will introduce in detail in the next two subsections.

1.2.2 One-dimensional bosons at zero temperature and Bethe ansatz

In 1963, E. Lieb and W. Liniger solved the Hamiltonian in Eq. (1.6) exactly in the thermodynamic and zero temperature limits, using the so-called Bethe ansatz [55, 56]. Hereafter, we review the approach quite into details, since it will be used for some of the calculations in Chapter 3. The ansatz proposes that the eigenfunction takes the form

$$\psi_{\rm B}(x_1 < x_2 < ... < x_N) = \sum_P A(P)e^{i\sum_n k_{P(n)}x_n} \tag{1.10}$$

with $x_1 < x_2 < ... < x_N$ the position of the N particles and P the $N!$ possible permutation of the particles, and $A(P)$ an amplitude which is initially unknown. The interpretation of the form in Eq. (1.10) is the following. We start from the non-interacting case where Eq. (1.6) is leaved with only the kinetic term. Thus, the N-particle wavefunction is the product of plane waves, up to the permutation. Then, we consider the interaction. We assume the atoms with momentum k_m and k_n will collides. Due to the 1D nature, they can only end up with either the same momenta or exchanging them. This process leads to a condition on the factor $A(P)$. If we assume P and P' only differ by the exchange of momenta k_m and k_n, according to the Shrödinger equation, we have

$$A(P) = \frac{k_m - k_n + i\tilde{g}}{k_m - k_n - i\tilde{g}} A(P') \tag{1.11}$$

with $\tilde{g} = mg/\hbar^2$ the dimensionless coupling parameter. In the hard-core limit $g \to +\infty$, the solution has been obtained in Refs. [68]. As pointed out by Ref. [40], the wavefunction can be written as

$$\psi_{\mathrm{B}}(x_1 < x_2 < ... < x_N) = S(x_1 < x_2 < ... < x_N)\psi_{\mathrm{F}}(x_1 < x_2 < ... < x_N) \tag{1.12}$$

with $S(x_1 < x_2 < ... < x_N) = \prod_{i>j} \mathrm{sign}(x_i - x_j)$ and $\psi_{\mathrm{F}}(x_1 < x_2 < ... < x_N)$ the wavefunction of spinless ideal fermions. In the limit of infinite interactions, the strong repulsive interaction prevents two particle from being at the same point. Thus, it forms a Pauli-like blocking in the position space and the system can be partially mapped to ideal fermions. Here, the function S is for compensating the sign exchange of the fermionic wavefunction. The gas in this regime is also known as the Tonks-Girardeau(TG) gas. In the case of TG gas, the total energy can be written as

$$E = \sum_n \frac{\hbar^2 k_n^2}{2m}. \tag{1.13}$$

Now, if we turn back to the Bethe ansatz which can be treated as a generalization of the TG solution. The condition Eq. (1.11) can be treated as a constraint on the quasi-momenta $\{k_n\}$, it yields

$$e^{ik_m L} = \prod_{n=1, n\neq m}^{N} \frac{k_m - k_n + i\tilde{g}}{k_m - k_n - i\tilde{g}} \tag{1.14}$$

Note that Eq. (1.14) actually holds for periodic boundary condition. Taking the logarithm of Eq. (1.14), we find

$$k_n = \frac{2\pi I_n}{L} + \frac{1}{L}\sum_n log\left(\frac{k_m - k_n + i\tilde{g}}{k_m - k_n - i\tilde{g}}\right) \tag{1.15}$$

with $\{I_n\}$ a set of integer numbers. Now, we introduce the momenta density $\rho(k_n) = 1/[L(k_{n+1} - k_n)]$ and take the continuum limit, Eq. (1.15) then yields

$$2\pi\rho(k) = 1 + 2\int_{-q_0}^{q_0} \frac{\tilde{g}\rho(k')}{(k-k')^2 + \tilde{g}^2} \tag{1.16}$$

where q_0 satisfies $\rho(k) = 0$ for any $|k| > q_0$. Within the continuous limit, the total energy in Eq. (1.13) could be rewrite as

$$E = L\int_{q_0}^{q_0} dk\ \frac{\hbar^2 k^2}{2m}\rho(k) \tag{1.17}$$

with the particle density ρ_0 found by

$$\rho_0 = \int_{-q_0}^{q_0} \rho(k) dk. \tag{1.18}$$

Then, using the dimensionless form,

$$G(q) = \rho(k/q_0); \quad \alpha = \frac{\tilde{g}}{q_0}; \quad \gamma = \frac{\tilde{g}}{\rho_0}, \tag{1.19}$$

one can write Eq. (1.17) and Eq. (1.18) as the so-called Lieb-Liniger equations,

$$\alpha = \gamma \int_{-1}^{+1} dq G(q) \tag{1.20}$$

$$G(q) = \frac{1}{2\pi} + \int_{-1}^{+1} \frac{d\ q'}{2\pi} G(q') \frac{2\alpha}{(q'-q)^2 + \alpha^2} \tag{1.21}$$

where G is the density of states corresponded to the proposed ansatz, q the quasi-momentum and γ is the Lieb-Liniger parameter. Here, one should notice that the definition of γ in Eq. (1.19) is consistent with what is discussed above, see Eq. (1.5). These two equations form a closed loop and the solution of it is unique. The solution depends on a single parameter, namely γ. With the quantities of α and $G(q)$, we shall be able to express the function $e(\gamma)$, which writes

$$e(\gamma) = \frac{\gamma}{\alpha(\gamma)} \int_{-1}^{+1} dq\ G(q;\gamma) q^2. \tag{1.22}$$

All ground state properties of the Bose gas can then be found from this function. For instance, the ground state energy E and the chemical potential μ, read

$$E = \frac{\hbar^2 L n^3}{2m} e(\gamma), \tag{1.23}$$

and

$$\mu = \left.\frac{\partial E}{\partial N}\right|_L = \frac{\hbar^2}{2m} n^2 \left[3e(\gamma) - \gamma e'(\gamma)\right]. \tag{1.24}$$

In particular, since γ is a function of the particle density n, Eq. (1.24) gives the equation of state, i.e. the chemical potential as a function of density $\mu = \mu(n)$. Here, we numerically solve the Bethe ansatz equations and find the equation of state, see the black solid line in Fig. 1.3. In the following paragraphs, we will discuss the behavior of 1D bosons in different interaction limits and compare it with the Bethe ansatz solution.

The strongly-interacting limit ($\gamma \to +\infty$): Tonks-Girardeau gases

As explained in the discussion of the Bethe ansatz, in the hard-core limit $g \to +\infty$, the repulsive interaction is so strong that the system can be mapped onto ideal fermions [40]. Here, one should notice that they are not strictly fermions since the wavefunction is still symmetric. However, we should still be able to calculate the total energy by the integral up to the Fermi momentum k_F and find

$$E = \int_{-k_\mathrm{F}}^{k_\mathrm{F}} \frac{L dk}{2\pi} \frac{\hbar^2 k^2}{2m} = \frac{\pi^2 \hbar^2 L n^3}{6m} \tag{1.25}$$

Then, with the relation $\mu = \partial E / \partial N$, we find the equation of state

$$n = \sqrt{\frac{2m\mu}{\pi^2 \hbar^2}} \tag{1.26}$$

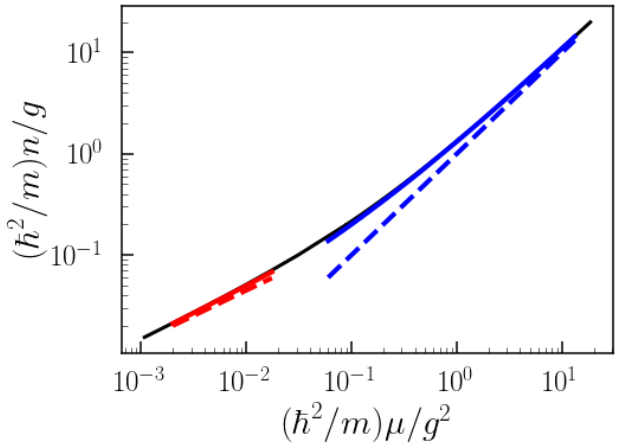

Figure 1.3: The equation of state for 1D bosons in the thermodynamic limit calculated from Bethe ansatz, see black solid line. We also show the analytical results for $\gamma \to \infty$ (red dashed line), $\gamma \gg 1$ (red solid line), $\gamma \to 0$ (blue dashed line) and $\gamma \ll 1$ (blue solid line).

Taking the limit $g \to +\infty$ in the Lieb-Liniger equation Eq. (1.21), we find the second term on the right hand side of Eq. (1.21) goes to zero which indicates $G(k) = 1/2\pi$. Then, in Eq. (1.20), we find $\alpha \to \infty$ and $\alpha/\gamma = 1/\pi$. Also, we shall find from Eq. (1.22) and Eq. (1.23) the total energy, which is consistent with Eq. (1.25).

In Fig. 1.3, we plot Eq. (1.26) as red dashed line. It fits well with the Bethe ansatz solution in the limit $\gamma \to \infty$ (equivalently $(\hbar^2/m)n/g \to 0$). Moreover, one can find a more elaborated solution with higher order term in the equation of state, which yields

$$n = \sqrt{\frac{2m\mu}{\pi^2\hbar^2}} + \frac{8\mu}{3\pi g} - \frac{2\sqrt{2}\mu^{1.5}}{\pi^2 g^2}. \tag{1.27}$$

We plot Eq. (1.27) in Fig. 1.3 as red solid line and find it fit well with the Bethe ansatz solution in a much larger range, for $\gamma \gg 1$ (equivalently $(\hbar^2/m)n/g \to \ll 1$).

The weakly-interacting limit ($\gamma \to 0$): Gross-Pitaevskii equation

In the limit $\gamma \to 0$, we can use the Gross-Pitaevskii equation to describe the system, which is

$$\mu\psi = -\frac{\hbar^2}{2m}\nabla^2\psi + V(x)\psi + g|\psi|^2\psi \tag{1.28}$$

where ψ is the wave function. In one dimension, all bosons are quasi-condensed in this regime. Therefore, the interaction shows up as a non-linear term. By solving the equation, one can find the chemical potential and the total energy

$$n = \frac{\mu}{g}, \tag{1.29}$$

$$E = \frac{1}{2}gn^2L. \tag{1.30}$$

To obtain this equations from the limit $\gamma \to 0$ of the Bethe ansatz is non-trivial, since it's not possible to ignore the integrated term in Eq. (1.21). However, from the numerical results of Bethe ansatz, the solution fit well with the equation above. In Fig. 1.3, we plot Eq. (1.29) as blue dashed line. It fits well with the Bethe ansatz solution in the limit $\gamma \to 0$

(equivalently $(\hbar^2/m)n/g \to \infty$). Similarly as the strongly-interacting case, one can even find a more elaborated solution with higher order term in the equation of state. It writes

$$n = \frac{\mu}{g} + \frac{1}{\pi}\sqrt{\frac{m\mu}{\hbar^2}} \tag{1.31}$$

We plot Eq. (1.31) in Fig. 1.3 as blue solid line and find it fit well with the Bethe ansatz solution in a much larger range, for $\gamma \ll 1$ (equivalently $(\hbar^2/m)n/g \to\gg 1$).

1.2.3 One-dimensional bosons at finite temperature and Yang-Yang thermodynamics

Now, we consider the case of a finite temperature. First, we discuss the thermal Bethe ansatz for solving the Lieb-Liniger Hamiltonian at finite temperature, which is the so called Yang-Yang thermodynamics. Then, we discuss the existence of the quasi-condensate.

The Yang-Yang thermodynamics

The Bethe ansatz we introduced previously works well for 1D bosons in the zero temperature limit. In 1969, C. N. Yang and C. P. Yang reported the extension of the Bethe ansatz to finite temperature, so-called Yang-Yang thermodynamics. According to Ref. [57], for such a system, they define a quantity called dressed energy $\epsilon(k)$ by

$$\frac{\rho_h}{\rho} = \exp[\epsilon(k)/k_{\mathrm{B}}T] \tag{1.32}$$

where ρ and ρ_h correspond to the density of filled states and holes. The dress energy simply describes the particle-hole distribution thanks to the excitation by temperature. In the mapping to fermions, we would have the Fermi-Dirac distribution for free Fermi gases

$$\rho = \frac{1}{e^{\epsilon/k_BT}+1} \tag{1.33}$$

with $\rho_h = 1-\rho$ and the chemical potential μ is included in the definition of $\epsilon(k)$. Therefore, the term $\epsilon(k)$ in Eq.(1.33) is interpreted as an effective single-particle energy in an ideal Fermi gas picture. Here, it is the energy of a boson dressed by the interaction with the other particles.

Similarly as the standard Bethe ansatz, one can treat the interaction as the collision of atoms, which leads to a condition on the momentum. One can find the equation similar as Eq. (1.16), which yields

$$2\pi(\rho(k)+\rho_h(k)) = 1 + 2\int_{-\infty}^{+\infty} dk'\ \frac{\tilde{g}\rho(k')}{(k-k')^2+\tilde{g}^2}. \tag{1.34}$$

Here, one may notice that we need to consider the contribution of the holes on the left-hand side, which is different from the zero temperature case. Moreover, the particle density n, the energy E and the entropy S can be written as a function of ρ and ρ_h. At temperature T, to calculate the dressed energy at thermal equilibrium, one need to compute the partition function $\exp(S/k_{\mathrm{B}} - E/k_{\mathrm{B}}T)$ and find the condition to maximize it. Combined with Eq.(1.34), we find that the Yang-Yang equation for the dressed energy writes

$$\epsilon(k) = \frac{\hbar^2k^2}{2m} - \mu - \frac{k_BT}{2\pi}\int_{-\infty}^{+\infty} dq \frac{g}{g^2/4+(k-q)^2}\ \ln\left[1+e^{-\frac{\epsilon(q)}{k_BT}}\right]. \tag{1.35}$$

This is a self-consistent equation where the form of $\epsilon(k)$ can be solved by numerically looping process. The detailed procedure for solving this equation will be presented in Chapter 3.

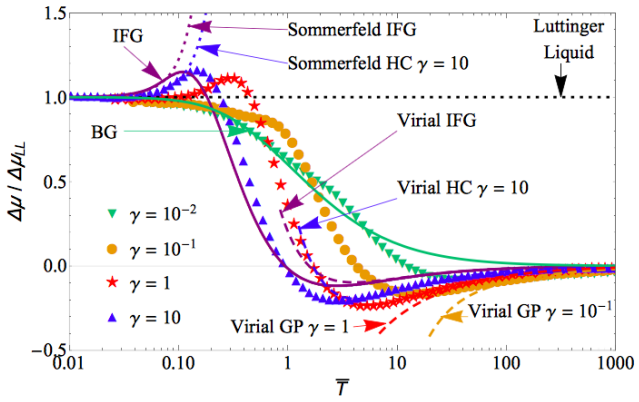

Figure 1.4: The thermal shift of the chemical potential $\Delta\mu/\mu_{\rm LL}$ as a function of the rescaled temperature $\mathcal{T} = k_{\rm B}T/mc^2$, with c the sound velocity. The symbols are the Yang-Yang solution. Different curves are results from various theories: Sommerfield expansion of the ideal Fermi gas (IFG) and Hartree-Fock (HF) theory, Bogoliubov theory(BG), virial ideal Fermi gas (virial IFG) and virial Gross-Pitaevskii (GP) predictions and Luttinger Liquid theory. This plot is from Ref. [69].

With the solution of $\epsilon(k)$, one can calculate thermodynamic quantities such as the grand potential density,

$$\Omega(\mu, g, T) = -\frac{k_B T}{2\pi}\int_{-\infty}^{+\infty} dq\, \ln\left[1 + e^{-\frac{\epsilon(q)}{k_B T}}\right]. \tag{1.36}$$

From the expression of Ω, we can calculate the density of the system using the thermodynamic relation

$$n = -\left.\frac{\partial\Omega}{\partial\mu}\right|_{T,g}. \tag{1.37}$$

One should notice that this equation is nothing but the equation of state. One example for the application of the Yang-Yang thermodynamics is presented in Ref. [69]. One of the main results is concluded in Fig. 1.4. In this paper, they use the Yang-Yang thermodynamics to calculate the difference of the chemical potential with the zero temperature solution $\mu_{\rm LL}$ (μ calculated from the Luttinger liquid theory, see detailed discussion in subsection 1.2.4), i.e. $\Delta\mu = \mu - \mu_{\rm LL}$ at different temperature. Also, they calculate the corresponding sound velocity c and plot $\Delta\mu/\mu_{\rm LL}$ as a function of rescaled temperature $\mathcal{T} = k_{\rm B}T/mc^2$ under different interactions, see symbols in Fig. 1.4. In the low temperature limit, we find the YY solution fits well with the Sommerfield expansion in the strong interaction regime which is expected for the fermionized bosons. In the weakly interacting regime, they also fit well with the Bogoliubov theory. At high temperature, we find the results fit well with the virial ideal Fermi gas and virial Gross-Pitaevskii (GP) prediction in the strong and weak interaction regimes correspondingly. Another example for application of the Yang-Yang thermodynamics is the computation of the Tan contact, which we will study in detail in Chapter 3. In that chapter, we will also take advantage of the Yang-Yang results to analysis the different regimes of degeneracy for Lieb-Liniger bosons in harmonic trap at finite temperature.

Quasi-condensate

For 1D bosons in homogeneous systems, it is well known that there is no condensation at any temperature. At sufficiently low temperature, the density fluctuations are suppressed but the phase fluctuations are not, which is the signature of a quasi-condensate.

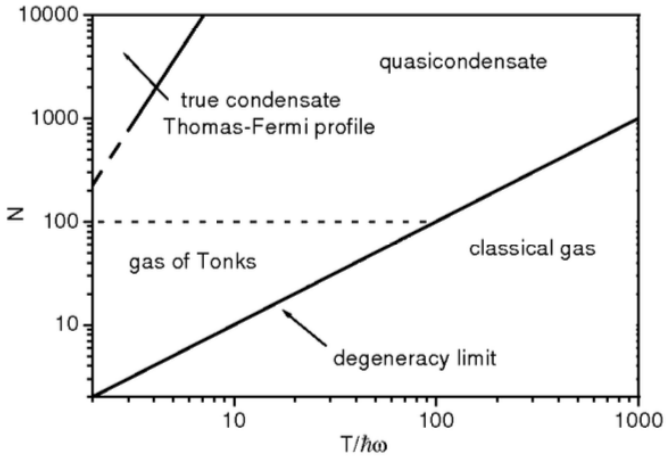

Figure 1.5: The regimes of degeneracy for 1D trapped bosons at finite temperature with the harmonic trap $\alpha = 10$. This plot is from Ref. [70].

However, at finite temperature, a true BEC may exist with a finite size system, such as the harmonically trapped system. In Ref. [70], D. Petrov et al have given the regime of degeneracy for 1D bosons at finite temperature, see Fig. 1.5. The diagram is plotted in presence of a certain harmonic trap $\alpha = 10$, where α defined by

$$\alpha = \frac{mga_{\text{ho}}}{\hbar^2} \tag{1.38}$$

with $a_{\text{ho}} = \sqrt{\hbar/m\omega}$ the oscillation length and ω the frequency of the harmonic trap. For this system, there are two relevant temperatures. One is the degeneracy temperature T_{D} below which the system shows quantum properties, i.e. Thomas-Fermi gases in weakly-interacting regimes and fermionized bosons in strongly-interacting regime. Another one is the coherence temperature $T_\phi = \hbar\omega T_{\text{D}}/\mu$ In the Thomas-Fermi regime, it is always much smaller than T_{D}. For $T < T_\phi$, both the density and phase fluctuations are negligible. In this case, we have the true condensate, see the left up corner in Fig. 1.5. Then, when $T_\phi < T < T_{\text{D}}$, the density fluctuations are still negligible but the phase fluctuations are visible. In the considered regime, the density profile is still Thomas Fermi kind but the phase coherence length extracted from the correlation function is smaller than the size of the system. This is what is referred as quasi-condensate in the plot. Finally, we have the Tonks gas in strong interaction limit $N \gg \alpha^2$ and the classical gas at high temperature $T > T_{\text{D}}$.

1.2.4 The field description: Luttinger liquid theory

Beyond the particle picture described in the last section, it's also possible to use the field operator to describe the system, which is known as the Tomonaga-Luttinger liquid theory [2, 71]. At low temperature, the 1D bosonic models exhibits a liquid phase where no continuous or discrete symmetry is broken. To be more precise, the model satisfies two main features: (i) the low energy excitations are collective modes with linear dispersion, (ii) at zero temperature, the correlation function shows an algebraic decay with exponents related to the parameters of the model. These two features define a universality class of 1D interacting bosonic systems which is known as the Tomonaga-Luttinger liquids [2, 71].

The collective nature of the low-energy excitations in 1D can be easily understood by the special space structure in 1D. Thanks to the existence of interaction, a particle has to push its neighbour while it is moving. Thus, when a particle is moving in a certain

direction, the individual motion will quickly be converted into a collective one. This can be fruitfully described by a field description [2, 72]. The boson field operator normally writes

$$\hat{\Psi}^\dagger = [\hat{\rho}(x)]^{1/2} e^{-i\hat{\theta}(x)} \tag{1.39}$$

where the two collective fields are the density $\hat{\rho}(x)$ and the phase $\hat{\theta}(x)$. Here, the two operators satisfy the commutation rule,

$$[\hat{\rho}(x), \hat{\theta}(x')] = i\delta(x - x'). \tag{1.40}$$

Considering a translationally invariant system, the ground state has a constant average density ρ_0. The full expression of the density operator writes [72]

$$\hat{\rho}(x) \simeq \left(\rho_0 - \frac{1}{\pi}\partial_x \hat{\phi}(x)\right) \sum_{j=-\infty}^{+\infty} a_j e^{2ij(\pi\rho_0 x - \hat{\phi}(x))}, \tag{1.41}$$

with $\hat{\phi}(x)$ a slowly varying quantum field. Here, all the oscillating term are included in the expression. To write the Hamiltonian under the field description, we can rewrite Eq. (1.6) as

$$\mathcal{H} = \int dx \left(\frac{\nabla\hat{\Psi}^\dagger \nabla\hat{\Psi}}{2m} + \frac{g}{2}\hat{\Psi}^\dagger\hat{\Psi}^\dagger\hat{\Psi}\hat{\Psi}\right) \tag{1.42}$$

To proceed further, we will do two approximations: (i) We assume the field $\hat{\phi}(x)$ is smooth on the scale of ρ_0^{-1}, thus the high order oscillating term in Eq (1.42) will vanish when performing the integral on x. (ii) We consider low enough temperature where the excitation satisfied the linear dispersion, thus the value k is small enough and we can ignore the high order term of k, i.e. the term $(\nabla^2\hat{\phi}(x))^2$. More details of the derivations can be found in Refs. [2, 3]. Finally, with the two approximations mentioned above, we can combine Eq (1.42), Eq (1.39) and Eq (1.41), and write the effective Hamiltonian in the field representation

$$\mathcal{H} = \frac{\hbar}{2\pi}\int dx \left(cK\left(\frac{\partial\hat{\theta}}{\partial x}\right)^2 + \frac{c}{K}\left(\frac{\partial\hat{\phi}}{\partial x}\right)^2\right) \tag{1.43}$$

where c is the sound velocity which leads to the linear dispersion $\omega = c|k|$. And K is the so-called Luttinger parameter which describes the relative weights of the phase and density terms in Eq. (1.43). Arguably, the most remarkable feature of Luttinger liquids is that the correlation functions all decay algebraically. While c sets the velocity scale, the parameter K describes universal features. For instance, for the one-body correlation function $g_1(x)$, one can show that it decays as

$$g_1(x) \propto \left(\frac{1}{x}\right)^{1/2K} \tag{1.44}$$

with the exponent related with K. Here, the algebraic decay of the correlation functions is a pivotal characteristics of Luttinger liquids. Also, one should notice that this approach is called *harmonic fluid approach* (also called "bosonization").

1.3 One-dimensional bosons in a lattice

In the previous section, we have considered the 1D bosons in a continuous system. Now, we turn to the case with the presence of a lattice, i.e. for the Hamiltonian Eq. (1.6) with the external potential $V(x) = V_0\cos(kx)$ with V_0 the amplitude of the lattice. We start with the deep lattice case, where we have the tight-binding Bose-Hubbard model. Then, we move to the more general case, where the problem can be solved either by the Sine-Gordon model analytically, or by the numerical Monte Carlo calculation.

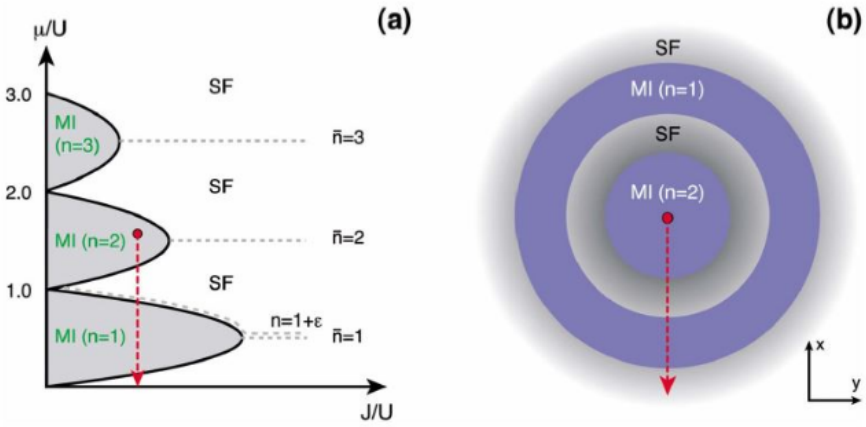

Figure 1.6: Mott transition in 3D Bose-Hubbard model, plot from Ref. [1]. (a). Schematic zero-temperature phase diagram of the 3D Bose-Hubbard model. Dashed lines of constant-integer density $n = 1, 2, 3$ in the SF hit the corresponding MI phases at the tips of the lobes at a critical value of J/U, which decreases with increasing density n. Here, the system is just holding by optical lattices without an harmonic trap. (b). The wedding cake model which presents the phase distribution of cold atoms in optical lattices with a harmonic trap. The starting point of the red arrow is the bottom of the trap. With the direction of the red arrow, the trap potential increases, which decreases the effective chemical potential $\mu(r) = \mu_0 - V_{\text{trap}}(r)$, creates several SF and MI regions.

1.3.1 One-dimensional Bose-Hubbard model

In the deep lattice limit, i.e. V_0 is the largest energy scale in the problem, we can use the tight-binding approximation and the eigenstate $\Psi(x)$ could be written in the basis of the Wannier function. Here, the meaning of the "large enough" lattice amplitude can be translated into two main points: (i) both the thermal and mean interaction energies at the single site are much smaller than the energy separating the ground Bloch band from the first excited band. It means Ψ has no component on the excited band. (ii) the Wannier function decay essentially within a single lattice site, which means only on-site interactions are taken into account. Under these assumptions, we can write the Bose-Hubbard (BH) model in one dimension

$$\mathcal{H} = \sum_j \Big[-J\Big(\hat{b}_j^\dagger \hat{b}_{j+1} + \text{H.c.}\Big) + \frac{U}{2}\hat{b}_j^\dagger \hat{b}_j^\dagger \hat{b}_j \hat{b}_j - \mu \hat{n}_i \Big] \tag{1.45}$$

where j is the index of the lattice site, $\hat{b}_j^\dagger$ and $\hat{b}_j$ are the bosonic creation and annihilation operators on lattice site j, and $\hat{n}_i = \hat{b}_j^\dagger \hat{b}_j$ is the site occupation operator. The pre-factor of the three terms are the tunneling J, interaction strength U and chemical potential μ. For cold atom systems, it's possible to compute the term J and U from first principles, see details in Ref. [1, 42]. The main interest of studying the BH model is the Mott transition, i.e. the transition between a compressible conducting phase named superfluid (SF) and an incompressible insulator phase named Mott insulator (MI).

Mott transition in the three-dimensional Bose-Hubbard model

We start with the phase diagram of SF-MI transition in 3D, and then moving to the case of 1D by comparing their similarities and differences. In 3D,D. Jaksch et al. firstly propose to study the SF-MI transition in cold atom systems theoretically in 1998 [42].

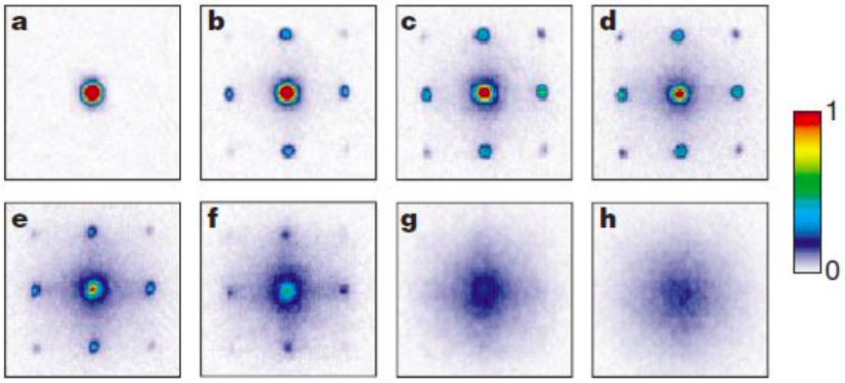

Figure 1.7: Absorption images of multiple matter-wave interference patterns after atoms were released from an optical lattice potential with a potential depth of (a) $0E_{\mathrm{r}}$, (b) $3E_{\mathrm{r}}$, (c) $7E_{\mathrm{r}}$, (d) $10E_{\mathrm{r}}$, (e) $13E_{\mathrm{r}}$, (f) $14E_{\mathrm{r}}$, (g) $16E_{\mathrm{r}}$, and (h) $20E_{\mathrm{r}}$. The ballistic expansion time was 15 ms. The interference pattern visible on panels (a) of the SF phase. In contrast, absence of interference signals the MI phase. This figure is from Ref. [43].

The theoretical phase diagram is plotted in Fig. 1.6. Figure 1.6(a) describes the phase diagram of the 3D BH model without an additional trap. In this diagram, the black solid line notes the transition points of the two phases. On the left side of the line, there exists several MI phases with integer atom number per lattice site. On the right side, there is the region of the SF phase where the atom number in each lattice site fluctuates, which can be associated with inter-site phase coherence. Following the red array, which scans the chemical potential with the fixed interactions, there exists several transitions between SF and MI. In the presence of a harmonic trap, the red arrow could be probed. Shown as Fig. 1.6(b), the phase distribution of the cold atoms in optical lattices with an additional harmonic trap $V_{\mathrm{trap}}(r) = m\omega^2 r^2/2$ is depicted. Here, the starting point of the red arrow is the bottom of the trap. Following the red arrows, the trap potential increases, which decreases the "local chemical potential" $\mu(r) = \mu_0 - V_{\mathrm{trap}}(r)$, and induces several phase transitions between MI and SF. In the red arrow of Fig. 1.6(b), the interaction U and tunneling J is fixed while $\mu(r)$ vanishes. Therefore, it equally corresponds to the red arrow in Fig. 1.6(a).

The first experimental observation of the Mott transition in 3D BH model was first done by M. Greiner et al. in 2002 [43]. In the experiment, they prepare a cold atom gas in a 3D optical lattice in the presence of the harmonic trap. They observe the transition phenomenon by scanning J/U while the atom number is approximately fixed. In their setup, they fixed the scattering length and scanned the parameter J/U by changing the lattice depth. The lattice depth is noted by the unit of the recoil energy $E_{\mathrm{r}} = 2k^2/2m$, which is a natural measure of energy scales in optical lattice potential. Under the scanning, the system enters the MI phase from the SF phase. Figure 1.7 shows the absorption images of the matter wave interference in the experiment which draws the phase transition between SF and MI. For small lattice depth, because of the coherence of SF phase, several interference peaks appear after an expansion period. On the opposite, when the lattice depth is large, the system reaches the MI region. Without any interference, the expansion picture shows a single Gaussian-like distribution, which is characteristic of localization of bosons in single sites. Therefore, from Figure 1.7(a) to Figure 1.7(h), with the increasing of the lattice depth, the phase transition from SF to MI is observed.

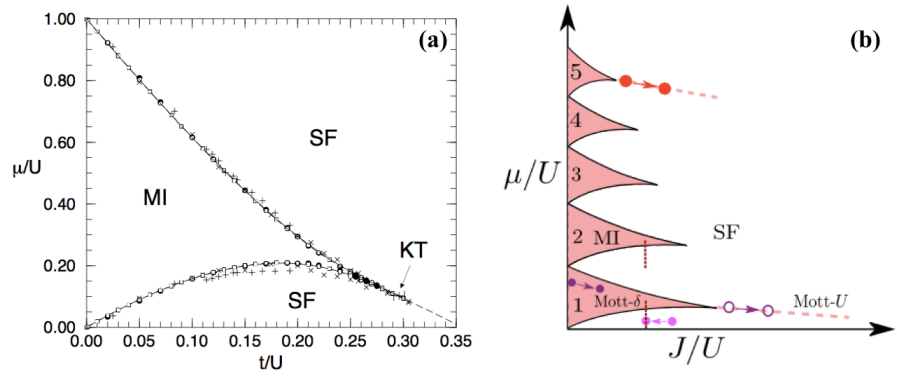

Figure 1.8: Phase diagram of 1D BH model at zero temperature. (a). Phase diagram at the region nearby the first MI lobes presented in Ref. [3]. It contains different set of results from different methods: quantumMonte Carlo results ("+" from Ref. [73] and "x" from Ref. [74]) , earlier DMRG results (filled circle from Ref. [75]), later DMRG results (empty boxes from Ref. [76]), and analysis of 12-th order strong-coupling expansions (solid line from Ref. [77]). (b). Schematic phase diagram of 1D BH model on a larger range of the chemical potential μ, from Ref. [36].

Mott transition in one-dimensional Bose-Hubbard model

Qualitatively, the SF-MI phase transition in optical lattices is similar in all dimensions. However, in one dimension, there are two main features which are different from the case of 3D. First, different from 3D, for arbitrary low potential amplitude, there always exists Mott insulator phase in the 1D lattice model. We will discuss this point in detail in the next subsection. Another main difference is the sharp tip structure of the Mott lobes. In Fig. 1.8, we show the phase diagram of the 1D BH model. In Fig. 1.8. (a), we show the phase diagram in the region of the first Mott lobe $n = 1$ from Ref. [3]. Here, the term t is the tunneling term which is equivalent to our parameter J, The plot consists of datas from different methods of calculations [73–77], see details in the caption. It indicates a sharp tip structure of the Mott lobe totally different from the 3D case. Moreover, in the different calculations, they both find the critical value $(J/U)_c$ on the tip nearby 0.3 with about 3% variation. In Fig. 1.8. (b), we show a schematic phase diagram on a larger range of μ from Ref. [36]. The scale of the diagram is comparable with Fig. 1.6(a) and one can clearly see the difference on the shape of the Mott lobes. Moreover, this plot also helps us to distinguish two main types of the phase transition in 1D:

- Mott-U transition (dashed pink and red line): Fix the fillings n and increasing the value of J/U, one cross from the MI phase to SF phase via the tip of the Mott lobe. This transition is of the Berezinskii-Kosterlitz-Thouless (BKT) type.

- Mott-δ transition (vertical dashed line): fixing the value of J/U and varying the chemical potential μ. The system crosses between a MI phase with commensurate filling and a SF phase with incommensurate filling. The transition is of Prokfovsky-Talapov type [3, 78] and is also called commensurate-incommensurate transition.

Here, one may notice that for the Luttinger parameter K which depicts the algebraic decay of the correlation function, it is finite in the SF phase and zero in the MI phase. In fact, the Luttinger liquid is valid in the SF phase. The MI phase is signalled by an instability and the Luttinger liquid description actually breaks down. For a commensurate order p, it has been shown that the critical values of K are $K_c = 1/p^2$ and $K_c = 2/p^2$ for the Mott-δ and Mott-U transition correspondingly, see details in Refs. [79–81].

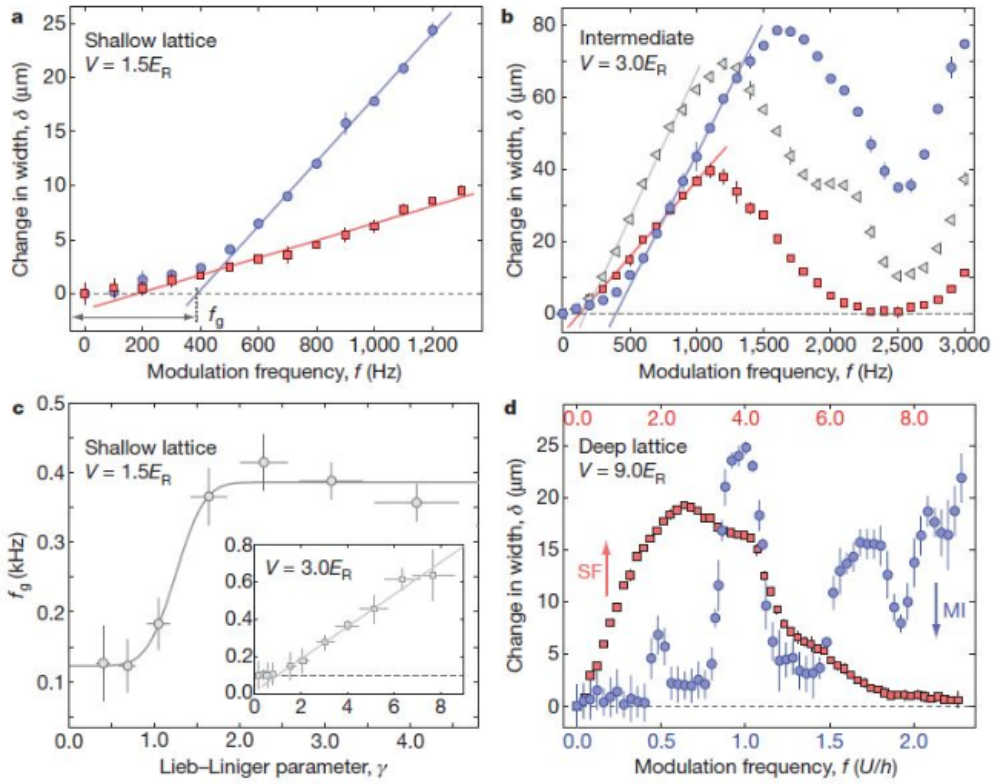

Figure 1.9: Modulation spectroscopy on bosons in shallow and deep optical lattices. (a),(b),(d) are the spectra for low(a), intermediate(b) and high(d) lattice depth V, which depicts the $\delta - f$ dependence. (c) shows the determination of the transition point for the case of the shallow lattice depth $V = 1.5E_r$. The diagram is from Ref. [13].

1.3.2 One-dimensional bosons in shallow periodic lattice

For the case of 1D shallow periodic lattices, the BH model is not effective anymore. Thus, we need a more general model or more powerful computation method for studying the phase diagram.

The Sine-Gordon model

To describe the 1D Bose gases in a shallow periodic potential, one proper way is the Sine-Gordon (SG) model [71]. It is the Luttinger Hamiltonian Eq. (1.43) complemented by a cosine term, which accounts for the shallow periodic potential. Note, however, that the amplitude V is not the bare amplitude of the potential because of the renormalization of the amplitude in the heuristic Hamiltonian. In the Sine-Gordon model, the Hamiltonian writes [13]

$$\mathcal{H} = \frac{\hbar c}{2\pi} \int dx \left(K \left(\frac{\partial \hat{\theta}}{\partial x} \right)^2 + \frac{1}{K} \left(\frac{\partial \hat{\phi}}{\partial x} \right)^2 + \frac{Vn\pi}{\hbar c} \cos(2\hat{\phi}) \right) \tag{1.46}$$

with V the amplitude of the lattice and n the particle density. Based on this model, it's possible to perform analysis and compute the important quantities such as the transition point and critical Luttinger parameters, see details in Refs. [2, 3].

The first experiment studying the 1D Mott transition in a shallow lattice was reported in Ref. [13]. Using a deep 3D lattice, they create the 3D ultracold gases in Mott-Hubbard state with one atom per lattice site. Reducing the lattice depth in one direction, they

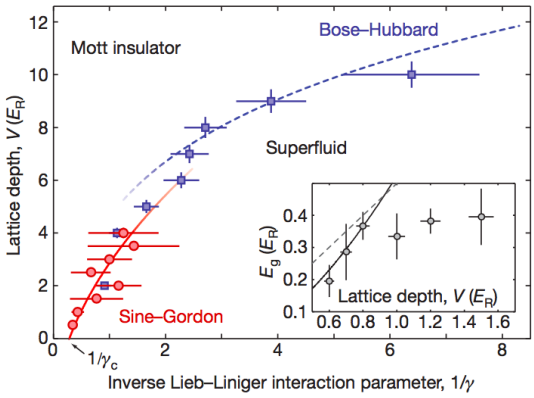

Figure 1.10: Phase diagram of 1D strongly-interacting bosons from Ref. [13]. The two parameters for the phase diagram are the inverse Lieb-Liniger parameter $1/\gamma$ and the lattice depth V in the unit of the recoil energy E_{r}. The inset shows the measured gap energy E_{g} as a function of V.

obtain arrays of 1D tubes in the presence of a periodic potential on the transverse direction. The phase of the system can be probed with the amplitude modulation spectroscopy, which detects the excitation gap and distinguish the gapped Mott insulator phase from the gapless superfluid phase. Firstly, they induce a modulation to the frequency f of the potential of the system. Then, they ramp down the lattice beams, give the system a suspended expansion of $40-60ms$, detect the atoms from time-of-flight, and determine the atomic spatial width δ by a Gaussian fit. By plotting the $\delta-f$ relation and studying the slope, one can obtain the information of the energy gap. The experimental results for different lattice depths are shown in Fig. 1.9(a),(b),(d). For shallow lattices in the strong interaction regime (blue circles), there is a sudden change in the slope which can be associated to the existence of an excitation gap and it is attributed to the signature of Mott insulator. In contrast, in the weak interaction regime (red square), the $\delta-f$ relation presents a linear dependence which reflects the gapless superfluid character of the gas. Similar interpretation can be taken out for the two cases of larger lattice depths, see Fig. 1.9(b) and (d). However, one may notice that the difference between Fig. 1.9(a) and Fig. 1.9(d) gives an obvious comparison to the two limit sides of the model, Sine-Gordon model and BHM model.

To further locate the transition point, one find the intercept of the linear fit with the axis of the curve in Fig. 1.9(a) and (b) which gives the frequency gap f_g. By scanning the Lieb-Liniger parameter γ, the diagram of the $f_g-\gamma$ is depicted in Fig. 1.9(c) (as well as its inset), which gives the transition point between SF and MI phase for a fixed, shallow potential. In the case of a deep lattice, the state of the system is determined by the transport measurement which is more sensitive in this regime. With all the results measure above, they plots the phase diagram for the 1D strongly-interacting bosons, see Fig. 1.10. The transition points are determined either by amplitude modulation spectroscopy (red circles) in the shallow lattice regime, or by transport measurement (blue squares) in the deep lattices regime. The solid and dashed lines are predictions from SG and BH models, which fit well with the experimental data within errorbars, respectively. Also, the value γ_c in the limit $V=0$ fits with the predicted value $\gamma_c=3.5$ in Ref. [82]. However, one may notice the significant errobars on the shallow lattice data points, which did not allow to draw an accurate phase diagram. Also, for the phase transition of an intermediate value of the potential amplitude, a powerful numerical technique is needed.

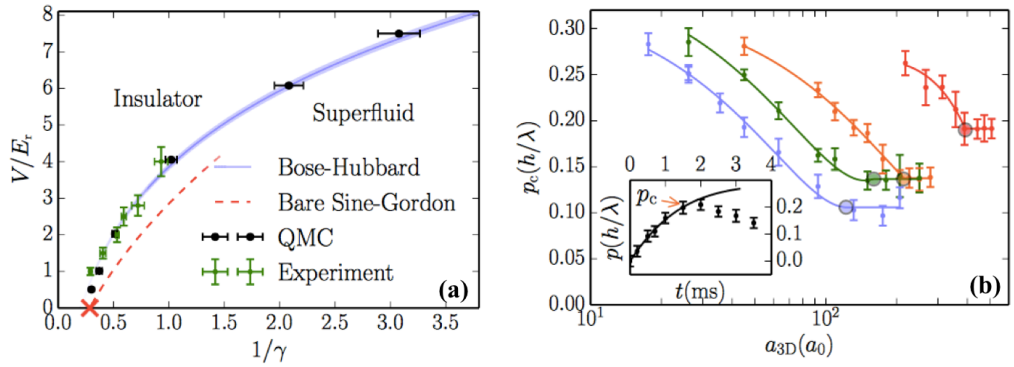

Figure 1.11: (a). Phase diagram in the g-V plane at the commensurate filling $na = 1$. The big black and small green points are QMC theoretical and experimental results. The solid blue line is the BHM prediction and the red dashed line is the result from bare sine-Gordon theory. (b). The critical momentum p_c versus 3D scattering length a_{3D} for different lattice depths: $V/E_r = 1$ (red), 2 (orange), 2.8 (green), 4 (blue). The inset is one example for the time evolution of the momentum distribution peak p for $a_{3D} = 109a_0$ and $V/E_r = 2$. The diagram is from Ref. [15].

The continuous space QMC

To determine the Mott transition point accurately at any values of lattice strength, one needs to seek for powerful numerical tools. The quantum Monte Carlo (QMC) method in continuous space appears to be a solution to this problem (see details about the technique in Chapter 2). From the QMC calculation, one can calculate the superfluid fraction f_s, compressibility κ and Luttinger parameter K. All these three quantities are finite for superfluid (compressible conductance) phase, but zero for Mott insulator (incompressible insulator) phase. From these data, one can locate the Mott transition accurately. In 2016, G. Boéris et al have performed such kind of calculation in Ref. [15]. The main results are shown in Fig. 1.11. In Fig. 1.11 (a), the black dots are the QMC solution. Different from the BH model (blue line) and the Sine-Gordon model (red line) mentioned above, this calculation has no range limitation of the lattice depth and the interaction strength, for it uses the continous space Lieb-Liniger Hamiltonian Eq. (1.6) without any approximation for the lattice potential $V(x) = V\sin^2(kx)$. Based on this Hamiltonian, with the appropriate QMC calculations, the transition curve could be accurately determined in both the shallow and deep lattice regimes. For small γ, the QMC data (black dot) fits well with the BH models (light-blue solid line). However, for large γ, the QMC data separate from the SG model (red dashed line), although they reach the same limit at $V = 0$. In fact, the SG is applicable but the lattice, even weak, significantly renormalize the Luttinger parameter which explains the deviation to the SG prediction with no renormalization (red dashed line).

An experimental measurement is also presented in the same reference. In the experiment, they start with the 3D Bose-Einstein condensate of ^{39}K atoms. With 2D horizontal optical lattice, they create 1000 vertical 1D tubes. By varying the 3D scattering length a_{3D}, they can tune the Lieb-Liniger parameter γ in the range $0.07 - 7.4$. In most of the tubes, they control the fillings $na = 1$. To detect the quantum phase, they suddenly switch off the magnetic field gradient which provides a shift of the potential and drags the system. After the atoms evolve in a time duration t, they switch off all the optical potentials and record the time-of-flight images, especially the momentum distribution peak p. One example of the function $p(t)$ is shown as the black dots in the inset of Fig. 1.11 (b). We can see that $p(t)$ increases up to a critical value p_c. By detecting the value p_c while varying

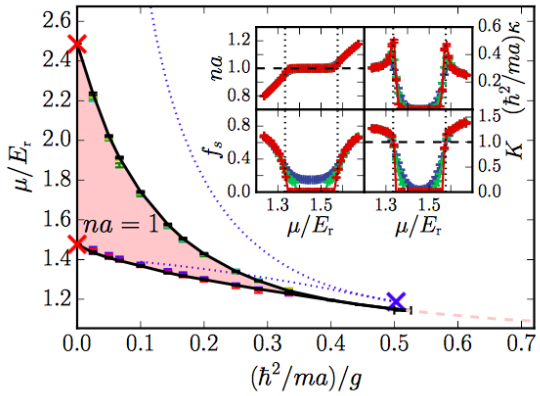

Figure 1.12: Phase diagram in the $g - \mu$ plane from QMC calculations at the potential $V = 2E_r$. There exists two quantum phases: the superfluid(white) and Mott insulator (red). The black points joined by lines are the phase transition points. The blue dashed lines are the prediction from the BH model. In the inset, there are the detailed plots for the four parameters computed from the QMC, namely the particle density n, the compressibility κ, the superfluid fraction f_s and the Luttinger parameter K. These data are at the interaction $g = 7\hbar^2/ma$ and various system sizes $L/a = 30, 50, 100$ (blue, green and red).

a_{3D}, we know that it should show strong dependence in the SF phase and remain constant in the MI phase, see several examples in the main plot of Fig. 1.11 (b). Here, one should notice that p_c should be zero for MI phase, however, some tubes are supefluid so that p_c shows a plateau instead of strictly vanishing. From this scan, one can get the transition point at different potential amplitude V, see green points in Fig. 1.11 (a). Here, we find that it is in good agreement with the theoretical results.

One main interesting outcome from this calculation is that the curve hits the $1/\gamma$ axis at the red cross point, which means that for an arbitrary small amplitude of the lattice potential, there always exists a Mott insulator phase. This is totally different from the 3D case, where below a critical lattice potential amplitude V_c, no MI phase is found. This special property of 1D bosons may be attributed to the specificity of the Tonks-Girardeau limit. In this limit, the Mott lobes can be mapped onto the band gap of ideal fermions in a lattice, which exists at any nonvanishing potential amplitude. Thus, it will form a incompressible insulator states.

Also, in this paper, the authors perform the QMC calculations for a fixed potential amplitude $V = 2E_r$ with various interaction g and chemical potential μ, see Fig. 1.12. In the plot, the black points joined by lines are the transition points determined by the QMC data. One example of which is shown in the inset plot. In the inset, they present the QMC data for the particle density n, the compressibility κ, the superfluid fraction f_s and the Luttinger parameter K at $g = 7\hbar^2/ma$ and various system sizes $L/a = 30, 50, 100$ (blue, green and red). By increasing the sizes, one finds that the transition gets sharper and sharper. Finally, by finding the position $\kappa = \kappa_c = 0$, $f_s = f_{sc} = 0$ and $K = K_c = 1$, they determine the transition points in the main plot (see inset of Fig. 1.12). There, surrounded by a superfluid region (white), they find the Mott lobes $na = 1$ (red) significantly different from the BH prediction. However, they still find the sharp tip structure of the Mott lobes which is different from the 3D case.

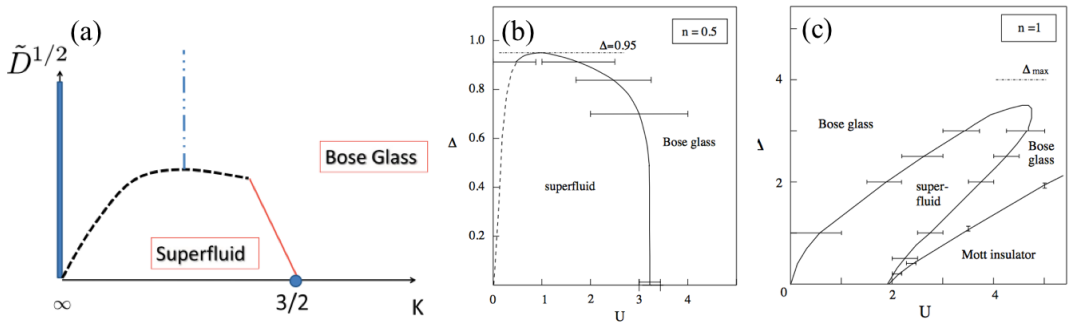

Figure 1.13: Phase diagrams of 1D bosons in disordered potentials at zero temperature. In each plots, the x-axis is the interaction strength and the y-axis is the disorder amplitude. (a). 1D bosons in continuum, calculated from renormalization group techniques. K is the Luttinger parameter and D is the disorder strength. The solid red line is the SF-BG transition calculated from RG calculations, which leads to $K_c = 3/2$ in the limit of zero disorder. The dashed blue line is still open. On the left side, the blue vertical line indicates the Anderson localization phase at zero interaction. This subfigure is from Ref. [3]. (b) and (c) are phase diagrams for 1D Bose-Hubbard model with the on-site energy follows a uniform random distribution in the range $[-\Delta, \Delta]$, calculated from density-matrix renormalization group (DMRG), with incommensurate filling $n = 0.5$ and commensurate filling $n = 1$. These two subfigures are from Ref. [83].

1.3.3 One-dimensional bosons in purely-disordered potentials

The interacting bosons in the presence of a disordered potential, known as the dirty boson problem, is one of the interesting topics on understanding the nature of quantum phases.

At zero temperature, the case of 1D Bose-Hubbard model with incommensurate fillings is similar to the continuous gases, in the presence of disorder. The Hamiltonian of the disordered Bose-Hubbard model writes

$$\mathcal{H} = \sum_j \Big[-J\Big(\hat{b}_j^\dagger \hat{b}_{j+1} + \text{H.c.}\Big) + \frac{U}{2}\hat{b}_j^\dagger \hat{b}_j^\dagger \hat{b}_j \hat{b}_j - V_j \hat{b}_j^\dagger \hat{b}_j \Big] \tag{1.47}$$

with V_j the random onsite energy. The phase diagram of such kinds of systems was first proposed in Ref [52]. The calculations were performed by bosonization and renormalization group (RG) techniques, where they treated the disorder as a perturbation. The results are shown in Fig. 1.13(a). Here, they find two phases: a compressible superfluid, and a incompressible insulator named Bose glass (BG). Different from the Mott insulator we mentioned before, the BG phase is gapless since the insulating property is induced by disorder. For the case of ideal gas ($K = \infty$), all the particles stay on the ground state which forms the Anderson localization. For finite but small interactions, more states are populated although the system remains insulating. In the intermediate interaction regime, when the disorder D is low enough, the conducting islands in the system connect with each other and the system becomes a superfluid. Further increasing the interaction, the bosons are pinned by the disordered potential and the superfluidity is destroyed again. In the strong interaction regime, the phase transition point are determined precisely in Ref [52], see red solid line in Fig. 1.13(a). They are found as BKT type and the critical Luttinger parameter hits $K_c = 3/2$ in the limit $D = 0$. On the contrary, the perturbative RG fails in the weak interaction regime, which is shown as the blue dashed line in Fig. 1.13(a). This part is further studied by numerics in Refs. [22, 83, 84]. In Ref. [83], the phase diagram of 1D BH model with incommensurate filling $n = 0.5$ is obtained by density matrix renormalization group (DMRG), see Fig. 1.13(b). This further confirms the structure

predicted in Fig. 1.13(a).

The case of 1D Bose-Hubbard model with commensurate fillings is slightly different. In the absence of disorder ($D = 0$), we already know from section 1.2.1 that a Mott insulator appears in the strongly-interacting regime. The phase diagram for this case was firstly proposed by Ref. [54] (see detailed discussion in Sec. 5.1.1). Then, a numerical study was performed in Ref. [83], see Fig. 1.13(c). As we expected, a Mott insulator was found in the strongly-interacting regime where the disorder is weak. Also, as argued by Ref. [54], the MI phase is totally surrounded by BG, which equivalently means that there is no direct transition from MI to SF. It has been shown to be correct even in higher dimension, see Ref [85].

In recent years, the case of a quasiperiodic potential, which is the intermediate between the periodic and disordered potentials, has drawn people's attention. Obtaining the phase diagram and study the phase transitions between the SF, MI and BG phases have become one of the main interesting questions to address. In Chapters 4 and 5 of this manuscript, we will introduce the question of quasiperiodic systems and study in detail its phase diagrams.

Conclusion and Outlook

1D bosons are special. In this chapter, we went through the basic knowledge of 1D bosons and some of the main aspect we shall build on in this thesis. We started with the general interest of the 1D bosonic systems, especially indicating its special properties which are totally different from 3D. Then, we introduced the basic concept for 1D continuous bosonic systems. We introduced the two main approaches for describing such kind of systems: the particle description Lieb-Liniger model and the field operator description Luttinger liquid model. Finally, we turn to the introduction of 1D bosons in the presence of an optical lattices, be it deep or shallow. We introduced several theoretical and experimental studies on the superfluid-Mott insulator transition.

Beyond the introduction we presented here, there are still many open questions to be investigates for 1D bosonic systems. These properties forms the basis on which we shall build in the thesis. On the one hand, we shall study the Tan contact in harmonically trapped Lieb-Liniger gases at arbitrary temperature, which is a central characteristics of interacting systems (Chap. 3). On the other hand we shall study localization properties in quasiperiodic potentials, extends the Mott transition in a shallow periodic potential (Chaps 4 and 5)

Chapter 2

Continuous-space quantum Monte Carlo for bosons

Schördinger equation is known to provide a correct description of any quantum system. However, for most of the cases of many-body problems, it is a tremendous challenge to calculate exactly the physical quantities from it, due to the exponential growth of the Hilbert space dimension with the number of particles. To solve this problem, physicists have explored plenty of methods dedicated to certain kinds of Hamiltonian, both analytically and numerically, over the last decades.

For a few Hamiltonians, the equation can be solved analytically. In 1D, see for instance the examples in section 1.2. Beyond those, numerical methods are necessary to an efficient calculation of the solution. For example, exact diagonalization works properly for single particle problem in various inhomogeneous potentials [31, 86], or for the lattice spin systems with a couple of tens of spins [87, 88]. For the Ising model, one can use mean-field approximation in high dimensions to obtain reliable results. In the case of weakly-interacting boson systems, the property could be described properly by the Gross-Pietaevskii equation and Bogoliubov theory [89–91]. However, all those techniques fail for strongly-interacting problems.

Quantum Monte Carlo (QMC) approaches can overcome the difficulty in certain cases. [92] The Monte Carlo approaches contains a large variety of different types and each of them has its pros and cons. The variational Monte Carlo (VMC) applies the variational methods to compute the ground states properties [93,94]. The method is simple but the accuracy of the results depend crucially on the trial wavefunction. The diffusive Monte Carlo (DMC) method generalizes DMC by working with complex wavefunctions and it calculates better the ground state properties by avoiding the systematic errors [95, 96]. To compute the finite-temperature properties, however, one needs to call for more powerful techniques, for instance the path intergral Monte Carlo (PIMC). This method was first introduced by Cerperley and Pollock [97–99], and it provides a first quantitative result for the Helium 4 superfluid transition. In this manuscript, the QMC we used is PIMC, since it solves perfectly the properties of ultracold bosonic systems in various inhomogeneous external potentials, at any regime of interaction and temperature. It fits well with the subject we study. Nevertheless, despite the method is powerful for the system we are interested, we have to point out that the extension of the PIMC to fermionic systems and time-depend problem is extremely difficult. There are other Monte Carlo methods which may overcome those problems in certain cases. For instance, bold diagrammatic Monte Carlo which alleviate the sign problem for fermions [100]. And time-dependent Monte Carlo which opens the way for the study of dynamics [101, 102].

In this Chapter, we first briefly introduce the path integral Monte Carlo in continuous space, which is the QMC method we used widely in our simulation. We shall describe

the basic PIMC as introduced in the pioneering work of Cerperley and Pollock [97–99]. Then, we present the building blocks of Monte Carlo methods, namely the basic moves with the so-called worm algorithm. It is first developed by Prokov'ev and Svistunov [58, 59], which improved strongly the computation efficiency for certain variables such as the superfluid fraction. Finally, we briefly describe how we compute the the physically-relevant observables in detail, which is the final goal of the QMC calculation.

2.1 Path-integral Monte Carlo for interacting bosons

In this section, we present the PIMC method for interacting bosons at finite temperature as in [97, 99]. There are two main ideas of the PIMC. First, using the Feynman path integral representation, one can map the quantum systems with interacting particles onto a classical system with interacting polymers. Then, we sample the partition function of such a system stochastically using the Monte Carlo approach. Finally, we obtain the targeted observables by the averaging values over the generated polymer configurations.

2.1.1 Feynman path integral for a single particle

Quantum mechanics, formulated by Dirac, Heisenberg, and Hilbert in 1920s, depicts the physical states of a system by vectors in a Hilbert space. The time evolution of such a state is controlled by the operator called Hamiltonian. Thanks to the "canonical quantization", classical quantities such as the position, the momentum, and the Hamiltonian, are promoted to operators satisfying certain commmutation relations.

The path integral approach is another formulation. It formulates quantum mechanics in such a way to recover the least action principle in the classical limit ($h \to 0$). The essential idea was first presented in the works of Wiener and Dirac [103–105], and formalized by Feynman [106]. The later has also proved that it's equivalence with standard quantum mechanics. Here, we start with the path integral formulation of a single particle, which is the conceptual basis of the PIMC.

Imaginary time path integral for a single particle

Considering a single particle evolving in a d-dimensional space, its Hamiltonian reads as

$$\hat{H} = \hat{H}_0 + V(\hat{\mathbf{r}}) \tag{2.1}$$

with $\hat{H}_0 = \frac{\hat{\mathbf{p}}^2}{2m}$ the kinetic term, $\hat{\mathbf{p}} = -i\hbar\nabla$ the momentum operator, m the particle mass and V the external potential. The main quantity of interest is the propagation amplitude $\langle \mathbf{r}_f | e^{-\tau \hat{H}} | \mathbf{r}_i \rangle$ between the initial and final points $\mathbf{r}_i$ and $\mathbf{r}_f$. If τ is a purely imaginary number, this quantity stands for the probability amplitude for the particle to propagate from $\mathbf{r}_i$ to $\mathbf{r}_f$ during the real time $\tau = it/\hbar$, under the Hamiltonian $\hat{H}$. In the following, we call τ the imaginary time, although it has the dimension of an inverse energy. Normally, this exponential term is difficult to be computed directly, since the kinetic and potential term in the Hamiltonian do not commute. To overcome this difficulty, we split the propagator into J pieces in the imaginary time, with each piece a shorter time propagator in a time interval $\epsilon = \tau/J$. Introducing the identity operator $\hat{I} = \int d\mathbf{r} |\mathbf{r}\rangle\langle\mathbf{r}|$ between each ϵ step, it writes

$$\langle \mathbf{r}_f | e^{-\tau \hat{H}} | \mathbf{r}_i \rangle = \int d\mathbf{r}_{J-1} ... d\mathbf{r}_1 \ \langle \mathbf{r}_f | e^{-\epsilon \hat{H}} | \mathbf{r}_{J-1} \rangle \times ... \times \langle \mathbf{r}_1 | e^{-\epsilon \hat{H}} | \mathbf{r}_i \rangle. \tag{2.2}$$

Using the primitive approximation $e^{-\epsilon(\hat{A}+\hat{B})} = e^{-\epsilon\hat{A}} e^{-\epsilon\hat{B}} + \mathcal{O}(\epsilon^2)$, we can write the short-time propagator as

$$\langle \mathbf{r}' | e^{-\epsilon \hat{H}} | \mathbf{r} \rangle = \langle \mathbf{r}' | e^{-\epsilon \hat{H}_0} | \mathbf{r} \rangle e^{-\epsilon V(\mathbf{r})} + \mathcal{O}(\epsilon^2). \tag{2.3}$$

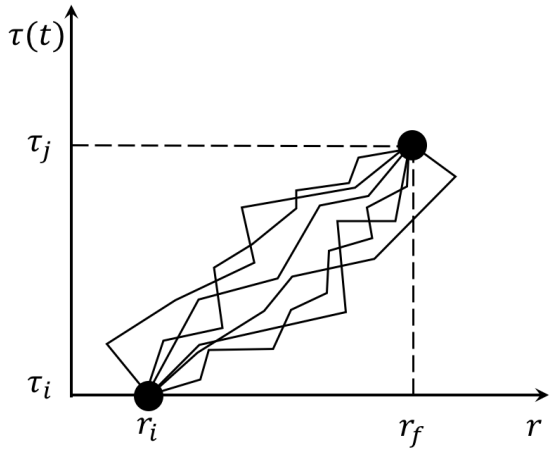

Figure 2.1: Path integral representation of the single particle propagator $\langle \mathbf{r}_f | e^{-\tau \hat{H}} | \mathbf{r}_i \rangle$. Its value is calculated by summing over the exponential weight over all the possible paths joining $\mathbf{r}_i$ and $\mathbf{r}_f$. The imaginary time of the two points are τ_i and τ_j.

The free propagator term can be computed in the momentum space,

$$\langle \mathbf{r}' | e^{-\epsilon \hat{H}_0} | \mathbf{r} \rangle = \Big(\frac{m}{2\pi\hbar^2 \epsilon} \Big)^{d/2} e^{-\frac{m}{\hbar^2} \frac{(\mathbf{r}-\mathbf{r}')^2}{2\epsilon}}. \tag{2.4}$$

In the end, the full propagator could be written as

$$\langle \mathbf{r}_f | e^{-\tau \hat{H}} | \mathbf{r}_i \rangle = \Big(\frac{m}{2\pi\hbar^2 \epsilon} \Big)^{Jd/2} \left\{ \int d\mathbf{r}_{J-1} ... d\mathbf{r}_1 e^{-\sum_{j=0}^{J-1} \left[\frac{m}{\hbar^2} \frac{(\mathbf{r}_{j+1} - \mathbf{r}'_j)^2}{2\epsilon} + \epsilon V(\mathbf{r}_j) \right]} + \mathcal{O}(\epsilon) \right\}. \tag{2.5}$$

with the notation $\mathbf{r}_0 = \mathbf{r}_i$ and $\mathbf{r}_J = \mathbf{r}_f$ for the initial and final positions. This expression describes the propagation of the particle from $\mathbf{r}_i$ to $\mathbf{r}_f$ during the imaginary time τ with time step ϵ. The quantity $\mathbf{r}_j$ gives the position of the particle at the time $j\epsilon$. Each possible sequence of $(\mathbf{r}_0, ..., \mathbf{r}_j, .., \mathbf{r}_J)$ corresponds to a possible trajectory along the imaginary timeline $[0, \tau]$. The integral over the $\mathbf{r}_j$ corresponds to the sum over all the possible paths between $\mathbf{r}_i$ and $\mathbf{r}_f$, with each path associated with a specific weight. Taking the continuous time limit $\epsilon \to 0$, we find the final formula for the expression

$$\langle \mathbf{r}_f | e^{-\tau \hat{H}} | \mathbf{r}_i \rangle \propto \int_{\mathbf{r}(0)=\mathbf{r}_i}^{\mathbf{r}(\tau)=\mathbf{r}_f} \mathcal{D}\mathbf{r}(\tau') e^{-\int_0^\tau d\tau' \left[\frac{m}{2\hbar^2} (\frac{d\mathbf{r}}{d\tau})^2 + V(\mathbf{r}) \right]}, \tag{2.6}$$

where the integral is performed over all the possible paths $\mathbf{r}(\tau')$ going from $\mathbf{r}_i$ to $\mathbf{r}_f$. Figure. 2.1 shows an illustration for such a integral. The exponential term in Eq. (2.6) gives a certain weight to each path and the propagator is calculated by summing over all the possible paths. One should notice that the paths can go beyond the initial $\mathbf{r}_i$ and final position $\mathbf{r}_f$.

Here, we shall make two remarks linked with the PIMC method. Firstly, the calculation of the propagator is accurate if the time step ϵ is small enough. Thus, the parameter ϵ is a numerical parameter in the actual code which will influence the efficiency and accuracy of the calculations. It is thus important to take proper care of this parameter. The actual approximation in the code goes beyond the primitive approximation, and it will be presented in the section 2.1.3. Secondly, the propagator is written as an weighted integral over all the configurations of propagation. In principle, it's very complicated to calculate such an integral. In PIMC, this integral is computed efficiently by the numerical Monte Carlo method, and it will be described in section 2.1.4 and 2.1.5.

Path integral in real time

For completeness, we provide the classical limit of the path integral formalism, which corresponds to the original one proposed by Dirac and Feynman. Using the correspondence $\tau \to it/\hbar$ with t the real time, we obtain

$$\langle \mathbf{r}_f | e^{-it\hat{H}/\hbar} | \mathbf{r}_i \rangle \propto \int_{\mathbf{r}(0)=\mathbf{r}_i}^{\mathbf{r}(t)=\mathbf{r}_f} \mathcal{D}\mathbf{r}(t') \; e^{\frac{i}{\hbar} S[\mathbf{r}(t']}, \tag{2.7}$$

with $S[\mathbf{r}(t'] = \int_0^{t'} [\frac{1}{2} m \dot{\mathbf{r}}^2 - V(\mathbf{r})]$ is the action of the classical system. Similarly, the real-time propagator is computed with the sum over all the possible paths with an assigned phase proportional to the classical action. In the limit $\hbar \to 0$, thanks to the stationary phase argument, only the paths which extremize the action contribute to the integral and the other ones are cancelled. This recovers exactly the principle of least action in classical mechanics.

Feynman-Kac formula

In Eq. (2.7), we drop the prefactor for simplicity. However, the term could actually blow up in the continuous limit. To avoid this difficulty, one possibility is to divide it by the free propagator $\langle \mathbf{r}_f | e^{-it\hat{H}_0/\hbar} | \mathbf{r}_i \rangle$. The prefactors are cancelled since they are identical in both cases. Then, one may recognize the term

$$\pi[\mathbf{r}(\tau')] = e^{-\int_0^\tau \; d\tau' \frac{m}{2\hbar^2} (\frac{d\mathbf{r}}{d\tau})^2} / \int_{\mathbf{r}(0)=\mathbf{r}_i}^{\mathbf{r}(\tau)=\mathbf{r}_f} \mathcal{D}\mathbf{r}(\tau') e^{-\int_0^\tau \; d\tau' \frac{m}{2\hbar^2} (\frac{d\mathbf{r}}{d\tau})^2} \tag{2.8}$$

is the probability density of a Brownian process with volatility $\sigma = \sqrt{\hbar^2/m}$. Because the process is fixed to start and end at certain fixed point, it's called a Brownian bridge between $\mathbf{r}_i$ and $\mathbf{r}_j$. Using the stochastic interpretation, one shall get the so-called Feynman-Kac formula [107],

$$\frac{\langle \mathbf{r_f} | e^{-\tau \hat{H}} | \mathbf{r_i} \rangle}{\langle \mathbf{r_f} | e^{-\tau \hat{H}_0} | \mathbf{r_i} \rangle} = \left\langle \exp \left[- \int_0^\tau d\tau' V(\mathbf{r}(\tau')) \right] \right\rangle_\pi \tag{2.9}$$

where $< ... >_\pi$ represents the expectation value under the Brownian measure Eq. 2.8. This formula will be useful in further calculations of the imaginary time propagator, see section 2.1.3.

2.1.2 Feynman path integral for many-body bosonic systems

Now, consider a N boson system in a d-dimensional continuous space. We will derive the path integral representation used in the PIMC algorithm. The main aim of the method is to compute the expectation value of an observable $\hat{A}$ of interest at thermodynamic equilibrium, in the canonical ensemble at temperature T. It can be written as

$$\langle A \rangle = \frac{1}{Z} \mathrm{Tr}[e^{-\beta \hat{H}} \hat{A}] \tag{2.10}$$

where $\beta = 1/k_\mathrm{B}T$ is the inverse temperature and $Z = \mathrm{Tr}[e^{-\beta \hat{H}}]$ is the partition function. Here, we use the variable $\mathbf{R} = (\mathbf{r_1}, \mathbf{r_2}, ..., \mathbf{r_N})$ to denote the positions of the N particles. To take into account the indistinguishability of identical bosons, we introduce the symmetrization operator

$$\hat{S} = \frac{1}{N!} \sum_{\sigma \in \Pi} |\sigma \cdot \mathbf{R}\rangle \langle \mathbf{R}| \tag{2.11}$$

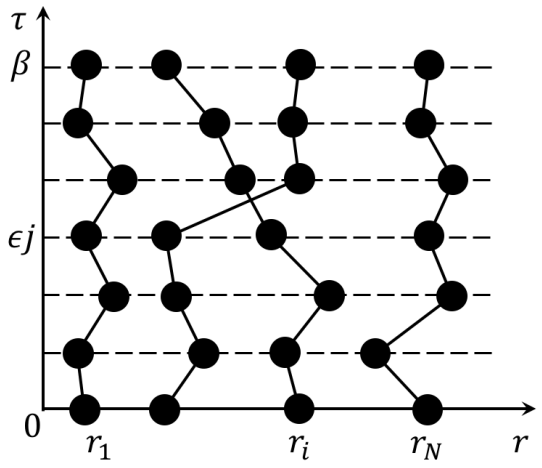

Figure 2.2: Path integral representation of the many particle propagator. The plot illustrate the configuration of N particles which enters the partition function.

where Π stands for the group of permutations of the N elements and $|\sigma\cdot\mathbf{R}\rangle = |\mathbf{r}_{\sigma_1}, \mathbf{r}_{\sigma_2}..., \mathbf{r}_{\sigma_N}\rangle$ is one of the possible permutations of $\mathbf{R}$. Therefore, the trace of an operator $\hat{X}$ should be written as

$$Tr[\hat{X}] = \int d\mathbf{R}\langle\mathbf{R}|\hat{X}\hat{S}|\mathbf{R}\rangle. \tag{2.12}$$

Then, similarly as the single particle case, splitting the inverse temperature axis $[0, \beta]$ in infinitesimal portions of step $\varepsilon = \beta/J$ with J the number of steps, we can finally write

$$Tr[e^{-\beta\hat{H}}\hat{A}] = \frac{1}{N!}\sum_{\sigma\in\Pi}\int d\mathbf{R_{J-1}}...d\mathbf{R_0}\langle\sigma\cdot\mathbf{R_0}|e^{-\epsilon\hat{H}}|\mathbf{R_{J-1}}\rangle\times...\times\langle\mathbf{R_2}|e^{-\epsilon\hat{H}}|\mathbf{R_1}\rangle\times\langle\mathbf{R_1}|e^{-\epsilon\hat{H}}\hat{A}|\mathbf{R_0}\rangle. \tag{2.13}$$

Here, one should notice that the expression is obtained thanks to the fact that $\hat{S}$ commutes with $\hat{H}$, $\hat{A}$ as well as $\hat{I}$, and it satisfies the condition $\hat{S}^2 = \hat{S}$.

In the expression Eq.(2.13), a possible distribution $(\mathbf{R_1}, \mathbf{R_2}, ..., \mathbf{R_J})$ is defined as a configuration $\mathcal{C}$. A typical example of configuration is shown in Fig. 2.2. In the plot, each particle propagates along a trajectory in imaginary time from $\tau = 0$ to β, which is called a worldline. The position of the i-th particle at time $j\epsilon$ is called bead. It is noted as r_i^j and depicted as a black disk. Moreover, one should notice that the condition $|\mathbf{R_J}\rangle = |\sigma\cdot\mathbf{R_0}\rangle$ due to the definition of trace, which implies β-periodicity along the imaginary time axis. It also indicates that one particle could choose to close at the initial position of another particle, which fits with the particle indistinguisability. The exchange cycle reflects the quantum exchange appearing at low temperature, especially involved in the phenomenon such as Bose-Einstein condensation and superfluidity.

In order to simply the notation, we may introduce the weight of the configuration $\mathcal{C}$,

$$\mathcal{W}(\mathcal{C}) = \frac{1}{N!}\langle\sigma\cdot\mathbf{R_0}|e^{-\epsilon\hat{H}}|\mathbf{R_{J-1}}\rangle\times...\times\langle\mathbf{R_1}|e^{-\epsilon\hat{H}}|\mathbf{R_0}\rangle \tag{2.14}$$

and the normalized weight $\pi(\mathcal{C}) = \mathcal{W}(\mathcal{C})/Z$. They satisfy the normalization $\int\pi(\mathcal{C})d\mathcal{C} = 1$. Moreover, we may define the path-integral estimator for observable $\hat{A}$, which presents as

$$\mathcal{A}(\mathcal{C}) = \frac{\langle\mathbf{R_1}|e^{-\epsilon\hat{H}}\hat{A}|\mathbf{R_0}\rangle}{\langle\mathbf{R_1}|e^{-\epsilon\hat{H}}|\mathbf{R_0}\rangle}. \tag{2.15}$$

We can then write the expectation value of the obervable $\hat{A}$ as

$$\langle\hat{A}\rangle = \int\pi(\mathcal{C})\mathcal{A}(\mathcal{C})d\mathcal{C} \tag{2.16}$$

In this formula, $\mathcal{A}(\mathcal{C})$ is the value of $\hat{A}$ we calculated associated to the configuration $\mathcal{C}$ and $\pi(\mathcal{C})$ is the corresponding statistical distribution. This expression is exact but remains hard to compute directly. Therefore, we shall introduce several extra approximation steps in the next section.

2.1.3 The imaginary time propagator

The configuration weight, $\mathcal{W}(\mathcal{C})$, is built out of the imaginary-time many-body propagator. We may notice that it is the density matrix $\rho(\mathbf{R}', \mathbf{R}, \epsilon) = \langle \mathbf{R}'|e^{-\epsilon \hat{H}}|\mathbf{R}\rangle$ up to a normalization factor. In this subsection, we introduce several approximations to compute the propagator in the limit $\epsilon \to 0$. For concreteness, we write the Hamiltonian of the typical bosonic system with two-body interactions$\hat{H} = \hat{H}_0 + \hat{H}_1 + \hat{H}_2$, with

$$\hat{H}_0 = \sum_{i=1}^{N} \frac{\hat{\mathbf{p}}_\mathbf{i}^{\,2}}{2m}, \quad \hat{H}_1 = \sum_{i=1}^{N} V_1(\hat{\mathbf{r}}_\mathbf{i}), \quad \hat{H}_2 = \sum_{i<j} V_2(\hat{\mathbf{r}}_\mathbf{i} - \hat{\mathbf{r}}_\mathbf{j}). \tag{2.17}$$

Here, the three terms in the Hamiltonian are respectively the kinetic term, the external potential and the two-body interactions. Then, we can write the density matrix

$$\rho(\mathbf{R}', \mathbf{R}, \epsilon) = \rho_0(\mathbf{R}', \mathbf{R}, \epsilon) e^{-U(\mathbf{R}', \mathbf{R}, \epsilon)}, \tag{2.18}$$

where ρ_0 is the free density matrix associated to the Hamiltonian H_0 and U is called the action. Usually, the action could be written as $U = U_1 + U_2$, with the one-body and two-body interaction potential terms correspondingly.

Free density matrix

Consider only the free particle Hamiltonian $\hat{H}_0$, it is trivial that the density matrix writes

$$\rho_0(\mathbf{R}', \mathbf{R}, \epsilon) = \prod_{j=1}^{N} \rho_0(\mathbf{r}'_\mathbf{j}, \mathbf{r}_\mathbf{j}, \epsilon), \tag{2.19}$$

where $\rho_0(\mathbf{r}'_\mathbf{j}, \mathbf{r}_\mathbf{j}, \epsilon) = (m/2\pi\hbar^2\epsilon)^{d/2} \exp(-m(\mathbf{r} - \mathbf{r}')^2/2\hbar^2\epsilon)$ is the free density matrix for one particle. The free density matrix actually introduces a strong condition on the configurations shown in Fig. 2.2. Since the particle position evolves in imaginary time steps by a Gaussian with standard deviation $\sqrt{\epsilon}$ in the unit of $\hbar^2/m$, two connected beads on a single worldline are seperated by at most several $\sqrt{\epsilon}$. In the limit $\epsilon \to 0$, the paths becomes Brownian process with volatility $\sqrt{\hbar^2\epsilon/m}$.

The one-body action: Trotter-Suzuki approximation

The main difficulty to calculate the action of the full Hamiltonian is the fact that the kinetic and potential terms of the Hamiltonian do not commute with each other in general. It forbids the splitting of the exponential of the Hamiltonian into separated exponential terms. However, for small ϵ, the splitting is possible thanks to the Trotter-Suzuki approximation [108, 109],

$$e^{-\epsilon(\hat{A}+\hat{B})} = e^{-\frac{1}{2}\epsilon\hat{B}} e^{-\epsilon\hat{A}} e^{-\frac{1}{2}\epsilon\hat{B}} + \mathcal{O}(\epsilon^3). \tag{2.20}$$

This approximation is an improved version of the primitive approximation introduced in section 2.1.1, with the validity of higher order of ϵ. Then, by setting $\hat{A} = \hat{H}_0 + \hat{H}_2$ and $\hat{B} = \hat{H}_1$, one can extract the one-body potential from the propagator. Therefore, the one-body action in the propagator writes finally

$$U_1(\mathbf{R}, \mathbf{R}', \epsilon) = \epsilon \sum_{j=1}^{N} \frac{V_1(\mathbf{r}'_\mathbf{j}) + V_1(\mathbf{r}_\mathbf{j})}{2}. \tag{2.21}$$

Then, the propagator terms for $\hat{H}_0 + \hat{H}_2$ will be evaluated using further assumptions in the next part. Here, one should notice that there are other possibilities for using the Trotter-Suzuki approximation. For instance, one can split the Hamiltonian by $\hat{A} = \hat{H}_0$ and $\hat{B} = \hat{H}_1 + \hat{H}_2$, in order to obtain the free particle and potential part separately. However, the first way of separating has an advantage that one can use the standard scattering theory, so we insist on this method for the QMC calculations in this thesis.

The two-body action: Pair-product approximation

Now, we compute the propagator with the term $\hat{A} = \hat{H}_0 + \hat{H}_2$. The first approximation we use here is the pair-product approximation [110], which allows us to write the many-body density matrix as a product of two-body density matrices. This approximation is sufficiently precise for dilute gases and short-range interactions, i.e. the system we studied. First of all, using the Feynman-Kac formula [99], we shall write the action

$$e^{-U_2(\mathbf{R}',\mathbf{R},\epsilon)} = \frac{\langle \mathbf{R}'|e^{-\epsilon(\hat{H}_0+\hat{H}_2)}|\mathbf{R}\rangle}{\langle \mathbf{R}'|e^{-\epsilon\hat{H}_0}|\mathbf{R}\rangle} = \left\langle \prod_{i<j} \exp\left[-\int_0^\epsilon d\tau V_2(\mathbf{r_i}(\tau) - \mathbf{r_j}(\tau))\right]\right\rangle \tag{2.22}$$

which average is performed over the Brownian bridges joining the two points $\mathbf{R}$ and $\mathbf{R}'$. If we assume that $\sqrt{\epsilon}$ and the typical potential range b are much smaller than the mean interparticle distance $n^{-1/d}$, one particular path will typically interact with at most one single other path. Then, the $N(N\text{-}1)/2$ factors on the right-hand side could be considered to be independent. Therefore, we shall write it as,

$$e^{-U_2(\mathbf{R}',\mathbf{R},\epsilon)} = \prod_{i<j} \left\langle exp\left[-\int_0^\epsilon d\tau V_2(\mathbf{r_i}(\tau) - \mathbf{r_j}(\tau))\right]\right\rangle \tag{2.23}$$

Using the Feynman-Kac formula again, we shall get

$$U_2(\mathbf{R}', \mathbf{R}, \epsilon) = \sum_{i<j} u_2(\mathbf{r_i'}, \mathbf{r_j'}, \mathbf{r_i}, \mathbf{r_j}, \epsilon) \tag{2.24}$$

where $u_2(\mathbf{r_i'}, \mathbf{r_j'}, \mathbf{r_i}, \mathbf{r_j}, \epsilon)$ is the action for two interacting particles. As we mentioned in the beginning, the derivation is performed under the assumption of a rapidly decaying interaction potential. However, for the case of long-range interactions, it's also guaranteed to be valid for small enough ϵ, although less precise. This is because in the limit $\epsilon \to 0$, it reduces to the Trotter approximation.

The two-body action: Change of reference

For further simplifying the two-body matrix, we turn to work in the center of mass frame. We introduce the center of mass coordinate $\mathbf{r}_{CM} = (\mathbf{r}_1 + \mathbf{r}_2)/2$, the relative coordinate $\mathbf{r}_{rel} = \mathbf{r}_1 - \mathbf{r}_2$, the total mass $M = 2m$ and the reduced mass $m* = m/2$. Then, the two-body Hamiltonian writes

$$\hat{H} = \frac{\hat{\mathbf{p}}_{CM}^2}{2M} + \frac{\hat{\mathbf{p}}_{rel}^2}{2m*} + V_2(\mathbf{r}_{rel}). \tag{2.25}$$

Thanks to the fact that the momentum operator $\hat{\mathbf{p}}_{CM}^2$ commutes with the term $\mathbf{r}_{rel}$, the two-body density matrix can be factorized as

$$\langle \mathbf{r}_1', \mathbf{r}_2'|e^{-\epsilon\hat{H}}|\mathbf{r}_1, \mathbf{r}_2\rangle = \langle \mathbf{r}_{CM}'|e^{-\epsilon\frac{\hat{\mathbf{p}}_{CM}^2}{2M}}|\mathbf{r}_{CM}\rangle \langle \mathbf{r}_{\mathrm{rel}}'|e^{-\epsilon\left[\frac{\hat{\mathbf{p}}_{\mathrm{rel}}^2}{2m*} + V_2(\mathbf{r}_{\mathrm{rel}})\right]}|\mathbf{r}_{\mathrm{rel}}\rangle. \tag{2.26}$$

Then, dividing both sides by the free density matrix, one shall find that the two-body action reduces to

$$u_2(\mathbf{r_1'}, \mathbf{r_2'}, \mathbf{r_1}, \mathbf{r_2}, \epsilon) = u_{rel}(\mathbf{r_1'} - \mathbf{r_2'}, \mathbf{r_1} - \mathbf{r_2}, \epsilon) = u_{rel}(\mathbf{r}_{\mathrm{rel}}', \mathbf{r}_{\mathrm{rel}}, \epsilon), \tag{2.27}$$

with u_{rel} the action for an effective particle of mass μ in the external potential V_2. For certain cases, this action can be calculated analytically. For instance, for the 1D delta interaction potential $\hat{H}_2 = g\sum_{j<\ell}\delta(x_j - x_\ell)$, i.e. the system we are interested, the two-body action writes [111]

$$\langle \mathbf{r}'_{\rm rel}|e^{-\epsilon[\frac{\hat{\mathbf{p}}^2_{\rm rel}}{2\mu}+V_2(\mathbf{r}_{\rm rel})]}|\mathbf{r}_{\rm rel}\rangle = 1 - \exp\left(-\frac{\mu(\mathbf{r}_{\rm rel}\mathbf{r}'_{\rm rel} + |\mathbf{r}_{\rm rel}\mathbf{r}'_{\rm rel}|)}{\epsilon\hbar^2}\right) \times \sqrt{\frac{\pi\mu\epsilon}{2}}\frac{g}{\hbar}{\rm erfc}(u){\rm exp}(u) \tag{2.28}$$

with $u = m*(|\mathbf{r}_{\rm rel}| + |\mathbf{r}'_{\rm rel}| + g\epsilon)/\sqrt{2m*\epsilon\hbar^2}$ and erfc is the complementary error function. In the actual calculations, instead of going through all pairs $\mathbf{r}_i$ and $\mathbf{r}_j$, we only compute the term with $|\mathbf{r}_i - \mathbf{r}_j| < r_{\rm judge}$ and $r_{\rm judge}$ is a threshold at several $\sqrt{\epsilon}$. The other terms are extremely small and can be ignored. This is consistent with the property of the short-range interactions and it improves the efficiency of the calculation.

Moreover, such an analytical forms for the two-body propagator are also available for delta range interactions at higher dimension [28, 111]. However, there are some other cases where the analytical form is not provided. In this case, one shall evaluate the value numerically using the procedure explained in the next paragraph.

The numerical method: Feynman-Kac formula and Matrix squaring technique

When an analytical formula for the propagator is not available, for instance the Hamiltonian contains certain types of long-range interactions, one should calculate the propagator using numerical procedures. Here, we propose two possible methods to do that.

First, one can evaluate the propagator using the Feynman-Kac formula [107]. For each considered pairs of $\mathbf{r}$ and $\mathbf{r}'$, one can calculate the right-hand side of Eq. (2.9) using a Monte-Carlo approach. We can discretize the Brownian bridge by a smaller time step $\eta = \epsilon/Q$ with Q some integer. Then, one can use the Lévy construction to sample the path [112] and obtain the action as an average over all the generated path.

A second possible method is called matrix squaring technique [107,113]. The main issue is that evaluating the propagator with direct use of Trotter approximation on discretization step ϵ is not accurate enough. Thus, one starts with the single-density matrix $M_0 = e^{-\eta\hat{A}}$ at a higher temperature $\eta = 2^{-K}\epsilon$ where K is a integer, i.e. a smaller resolution step. Then, we are allowed to use the Trotter approximation to separate the interaction term and we have

$$M_0(\mathbf{r}_{\rm rel}, \mathbf{r}_{\rm rel'}) = e^{\frac{\eta}{2}[V_2(\mathbf{r}_{\rm rel})+V_2(\mathbf{r}_{\rm rel'})]}\rho_0(\mathbf{r}_{\rm rel'}, \mathbf{r}_{\rm rel}, \epsilon). \tag{2.29}$$

Then, we can generate a sequence of matrices by $M_{k+1} = M_k^2$ and after K iterations, we can get the matrix at the temperature ϵ.

2.1.4 Sampling the configurations using the Monte Carlo approach

In the previous paragraphs, we have introduced the path-integral formulation to describe the quantum many-body system by a picture of classical statistical physics with interacting polymers. The thermodynamical observables are then calculated by the Eq. (2.16), with $\pi(\mathcal{C})$ the weight Eq. (2.14) calculated by the method introduced in section 2.1.3 at small ϵ limit. However, it is still hard to evaluate the integral (2.16) over all the possible configurations.

The rectangular method, which numerically calculate the value of integrals $A = \int f(x)dx$ by dividing the configuration space into small cells and summing the integrand on the points of the grids times the elementary volume of the cell, i.e. $A \simeq \sum_i f(x_i)dx_i$,are widely used in various calculations. However, the computing cost grows exponentially with the dimensionality of the integrated element dx. In the integral Eq. (2.13), the dimension of

the configuration space is NdJ, which grows to infinitely large at small ϵ limit. Thus, one calls for methods beyond the rectangular one and compute the result efficiently. The Monte Carlo approach, which samples the configurations stochastically, is one of the good choices for this situation. One of the key reasons for its success is that they can perform *importance sampling*, which means the highly probable configurations are generated much more than the one with low probability. On the contrary, the rectangular method treats all the configurations equally. In this section, we first describe the Monte Carlo approach from the general point of view, and then move to the specific case which we are interested in.

Monte Carlo method for calculating integrals numerically

Now, we explain the core idea about the Monte Carlo approach [1] for calculating integrals. Considering a real-valued function $f : \mathbb{R}^D \to \mathbb{R}$, we want to calculate

$$I = \int_{\mathbb{R}^D} f(x)dx \tag{2.30}$$

Now, we introduce a random variable X, which takes values in the integration space $\mathbb{R}^D$. The probability distribution of X is noted as π which is normalized to unity, $\int \pi(x)\mathrm{d}x = 1$. We should notice that a hidden condition here is that π is strictly positive since it represents the probability density. Then, the integral may be rewritten as

$$I = \int_{\mathbb{R}^D} \frac{f(x)}{\pi(x)}\pi(x)dx = \langle \mathcal{I}(X) \rangle_\pi \tag{2.31}$$

where $\mathcal{I}(X) = f(X)/\pi(X)$ is a random variable linked with X and thus the value of I can be understood by the expectation value of $(I)(X)$ under the probability distribution π. The Monte Carlo approach propose to compute this integral using the law of large numbers. The basic idea is to generate a large number of independent samples $X_1, X_2, ..., X_n$ following the probability density π, and to estimate the integral I by calculating the average

$$\hat{I} = \frac{\mathcal{I}(X_1) + \mathcal{I}(X_2) + ... + \mathcal{I}(X_n)}{n}. \tag{2.32}$$

In the limit $n \to \infty$, the estimator $\hat{I}$ converges to the value of the integral almost surely. However, in actual simulation, only finite number of samples are generated. Therefore, the a statistical error $\hat{I} - I$ enters into the estimation. The error can be evaluated precisely using the central limit theorem (CLT). It states that a random variable $\hat{I} - I$ follows a Gaussian distribution with standard deviation

$$\epsilon_I = \frac{\sigma_I}{\sqrt{n}} \tag{2.33}$$

where σ_I is the standard deviation of $\mathcal{I}(X)$. A more detailed analysis of the errorbar will be presented at the end of this subsection.

Now, we turn back to the evaluation of the observable given by the path integral Eq. (2.16). For Bosons, the weight function $\pi(\mathcal{C})$ is always positive since $\mathcal{W}(\mathcal{C})$ is always

[1] The original birth of the Monte Carlo method should go back to the atomic bomb project at Los Alamos in 1946. Physicist Stanislaw Ulam, who was a member of the project, was recovering from a surgery. To occupy his own mind from boring, he tried to play solitaire in an IQ demanded way: calculating the probability of winning the game. His answer is simple: play it 100 times, count the number of wins and you will have a pretty good estimation. Thanks to the availability of the computer at the time, this method became quite practical for a variety of questions, such as the mechanical simulation of random diffusion of neutrons. As a secret government work, a code name is asked. The name of the Moncaco city "Monte Carlo", is given to this approach, since it's the town where Ulam's uncle frequently gambled.

positive. This can be seen from Eq. (2.14) combined with Eq. (2.18) and Eq. (2.19). Since it also satisfies the condition $\int \pi(\mathcal{C})d\mathcal{C} = 1$, it can play the role of the probability distribution in Eq. (2.31). The PIMC then proceeds as follows. We can produce a large number of configurations $\mathcal{C}_1, \mathcal{C}_2, ..., \mathcal{C}_n$ according to the probability distribution π. The corresponding path integral estimator $\mathcal{A}(\mathcal{C}_k)$ will be calculated for each configuration. Then, we can get the approximate expectation value of observable $\hat{A}$ by

$$\langle A \rangle \cong \frac{\mathcal{A}(\mathcal{C}_1) + ... + \mathcal{A}(\mathcal{C}_n)}{n}. \tag{2.34}$$

Having introduced the idea of general Monte Carlo method, we will proceed to describe the detail technique for generating $\mathcal{C}$ in the next paragraphs.

Markov Chain Monte Carlo

The direct sampling of certain probability distributions is typically possible for a number of simple laws, such as Gaussian distributions or uniform distributions. However, it is impossible to generate the configurations with the weight as complex as the one in Eq. (2.14). The solution is to use a Markov chain to perform a random walk in the configuration space. It means that we generate a sequence of configurations iteratively,

$$\mathcal{C}_1 \to \mathcal{C}_2 \to ... \to \mathcal{C}_k \to ... \tag{2.35}$$

The probability to go from the configuration $\mathcal{C}_k = \mathcal{C}$ to $\mathcal{C}_{k+1} = \mathcal{C}'$ is given by a transition matrix $p(\mathcal{C} \to \mathcal{C}') = M_{CC'}$. Here, one should notice that the term of Markov chain means that the probability of a configuration at time $k+1$ only depends on the configuration at time k, and not the older configurations. If appropriate ergodicity hypothesis is satisfied, the long-time distribution will go towards to a unique stationary π_{stat} which satisfies the condition $M\pi_{\text{stat}} = \pi_{\text{stat}}$. Therefore, with proper choice of M, we shall reproduce the correct statistical distribution $\pi(\mathcal{C})$ by π_{stat}. Since there is a large number of admissible transition matrices for a given law π, one usually restricts itself to the matrices satisfying the *detailed balance condition*

$$\pi(\mathcal{C})p(\mathcal{C} \to \mathcal{C}') = \pi(\mathcal{C}')p(\mathcal{C}' \to \mathcal{C}) \tag{2.36}$$

which just directly implies the stationary condition but simpler to implement.

Hasting-Metropolis algorithm

For finding a proper process that satisfies the condition Eq. (2.36), the Hasting-Metropolis algorithm [114, 115] is introduced. The transition from $\mathcal{C}_k$ to $\mathcal{C}_{k+1}$ contains two steps: propose and judge. Firstly, a new configuration $\mathcal{C}_{k+1} = \mathcal{C}'$ is proposed with probability $p_{prop}(\mathcal{C} \to \mathcal{C}')$. Then, we judge whether we want to accept this propose or not, according to the acceptance probability

$$p_{\text{accept}}(\mathcal{C} \to \mathcal{C}') = \min\left(1, \frac{\pi(\mathcal{C}')p_{prop}(\mathcal{C}' \to \mathcal{C})}{\pi(\mathcal{C})p_{prop}(\mathcal{C} \to \mathcal{C}')}\right) \tag{2.37}$$

Therefore, the Markov chain may jump to $\mathcal{C}_{k+1} = \mathcal{C}'$ with the probability p_{accept} or stay in the previous configuration with the probability $1 - p_{accept}$. This definition also makes sure that the transition probability $p(\mathcal{C} \to \mathcal{C}') = p_{prop}(\mathcal{C} \to \mathcal{C}')p_{accept}(\mathcal{C} \to \mathcal{C}')$ follows the detailed balance condition and that the Markov chain also samples the distribution π. In actual computations, we should propose new configurations in such a way that the ratio in Eq. (2.37) is at the magnitude of 1, in order to keep the high acceptance rate and make the move efficient. One typical way for achieving that is to use local updates, which means we normally modify a small part of the configuration in one single propose, and the unlikely

configuration is prevented. More details about the moves for PIMC will be presented in section 2.1.5.

Systematic and Statistical errors in PIMC

The results obtained from the PIMC calculation contains two typical types of errors. The first one is the *systematic error* coming from the discretization of the worldlines, i.e. the finite value of ϵ. The influence of the finite ϵ value presents in all the calculations of the propagators. For getting rid of this error, one normally performs the simulation with decreasing value of ϵ and study the convergence of limit $\epsilon \to 0$. For instance, in the study of Tan's contact for 1D interacting bosons, a careful analysis of ϵ is necessary. We shall discuss more details in section 3.1.3 of Chapter. 3.

The second type of error is the statistical error, due to the finite number of configurations generated during the simulation. In principle, when the sampled configurations are independent, the errorbar can be estimated using the CLT by Eq. (2.33). However, the configurations by Markov Chain process are highly correlated since the typical moves only updates small part of the configurations. Therefore, a more complicated error analysis is necessary. Thanks to the ALPS packages, two types of error analysis are performed in our PIMC calculation [116, 117]. The first one is called *simple binning method*. For simplicity, we note $\mathcal{A}_i = \mathcal{A}(\mathcal{C}_i)$. Then, we define an autocorrelation time of the accumulated data

$$\tau_{\mathcal{A}} = \frac{\sum_{t=1}^{\infty}(\langle \mathcal{A}_{i+t}\mathcal{A}_i\rangle - \langle \mathcal{A}\rangle^2)}{\sigma_{\mathcal{A}}^2}. \tag{2.38}$$

Then, the real statistical error of the ensemble should write

$$\epsilon_{\mathcal{A}} \simeq \sqrt{\frac{\tau_{\mathcal{A}}}{n}}\sigma_{\mathcal{A}}. \tag{2.39}$$

Therefore, in actual computation, the main task of the error estimation is to find the proper $\tau_{\mathcal{A}}$ for the obtained data. The simple binning method calculate the average and errors with different bin sizes along the Monte Carlo step, i.e. it perform a binning analysis to estimate the integrated autocorrelation time and returns a trustable value of the errorbar. However, this method is not sufficient if the observable we compute comes from a function of several correlated measurements. In this case, one needs to use another method which is called *jackknife method*. It re-samples the data by throwing one single sampling and evaluate the expectation value from the left $N-1$ samples, then performing all the possible throwing and evaluation process and obtain the final expectation value and errors on top of those data. It is the most trustable analysis, but also the most expensive one in time and memory. In the computations of this manuscript, we always use one of these two methods of analysis, depending on the quantity we calculate. For details of the two error estimations, one can find them in Refs. [116, 118].

2.1.5 Standard moves for path-integral Monte Carlo

Now we provide the details about the Monte Carlo moves, which are used to generate new samples of configurations. The essential idea is to guarantee the ergodicity of the Markov chain. It means that the whole configuration space must be accessible from any initial configuration. This is satisfied by defining two basic types of moves, namely *reshape* and *swap*. The illustration of the two moves are shown in Fig. 2.3. Further advanced types of moves can be introduced to improve the efficiency of the simulation, see section 2.2.

Reshape

The first type of move is to change the shape of one chosen path. Here, we assume the move starts from configuration $\mathcal{C}$. We introduce an integer M the number of beads

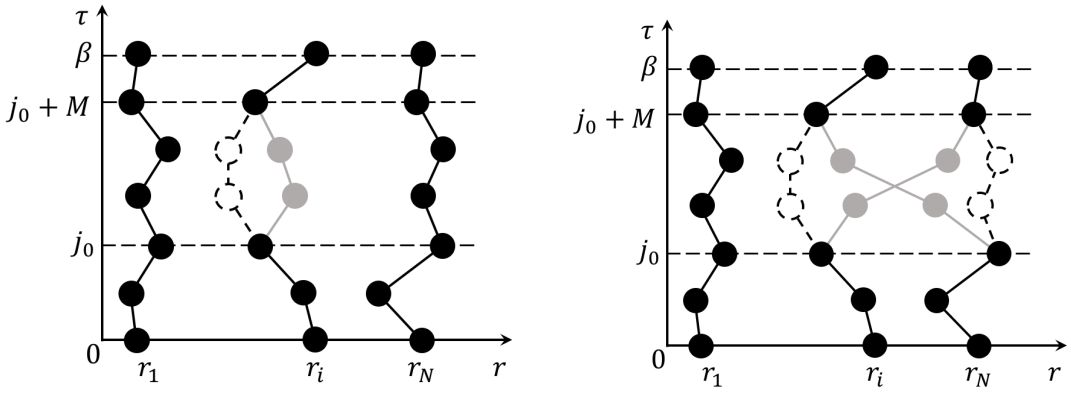

Figure 2.3: Two basic moves of standard PIMC methods. Here, we always indicate the unchanged beads in black, the old beads to be changed as dashed elements, and the new position of the beads in solid grey. The left and right figures correspond to the two moves named reshape and swap, respectively.

modified by the move. It maintains the same definition in all the following statement of the other moves. Then, we select one bead randomly among the whole configuration and name the position index i and the time slice index j_0. Thus, its position is noted as $\mathbf{r}_{j_0}$ and the trajectory we would like to change is $(\mathbf{r}_{j_0}, \mathbf{r}_{j_0+1}, ..., \mathbf{r}_{j_0+M-1}, \mathbf{r}_{j_0+M})$. Using the Lévy construction [112], we propose a Brownian bridge between $\mathbf{r}_{j_0}$ and $\mathbf{r}_{j_0+M}$ and name the new path $(\mathbf{r}_{j_0}, \mathbf{r}'_{j_0+1}, ..., \mathbf{r}'_{j_0+M-1}, \mathbf{r}_{j_0+M})$, corresponding to the new configuration $\mathcal{C}'$. Then, we can write the weight of the old and new configurations,

$$\pi(\mathcal{C}) = K\rho_0(\mathbf{r}_{j_0}, \mathbf{r}_{j_0+1}, \epsilon)...\rho_0(\mathbf{r}_{j_0+M-1}, \mathbf{r}_{j_0+M}, \epsilon)e^{-U} \tag{2.40}$$

$$\pi(\mathcal{C}') = K\rho_0(\mathbf{r}_{j_0}, \mathbf{r}'_{j_0+1}, \epsilon)...\rho_0(\mathbf{r}'_{j_0+M-1}, \mathbf{r}_{j_0+M}, \epsilon)e^{-U'} \tag{2.41}$$

where K is the production of free density matrices on the unaffected path segments and it is thus the same for both configurations. The quantity U and U' are the actions for the old and new configurations respectively. Then, using the free density matrices to construct the probability density for a Brownian bridge, we writes the probabilities to propose the direct and reciprocal moves,

$$p_{\text{prop}}(\mathcal{C} \to \mathcal{C}') = \frac{1}{JN} \frac{\rho_0(\mathbf{r}_{j_0}, \mathbf{r}'_{j_0+1}, \epsilon)...\rho_0(\mathbf{r}'_{j_0+M-1}, \mathbf{r}_{j_0+M}, \epsilon)}{\rho_0(\mathbf{r}_{j_0}, \mathbf{r}_{j_0+M}, M\epsilon)} \tag{2.42}$$

$$p_{\text{prop}}(\mathcal{C}' \to \mathcal{C}) = \frac{1}{JN} \frac{\rho_0(\mathbf{r}_{j_0}, \mathbf{r}_{j_0+1}, \epsilon)...\rho_0(\mathbf{r}_{j_0+M-1}, \mathbf{r}_{j_0+M}, \epsilon)}{\rho_0(\mathbf{r}_{j_0}, \mathbf{r}'_{j_0+M}, M\epsilon)}. \tag{2.43}$$

Here, the factor JN is due to the probability of choosing an initial bead. Then, according to Eq. (2.37), we find the acceptance probability

$$p_{\text{accept}}\left(\mathcal{C} \to \mathcal{C}'\right) = \min(1, e^{-\Delta U}) \tag{2.44}$$

where $\Delta U = U' - U$ is the difference between the old and new action. Here, we use this move to serve as an example to give the detail derivation of the probability of propose and acceptance. In the following statement of the other moves, we shall skip the detail and give directly the final formulas.

Swap

The move reshape cannot introduce the quantum exchange between different worldlines. Thus, it cannot change the topology of the configuration. To correctly perform the sample

considering all the permutations in Eq. (2.13), we introduce the move swap which can exchange the worldline of the two particles. One starts by choosing a random particle with index i_1 and choose a bead at time slice j_0 on its path. Then, we choose a second particle i_2 with the probability

$$p(i_2) = \frac{t_{i_1,i_2} t_{i_2,i_1}}{\sum_{i=1}^{N} t_{i_1,i} t_{i,i_1}} \tag{2.45}$$

with $t_{i,i'} = \rho_0(\mathbf{r}^i_{j_0}, \mathbf{r}^{i'}_{j_0+M}, M\epsilon)$. If $i_1 = i_2$, the move is rejected. Otherwise, we generate two Brownian bridges between $\mathbf{r}^{i_1}_{j_0}$ and $\mathbf{r}^{i_2}_{j_0+M}$ on the one hand, and $\mathbf{r}^{i_2}_{j_0}$ and $\mathbf{r}^{i_1}_{j_0+M}$ on the other hand. Finally, the move is accepted with probability given by Eq. (2.44). Here, one should notice that the way of choosing the second particle here ensures the distance $|\mathbf{r}^{i_1}_{j_0} - \mathbf{r}^{i_2}_{j_0+M}|$ is of the order $\sqrt{M\epsilon}$, thus the exchange is likely to be accepted and the sampling process can move efficiently in the configuration space.

2.2 Worm algorithm

The PIMC simulation described previously has been successfully used to the study of quantum liquids in continuous space. [97, 119, 120] They are very efficient for calculating observables obtained from local estimators, such as the particle density and the average energy. However, this method faces difficulty while working on properties related to particles indistinguishability, such as computation of the superfluid fraction. This situation is annoying, since the superfluid fraction is one of the key quantities to study quantum phase transitions at low temperature, especially the transition to the superfluid phase. The core difficulty is the existence of long exchange cycles in superfluid phase which contains a macroscopic number of particles. However, the standard PIMC simulation only proposes moves performing local modification and the topology of cycles in the whole configurations is hard to be changed efficiently. As a consequence, the superfluid fraction can only be calculated for small sizes of the system, which hardly reflect the physics in the thermodynamic limit.

In Refs. [58, 59], an implementation technique named *worm algorithm* is proposed to solve the permutation problem by introducing an open worldline. This sort of worldline is called *worm*. It breaks the closed one and enables efficient change for the topology of configurations. Fig. 2.4 gives an example for such kind of configurations. On the right

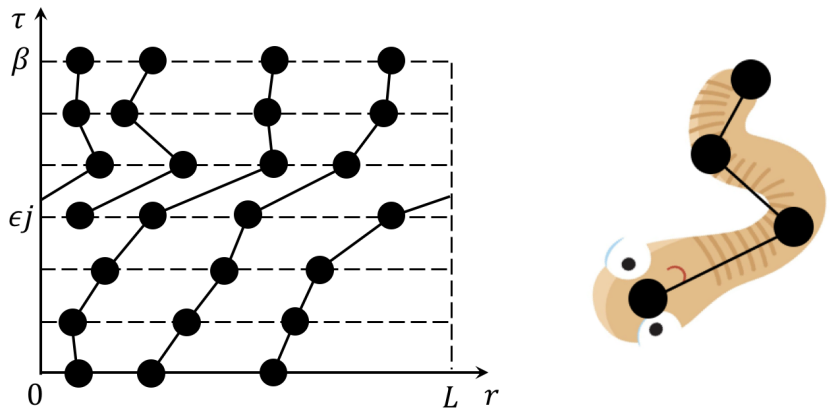

Figure 2.4: Left- Configuration with 4 particles involved in a quantum exchange. The configuration contains both open and close worldlines. Right- One image of keyword "worm" from google images and its fit with the top left open worldline in the Feynman diagram.

subplot, we show an image of worm from random search in google images and we find it fits well with the open worldline on the top left. With gradual shrinking and growing of the worm, the particle numbers can change continuously and it allows huge jump of the sample in the configuration space. In Fig. 2.5, we show an example that the system performs huge jump between two different configurations in Z-sector via the channel of G-sector. The number of particles also suddenly jumps from 1 to 3. Therefore, we shall conclude that this implementation establishes an efficient grand-canonical algorithm, while the standard PIMC are more performed in the canonical ensemble.

2.2.1 The winding number

An important property of the worm is that they like to twist or wind on a curved structure, such as fruits or trunks of plants. In fact, this also applies to the worms in our model. In our configuration, by introducing periodical boundary conditions on the $\mathbf{r}$ axis, we produce a curved structure in the position space for the worm to wind. The worm algorithm will generate efficiently the process of winding. For instance, in Fig. 2.5 (c), there are one worm who successfully cross the border $\mathbf{r} = L$ and twist back at $\mathbf{r} = 0$ thanks to the winding process. This process is important since it counts for the long exchange cycles appearing at low temperature. Furthermore, we introduce the *winding number* which is the number of times a cycle crosses the boundaries of the simulation box. More precisely, we define the winding number estimator

$$\mathbf{W} = \sum_{i=1}^{N} \sum_{j=0}^{J-1} (\mathbf{r}_i^{j+1} - \mathbf{r}_i^j). \tag{2.46}$$

For example, for a 1D configuration on the x axis, the quantity W_x/L equals to the number of times the worldlines exit the simulation box at $x = L$ and enter back at $x = 0$. In Fig. 2.5 (d), we can find a winding number equals of 1. The average of this quantity is at the heart of the estimator for the superfluid fraction, as we will explain in section 2.3.

To ensure that we calculate the average of the winding number properly, we must introduce moves which can change efficiently the winding number of the systems. However, since the winding number is a topological property of the configuration concerning a macroscopic number of particles, the local moves in standard PIMC cannot change its value. The worm algorithm conquers the problem since it facilitates the transitions between configurations with different winding numbers. For instance, in Fig. 2.5, the winding number goes from 0 to 1 by removing, advancing and closing. Thus, it improves considerably the averaging procedure to find the relevant physical quantities such as the superfluid fraction. In the next two subsection, we shall introduce in detail the worm algorithm and its moves.

2.2.2 The extended partition function: Z-sector and G-sector

As explained in the beginning of this section, the worm algorithm works in an extended configuration space. It can be divided into two subspaces, or we can call it two sectors. The first sector contains only the closed worldline configurations and it is called Z-sector. We use the letter "Z" since it stands for the notation of the standard partition function. This sector corresponds to all the configurations in the standard PIMC and we call those configurations the diagonal configurations. Naturally, the second sector contains configurations with an open worldline, thus the worm. We call it G-sector since it samples the green function (see detail in section 2.3.3). The configurations in the G-sector are called off-diagonal configurations. The Z-sector contains the physical configurations, while the G-sector contains the unphysical one which are however useful intermediates between the

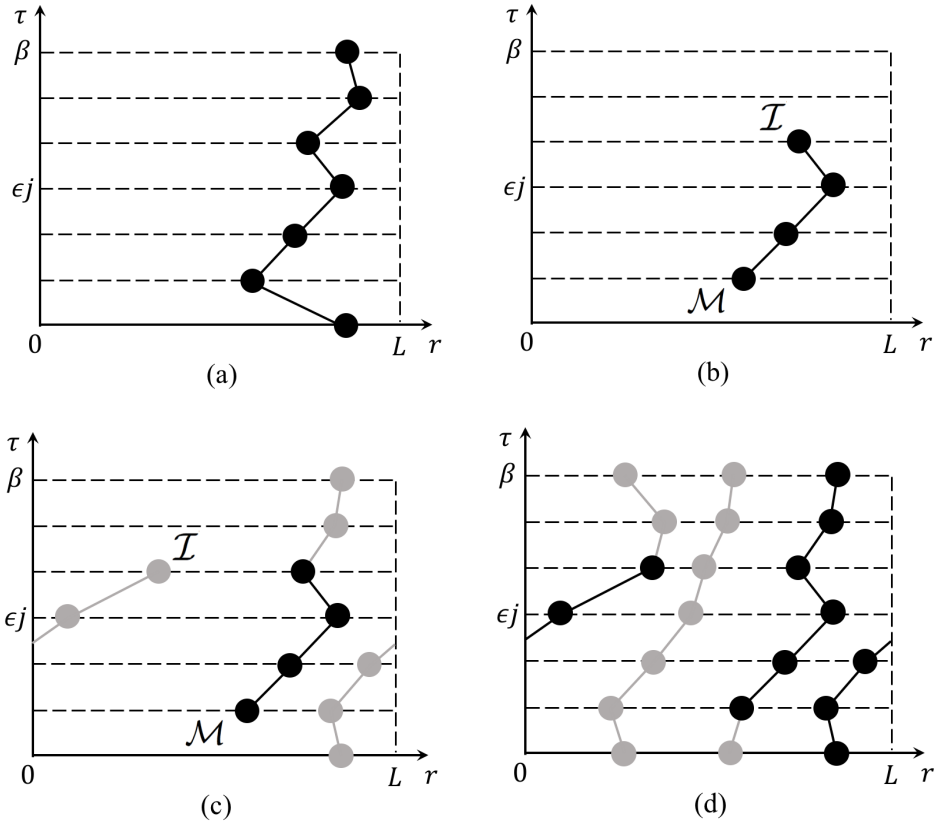

Figure 2.5: The process of destroying a Z-sector configuration and re-building a configuration with increasing winding numbers in the worm algorithm. It contains a series of remove, advance and close moves. The panels (a) and (d) are in Z-sector while the panel (b) and (c) are in G -sector. The final configuration has a winding number equals to 1.

physical configurations. The existence of G-sector allows to move efficiently between topologically inequivalent configurations in Z-sector. In the following, we will give detail about these two sectors.

Z-sector

Since the worm algorithm is established in the grand-canonical ensemble, we should rewrite the partition function and configuration weight with the grand-canonical Hamiltonian $\hat{K} = \hat{H} - \mu N$, with μ the chemical potential and $\hat{N}$ the particle number operator. Similarly as the previous statement, the partition function should write $Z = \mathrm{Tr}[e^{-\beta\hat{K}}]$. Expanding it as a sum over particle numbers and particle spatial positions, we find

$$Z = \sum_{N=0}^{+\infty} \frac{1}{N!} \sum_{\sigma\in\Pi} \int \mathrm{d}\mathbf{R}_0 \langle \sigma\cdot\mathbf{R_0}|e^{-\beta\hat{K}}|\mathbf{R_0}\rangle. \tag{2.47}$$

Then, dividing β into small time steps ϵ, we can define naturally the weight similarly as the path-integral picture (2.14),

$$\mathcal{W}(\mathcal{C}) = e^{\beta\mu N}\langle\sigma\cdot\mathbf{R_0}|e^{-\epsilon\hat{H}}|\mathbf{R_{J-1}}\rangle \times ... \times \langle\mathbf{R_1}|e^{-\epsilon\hat{H}}|\mathbf{R_0}\rangle. \tag{2.48}$$

for a configuration $\mathcal{C}$ containing N closed worldlines. Here, one should pay attention to how the term $N!$ disappears. In standard PIMC which is in canonical ensemble, the factor $N!$ in Eq. 2.13 is identical for all configurations. Therefore, we exclude this term in the expression

of the weight because it will not change the Hasting-Metropolis transition probability anyway. However, the situation is different in the grand-canonical ensemble. The weight of configurations with different numbers of particles must be considered properly. The idea is that with the notation of the position space $|\mathbf{R}\rangle = |\mathbf{r}_1, ..., \mathbf{r}_i, ..., \mathbf{r}_N\rangle$, the particles are labeled by the index i and we could thus follow the propagation of each single particles. However, in actual Monte Carlo simulation, we don't label the worldlines and only the structure of the path is stored. Therefore, each configuration in the simulation corresponds to $N!$ possibilities of labels in Eq. (2.47) and it cancels the factor $1/N!$ in the front. Finally, we should omit this term in the expression of the configuration weight.

G-sector

The configurations in the G-sector always contains an open worldline, for example the Fig. 2.5 (b) and (c). They normally also include closed world lines similar as in the Z-sector. For historical reasons, we call the first and last beads of the worm Masha ($\mathcal{M}$) and Ira ($\mathcal{I}$). Then, the weight in the G-sector can be expressed as

$$\mathcal{W}(\mathcal{C}) = Ce^{\epsilon\mu N_{\text{link}}}\langle\sigma\cdot\mathbf{R_0}|e^{-\epsilon\hat{H}}|\mathbf{R_{J-1}}\rangle\times ...\times\langle\mathbf{R_1}|e^{-\epsilon\hat{H}}|\mathbf{R_0}\rangle. \tag{2.49}$$

where N_{link} is the number of linked bead pairs in the configuration, and C is some positive constant which will be explained in detailed later. Here, one should notice that the vector $\mathbf{R}_j$ doesn't have the same number of elements. They contain N particles if $j_{\mathcal{M}} < j < j_{\mathcal{I}}$ and $N+1$ particles if $j_{\mathcal{I}} < j < j_{\mathcal{M}}$. And the factor $e^{\epsilon\mu N_{\text{link}}}$ is compatible with the $e^{\beta\mu N}$ term in the Z-sector and it ensures the configuration weight increase progressively with the length of the worm and allow the worm to grow and shrink gradually. The constant C here is to control the relative weight of Z- and G- sectors. If C is too small, the algorithm will spend most of the time in the Z-sector and the sampling will not be efficient. It will lead to long correlation times and be hard to converge. On the other hand, if C is too large, the Z-sector is hardly visited and it will cause a low measurement number for most of the observables (except the correlation function) and induces a high statistical error. Therefore, a proper choice of C is important for obtaining the correct result with small error bar, correlation time and execution time. According to Refs. [58, 59], a proper choice would be

$$C \sim \frac{\epsilon^2}{V\beta} \tag{2.50}$$

where V is the volume of the simulated system. Moreover, integrating all the configurations in the G-sector, one can define the partition function

$$Z_G = \int_G \mathcal{W}(\mathcal{C})d\mathcal{C} \tag{2.51}$$

Then, the total partition function of the whole configuration space should write $Z_W = Z + Z_G$.

2.2.3 Monte Carlo moves in the worm algorithm

In the worm algorithm, the configuration space is extended with open configurations. Thus, we need to introduce new moves which allow us to switch between Z- and G-sectors, as well as inside G-sector itself. The illustration of all these moves are presented in Fig. 2.6. In the following, we will provide details about each move and its acceptance probability which follows the Hasting-Metropolis algorithm. We always note j_0 the starting timeslice of the modification, M the number of modified beads and J the total imaginary time step. The number M is a random number chosen from the interval $[0, \bar{M}]$, with $\bar{M}$ the maximum number of modified beads which is set in the beginning of the simulation.

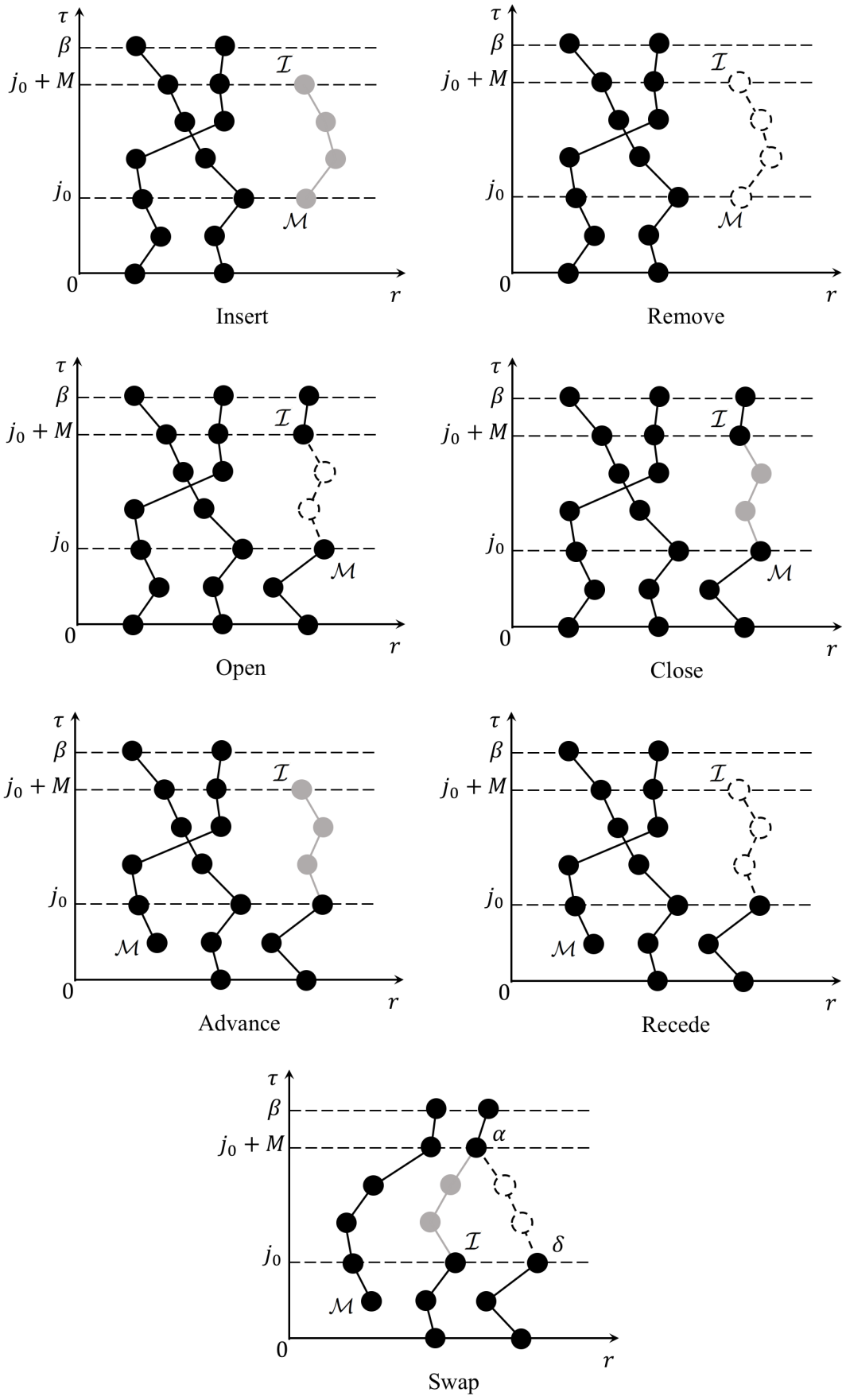

Figure 2.6: Moves used in worm algorithm. The dashed beads and grey beads mean the erased and added beads, respectively The black bead stands for the unchanged ones.

Insert (Z→ G)

In this move, we choose Masha at position $\mathbf{r}_M$ and the time slice j_0 with probability law. Then, M consecutive beads are added at the following time slice, by using the free-propagator generator. The acceptance probability for this move is

$$p_{\text{insert}}(\mathcal{C} \to \mathcal{C}') = \min\left(1, CVJ\overline{M}e^{-\Delta U+\mu M\epsilon}\right). \tag{2.52}$$

Remove (G→ Z)

If the length of the worm in the configuration is between 1 and $\bar{M}$, we propose to remove the worm. The acceptance probability is

$$p_{\text{remove}}(\mathcal{C} \to \mathcal{C}') = \min\left(1, e^{-\Delta U-\mu M\epsilon}/CVJ\overline{M}\right). \tag{2.53}$$

Open (Z→ G)

This move starts from a closed configuration. It chooses a bead at random and removes the M following links, which transfers the configuration into an open one. Here, we define $\mathbf{r}_{\mathcal{I}}$ and $\mathbf{r}_{\mathcal{M}}$ the position of Ira and Masha. We also note $N_{\text{bd}} = NJ$ the total number of beads in the initial configuration. Then, the acceptance probability is

$$p_{\text{open}}(\mathcal{C} \to \mathcal{C}') = \min\left(1, C\bar{M}N_{\text{bd}}e^{-\Delta U-\mu M\epsilon}/\rho_0(\mathbf{r}_{\mathcal{I}}, \mathbf{r}_{\mathcal{M}}, M\epsilon)\right). \tag{2.54}$$

Close (G→ Z)

The move starts from an open configuration. If the distance between Ira and Masha along the imaginary time slice is not between 1 and $\bar{M}$, then we reject the move. Otherwise, we generate a Brownian bridge between Ira and Masha. The move is accepted with probability

$$p_{\text{close}}(\mathcal{C} \to \mathcal{C}') = \min\left(1, \rho_0(\mathbf{r}_{\mathcal{I}}, \mathbf{r}_{\mathcal{M}}, M\epsilon)e^{-\Delta U+\mu M\epsilon}/C\bar{M}N_{\text{bd}}\right). \tag{2.55}$$

Advance (G→ G)

This move starts from a configuration in the G-sector. It proposes to increase the size of the worm by adding M beads to Ira with the free propagator. The acceptance probability is

$$p_{\text{advance}}(\mathcal{C} \to \mathcal{C}') = \min\left(1, e^{-\Delta U+\mu M\epsilon}\right). \tag{2.56}$$

Recede (G→ G)

This move starts from a configuration in the G-sector. It proposes to reduce the size of the worm by removing M beads to Ira with the free propagator. The acceptance probability is

$$p_{\text{recede}}(\mathcal{C} \to \mathcal{C}') = \min\left(1, e^{-\Delta U-\mu M\epsilon}\right). \tag{2.57}$$

Swap (G→ G)

The move swap in the G-sector is the counterpart of the standard swap move introduced in section 2.1. However, different from the one in standard PIMC, the swap move in the G-sector can change the winding number of the configuration efficiently. In this move, we choose two beads α and δ with $\bar{M}$ time slices in between along the same worldline, under

the condition that δ is on the same time slice as Ira. Then, we destroy the path between α and δ, and establish a Brownian bridge between α and $\mathcal{I}$, which leads to δ become the role of Ira of the new configuration.

To force the algorithm to propose and accept the swap move efficiently, one must choose a bead α that is close enough to Ira, typically with a distance of the order of $\sqrt{\bar{M}\epsilon}$. Otherwise, the proposed configuration will be easily rejected. Therefore, we propose an updated version of the swap move. We divide the simulation box into small hypercubic bins with each bin containing typically several particles. The beads in the same or neighbor bins are considered to be *close*. The beads at time slice $j_{\mathcal{I}} + M$ which are close to Ira are collected to a list. We choose one of them called α with probability $\rho_0(r_{\mathcal{I}}, r_\alpha, \bar{M}\epsilon)/\Sigma_{\mathcal{I}}$ where $\Sigma_{\mathcal{I}}$ is the normalization constant given by the sum of $\rho_0(r_{\mathcal{I}}, r_\eta, \bar{M}\epsilon)$ over all beads η in the list. The bead on the same worldline of α at $\bar{M}$ links before is called δ. If δ is not close to $\mathcal{I}$, the move is rejected. Otherwise, we erase the path between α and δ and connect α and $\mathcal{I}$ using a Brownian bridge. Finally, the move is accepted with the probability

$$p_{\text{swap}}(\mathcal{C} \to \mathcal{C}') = \min\left(1, e^{-\Delta U}\Sigma_{\mathcal{I}}/\Sigma_\delta\right). \tag{2.58}$$

The term Σ_δ is the sum of $\rho_0(r_\delta, r_\eta, \bar{M}\epsilon)$ over the beads η close to δ at time slice $j_{\mathcal{I}+M}$. One should notice that the swap move has no reciprocal move as the other moves before, since it is its own inverse move.

2.3 Computation of observables

The aim of the Monte Carlo calculation is to compute the average value of relevant observable $\hat{A}$ in the canonical or grand canonical ensemble. To this aim, one must firstly give an appropriate path integral estimator $\mathcal{A}$ for the observable $\hat{A}$ as in Eq. (2.15). Then, we can find $\langle\hat{A}\rangle$ by the average of $\mathcal{A}(\mathcal{C})$ over the configurations $\mathcal{C}$ generated by the Markov Chain sampling. In this section, we introduce the estimators for computing all the important quantities in this thesis.

2.3.1 Particle density and compressibility

The number of worldlines contained in a Z-sector configuration directly gives the number of particles in the system $\langle N\rangle_Z$. Here, the Z subscript means the average is only performed over the Z-sector. Then, the particle density n can be directly obtained from the estimator

$$n = \frac{1}{L^d}\langle N\rangle_Z \tag{2.59}$$

where L is the system size, d the dimension of the system and N is the number of worldlines contained in the configuration.

In practice, the system we studied is normally inhomogeneous, with an external potential $V(\mathbf{r})$. Then, the density profile also becomes inhomogeneous and the detail information of the distribution $n(\mathbf{r})$ is useful in many cases. Since the local density is diagonal in the position representation, the expression Eq. (2.15) reduces to $\langle \mathrm{R}_0|n(\mathbf{r})|\mathrm{R}_0\rangle = \sum_{i=1}^N \delta(\mathbf{r}-\mathbf{r}_i^0)$. Thanks to the translational invariance in the imaginary time of the path integral representation, in reality one can use any timeslice to calculate the observable. Thus, it leads to an improved version of the distribution:

$$n(\mathbf{r}) = \frac{1}{J}\left\langle \sum_{j=0}^{J-1}\sum_{i=0}^{N}\delta(\mathbf{r}-\mathbf{r}_i^j)\right\rangle_Z \tag{2.60}$$

which takes advantage of all the information contained in the full configuration. In practice, we divide the simulation space into a grid of hypercubes in d dimensions with linear size a,

located at discrete positions $\mathbf{r}$. The singular delta function is then replaced by a discrete version $\delta_{\mathbf{r},\mathbf{r}_i^j}/a^d$, with $\delta_{\mathbf{r},\mathbf{r}_i^j}$ indicating whether the bead $\mathbf{r}_i^j$ belongs to the bin at $\mathbf{r}$.

Another important quantity which is related is the compressibility κ. It measures the change of the number of particles when the chemical potential is changed at fixed temperature

$$\kappa = \left.\frac{\partial n}{\partial \mu}\right|_T. \tag{2.61}$$

Differentiating the expression $n = Tr[\hat{N}e^{-\beta(\hat{H}-\mu\hat{N})}]/L^d Z$ with respect to μ, we can find the link between the compressibility and particle number fluctuation,

$$\kappa = \frac{\beta}{L}[\langle N^2\rangle_{\mathrm{Z}} - \langle N\rangle_{\mathrm{Z}}^2]. \tag{2.62}$$

In practice, since the chemical potential μ is the input of the calculation, one can either use Eq. (2.61) or Eq. (2.62) to calculate the compressibility, depending on the situation.

2.3.2 Superfluid density

The superfluid density is defined by the non-classical moment of intertia of the system. For the following discussion, we focus on only the x-axis and study the case of one dimension. The analysis can be generalized to higher dimension. We assume the fluid system is in a container moving with velocity $\mathbf{v} = v\mathbf{e}_x$ with respect to the frame of reference. For a fully viscous fluid, the momentum of the system in the reference frame is $\langle P_x\rangle_v = Mv$ with M the mass of the system. However, the portion of superfluid shall not move with the system. Therefore, the superfluid mass can be derived from the equation

$$M_s = M - \frac{\partial\langle P_x\rangle_v}{\partial v} \tag{2.63}$$

Then the superfluid density writes $n_{\mathrm{s}} = M_{\mathrm{s}}/mL^d$ with m the mass of a single particle. We shall rewrite Eq. (2.63) as

$$n_s = n - \frac{1}{mL^d}\frac{\partial\langle P_x\rangle_v}{\partial v} \tag{2.64}$$

To calculate the average momentum, one can weight the state with the partition function of the Hamiltonian in the moving frame $\hat{H}_v = \hat{H} - \mathbf{v}\cdot\hat{\mathbf{P}}$,

$$\langle P_x\rangle_v = \frac{1}{Z}\mathrm{Tr}[\hat{P}_x e^{-\beta\hat{H}_v}] \tag{2.65}$$

For obtaining the expression of superfluid fraction with Eq. (2.64), we need to compute the derivation of Eq. (2.65) to the velocity v. Thanks to the Duhamel formula

$$\partial_t e^{\hat{A}(t)} = \int_0^1 e^{s\hat{A}(t)}\partial_t\hat{A}(t)e^{(1-s)\hat{A}(t)}ds \tag{2.66}$$

and applying it by treating $\hat{H}(v)$ as $\hat{A}(t)$, we find the derivation of the trace reads

$$\partial_v\mathrm{Tr}[\hat{P}_x e^{-\beta\hat{H}_v}] = \mathrm{Tr}[\hat{P}_x\int_0^\beta e^{\tau\hat{H}(v)}\hat{P}_x e^{(\beta-\tau)\hat{H}(v)}\,d\tau] = \int_0^\beta \mathrm{Tr}[\hat{P}_x e^{\tau\hat{H}(v)}\hat{P}_x e^{(\beta-\tau)\hat{H}(v)}]\,d\tau. \tag{2.67}$$

Combining Eq. (2.67) with Eq. (2.64) and Eq. (2.65), we find

$$n_{\mathrm{s}} = n - \frac{1}{mL^d}\int_0^\beta d\tau\ \langle P_x(\tau)P_x(0)\rangle. \tag{2.68}$$

Here, one may notice that the key point to proceed is to calculate the correlator in the integral.

Now, we rewrite the integral in Eq. (2.68) in the path-integral representation. Replacing the integral $\int_0^\beta$ by the discrete sum $\epsilon \sum_{j=0}^{J-1}$ and taking advantage of the translational invariance of the imaginary time axis, we write

$$\int_0^\beta d\tau \ \langle P_x(\tau) P_x(0)\rangle = \frac{\epsilon}{J} \sum_{j,j'} \langle P_x(j'\epsilon) P_x(j\epsilon)\rangle \tag{2.69}$$

This equation cannot be estimated by Eq. (2.15) because it has an explicit dependence on the imaginary time. Therefore, we need to compute explicitly the correlator at different imaginary times. Separating the terms $j \neq j'$ and $j = j'$, we find

$$\begin{aligned}
&\frac{\epsilon}{J} \sum_{j,j'} \langle P_x(j'\epsilon) P_x(j\epsilon)\rangle = \\
&\frac{\epsilon}{J} \sum_{j\neq j'} \left\langle \frac{\langle \mathbf{R}_{j+1}|\hat{P}_x e^{-\epsilon\hat{H}}|\mathbf{R}_j\rangle}{\langle \mathbf{R}_{j+1}|e^{-\epsilon\hat{H}}|\mathbf{R}_j\rangle} \frac{\langle \mathbf{R}_{j'+1}|\hat{P}_x e^{-\epsilon\hat{H}}|\mathbf{R}_{j'}\rangle}{\langle \mathbf{R}_{j'+1}|e^{-\epsilon\hat{H}}|\mathbf{R}_{j'}\rangle} \right\rangle_Z + \frac{\epsilon}{J} \sum_j \left\langle \frac{\langle \mathbf{R}_{j+1}|\hat{P}_x^2 e^{-\epsilon\hat{H}}|\mathbf{R}_j\rangle}{\langle \mathbf{R}_{j+1}|e^{-\epsilon\hat{H}}|\mathbf{R}_j\rangle} \right\rangle_Z
\end{aligned} \tag{2.70}$$

Using the primitive approximation, one can then expand the evolution operator $e^{-\epsilon\hat{H}}$. The contribution from the potential terms cancels out and the result only depends on the free density matrix. The matrix element for single particles are

$$\langle \mathbf{r}'|\hat{p}_x e^{-\epsilon\hat{H}_0}|\mathbf{r}\rangle = \frac{im}{\hbar\epsilon}(x'-x)\langle \mathbf{r}'|e^{-\epsilon\hat{H}_0}|\mathbf{r}\rangle \tag{2.71}$$

$$\langle \mathbf{r}'|\hat{p}_x^2 e^{-\epsilon\hat{H}_0}|\mathbf{r}\rangle = \left[-(\frac{m}{\hbar\epsilon})^2 (x'-x)^2 + \frac{m}{\epsilon} \right] \langle \mathbf{r}'|e^{-\epsilon\hat{H}_0}|\mathbf{r}\rangle \tag{2.72}$$

Combining Eq. (2.71) with Eq. (2.70) and comparing it with Eq. (2.46), we find the final expression

$$n_\mathrm{s} = \frac{1}{\beta L^d} \frac{m}{\hbar^2} \langle W_x^2\rangle_Z. \tag{2.73}$$

Here, we realise that the superfluid fraction is linked with the winding number estimator. Thus, the worm algorithm which provides us with an efficient modification of configurations is important to study the superfluid density. Moreover, the statement here is restricted along x-axis only but one can extend it for other directions.

2.3.3 Green's function

In the previous section, we mentionned that the exploration of the G-sector is mainly for improving the sampling efficiency in the Z-sector. However, the G-sector itself can also be used for calculating interesting physical quantities. In particular, it gives access to the Matsubara Green's function

$$G(\mathbf{r}_1, \mathbf{r}_2, \tau) = \langle \mathcal{T} \hat{\psi}(\mathbf{r}_1, \tau) \hat{\psi}^\dagger(\mathbf{r}_2, 0)\rangle \tag{2.74}$$

with the function $\hat{A}(\tau) = e^{\tau\hat{H}} \hat{A} e^{-\tau\hat{H}}$ the Heisenberg representation of operator $\hat{A}$ in imaginary time and $\mathcal{T}$ the time-order operator. The connection of this quantity to the G-sector is natural, since the worm itself corresponds to create a particle at time $j_\mathcal{M}$ and annihilate it at $j_\mathcal{I}$. In the following, we assume the interested imaginary time τ is located at the Q-th timeslice, namely $\tau = Q\epsilon$. Here, we only treat the case $\tau > 0$ while the derivation remains

the same for the opposite case. We first insert an identity at timeslice Q into Eq. (2.74) and find

$$G(\mathbf{r}_1,\mathbf{r}_2,\tau)=\frac{1}{Z}\sum_{N=0}^{+\infty}e^{-\beta\mu N}\int d\mathbf{R}_Q d\mathbf{R}_0\langle\mathbf{R}_0|\hat{S}e^{-(J-Q)\epsilon\hat{H}}|\mathbf{R}_Q\rangle\langle\mathbf{R}_Q|\hat{\psi}(\mathbf{r}_1)e^{-Q\epsilon\hat{H}}\hat{\psi}^\dagger(\mathbf{r}_2)|\mathbf{R}_0\rangle. \tag{2.75}$$

We write the creation operator in the first quantization picture and apply it on the vector $|\mathbf{R}\rangle$ which contains N particles. It creates a particle in position $\mathbf{r}$ and generate $\hat{\psi}^\dagger(\mathbf{r})|\mathbf{R}\rangle=\hat{S}|\mathbf{R},\mathbf{r}\rangle$. Then, the integrand in Eq. (2.75) becomes

$$\langle\mathbf{R}_0|\hat{S}e^{-(J-Q)\epsilon\hat{H}}|\mathbf{R}_Q\rangle\langle\mathbf{R}_Q,\mathbf{r}_1|e^{-Q\epsilon\hat{H}}\hat{S}|\mathbf{R}_0,\mathbf{r}_2\rangle. \tag{2.76}$$

Cutting the propagator terms into slices of step ϵ, one can recover the configuration weight Eq. (2.49) up to a factor. Then, the green function can be written as

$$G(\mathbf{r}_1,\mathbf{r}_2,\tau)=\frac{1}{Z}\frac{e^{-Q\epsilon\mu}}{CJ}\int_{G_Q}d\mathcal{C}\mathcal{W}(\mathcal{C})\delta(\mathbf{r}_1-\mathbf{r}_\mathcal{I})\delta(\mathbf{r}_2-\mathbf{r}_\mathcal{M}) \tag{2.77}$$

Here, one should notice that the integral is performed in the subspace G_Q of the G-sector where the distance between the worm endpoints in imaginary time, $j_\mathcal{I}-j_\mathcal{M}$ mod $[J]$, equals Q. Dividing the r.h.s. of the above equation by the partition function of the Q sector, we finally obtain the Monte Carlo estimator

$$G(\mathbf{r}_1,\mathbf{r}_2,\tau)=\frac{e^{-Q\epsilon\mu}}{CJ}\frac{\langle\delta^{(G_Q)}\rangle_W}{\langle\delta^{(Z)}\rangle_W}\langle\delta(\mathbf{r}_1-\mathbf{r}_\mathcal{I})\delta(\mathbf{r}_2-\mathbf{r}_\mathcal{M})\rangle_{G_Q} \tag{2.78}$$

The symbol $\delta^{(Z)}(\mathcal{C})$ equals 1 if $\mathcal{C}$ is in the Z-sector and 0 otherwise. A similar definition holds for $\delta^{(G_Q)}$. In practice, we divide our space with hypercubes of linear size a similarly as for the density estimator. With the statistics of the bins, we calculate the Green function at imaginary time $\tau=Q\epsilon$ from the histogram of the endpoints of the worm for fixed worm length Q. This discretization may introduce systematic error and it can be improved with the method mentioned in Refs. [58, 59].

2.3.4 Correlation function and momentum distribution

The first order correlation function, also known as one-body density matrix, is defined by

$$g^{(1)}(\mathbf{r},\mathbf{r}')=\langle\hat{\psi}^\dagger(\mathbf{r})\hat{\psi}(\mathbf{r}')\rangle \tag{2.79}$$

It measures the spatial coherence of the system and gives very important information about the quantum phase of the cold atom system. It can be given by the Green function at equal time, thus $g^{(1)}(\mathbf{r},\mathbf{r}')=G(\mathbf{r},\mathbf{r}',0)$. Then, the estimator writes

$$g^{(1)}(\mathbf{r},\mathbf{r}')=\frac{1}{CJ}\frac{\langle\delta^{(G_0)}\rangle_W}{\langle\delta^{(Z)}\rangle_W}\langle\delta(\mathbf{r}_1-\mathbf{r}_\mathcal{I})\delta(\mathbf{r}_2-\mathbf{r}_\mathcal{M})\rangle_{G_0} \tag{2.80}$$

Here, the subspace G_0 indicates that Ira and Masha are located on the same timeslice.

Another related quantity which can be calculated here is the momentum distribution. It's defined by $n(\mathbf{k})=\langle\hat{a}^\dagger_\mathbf{k}\hat{a}_\mathbf{k}\rangle$, where $\hat{a}^\dagger_\mathbf{k}$ is the creation operator which adds a particle with momentum $\mathbf{k}$. It measures the particle density with momentum $\mathbf{k}$ of the system. This quantity is important since it can be measured from experiments directly with the time-of-flight in ultracold atom gases for instance. Thanks to the relation with the field operator $\hat{a}^\dagger_\mathbf{k}=\frac{1}{L^{d/2}}\int\hat{\psi}^\dagger(\mathbf{r})e^{i\mathbf{k}\cdot\mathbf{r}}d\mathbf{r}$, we find

$$n(\mathbf{k})=\frac{1}{L^d}\int\langle\hat{\psi}^\dagger(\mathbf{r})\hat{\psi}(\mathbf{r}')\rangle e^{i\mathbf{k}\cdot(\mathbf{r}-\mathbf{r}')}\,d\mathbf{r}d\mathbf{r}'. \tag{2.81}$$

Here, one may realize that the momentum distribution is simply the Fourier transform of the one-body correlation function. We normalize the momentum distribution with the condition $\int \frac{d\mathbf{k}}{2\pi} n(\mathbf{k}) = n$, with n the average density of the system. Inserting Eq. (2.80) into Eq. (2.81), we find

$$n(\mathbf{k}) = \frac{1}{CJL^d} \frac{\langle \delta^{(G_0)} \rangle_W}{\langle \delta^{(Z)} \rangle_W} \langle e^{i\mathbf{k}\cdot(\mathbf{r}_\mathcal{M} - \mathbf{r}_\mathcal{I})} \rangle_{G_0}. \tag{2.82}$$

Conclusion

In this chapter, we introduced the quantum Monte Carlo technique for bosons which is used for the rest of the manuscript. We described the standard PIMC approach which maps the quantum problem into classical interacting polymers thanks to Feynman path integral representation. It evolves in an additional dimension called imaginary time. The weight of the polymer configurations are calculated by the many-body propagator, combined with several analytical and numerical techniques such as Trotter approximation, pair-product approximation and etc. Then, the physical quantities are computed by the Markov chain Monte Carlo based on the Hasting-Metropolis algorithm. We introduced the worm algorithm which implements the PIMC with open worldlines. It allows for a more efficient way of sampling and provides new estimators like the Green function.

With the numerical tools introduced in this chapter, we can now investigate the physical properties for the 1D bosonic systems that is difficult to reach by other methods. In the remainder of this thesis, we shall make extensive us of it.

Chapter 3

Tan's contact for trapped Lieb-Liniger bosons at finite temperature

Describing strongly correlated quantum systems with universal relations is one of the main challenges for modern many-body physics. For strongly-correlated systems with pointlike interactions, it has been shown that for the momentum distribution $n(k)$, the large momentum tails always show an algebraic behavior [121, 122], $n(k) \simeq C/k^4$. We call the weight C the Tan contact. It is a fundamental quantity which can be related to many useful thermodynamic properties of quantum systems. A number of such relations have been derived by Shina Tan [122–124]. Nevertheless, one may notice that the first calculation for the k^{-4} tail of zero temperature gas is indicated in [121]. The existence of the k^{-4} scaling is universal for the many-body systems with short-range interactions, which means it holds irrespective of the dimension, temperature, interaction strength as well as the quantum statistics (bosons or fermions).

In the recent years, the study of the Tan contact attracts a lot of attention, mainly for three reasons.

First, there is a direct access from experiment. Time-of-flight (TOF), known as one of the most widely used techniques in cold atom experiments, can measure the full momentum distribution of the atomic systems. By probing accurately the data at large k tail, one can directly extract the contact from the TOF data. For instance, in the experiment of Ref. [125], they prepare a 3D ^{4}He BEC system and manage to detect the momentum distribution with a good accuracy over 6 orders of magnitudes decaying, see Fig. 3.1.(a). It shows that in principle one can measure the momentum distribution accurate enough and obtain the value of the contact. In this experiment, however, the value of the contact is not measured owing to the collisions with atoms in different internal states. There also exists other examples of measurement such as the one in Ref. [126]: with the radio frequency spectroscopy, they are able to detect the contact for 3D $^{8}5$Rb system at various scattering length, see Fig. 3.1.(b). A series of detection in fermionic systems have also been performed in recent years [127–132]. Moreover, thanks to the development of optical lattices and atom chips [9, 12, 133], it provides the possibility to measure the Tan contact in lower dimension and different regimes.

Second, the Tan contact can give fruitful information about the many-body systems which is hard to detect with standard techniques. With the so-called Tan sweep relations [123], it gives the link between the contact and other macroscopic thermodynamic quantities such as the grand potential Ω, the pressure P and the entropy S. Moreover, the microscopic version of the relation connects the contact with the interaction energy of the system, which is normally hard to measure in the cold atom systems. Therefore,

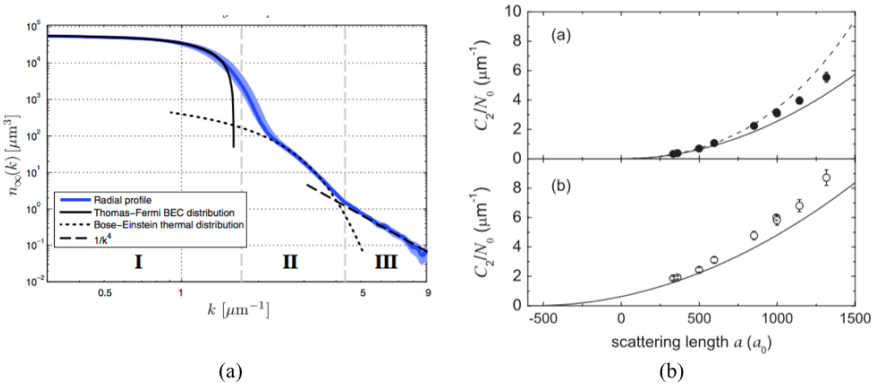

Figure 3.1: Two examples of the potential detection for the Tan contact. (a). The detection in Ref. [125], where the contact is found from the TOF for 3D ^{4}He systems. (b). The detection in Ref. [126], where the contact is found from the radio frequency spectroscopy for 3D ^{8}5Rb systems.

one key motivation to study the contact is that the measurement of the contact gives the possibility to access the information about the quantities mentioned above, which are hard to detect with normal measurement techniques.

Third, the contact is valuable for characterizing different regimes in 1D. Interacting 1D bosons displays different physical regimes at varying interactions and temperatures. The probe of the contact could possibly serve for charaterizing those regimes. Thus, it will be interesting to investigate the behavior of the contact for 1D interacting bosons at various interactions and temperatures. While the homogeneous 1D gas is exactly solvable by Bethe ansatz, the trapped system is not integrable, therefore requiring approximate or *ab initio* numerical approaches. Previously, there have been fruitful theoretical studies on contact in different limits, such as the homogeneous bosons at finite temperature [134, 135], trapped bosons at zero temperature [17, 121], and at finite temperature in the Tonks-Girardeau limit [18]. Several examples of certain set of parameters for the momentum distributions of strongly interacting, trapped bosons at finite temperature were also computed by quantum Monte Carlo methods [136]. However, a complete characterization for trapped Lieb-Liniger bosons at finite temperature is still lacking.

In this chapter, we study the Tan contact for Lieb-Liniger bosons at finite temperature, in the presence of a harmonic trap, at any interaction and temperature [137]. We first prove that the contact follows a two-parameter scaling, and calculate it with a combination of Yang-Yang thermodynamics with local density approximation (LDA), as well as QMC techniques. Then, we identify the behavior of the contact in various regimes of interaction and temperature. For the weakly-interacting regime, the contact is well described by the Gross-Pitaevskii equation and Bogoliubov excitations. More interestingly, for the strongly-interacting regime, the temperature dependence presents a maximum which provides a clear signature of the fermionization of the bosons. Finally, we compute the full momentum distribution in various regimes and analyze the conditions for experimental observation.

Before going into the details about our results, we shall present here several important equations for the contact. The first one is the Tan sweep relation linked with the thermodynamic quantities. In Ref. [123], S. Tan gives the first sweep relation of the contact for 3D fermions, which links it to the total energy E of the system, it writes

$$-\frac{dE}{d(1/a)} = \frac{\hbar^2 C}{2\pi m} \tag{3.1}$$

with a the 3D scattering length of the system. Suggested by Ref. [138], one can rewrite

the relation in lower dimensions. For one-dimensional bosons, we get

$$C = \frac{4m}{\hbar^2} \left. \frac{\partial \Omega}{\partial a_{1\mathrm{D}}} \right|_{T,\mu} \tag{3.2}$$

where Ω is the grand potential. Moreover, one can extend the sweep relation to a form linked with the interaction energy. Using the grand canonical description of the grand potential, we can rewrite Eq. (3.2) as

$$C = \frac{2gm^2}{\hbar^4} \langle \mathcal{H}_{\mathrm{int}} \rangle, \tag{3.3}$$

with $\langle \mathcal{H}_{\mathrm{int}} \rangle$ the interaction energy of the system. This quantity is normally hard to measure separately from the total energy and linked to the pair correlation $g_2(x)$.

3.1 Two-parameter scaling function

The Tan contact of trapped Lieb-Liniger bosons at finite temperature should naturally depend on four parameters. They are the total number of particles N, the temperature T, the trap frequency ω and the coupling constant g. In this section, we firstly show that the contact can actually be written as a scaling function of only two parameters, which characterizes the regimes of the temperature and interaction correspondingly. Then, we calculate the scaling function using two different techniques, namely the Yang-Yang thermodynamics and quantum Monte Carlo. The results of the two different methods are complementary to each other and they also fit well.

3.1.1 The two-parameter scaling

Derivation of the grand potential

In this chapter, we consider a gas of quantum particles, subjected to contact interactions and in the presence of a harmonic confining potential $V(x) = m\omega^2 x^2/2$, in arbitrary dimension d. Here m is the atomic mass, x is the d-dimensional coordinate, and ω is the trap angular frequency. The dynamics is governed by the first-quantization Hamiltonian

$$H = \sum_{j=1}^{N} \left[-\frac{\hbar^2}{2m} \frac{\partial^2}{\partial x_j^2} + V(x_j) \right] + g \sum_{j<\ell} \delta(x_j - x_\ell), \tag{3.4}$$

where x_j and x_ℓ span the ensemble of N particles. For proceeding, we start with the homogenous case $V(x) = 0$. In any dimension but $d = 2$, the coupling constant g in the Hamiltonian defines the natural length scale $a_{\mathrm{sc}} \sim (2mg/\hbar^2)^{1/(d-2)}$, known as the scattering length. In dimension $d = 2$, the rescaled coupling constant $mg/\hbar^2$ is dimensionless. But one can recover the following derivation with the same logic which we will not give details. First of all, working in the grand-canonical ensemble, we write the expression for the grand-potential

$$\Omega = -k_{\mathrm{B}} T \ln \left[\mathrm{Tr}\ \mathrm{e}^{-(\mathcal{H} - \mu\mathcal{N})/k_{\mathrm{B}}T} \right] \tag{3.5}$$

where k_{B} is the Boltzmann constant, $\mathcal{N}$ the particle number operator, and μ the chemical potential. The other thermodynamic properties can be derived from it. Here, We propose a rescaling approach by using $k_{\mathrm{B}}T$ as the unit energy and, correspondingly, the thermal de Broglie wavelength $\lambda_T = \sqrt{2\pi\hbar^2/mk_{\mathrm{B}}T}$ as the unit length. Then, we can readily find that the grand potential Ω divided by the temperature is a universal function that

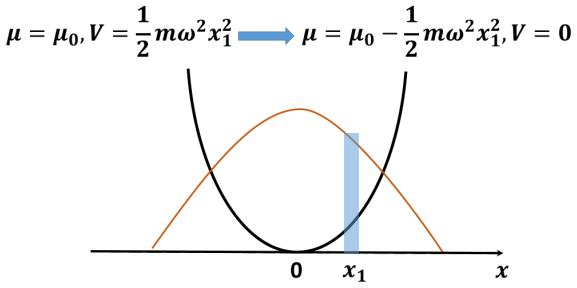

Figure 3.2: Sketch of the LDA. Here, we present a one-dimensional atom system trapped by a harmonic potential. The brown curve presents the trap potential which is a parabola, while the black curve stands for the density distribution of the atoms.

depends only on the two dimensionless quantities $\alpha = \mu/k_{\mathrm{B}}T$ (logarithm of the fugacity) and $\xi_{\mathrm{T}} = |a_{\mathrm{sc}}|/\lambda_T$,

$$\frac{\Omega}{k_{\mathrm{B}}T} = \frac{L^d}{\lambda_T^d}\mathcal{A}_{\mathrm{h}}\left(\frac{\mu}{k_{\mathrm{B}}T}, \frac{|a_{\mathrm{sc}}|}{\lambda_T}\right), \tag{3.6}$$

with $\mathcal{A}_{\mathrm{h}}$ a dimensionless function stemming from Eqs. (5.9) and (3.5). Because all the thermodynamic quantities can be found from Ω by partial derivatives, the scaling forms of the thermodynamic quantities then follow from Eq. (3.6)

Then, we move to a gas under harmonic confinement which applies to a cold gas in an optical or magnetic trap, within harmonic approximation. Here, the additional energy scale $\hbar\omega$ emerges, associated to the length scale $a_{\mathrm{ho}} = \sqrt{\hbar/m\omega}$. In this situation, we need to use the local density approximation (LDA). A simple explanation of the LDA is illustrated by Fig. 3.2. For a fixed position point x_1, instead of saying that it's a point of inhomogeneous system with chemical potential μ_1 and trap potential $V(x_1) = \frac{1}{2}m\omega^2 x_1^2$, we treat it as a locally homogeneous point at the chemical potential $\mu_1' = \mu_1 - V$ and trap potential $V = 0$. Within LDA, we show here that the thermodynamic properties of the harmonically trapped gas depend again on only two parameters, found as combinations of N, a_{sc}, a_{ho}, and $k_{\mathrm{B}}T$. To proceed, we first find the LDA expression for the grand potential,

$$\frac{\Omega}{k_{\mathrm{B}}T} = \int \frac{d^d x}{\lambda_T^d}\,\mathcal{A}_{\mathrm{h}}\left[\mu - V(x), T, g\right]. \tag{3.7}$$

Using the scaling form (3.6) and rescaling the position x in each of the position by the quantity $2\sqrt{\pi}a_{\mathrm{ho}}^2/\lambda_T$ in the integral, we then find

$$\frac{\Omega}{k_{\mathrm{B}}T} = \left(\frac{a_{\mathrm{ho}}}{\lambda_T}\right)^{2d}\mathcal{A}\left(\frac{\mu}{k_{\mathrm{B}}T}, \frac{|a_{\mathrm{sc}}|}{\lambda_T}\right). \tag{3.8}$$

with $\mathcal{A}$ a dimensionless function stemming from $\mathcal{A}_{\mathrm{h}}$. As a result, since all thermodynamics quantities can then be computed from Eq. (3.8), we conclude that any thermodynamic quantities in appropriate unit can be written as a function of these two parameters. For example, the number of particles in found using the thermodynamic relation

$$N = -\left.\frac{\partial\Omega}{\partial\mu}\right|_{T,a_{\mathrm{sc}}}. \tag{3.9}$$

Combining with Eq. (3.8), it yields

$$N = \left(\frac{a_{\mathrm{ho}}}{\lambda_T}\right)^{2d}\mathcal{A}_N\left(\frac{\mu}{k_{\mathrm{B}}T}, \frac{|a_{\mathrm{sc}}|}{\lambda_T}\right) \tag{3.10}$$

with $\mathcal{A}_N$ a dimensionless function stemming from $\mathcal{A}$.

Finally, we focus on the case $d = 1$, which is the situation for Lieb-Liniger bosons. Then, Eq. (3.8) can be written as

$$\frac{\Omega}{k_{\mathrm{B}}T} = \big(\frac{a_{\mathrm{ho}}}{\lambda_T}\big)^2 \mathcal{A}\big(\frac{\mu}{k_{\mathrm{B}}T}, \frac{a_{1\mathrm{D}}}{\lambda_T}\big). \tag{3.11}$$

Also, taken $d = 1$ in Eq. (3.10), we find the number of particles N writes

$$N = \big(\frac{a_{\mathrm{ho}}}{\lambda_T}\big)^2 \mathcal{A}_N\big(\frac{\mu}{k_{\mathrm{B}}T}, \frac{a_{1\mathrm{D}}}{\lambda_T}\big). \tag{3.12}$$

Changing variables

In actual experiments, the observed parameters are the temperature T, the number of particles N, the scattering length $a_{1\mathrm{D}}$ and the trap frequency ω. There is no direct access to the chemical potential μ. Therefore, it is fruitful to change the variables in the scaling function into the experimental parameters by replacing μ. In Eq. (3.12), we can normalize the right-hand side's factor to 1, and find the left-hand side write $N\lambda_T^2/a_{\mathrm{ho}}^2$. Then, one can rewrite it by exchanging the variables on the two counterparts and find

$$\frac{\mu}{k_{\mathrm{B}}T} = \mathcal{U}\big(\frac{N\lambda_T^2}{a_{\mathrm{ho}}^2}, \frac{a_{1\mathrm{D}}}{\lambda_T}\big) \tag{3.13}$$

with $\mathcal{U}$ some function stemming from Eq. (3.12). Equivalently, we can rewrite the two parameters and finally find

$$\xi_\gamma = -a_{\mathrm{ho}}/a_{1\mathrm{D}}\sqrt{N}, \tag{3.14}$$

$$\xi_{\mathrm{T}} = -a_{1\mathrm{D}}/\lambda_T, \tag{3.15}$$

Here, the parameter ξ_γ is simply the square root of the inverse of the first parameter in Eq. (3.13). With the two new parameters, we can also rewrite Eq. (3.13) as

$$\frac{\mu}{k_{\mathrm{B}}T} = \tilde{\mathcal{U}}(\xi_\gamma, \xi_{\mathrm{T}}). \tag{3.16}$$

Then, for any scaling function A we calculated previously, it can write

$$A\big(\frac{\mu}{k_{\mathrm{B}}T}, \frac{a_{1\mathrm{D}}}{\lambda_T}\big) = A\big(\tilde{\mathcal{U}}(\xi_\gamma, \xi_{\mathrm{T}}), \xi_{\mathrm{T}}\big) = \tilde{A}(\xi_\gamma, \xi_{\mathrm{T}}) \tag{3.17}$$

For instance, the final scaling function of the grand potential writes

$$\frac{\Omega}{k_{\mathrm{B}}T} = \big(\frac{a_{\mathrm{ho}}}{\lambda_T}\big)^2 \tilde{\mathcal{A}}(\xi_\gamma, \xi_{\mathrm{T}}) \tag{3.18}$$

One may notice that these two parameters ξ_γ and ξ_{T} will be the final parameters we use, and they characterize the interaction and temperature strength for the systems.

Application to the Tan contact

Finally, we can apply the two parameters scaling to the contact. First, by inserting Eq. (3.11) into the Tan sweep relation Eq. (3.2), we find

$$C = \frac{a_{\mathrm{ho}}^2}{a_{1\mathrm{D}}^5} \mathcal{A}_C\big(\frac{\mu}{k_{\mathrm{B}}T}, \frac{a_{1\mathrm{D}}}{\lambda_T}\big) \tag{3.19}$$

Using Eq. (3.16) and writing $\mu/k_{\mathrm{B}}T$ as a function of ξ_γ and ξ_{T}, it yields

$$C = \frac{a_{\mathrm{ho}}^2}{a_{1\mathrm{D}}^5} f\left(\xi_\gamma, \xi_{\mathrm{T}}\right), \tag{3.20}$$

Then, with the help of Eq. (3.12) and the fact that $\xi_{\mathrm{T}} = -a_{1\mathrm{D}}/\lambda_T$, we can replace the parameter $a_{1\mathrm{D}}$ by N in the prefactor of Eq. (3.20) and finally find

$$C = \frac{N^{5/2}}{a_{\mathrm{ho}}^3} f\left(\xi_\gamma, \xi_{\mathrm{T}}\right), \tag{3.21}$$

with f a dimensionless function. In the following, we shall use this two-parameter scaling form and calculate in detail the function f. Note that the choice of the scaling parameters is not unique For instance, one can also choose $2mk_{\mathrm{B}}T/(\hbar^2 n_0^2)$ and $mg/(\hbar^2 n_0)$ as in Ref. [136], with n_0 being the density at the trap centre. One can relate our scaling parameters to those ones since N is always function of n_0 and a_{ho}. Moreover, the procedure used to find the scaling form (3.21) is general and can be straightforwardly extended to higher dimensions and Fermi gases.

Here, one should notice that the whole derivation is working within the grand-canonical ensemble. This is the same with the YY calculation mentioned in section 1.2.3 as well as the PIMC technique presented in Chapter 2 . Therefore, in the next sessions, we compute the scaling function with both of these two methods.

3.1.2 Computing the scaling function using the Yang-Yang theory

Now, we want to find the scaling function f for interacting 1D bosons. In this subsection, we propose to tackle this issue by combining the YY thermodynamics with the local density approximation (LDA), although the validity of LDA for 1D bosons are questionable. We shall further implement the calculation of QMC to verify its validity in the next subsection.

Yang-Yang thermodynamics for 1D bosons

Here, we recall the Yang-Yang equation for 1D homogeneous bosons which we have introduced in section 1.2.3. It writes

$$\epsilon(k) = \frac{\hbar^2 k^2}{2m} - \mu - \frac{k_B T}{2\pi} \int_{-\infty}^{+\infty} dq \frac{g}{g^2/4 + (k-q)^2} \ln\left[1 + e^{-\frac{\epsilon(q)}{k_B T}}\right]. \tag{3.22}$$

where $\epsilon(k)$ is the dress energy, μ is the chemical potential, g the coupling constant and T is the temperature. The term $\epsilon(k)$ is related to the ratio of density between particle and holes at quasi-momentum k, and it is linked with many thermodynamic quantities, such as the grand potential density

$$\Omega_h/L = -k_{\mathrm{B}} T \int \frac{dq}{2\pi} \ln\left[1 + e^{-\frac{\epsilon(q)}{k_{\mathrm{B}} T}}\right]. \tag{3.23}$$

Moreover, based on the solution of Ω, one can find the particle density by Eq. (3.9).

Now, we will explain in detail how we solve the Yang-Yang equations numerically. The procedure is the following:

- 1. For a given set of values (T, g, μ, ω), we start with a initial setup $\epsilon_0(k)$, which is not far from the true solution. In principle, one can start with any $\epsilon_0(k)$. However, for practical purpose, it is better to start from a set not far from the solution. It can be done by starting at the zero temperature and strongly-interacting limit, and then calculating successively the solutions for decreasing g and increasing μ and T.

- 2. Inserting the initial values of $\epsilon_0(k)$ into the r.h.s. of Eq. (3.22), we obtain a in $\epsilon_1(k)$ from the l.h.s.

- 3. With $\epsilon_1(k)$, redo the step 2, we find $\epsilon_2(k)$. Then, similarly, we get $\epsilon_3(k)$... and $\epsilon_n(k)$.

- 4. After m loops, when $\epsilon_m(k)$ are converged with $\int |\epsilon_m(k) - \epsilon_{m-1}(k)| < 10^{-3} k_B T$, we stop the iterations and the quantity $\epsilon_m(k)$ is a good approximation of the solution we want. Here, one should notice that the convergence condition may be more strict for special groups of parameters.

Then, with the final solution of $\epsilon(k)$, we can calculate the thermodynamic quantities we are interested. For instance, we can get the grand potential Ω and density n from Eq. (3.23) and Eq. (3.9). One successive example of solving the Yang-Yang thermodynamics has been shown in sec. 1.2.3, see Fig. 1.4 and its discussion.

Then, we can calculate the thermodynamic quantities in the trapped case with LDA. First, we shall write the grand potential of the inhomogeneous system by doing the integral of the local grand potential density. In 1D, Eq. (3.7) yields

$$\Omega = \frac{1}{L} \int dx \Omega_h(\mu - V(x), g, T), \tag{3.24}$$

with the potential $V(x) = m\omega^2 x^2/2$ for a harmonic trap. Then, we can also write the number of particles by integrating the density,

$$N = \int dx\ n(\mu - V(x), g, T). \tag{3.25}$$

Finally, inserting Eq. (3.24) the sweep relation Eq. (3.2), we can find the Tan contact for a trapped system.

The Yang-Yang solution for the Tan contact

With the procedure of Yang-Yang calculation we discussed above, we calculate the scaling function f, namely the rescaled contact $a_{\mathrm{ho}}^3 C/N^{5/2}$ as a function of the parameters ξ_γ and ξ_{T}, for 1D bosons under harmonic confinement from YY theory and LDA. The final result is shown in Fig. 3.3. Here, the parameters ξ_γ covers the weak to strong interaction regimes when it goes from 10^{-2} to 10^{1}. Similarly for ξ_{T} since it scans over the low to high temperature regimes when ranges from 10^{-2} to 10^{2}. For low temperature (small ξ_{T}), as ξ_γ increases, the rescaled contact increases slower and slower, and reaches a constant in the end. This behavior fits with the Bethe ansatz prediction of the zero temperature limit in Ref. [121]. Conversely, for high temperature (large ξ_{T}), the rescaled contact keeps increasing while ξ_γ increases. Moreover, in the weakly-interacting regime (small ξ_γ), only a weak temperature dependence is observed. However, for the strongly-interacting regime (large ξ_γ), when the temperature increases, the rescaled contact firstly behaves like a constant, then increases with T , and finally decreases with T, where an interestingly non-monotonic temperature dependence appears.

Here, one should notice that the results presented here need to be checked owing to two reasons. On the one hand, the presence of quasi long-range correlation in low temperature 1D Bose gases may break the LDA calculation. On the other hand, the Y-Y thermodynamics is valid in the thermodynamic limit and our calculation is performed in presence of a harmonic trap, i.e. finite size and finite number of particles. Therefore, it's not clear that for the system and quantity we study, whether the LDA is correct or not. Thus, beyond calculating the result from Y-Y dynamics combined with LDA, it is useful to check its validity by comparing with the QMC and true experimental data.

3.1.3 Validation of the scaling function using quantum Monte Carlo

To validate the two parameter scaling and the accuracy of the LDA, we perform *ab initio* quantum Monte Carlo (QMC) calculations. We use the path integral Monte Carlo with worm algorithm implementation as described in Chapter 2. The continuous-space path

integral formulation allows us to simulate the exact Hamiltonian in Eq. (5.9), for an arbitrary trap $V(x)$, within the grand-canonical ensemble. With a certain input of chemical potential μ, temperature T, interaction strength g and trap frequency ω, the statistical average of the number of worldlines yields the total number of particles N. By cutting the system into small pixels, we can further compute the density profile $n(x)$. Moreover, the interaction energy $\langle H_{\rm int}\rangle$ can be calculated from the statistical average of the action U. The U can be extracted from the numerics restricted in the Z-sector $\langle U\rangle_Z$. By definition, it equals to the sum of the external potential energy E_1 and interaction energy E_2. Then, with the calculated density profile $n(x)$ from the QMC, one can obtain the term E_1 by $E_1 = \int dx\, V(x)n(x)$. Thus, we can find the interaction energy by the difference of the two terms

$$E_2 = \frac{\langle U\rangle_Z}{\beta} - \int dx\, V(x)n(x) \tag{3.26}$$

Finally, the contact is found using the thermodynamics relation Eq. (3.3).

Finite-ϵ scaling of QMC computation

In QMC calculations, the worldlines are cut into an adjustable number M of slices of imaginary propagation time $\epsilon = 1/Mk_BT$ and sampled efficiently using worm algorithm [58, 59]. As explained in Chapter 2, the QMC results are exact only in the $\epsilon \to 0$ limit. In order to find the proper final results, we actually perform a finite-ϵ analysis. For each set of physical parameters (interaction strength, chemical potential, temperature, and trap frequency), we perform a series of QMC calculations for different values of ϵ and extrapolate the result to the limit $\epsilon \to 0$. Here, we give the detail of such an analysis.

For most of the calculations, we are able to use a sufficiently small value of ϵ and a linear extrapolation is sufficient. We fit the QMC data with $a_{\rm ho}^3 C/N^{5/2} = a + b(\epsilon/\beta)$, with a and b as fitting parameters. Then, we use the quantity a as the final result for $a_{\rm ho}^3 C/N^{5/2}$. An example is shown on the left panel of Fig. 3.4 below. In this case, the linear extrapolation only corrects the QMC result for the smallest value of ϵ ($\epsilon/\beta = 0.01$) by less than 4%.

In some other cases, however, the linear fit is not sufficient for extrapolating correctly the QMC results. This occurs mostly in the strongly-interacting regime for low to intermediate temperatures. In such cases, we use a third-order polynomial, $a_{\rm ho}^3 C/N^{5/2} = a + b(\epsilon/\beta) + c(\epsilon/\beta)^2 + d(\epsilon/\beta)^3$, to extrapolate the finite-ϵ numerical data. An example is shown on the right panel of Fig. 3.4. In this case, the extrapolation corrects the QMC

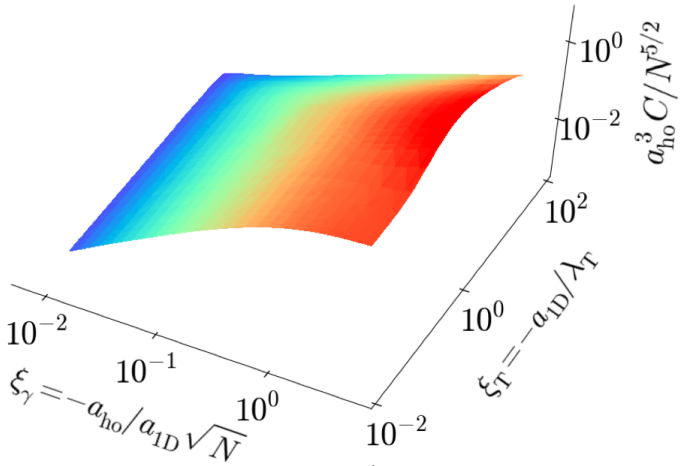

Figure 3.3: Reduced Tan contact $a_{\rm ho}^3 C/N^{5/2}$ for 1D Bose gases in a harmonic trap, versus the reduced temperature $\xi_{\rm T} = -a_{\rm 1D}/\lambda_T$ and the reduced interaction strength $\xi_\gamma = -a_{\rm ho}/a_{\rm 1D}\sqrt{N}$. The results are found using thermal Bethe ansatz solutions combined with local density approximation.

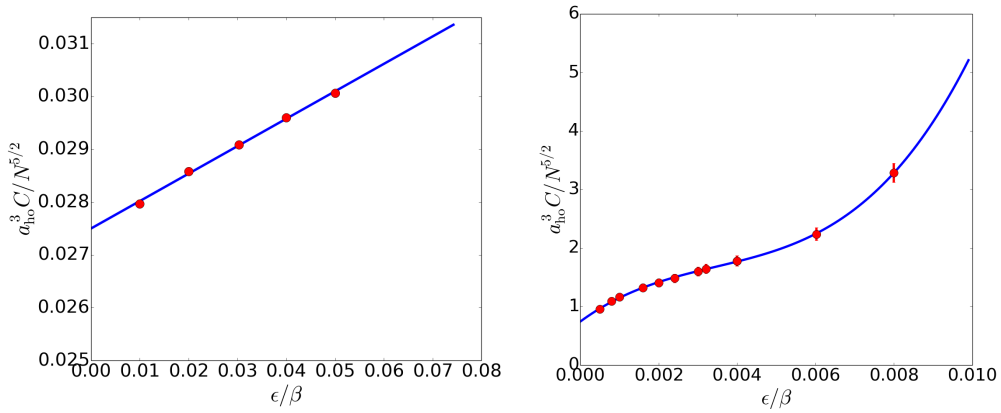

Figure 3.4: Quantum Monte Carlo (QMC) results for the reduced Tan contact for $\xi_T = |a_{1D}|/\lambda_T = 0.28$ and $\xi_\gamma = a_{ho}/|a_{1D}|\sqrt{N} = 0.1$ (left panel) and for $\xi_T = 0.0085$ and $\xi_\gamma = 4.47$ (right panel). The red points show the QMC results for various values of the dimensionless parameter ϵ/β, where $\beta = 1/k_B T$ is the inverse temperature, together with a linear (left panel) or third-order polynomial (right panel) fit.

result for the smallest value of ϵ ($\epsilon/\beta = 0.0005$) by roughly 25%.

Nevertheless, for all the QMC results reported in this thesis, we have performed a systematic third-order polynomial extrapolation, even when a linear extrapolation was sufficient.

The validation of the scaling function

For checking the validation of the scaling as well as LDA, we check in detail the QMC data along cuts on Fig. 3.3. In Fig. 3.5(a), we plot the contact $a_{1D}^3 C$ as a function of the interaction strength ξ_γ for various values of the temperature via the quantity $\xi_T = -a_{1D}/\lambda_T = 0.0085$ (blue), 0.28 (green), and 18.8 (red). For each ξ_T, we also try to cover a broad set of parameters, which corresponds to the various symbols $|a_{1D}|/a_{ho} = 9.5$ (red squares), 0.032 (red diamonds), 1.41 (green squares), 0.14 (green diamonds), 0.14 (blue squares), and 2.02 (blue diamonds). Here, one may notice that the scaling of the contact

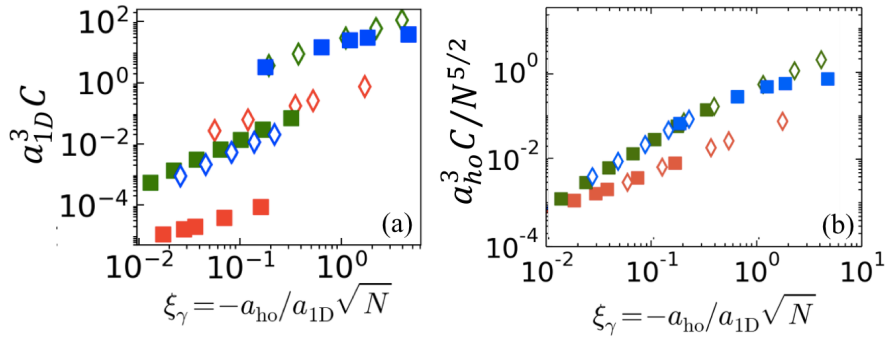

Figure 3.5: Tan contact versus the scaling parameters from QMC calculations (points). The contact is rescaled in two different ways: (a). The Monte-Carlo scaling $a_{1D}^3 C$. (b). The scaling in the function f: $a_{ho}^3 C/N^{5/2}$. The colors indicate the fixed temperatures $\xi_T = -a_{1D}/\lambda_T = 0.0085$ (blue), 0.28 (green), and 18.8 (red). The different symbols indicate different set of parameters, namely $|a_{1D}|/a_{ho} = 9.5$ (red squares), 0.032 (red diamonds), 1.41 (green squares), 0.14 (green diamonds), 0.14 (blue squares), and 2.02 (blue diamonds).

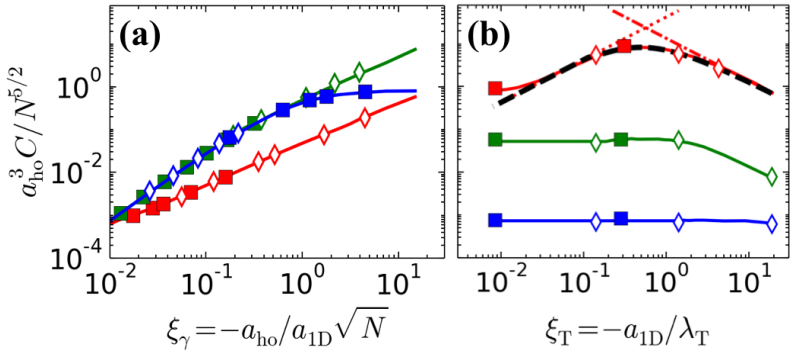

Figure 3.6: Reduced Tan contact $a_{\rm ho}^3 C/N^{5/2}$ versus the scaling parameters, as found from LDA (solid lines) and QMC calculations (points). (a) Reduced contact versus the interaction, $\xi_\gamma = -a_{\rm ho}/a_{\rm 1D}\sqrt{N}$, at the fixed temperatures $\xi_{\rm T} = -a_{\rm 1D}/\lambda_T = 0.0085$ (blue), 0.28 (green), and 18.8 (red). (b) Reduced contact versus the temperature via the quantity $\xi_{\rm T}$ at the fixed interaction strengths $\xi_\gamma = 10^{-2}$ (blue), 1.58×10^{-1} (green), and 15.0 (red). The black dashed, red dotted, and red dash-dotted lines correspond to Eqs. (3.54),(3.38), and (3.49) respectively. The QMC data are found from various sets of parameters, corresponding to the various symbols.

$a_{\rm 1D}^3 C$ is not the scaling we proposed and just directly what is returned by the numerical QMC codes. Apparently, without the proper scaling, the data for a fixed $\xi_{\rm T}$ stays apart. Thus, we plot the same data with the scaling we proposed $a_{\rm ho}^3 C/N^{5/2}$ in Fig. 3.5(b). We find the data points for the same $\xi_{\rm T}$ collapse and get aligned. It confirms that $a_{\rm ho}^3 C/N^{5/2}$ is a function of the two parameters $\xi_{\rm T}$ and ξ_γ, hence validating the scaling Eq. (3.21).

The validation of the local density approximation

Moreover, in Fig. 3.6(a), we plot on top of the Fig. 3.5(b) the results from YY+LDA (solid lines) for a quantitative comparison. Clearly, the QMC data falls onto the LDA lines. We even perform the computation inversely, i.e. the rescaled contact as a function of $\xi_{\rm T}$ for various values of ξ_γ in Fig. 3.6(b). Different colors represent the interaction strength $\xi_\gamma = 10^{-2}$ (blue), 1.58×10^{-1} (green), and 15.0 (red). Also, the different symbols stand for different sets of parameters $|a_{\rm 1D}|/a_{\rm ho} = 10$ (blue squares), 31.62 (blue diamonds), 0.45 (green squares), 1.41 (green diamonds), 75.0 (red squares) and 47.4 (red diamonds). We still find the collapsing of the QMC data points from different sets of parameters validates the scaling function, and the matches between QMC and YY+LDA results prove that the LDA is very accurate in computing the contact for the trapped LL model. Quite remarkably, the agreement holds also in the low-temperature and strongly interacting regime where the particle number is as small as $N \simeq 5$, within less that 3%.

3.2 The behavior of the contact and regimes of degeneracy

In this section, we study in detail the behavior of the contact in different regimes. In fact, the Tan contact is a good quantity to characterize different regimes of bosons, at least in 1D. The function f behaves very differently in different regimes. We firstly recall the known the results for the homogeneous case, and then move to the study of our scaling function in the trapped case. By studying the contact as a function of the two parameters ξ_γ and $\xi_{\rm T}$, one can recognize which regime the system is in. In each regime, we can find the function f analytically under certain approximations. Then, we compare it with our numerical results and find they fit well with each other. Finally, we especially announce the onset of the maximum in the strongly-interacting regime, which is a signature of the

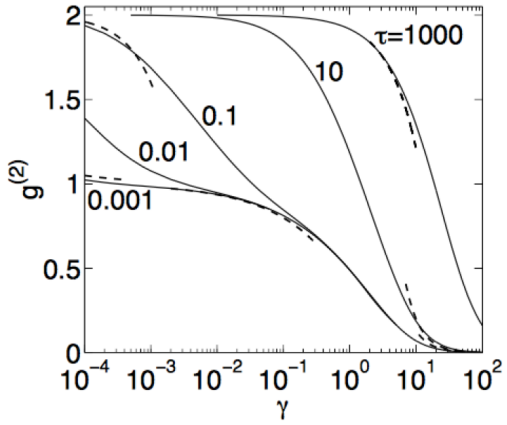

Figure 3.7: The local correlation $g^{(2)}$ versus interaction γ at different temperature τ. The solid curves are exact numerical results while the dashed lines are analytical formulas. The plot is from [134].

crossover to fermionized regime.

3.2.1 The behavior of the contact in the homogeneous case

Before discussing the behavior of the contact for the 1D trapped bosons, we firstly present the known results of the contact in homogeneous case. In [134], the authors studied the two-body correlation function $g^{(2)} = \langle\hat{\Psi}^\dagger\hat{\Psi}^\dagger\hat{\Psi}\hat{\Psi}\rangle/n^2$ for 1D homogeneous bosons in various regimes, with $\hat{\Psi}$ the field operator. The interaction and temperature parameters are chosen as the Lieb-Liniger parameter γ and the reduced temperature $\tau = T/T_\mathrm{d}$ with $T_\mathrm{d} = \hbar^2 n^2/2m$ the degeneracy temperature. The result is shown in Fig. 3.7.

In the case of 1D homogeneous bosons, the Tan contact C can be mapped to the quantity $g^{(2)}$ by the relation

$$g^{(2)} = \frac{\hbar^4}{m^2 g^2 n^2 L} C. \tag{3.27}$$

Therefore, the results shown in Fig. 3.7 reflects the behavior of the contact. In low temperature limit (see for instance $\tau = 0.001$), the result fits well with the prediction of Sommerfield expansion of ideal fermions in the strongly-interacting regime, while it matches the Gross-Pitaevskii prediction in the weakly-interacting regime. In the high temperature limit (see for instance $\tau = 1000$), the quantum degeneracy is broken and the behavior fits well with what is predicted by the decoherent bosons. Here, we would like to draw the attention of readers to an important point. According to the results in Fig. 3.7, at any regimes, for a fixed coupling constant g and particle density n, the Tan contact always increases with temperature. In the next subsection, we will see that the contact behaves non-monotonically due to the influence of the harmonic trap, where an interesting phenomenon appears.

3.2.2 The scaling function in different regimes

The regimes of degeneracies for the 1D trapped bosons have been discussed in Refs. [70,134], with another pair of parameters N and $T/\hbar\omega$ and a fixed value $-a_\mathrm{ho}/a_\mathrm{1D} = 10$. Here, we extend the discussion to more general cases using the two scaling parameters we mentioned above, namely the temperature parameter ξ_T and the interaction parameter ξ_γ, see Fig. 3.8. In the following, we will explain the condition of each regime, and then give the analytical form for the contact.

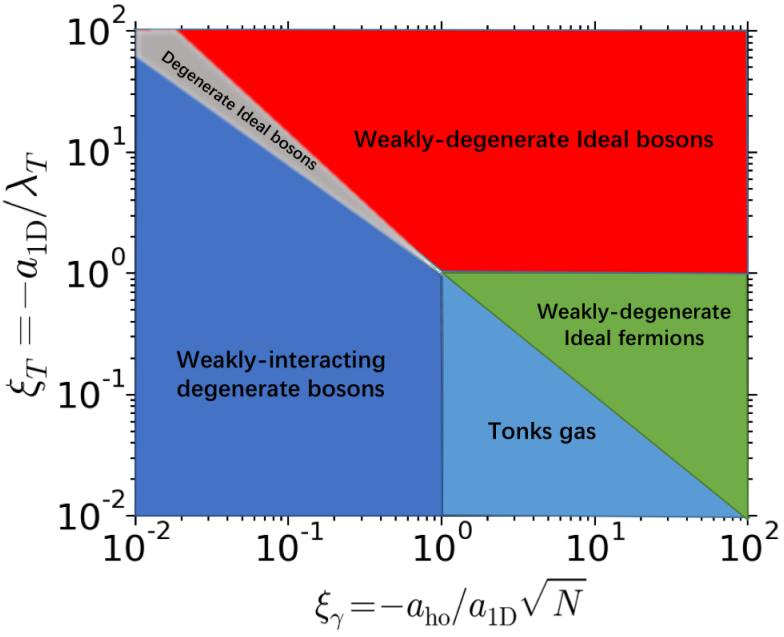

Figure 3.8: The regime of degeneracy for 1D Lieb-Liniger bosons at finite temperature, in presence of a harmonic trap.

Strongly-interacting regime at low temperature ($\xi_T \lesssim \xi_\gamma^{-1} \lesssim 1$)

As explained in the first chapter, the strongly-interacting bosons at low temperature behaves like ideal fermions, which is also known as the Tonks-Girardeau gases. There are two conditions for this regime. On the one hand, the Lieb-liniger parameter $\gamma_0 = mg/\hbar^2 n_0$, with n_0 the density in the centre of the trap, should be large enough, i.e. $\gamma_0 \gtrsim 1$. Since the density decreases from the trap center to edges, it guarantees that all the gas is strongly-interacting. On the other hand, the temperature T should be smaller than the quantum degeneracy temperature for fermions,

$$T_d = \frac{\hbar^2 n_0^2}{2mk_B}. \tag{3.28}$$

This ensures that the equivalent ideal Fermi gas is strongly degenerated and weakly affected by temperature effects. It can thus be considered at zero temperature. Combining the two conditions and using our scaling parameters, we find

$$\xi_T \lesssim \xi_\gamma^{-1} \lesssim 1. \tag{3.29}$$

In this regime, the gas is strongly degenerated and the density profile is frozen by Pauli blocking to the fermionic Thomas-Fermi (TF) form

$$n(x) = n_0\sqrt{[1-(x/L_{TF})^2]}, \tag{3.30}$$

with $n_0 = \sqrt{2m\mu/\pi^2\hbar^2}$ the density in the center of the trap, $L_{TF} = \sqrt{2\mu/m\omega^2}$ the TF half-length and μ the chemical potential. Integrated Eq. (3.30) for x in range $[-L_{TF}, L_{TF}]$, we find the total number of particles follows $N \sim n_0 L_{TF}$. Since $n_0 \sim L_{TF}/a_{ho}^2$, it yields $N \sim L_{TF}^2/a_{ho}^2$. Thus, the typical density yields $n \sim N/L_{TF} \propto \sqrt{N}/a_{ho}$ Moreover, the kinetic energy density in this regime writes

$$e_K(x) = \pi^2\hbar^2 n(x)^3/2m. \tag{3.31}$$

The contact can then be found from the Bose-Fermi mapping [139]

$$C = (4m/\hbar^2) \int dx\, n(x) e_K(x). \tag{3.32}$$

Inserting the Eq. (3.30) and Eq. (3.31) into the Fermi formula above and computing the integration, we find

$$C = \frac{256\sqrt{2}}{45\pi^2} \frac{N^{5/2}}{a_{\rm ho}^3}, \quad \xi_{\rm T} \lesssim \xi_\gamma^{-1} \lesssim 1. \tag{3.33}$$

This formula also matches the results in Ref. [121], where the authors obtain it from the Bethe ansatz result of the strong interaction limit.

Strongly-interacting regime at intermediate temperature ($\xi_\gamma^{-1} \lesssim \xi_{\mathbf{T}} \lesssim 1$)

When we are in the condition

$$1 \lesssim \frac{T}{T_{\rm d}} \lesssim \gamma_0^2, \tag{3.34}$$

the temperature is larger than the Fermi degeneracy temperature. Moreover, rewriting $T/T_{\rm d} \lesssim \gamma_0^2$, we find $a_{\rm 1D} \lesssim \lambda_T$, which indicates the 1D scattering length $a_{\rm 1D}$ is still smaller than the De Broglie wavelength λ_T. In this regime, both quantum and thermal fluctuations are dominated by repulsive interactions and the gas is still fermionized although with weak degeneracy. Thus, the gases can be treated as weakly-degenerate Fermions. Rewriting the condition of the regime Eq (3.34) with our scaling parameters, we find

$$\xi_\gamma^{-1} \lesssim \xi_{\rm T} \lesssim 1 \tag{3.35}$$

Since the gas is weakly degenerate, the kinetic energy density of the equivalent ideal Fermi gas follows from the equipartition theorem of the kinetic part, i.e.

$$e_{\rm K}(x) = \frac{n(x) k_{\rm B} T}{2} \tag{3.36}$$

and the density profile can be taken as the noninteracting one,

$$n(x) = \left(\frac{N}{\sqrt{2\pi} L_{\rm th}} \right) \exp(-x^2/2L_{\rm th}^2) \tag{3.37}$$

with $L_{\rm th} = \sqrt{k_{\rm B}T/m\omega^2}$. The contact is then found from the Bose-Fermi mapping Eq. (3.32). It yields

$$C = \frac{2\sqrt{2} N^{5/2} \xi_\gamma \xi_{\rm T}}{a_{\rm ho}^3}, \quad \xi_\gamma^{-1} \lesssim \xi_{\rm T} \lesssim 1, \tag{3.38}$$

which increases as $\sqrt{T}$ with temperature. It thus recovers the results of Ref. [18] by a different approach where the regime is called non-degenerate fermions.

The weakly interacting regime at low temperature ($1, \xi_{\mathbf{T}} \lesssim \xi_\gamma^{-1}$)

In the weakly-interacting regime, $\gamma_0 \lesssim 1$, the gas is never fermionized. At low enough temperature, i.e. $k_{\rm B}T \lesssim N\hbar\omega$, the gas forms a quasicondensate characterized by suppressed density fluctuations and the density profile follows the one of Thomas-Fermi type [70,134]. [1] We can rewrite the conditions mentioned above with our scaling parameters. On the one hand, since $n \sim \sqrt{N}/a_{\rm ho}$ (demonstration similarly as the Thomas-Fermi profile in the strongly-interacting regime), the condition $\gamma_0 \lesssim 1$ indicates $\xi_\gamma \lesssim 1$. On the other hand,

[1] Within this regime, when $k_{\rm B}T < N\hbar^2\omega^2/2\mu$, the phase fluctuation is also suppressed and the system forms a true condensate.

for the condition $k_{\mathrm{B}}T \lesssim N\hbar\omega$, replacing the term N and T with proper power of ξ_γ and ξ_{T} correspondingly, we find $\xi_{\mathrm{T}}\xi_\gamma \lesssim 1$. Combining the two conditions, it yields

$$1, \xi_{\mathrm{T}} \lesssim \xi_\gamma^{-1}. \tag{3.39}$$

This regime is named as "Weakly-interacting degenerate bosons" in Fig. 3.8. It is also called "GP regime" in Ref. [134], since the system can be described by the Gross-Pitaevskii equation. The contact can be found from the mean-field expression for the interaction energy,

$$\langle \mathcal{H}_{\mathrm{int}} \rangle = \frac{1}{2}\int dx\ gn(x)^2, \tag{3.40}$$

where the density profile can be described by the Thomas-Fermi (TF) density profile

$$n(x) = \frac{\mu}{g}(1 - x^2/L_{\mathrm{TF}}^2) \tag{3.41}$$

with $L_{\mathrm{TF}} = \sqrt{2\mu/m\omega^2}$. Inserting Eq. (3.41) into Eq. (3.40), we shall obtain the interaction energy. Thanks to the sweep relation Eq. (3.3), we then find the contact

$$C = \eta\frac{N^{5/2}\xi_\gamma^{5/3}}{a_{\mathrm{ho}}^3}, \quad 1, \xi_{\mathrm{T}} \lesssim \xi_\gamma^{-1} \tag{3.42}$$

with $\eta = 4 \times 3^{2/3}/5$. It's possible to find the very weak Bogouliubov corrections on top of it and one can show that the small temperature effect in low temperature regime leads to a very weak increase of the contact versus the temperature.

The weakly interacting regime at intermediate temperature ($\xi_\gamma^{-1} \lesssim \xi_{\mathrm{T}} \lesssim \xi_\gamma^{-2}$)

When $k_{\mathrm{B}}T > N\hbar\omega$, the gas enters a decoherent regime. Equivalently it writes $\xi_{\mathrm{T}}\xi_\gamma \gtrsim 1$. In this regime, the Thomas-Fermi profile is not valid any more, since the interactions are negligible and the bosons form a nearly ideal degenerate gas [70, 134]. However, if the temperature is smaller than the quantum degeneracy temperature, i.e. $T \lesssim T_{\mathrm{d}}$, the density profile remains its quantum property and writes

$$n(x) = \lambda_T^{-1}\mathrm{Li}_{1/2}\left[\exp\left(\alpha - \frac{x^2}{2L_{\mathrm{th}}^2}\right)\right] \tag{3.43}$$

with $\alpha(\xi_\gamma, \xi_{\mathrm{T}}) = \ln[1 - \exp(-1/(2\pi\xi_\gamma^2\xi_{\mathrm{T}}^2))]$. This regime is referred as "Degenerate ideal bosons" in Fig. 3.8. Here, one should notice that although the parameter T_{d} is introduced by Eq. (3.28) as the degeneracy temperature for the fermionized bosons in strongly-interaction regime, it also characterizes the competition between the inter-particle separation and the de Broglie wavelength. Taking into consideration $n \sim N/L_{\mathrm{th}}$, the condition for the weakly-interacting degenerate Bose regime can be rewritten with the scaling parameters as

$$\xi_\gamma^{-1} \lesssim \xi_{\mathrm{T}} \lesssim \xi_\gamma^{-2} \tag{3.44}$$

Insert the profile of this regime into the interaction energy Eq. (3.40) and calculate the contact with the sweep relation Eq. (3.3), we shall find

$$C = \frac{16\sqrt{\pi}N^{5/2}\xi_\gamma^5\xi_{\mathrm{T}}^3}{a_{\mathrm{ho}}^3}\ G(\alpha), \quad \xi_\gamma^{-1} \lesssim \xi_{\mathrm{T}} \lesssim \xi_\gamma^{-2} \tag{3.45}$$

with $G(\alpha)$ the integration of the polylogarithm function, which writes

$$G(\alpha) = \int dx\ \mathrm{Li}_{1/2}^2[\exp(\alpha - x^2)]. \tag{3.46}$$

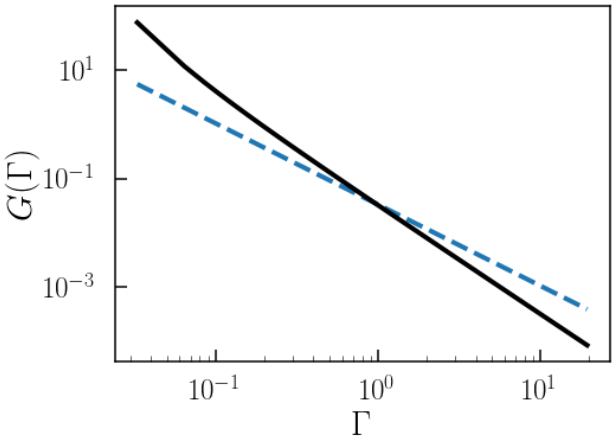

Figure 3.9: The function $G(\Gamma)$ with $\Gamma = \xi_{\mathrm{T}}^2\xi_\gamma^2$ (solid black line). The dashed blue line is $H(\Gamma) = 0.03\Gamma^{3/2} \sim \xi_{\mathrm{T}}^3$ which indicates that $G(\Gamma)$ decreases faster than ξ_{T}^3.

Studying the temperature dependence of the function $G(\alpha)$, we define $\Gamma = \xi_{\mathrm{T}}^2\xi_\gamma^2$ and plot the function $G(\Gamma)$, see solid black line in Fig. 3.9. In comparision, we also plot $H(\Gamma) = 0.03\Gamma^{3/2}$ which is proportional to ξ_{T}^3, see blue dashed line. In the log-log scale, it is clear that $G(\alpha)$ decreases faster than ξ_{T}^3 in the regime $\xi_{\mathrm{T}}\xi_\gamma \sim 1$. Using Eq. (3.45), it indicates that the contact C decreases with the temperature T. Here, we recall C increases with T in the low temperature regime, hence it indicates that there is a maximum of the contact even in the weakly-interacting regime. We will study the property of this maximum in the next section.

High temperature classical regime ($\xi_\gamma^{-1}, 1 \lesssim \sqrt{\xi_{\mathrm{T}}}$)

For both the strongly- or weakly-interacting gases, the high temperature regime presents the same property and its condition yields the temperature is higher than any relevant temperature scale: $T > T_{\mathrm{d}}$ and $a_{1\mathrm{D}} > \lambda_T$. Rewriting this two conditions in our scaling parameters (demonstration similar as before), we find

$$1, \gamma_0^2 \lesssim \frac{T}{T_{\mathrm{d}}}. \tag{3.47}$$

Rewritting it with our scaling parameters, we find

$$\xi_\gamma^{-1}, 1 \lesssim \sqrt{\xi_{\mathrm{T}}}. \tag{3.48}$$

In this regime, one obtains a weakly degenerate Bose gas dominated by thermal fluctuations. We refer it as "Weakly-degenerate ideal bosons" in Fig. 3.8. In this case, the contact can still be estimated by the mean-field expression of the interaction energy Eq. (3.40). However, the density profile loses its quantum property and behaves like the thermal Boltzman distribution Eq. (3.37). Combining these two equations with the sweep relation Eq. (3.3), we find

$$C \simeq \frac{2\sqrt{2}N^{5/2}\xi_\gamma}{\pi\xi_{\mathrm{T}}a_{\mathrm{ho}}^3}, \quad \xi_\gamma^{-1}, 1 \lesssim \sqrt{\xi_{\mathrm{T}}}. \tag{3.49}$$

Here, at any interaction but high temperature, we may notice that the contact decreases with temperature as $1/\sqrt{T}$. And it recovers what is expected from high temperature strongly-interacting bosons in Ref. [18].

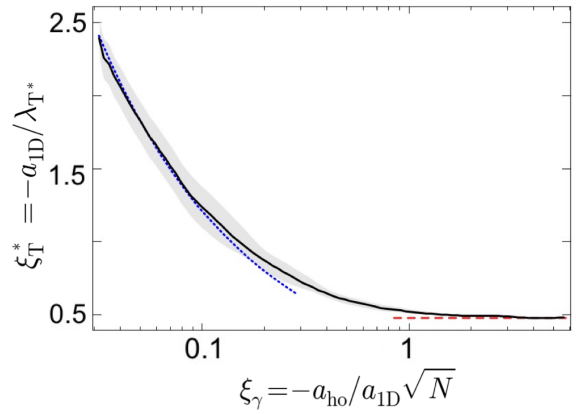

Figure 3.10: Behavior of the temperature at which the contact is maximum versus the interaction strength. Shown is the value of ξ_{T}^* (solid black line with shaded gray error bars) as found from the data of Fig. 3.3, together with the asymptotic behaviors $\xi_{\mathrm{T}}^* \simeq 0.49$ for the strongly interacting regime (dashed red line) and $\xi_{\mathrm{T}}^* \propto \xi_{\mathrm{T}}^{\nu_{\mathrm{fit}}}$, with $\nu_{\mathrm{fit}} \simeq 0.6$ for the weakly interacting regime (dotted blue line).

3.2.3 The onset of maximum

As we already announced in the previous section, the particularly interesting outcome here is the nonmonotonicity of C versus temperature and the onset of a maximum, for example see Fig. 3.6(b). In fact, this behavior strongly contrasts with the previous results found for the homogeneous gas and the trapped gas in the Tonks-Girardeau limit ($a_{1\mathrm{D}} \to 0$), which are both characterized by a systematic increase of the contact versus temperature [18,134]. In the trapped case, the maximum in the contact as a function of ξ_{T} is found irrespective to the strength of interactions but is significantly more pronounced in the strongly interacting regime. From the data of Fig. 3.3, we extract the temperature T^* at which the contact is maximum at fixed ξ_γ. In Fig. 3.10, we plot the corresponding $\xi_{\mathrm{T}}^* = -a_{1\mathrm{D}}/\lambda_T^*$ as a function of ξ_γ. As we can see, ξ_{T}^* shows significantly different behavior in the strongly and weakly interacting regimes. It depends on the value of ξ_γ in the weakly-interacting regime and remain constant in strongly-interacting regime. Now, we study in detail the origin of the maximum and its physical meaning.

Maximum in the strong interaction regime

In strongly-interacting regime, $\rho(0)|a_{1\mathrm{D}}| \lesssim 1$, we stress that both Eqs. (3.38) and (3.49) are in good agreement with the numerical calculations, see red-dotted and dash-dotted lines in Fig. 3.6(b). These expressions show that the contact increases with temperature in the fermionized regime but decreases when thermal fluctuations dominate over interactions, which is the origin of the existence of maximum. It provides a nonambiguous signature of the crossover to fermionization and we will analysis this into detail now.

We can obtain the analytical expression for the contact using the virial expansion. Here, I would like to point out that the whole derivation in this part has been done by Prof. Patrizia Vignolo. To start with, we recall the expression of the grand potential in statistical physics,

$$\Omega = -k_{\mathrm{B}} T \ln Z \tag{3.50}$$

with Z the partition function. By performing the virial expantion to the grand potential as in Ref. [18,140], it writes

$$\Omega = -k_{\mathrm{B}} T Q_1 (z + b_2 z^2 + b_3 z^3 + ...) \tag{3.51}$$

with $z = e^{\beta\mu}$ the fugacity and b_n the n-th virial expansion coefficient related with $Q_n = Tr_n[\exp(-H/k_{\rm B}T)]$. The b_n can be calculated from the cluster partition functions [141], for instance, $b_2 = Q_2/Q_1 - Q_1/2$. Using the Tan sweep relation Eq. (3.2) and keeping only the z^2 term, one can find

$$C = \frac{4m\omega}{\hbar\lambda_T} N^2\, c_2 \tag{3.52}$$

where $c_2 = \lambda_T \dfrac{\partial b_2}{\partial |a_{\rm 1D}|}$ and $b_2 = \sum_\nu e^{-\beta\hbar\omega(\nu+1/2)}$. The ν's are the solutions of the transcendental equation [142]

$$f(\nu) = \frac{\Gamma(-\nu/2)}{\Gamma(-\nu/2+1/2)} = \sqrt{2}\frac{a_{\rm 1D}}{a_{\rm ho}}. \tag{3.53}$$

Then, with further mathematical derivation, one can solve the solution for ν in Eq. (6.2) and infer the term c_2 in Eq. (6.1). The detail of this derivation is shown in the Appendix. With the solution of c_2, one can find the analytical form for the contact by Eq. (6.1), it yields

$$C = \frac{2N^{5/2}}{\pi a_{\rm ho}^3}\frac{\xi_\gamma}{\xi_{\rm T}}\left(\sqrt{2} - \frac{{\rm e}^{1/2\pi\xi_{\rm T}^2}}{\xi_{\rm T}}{\rm Erfc}(1/\sqrt{2\pi}\xi_{\rm T})\right), \tag{3.54}$$

see black dashed line in Fig. 3.6(b). Solving $\partial C/\partial T = 0$ in Eq. 3.54, we can locate a maximum at $\xi_{\rm T}^* = 0.485$, which is in very good agreement with the asymptotic scaling $\xi_{\rm T}^* \simeq 0.490 \pm 0.005$ extracted from the data (dashed red line in Fig. 3.10).

From Eq. (3.3), we can infer that the maximum of the contact is equivalent to the maximum of the interaction energy, while fixing g. Then, the existence of the maximum can actually be understood by the competition of two processes. On the one hand, at low temperature, the bosons can never overlap since they are blocked by the strong repulsive interaction, which is equivalent to Pauli blocking in the equivalent ideal Fermi gas. With the increase of temperature, the bosons gain enough energy repulsion to overcome the blockade and allow a spatial overlap, thus increasing the interaction energy locally, i.e. increase the contact C. On the other hand, since the system is a many-body system confined in a harmonic trap, increasing the temperature will enlarge the size of the system and dilute the gas. Therefore, the interaction energy will be reduced globally, i.e. the contact C will decrease. As a consequence, the competing of these two processes leads to the non-monotonic temperature effect of the contact. It forms a maximum when the effect of both are on the same scale. In another word, due to the competition of interaction and temperature, the maximum contact should appear at the temperature where the interaction and dilution effect reaches the same magnitude. According to Fig. 3.8, this crossover happens at $\xi_{\rm T} \sim 1$ when $\xi_\gamma > 1$, i.e. in length scale $a_{\rm 1D} \sim \lambda_T$, which fit well with what we find in the previous calculations.

We further argue that the existence of this maximum is extremely interesting, since it is a direct consequence of the dramatic change of correlations and thus provides an unequivocal signature of the crossover to fermionization in the trapped 1D Bose gas. For other detected quantities such as the density profile, they normally show a smooth variation while going through the crossover. However, the maximum of the contact provides the probability to probe it accurately with sharp change of behavior.

Maximum in the weak interaction regime

The maximum in the weak interaction regime is much weaker, but it is still possible for us to capture it from the theoretical point of view. For low temperature regimes, the contact follows Eq. (3.42) with Bogoliubov correction term increasing with T. Then, for higher temperature, the contact follows Eq. (3.45) where C decreases with the temperature thanks to the property of G as we discussed above. Since the contact increases with temperature

at low T, due to the weak Bogoliubov excitations, we can conclude that there also exists the maximum contact in the weakly-interacting regime and it signals the crossover from the quasicondensate regime to the ideal Bose gas regime. The position of the maximum of the contact may be estimated by equating Eqs. (3.42) and (3.45). The calculation is significantly simplified by neglecting quantum degeneracy effects and treat the density profile as a Gaussian in Eq. (3.45). Then, it yields

$$G(\alpha) \simeq \sqrt{\pi/2}\exp(2\alpha) \tag{3.55}$$

Performing the Taylor expansion for $G(\alpha)$ as a function of $\Gamma = \xi_{\mathrm{T}}^2\xi_\gamma^2$, we find $G(\alpha) \simeq \Gamma^{-2} \sim 1/\xi_\gamma^4\xi_{\mathrm{T}}^4$ and we have checked by numerical plotting that this approximation is valid up to the regime $\xi_\gamma\xi_{\mathrm{T}} \sim 1$. Then, equating Eqs. (3.42) and (3.45) with the function $G(\alpha)$ above, we finally find

$$\xi_{\mathrm{T}}^* \sim \xi_\gamma^{-\nu}, \quad \nu = 2/3. \tag{3.56}$$

To check this prediction, we have fitted by Eq. (3.56) with ν as an adjustable parameter (see dotted blue line in Fig. 3.10), yielding $\nu_{\mathrm{fit}} = 0.6 \pm 0.06$, in good agreement with the theoretical estimate $\nu_{\mathrm{th}} = 2/3$. However, quantum degeneracy effects tend to increase the value of ν for small values of ξ_γ. In the asymptotic limit $\xi_\gamma \to 0$, they become dominant. In this limit, we find $G(\alpha) \simeq \pi^2/\sqrt{|\alpha|}$ and it yields $\nu \simeq 1$. Nevertheless, we should point out that the maximum is extremely weak and hardly visible in practice in this regime.

The maximum of entropy

To further interpret the onset of a maximum contact versus temperature, we realise that it is actually equivalent to the onset of a maximum entropy S versus interaction strength. For a fixed number of particles, it is a direct consequence of the Maxwell identity. Here, we recall the definition of the free energy F in thermodynamics

$$F(N, T, a_{1\mathrm{D}}) = \Omega(\mu, T, a_{1\mathrm{D}}) + \mu N, \tag{3.57}$$

where we change the variables from μ to N. Then, we can rewrite the sweep relation for the contact in term of the free energy and it gives

$$C = \frac{4m}{\hbar^2}\left.\frac{\partial F}{\partial a_{1\mathrm{D}}}\right|_{T,N}. \tag{3.58}$$

Moreover, we use the thermodynamic definition of the entropy

$$S = -\left.\frac{\partial F}{\partial T}\right|_{a_{1\mathrm{D}},N}. \tag{3.59}$$

Combining Eq. (3.58) and Eq.(3.59), we find

$$\left.\frac{\partial C}{\partial T}\right|_{a_{1\mathrm{D}},N} = -\frac{4m}{\hbar^2}\left.\frac{\partial S}{\partial a_{1\mathrm{D}}}\right|_{T,N}, \tag{3.60}$$

which indicates that the two maximums appear at the same set of parameters. In the homogeneous LL gas, the entropy at fixed temperature and number of particles decreases monotonically versus the interaction strength, since repulsive interactions inhibit the overlap between the particle wavefunctions. Hence, the supression of free space for particles diminishes the number of available configurations. In the trapped gas, however, this effect competes with the interaction dependence of the available volume. More precisely, starting from the noninteracting regime, the system size increases sharply with interaction strength, while the particle overlap varies smoothly. Therefore, in this regime, the number of available configurations and the entropy increase with the interaction strength. At the

onset of fermionization, interaction-induced spatial exclusion becomes dramatic and the particles strongly avoid each other. In turn, as opposed to the weakly-interacting regime, the volume increases very slightly. In this regime, the number of available configurations thus decreases when the interactions increase. This picture confirms that the maximum of the entropy as a function of the interaction strength, consistently with the maximum of the contact as a function of the temperature. Thus, it also signals the fermionization crossover.

3.3 Experimental observability

In this section, we discuss the experimental observability of the contact and its properties, especially the maximum contact in strongly-interaction regimes which signatures the crossover to fermionization. We mainly focus on three aspects, namely the detection accuracy, the validity of the purely 1D gas model, and the consequence of averaging over 1D gases with different number of particles, as relevant in experiments creating a 2D array of 1D tubes.

3.3.1 Accuracy of detection

As we discussed at the beginning of this chapter, our predictions can be investigated with quantum gases where the Tan contact is extracted from radio-frequency spectra or momentum distributions [125–127, 130]. To understand better the observation condition in the later case, we compute the momentum distribution. Here, one should notice that the momentum distribution cannot be found from Y-Y thermodynamics. In turn, QMC calculation can do it efficiently, see Section 2.3.4.

Figure 3.11 shows momentum distributions found from QMC calculations in the strongly interacting regime for two typical temperatures. Figure. 3.11(a) is close to zero temperature ($\xi_{\mathrm{T}} \ll 1$) and Fig. 3.11(b) is at the temperature for the maximum contact $\xi_{\mathrm{T}} \simeq \xi_{\mathrm{T}}^{*}$. In both cases, an algebraic decay at large momenta is observed, with an amplitude matching our estimate for the contact. Here, one should note the log-log scale in the main panels and the lin-lin scale are plotted as insets. Fitting the tails of the momentum distributions found from the QMC calculations by $n(k) \simeq C_{\mathrm{fit}}/k^{p_{\mathrm{fit}}}$, where we obtain p_{fit} and $\widetilde{C}_{\mathrm{fit}} = a_{\mathrm{ho}}^{3} C_{\mathrm{fit}}/N^{5/2}$. For Fig. 3.11(a), we find $p_{\mathrm{fit}} = 3.80 \pm 0.20$ and $\widetilde{C}_{\mathrm{fit}} = (1.01 \pm 0.14) \times 10^{-3}$ while $\widetilde{C} \simeq 0.97 \times 10^{-3}$. For Fig. 3.11(b), we find $p_{\mathrm{fit}} = 3.72 \pm 0.10$ and $\widetilde{C}_{\mathrm{fit}} = 0.23 \pm 0.04$ while $\widetilde{C} \simeq 0.22$. The agreement with the expected exponent $p = 4$ is better than 7% and with the contact C better than 5%. Here, we notice that for the two examples shown here, the momentum distributions decay over three to four decades. Such a range is quite unusual. Helium atoms can however measure momentum distribution in such a range taking advantage of single-particle resolution. For instance, measurement of momentum distributions in Ref. [125] covers up to six decades.

3.3.2 Validity condition of the quasi-1D regime

Focusing on the observability of the maximum, one should also be careful with the condition to have really one-dimensional tube instead of 3D (also named as quasi-1D). In ultracold atoms, the tubes are induced either by a magnetic field or a transverse optical lattice. In the second case, the system consists of arrays of 1D tubes, see Fig. 1.1. In both cases, it creates a local transverse harmonic trap with frequency $\omega_{\perp}$. The condition for the such kinds of systems to be in strictly-1D regime writes $k_{\mathrm{B}}T, \mu \ll \hbar\omega_{\perp}$. The condition simply means that the system remains in ground state for the freedom of the transverse harmonic oscillation and no significant excitation is created, see details in for instance Ref. [62].

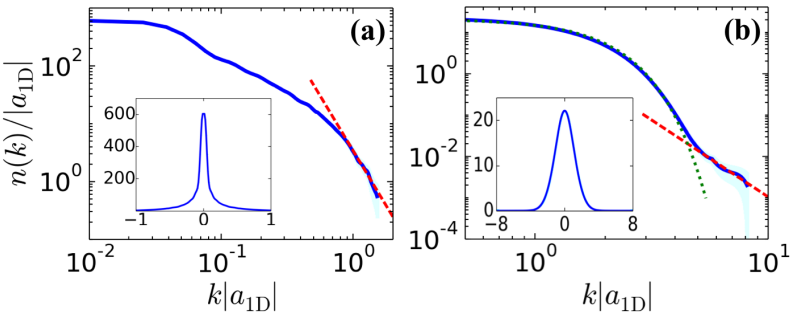

Figure 3.11: Log-log plots of momentum distributions found by QMC calculations in the strongly interacting regime. (a) Low temperature: $\xi_\gamma = 4.47$ and $\xi_T = 0.0085$. (b) Temperature at the maximum contact: $\xi_\gamma = 1.26$ and $\xi_T = 0.49$. The solid blue lines with shaded statistical error bars are the QMC results, the dashed red lines are algebraic fits to the large-k tails, and the dotted green lines are the momentum distributions of the non-degenerate ideal gas. The insets show the same data in lin-lin scale.

This condition may be re-written using the scaling parameters $\xi_\gamma = -a_{ho}/a_{1D}\sqrt{N}$ and $\xi_T = -a_{1D}/\lambda_T$. Using the relations $a_{ho} = \sqrt{\hbar/m\omega}$, $\lambda_T = \sqrt{2\pi\hbar^2/mk_BT}$, and

$$\xi_T\xi_\gamma = \frac{1}{\sqrt{2\pi N}}\sqrt{\frac{k_BT}{\hbar\omega}}, \tag{3.61}$$

it reads as

$$\xi_T\xi_\gamma \ll \frac{1}{\sqrt{2\pi N}} \times \sqrt{\frac{\omega_\perp}{\omega}}. \tag{3.62}$$

In experiments, the typical value of $\omega_\perp/\omega$ varies from a few hundreds to a few thousands.

In Fig. 6.1, we reproduce the Fig. 3.10, together with the condition (3.62) for two values of the atom number N and the parameters of Ref. [12], $\omega/2\pi = 15.8$Hz and $\omega_\perp/2\pi = 14.5$kHz. The regions where the validity condition is not fulfilled (i.e.quasi-1D) is shown in purple for $N = 2$ and orange for $N = 10$. From the figure, we conclude that the value ξ_T^* corresponding to the maximum of the contact is well inside the validity regime deep enough in the strongly-interacting regime, $\xi_\gamma \gg 1$. It is thus possible to observe the maximum contact in this regime. Moreover, one can further extend the validity region by increasing the value of the ratio $\omega_\perp/\omega$, i.e. by increasing the transverse confinement.

3.3.3 Tube distributions

A single tube of 1D weakly-interacting bosons can be obtained by the atom chip techniques [11, 12]. However, for generating 1D quantum gases with stronger interactions, one requires a stronger confinement that is easier to realize optically. One uses optical lattice but it creates 2D arrays of 1D tubes. In most cases, strong transverse confinement is realized by applying a 2D optical lattice in the directions y and z, orthogonal to the 1D direction x. For sufficiently strong lattices, it creates an array of independent 1D tubes, indexed by the labels $(j, \ell) \in \mathbb{Z}^2$. Since the tubes are independent, the momentum distribution $D(p)$ is simply the sum of that for all the tubes, i.e. $D(p) = \sum_{j,\ell} D_{(j,\ell)}(p)$. In particular, the Tan contact is also the sum of that for all the tubes, and it writes

$$C = \sum_{j,\ell} C(j, \ell), \tag{3.63}$$

where $C(j, \ell)$ is the contact in the corresponding tube. Each tube is populated with a number $N(j, \ell)$ of atoms, which depends on the loading procedure of the atoms in the 2D

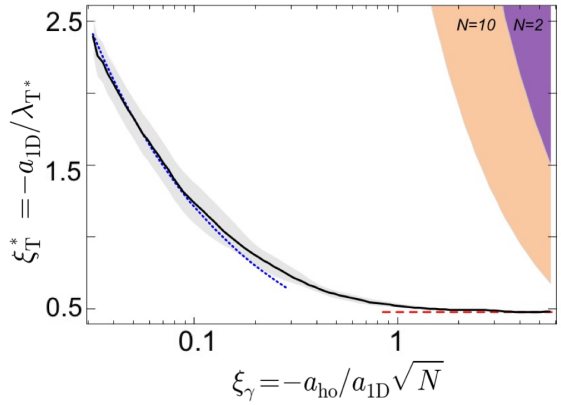

Figure 3.12: Reproduction of Fig. 3.10 together with the validity condition of the quasi-1D regime (equivalently the regime for the failure of purely-1D gas), Eq. (3.62), for $\sqrt{\omega_\perp/\omega} = 30$, relevant for the experiments of Ref. [12]. The dark regions show the excluded regions for $N = 2$ atoms (purple) and $N = 10$ atoms (orange).

lattice. Since the number of atoms is maximum in the central tube ($j = \ell = 0$), we have $\xi_\gamma(j,\ell) \geq \xi_\gamma(0,0)$, and the condition for having all tubes in the strongly-interacting regime reduces to $\xi_\gamma(0,0) \gg 1$.

In that regime, the temperature dependence of the contact around the maximum is independent of ξ_γ, and thus independent of the tube. Indeed, as shown by Eq. (3.54), the parameter ξ_γ just appears as a prefactor. In particular, the maximum contact is located at the universal value $\xi_T^* \simeq 0.485$, which is identical for the tubes. Using Eq. (3.54), we then find

$$C^* \simeq 0.55 \times \sum_{j,\ell} \frac{N(j,\ell)^{5/2}\xi_\gamma(j,\ell)}{a_{ho}^3}. \tag{3.64}$$

At zero temperature, the contact may be found using the mapping between the strongly-interacting Bose gas and the strongly-degenerate ideal Fermi gas. It yields the value of the contact at zero temperature [121]

$$C^0 \simeq 0.82 \times \sum_{j,\ell} \frac{N(j,\ell)^{5/2}}{a_{ho}^3}. \tag{3.65}$$

We then find that the relative amplitude of the maximum contact with respect to its zero-temperature value fulfils the inequality

$$\frac{C^*}{C^0} \gtrsim 0.68 \times \xi_\gamma(0,0). \tag{3.66}$$

Therefore, the relative amplitude of the maximum contact is larger than a fraction of the interaction parameter $\xi_\gamma(0,0) \gg 1$ and should be observable. For instance, for the parameters of Ref. [12], we find $\xi_\gamma(0,0) \simeq 7.5$ and $C^*/C^0 \gtrsim 5.1$.

Note that the lower bound in Eq. (3.66) is universal in the sense that it does not depend on the distribution of atoms in the various lattice tubes. Note also that it is immune to shot-to-shot fluctuations of the atom numbers in the tubes.

Finally, a more precise value of the relative amplitude of the maximum contact is found by computing the sums in Eqs. (3.64) and (3.65) for realistic distributions of the atom numbers among the tubes. Here, using the estimation that the initial 3D BEC follows the Thomas-Fermi profile and the loading process is fast, we shall write

$$N_{j,\ell} = \left[1 - \frac{2\pi N(0,0)}{5N}\left(j^2+\ell^2\right)\right]^{3/2}, \tag{3.67}$$

which is relevant to the experiments of Refs. [9, 12]. With Eq. (3.67), we find $C^*/C^0 \simeq 0.8 \times \xi_\gamma(0,0)$, which is only about 20% larger than the atom distribution-independent lower bound, Eq. (3.66). For the parameters of Ref. [12], it yields $C^*/C^0 \gtrsim 6.1$. It may be further increased by lowering the total number of atoms, although at the expense of atom detectability.

Conclusion

In this chapter, we have provided a complete characterization of the Tan contact for the trapped Lieb-Liniger gas with arbitrary interaction strength, number of particles, temperature, and trap frequency. We first derived a universal scaling function of only two parameters, which stand for the temperature and interaction strengths. We have shown that it is in excellent agreement with the numerically exact QMC results as well as the Yang-Yang calculations over a wide range of parameters. In different regimes of degeneracy, we found that the results of the contact fit well with the asymptotic formula as we expected. As a pivotal result, we found that the contact exhibits a maximum versus the temperature for any interaction strength. This behavior is mostly marked in the gas with large interactions and provides an unequivocal signature of the crossover to fermionization. Finally, we also analyzed the experimental observation condition for the contact, especially the maximum.

In the outlook, our theoretical results provides fruitful physics to be detected in experiments. On the one hand, its behavior as a function of the temperature and interaction can identify regimes of degeneracy and critical behaviors. It also provides plenty of information such as the interaction energy, correlation function, as well as the behaviors of the thermodynamic quantities. On the other hand, 1D ultracold atoms created by optical lattices is a good candidate for such a detection, since it can observe the momentum distribution with a good accuracy over 6 orders of magnitudes decaying [125], as well as entering the strong interacting regimes with $\xi_\gamma \gtrsim 10$ [12].

Chapter 4

Critical behavior in shallow 1D quasiperiodic potentials: localization and fractality

Anderson localization, known as the absence of diffusion of waves in a disordered medium, is one of the hottest topic of research since 20-th centry, in the framework of both condensed matter and quantum simulations. In a homogeneous system, all the single-particle wave functions are extended. In contrast, they may be exponentially localized in the presence of disorder owing to the breaking of translational invariance [143]. The effect of the phase transition between the extended and localized state is known as the Anderson localization. It is a single-particle effect caused by disorder as well as a fundamental and ubiquitous phenomenon at the origin of metal-insulator transitions in many systems [144].

The Anderson localization and its phase transition have been widely studied in the purely disordered systems, both the single-particle case [143, 145–148] and the interacting many-body systems [46–51, 149]. The influence of disorder in fermionic systems are also studied [150–153]. The quasiperiodic models, known as the intermediate between the periodic and fully disordered systems, hold a special place. An illustration for the three kinds of system is shown in Fig. 4.1. While a single trigonometric function stands for the purely periodic system, the disordered system is the opposite case where its Fourier components contain infinite and dense values of different frequencies. The quasiperiodic system is the intermediate of the two, which can be understood by a sum of two or trigonometric function which frequencies has an incommensurate ratio between each other and form a finite or discrete set, i.e. no true periodicity exists. In recent years, it attracts a lot of attentions and interests of research.

"Quasiperiodic model" describes a variety of systems. On the condensed matter side, it includes quasicrystals [154], electronic materials in orthogonal magnetic fields [155–157] or with incommensurate charge-density waves [158], Fibonacci heterostructures [159], photonic crystals [160], and cavity polaritons [161]. Moreover, on the research field of cold atoms, it can be achieved by realizing external quasiperiodic potentials on top of the cold atomic gases. This kind of systems have proved pivotal in quantum gases [153, 162, 163] to investigate Anderson localization of matter waves [8, 164, 165] and interacting Bose gases [41], the emergence of long-range quasiperiodic order [19, 166, 167], Bose-glass physics [14, 20, 21, 164, 165, 168], and many-body localization [16, 169–171].

In a disordered system, a phase transition between the Anderson-localized and extended phases occurs only in dimension strictly higher than 2 [172]. However, in quasiperiodic systems, the behavior is significantly different and a phase transition may occur. The most celebrated example is the Aubry-André (AA) Hamiltonian, obtained from the tight-binding model generated by a strong lattice, combined with a second, weak, incommensurate lattice

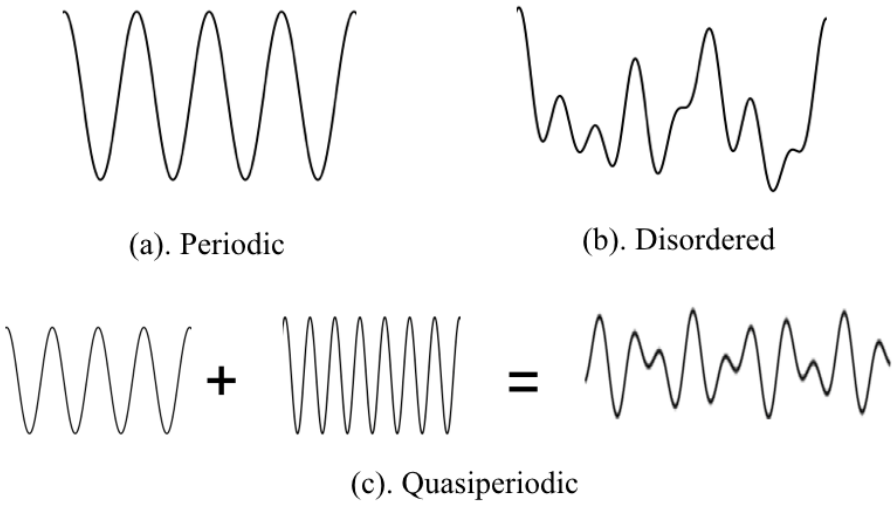

Figure 4.1: The typical shape for three kinds of potential: (a). Periodic. (b). Disordered. (c). Quasiperiodic, which may be a sum of several periodic potentials with incommensurate ratio of lattice spacings.

serving as the quasi-disorder. In the AA model, the localization transition occurs at a critical value of the quasiperiodic potential, irrespective of the particle energy [173]. This behavior results from a special symmetry, known as self-duality. When the latter is broken, an energy mobility edge (ME), i.e. a critical energy separating localized and extended states, generally appears, as demonstrated in a variety of models [31, 174–179]. One of the simplest examples is obtained by using two incommensurate lattices of comparable amplitudes, which refers to a shallow or continuous bichromatic lattice. This model attracts significant attention in ultracold-atom systems owing to the fact that it is generally easier to realize compared to truly disordered systems [180, 181]. They have been used to study many-body localization in a 1D system exhibiting a single-particle ME [16]. Recently, the localization properties and the ME of the single-particle problem have been studied both theoretically [181] and experimentally [182]. However, important critical properties of this model are still unknown. For instance, whether an intermediate phase appears in between the localized and extended phases remains unclear.

In this chapter, we study the critical properties and the fractality of noninteracting particles in shallow quasiperiodic potentials [86]. We firstly introduce the important concepts in this problem, such as the definition of a localized state, the critical potential and the mobility edge(ME). Then, we start the study with balanced bichromatic lattices. With balanced amplitude, we find that a finite energy ME exist above a certain critical amplitude of potential V_c. We determine its value from the scaling of the inverse participation ratio and find the universal critical exponent $\nu \simeq 1/3$. We further extend the investigation to more generalized case, i.e. bichromatic lattices with imbalanced amplitudes as well as trichromatic lattices, and we find the results remain the same. Finally, we find the ME is always found in one of the energy gaps, which are dense thanks to the fractal character of the energy spetrum. We propose a method to compute the critical Hausdorff dimension and find values significantly different from that found for the AA model, showing that it is a non-universal quantity. In all the considered cases, we remain the lattice amplitudes on the scale of the recoil energy $E_r = \hbar^2 k^2/2m$, to maintain in the shallow potential regime.

4.1 Localization, disorder and quasiperiodicity

In this section, we introduce the basic concepts and standard models used in this chapter. We first demonstrate several important definitions in this chapter, such as the extended and localized states, the mobility edge(ME) and the critical potential (V_c). Then, we go through some well-known examples and discuss in detail the localization property.

4.1.1 Basic concepts for localization

Before we move on to present the scientific results, it's important to give the rigorous definition of several key quantities at this stage.

Extended and localized phases

The difference between the extended and localized phases is illustrated on Fig. 4.2. In the diagram, the black curve stands for the external potential and the blue wave packets stand for the eigenstate wavefunction. We use L for the size of the system and l the typical width of the certain eigenstate. From the left panel to the right panel, we double the size of the system and keep all the other parameters unchanged. On the upper row, the system is in the localized phase so that the width of the eigenstate remains constant. On the lower row, the width of the eigenstate also doubles similarly as the size of the system, thus it is defined as extended state.

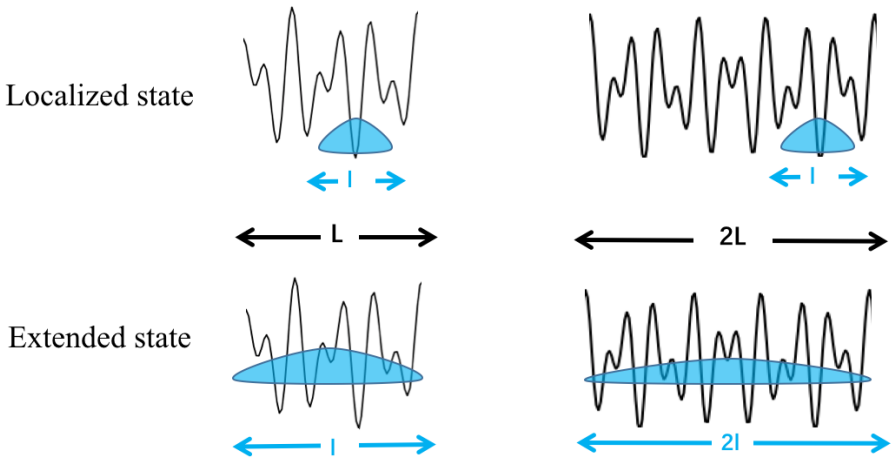

Figure 4.2: Illustration of the difference between localized and extended states. The black curve stands for the external potential and the blue wave package stand for the eigenstate. L is the size of the system and l is the width of the eigenstate.

The localization property of an eigenstate ψ can be characterized by the second-order inverse participation ratio (IPR) [183],

$$\mathrm{IPR} = \frac{\int dx\, |\psi_n(x)|^4}{\left(\int dx\, |\psi_n(x)|^2\right)^2}. \tag{4.1}$$

with $\psi_n(x)$ the wavefunction of the n-th eigenstate. If the state $\psi_n(x)$ is a wavepacket with typical size l, then we have IPR $\sim 1/l$ and the value of itself thus gives an estimation of the localization. However, we have to be careful that it is rather a measure of the fraction of space that it covered by the space. Thus, there exists cases where the value of IPR does not say much about the localization. For instance, for a deep periodic lattices, the local compression at the bottom of the wells leads to IPR $\gg 1$ although the state is extended.

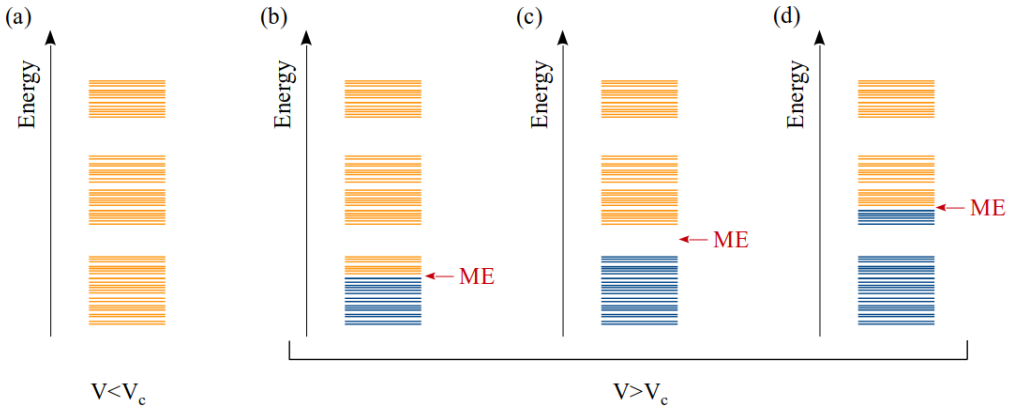

Figure 4.3: General picture of the localization property in energy spectrum. The extended states are shown in yellow and the localized states in blue. (a) Case $V < V_c$ where all the states are extended. (b), (c), and (d) Three examples in the case $V > V_c$, with different values of the mobility edge E_c. The potential V increases from (b) to (d).

Therefore, to better distinguish the localized and extended state, we should study the scaling of IPR with the system size L. It generally scales as IPR $\sim 1/L^{\tau}$, with $\tau = 1$ for an extended state and $\tau = 0$ for a localized state. Thus, studying the exponential behavior between IPR and system size L, we can identify the phase of a certain state. Here, one should note that in some other works, people may choose a large enough value of L and expect IPR~ 0 for extended state and finite for localized state. We argue that this method is generally proper for most of the cases. However, there exists exceptions for such kind of detection. One example is an extended state in deep periodical lattices. The wavefunction is periodically peaked but narrow. Thus, one may find a finite value of IPR for large L even though the state is extended. Therefore, the rigorous definition of the localization property should still be extracted from the exponent τ.

Mobility edge and critical potential

Another pair of important concepts are the mobility edge (ME) and the critical potential (V_c), which is demonstrated by Fig. 4.3. From the left to the right, we show the energy spectrum in four different cases with increasing amplitude of the disordered potential. The color of the eigenstate indicates whether it's localized (blue) or extended (yellow). When the potential is low enough, all the states are extended as Fig 4.3.(a). Then, localized state starts to appear in the spectrum while the potential amplitude is above a critical potential, which is named as V_c. When $V > V_c$, we expect the existence of both localized and extended states. For a fixed V, the transition point between the localized and extended state is called the mobility edge (ME). By increasing V, more states become localized and the ME changes its position in the spectrum. [1] However, in many cases, one should notice that a finite V_c and ME even don't necessarily exist (see examples below).

4.1.2 Localization in different kinds of system

At the single-particle level, the phase transition between extended and localized states are widely studied in different kinds of systems. In this subsection, we briefly review some

[1] One should notice that it's not necessary the localized states are at the lower energy state comparing with the extended states. For instance, if one take the discrete disordered model, such as the Anderson model, the localized states are at both the low and high band edges, while the center of the band is extended. Moreover, for quasiperiodic systems, there also exists cases where the localized states are found at higher energy of extended state, see [184] .

results in one dimension.

Periodic and disordered system

The 1D periodic system is a standard model for electronic systems, see for instance the Bloch theorem. The ultracold atomic system is a clean realization where the external potential is exactly trigonometric function $V(x) = V\cos(2k_x)$ with V the potential amplitude and k the wave vector. The lattice spacing $a = \pi/k$ gives the spatial period. In such kind of systems, it is well known that all single particle states are extended no matter how large the amplitude of the potential. Thus, there is no critical potential and ME in such a system.

The situation is opposite in the purely disordered system. In this case, there is no phase transition in one dimension and all the eigenstates are localized as soon as the potential is non-zero. Thus, there is no V_c and ME in this situation. A phase transition between the Anderson-localized and extended phases can only occur in dimension strictly higher than 2 [172]. Therefore, as an intermediate situation between periodic and disordered one, we may expect that in a one-dimensional quasiperiodic system, we can obtain a finite V_c and a finite ME.

Aubry-André model

The typical form of the bichromatic quasiperiodic lattices writes

$$V(x) = \frac{V_1}{2}\cos(2k_1 x) + \frac{V_2}{2}\cos(2k_2 x + \varphi), \tag{4.2}$$

where the quantities V_j $(j = 1, 2)$ are the amplitudes of two periodic potentials of incommensurate spatial periods π/k_j with $k_2/k_1 = r$, an irrational number. The Aubry-André (AA) model is one of the most widely studied bichromatic quasiperiodic model in 1D since 1950s [173]. The external potential takes the tight-binding limit of Eq. (4.2) generated by a strong lattice. The second is weak and has an incommensurate lattice spacing with the first lattice $r = (\sqrt{5}-1)/2$. Equivalently, it yields the condition

$$V_1 \gg V_2, E_r, E_r' \tag{4.3}$$

with $E_r = \hbar^2 k_1^2/2m$ and $E_r' = \hbar^2 k_2^2/2m$ the recoil energy of the first and second lattice. Since V_1 is much larger than any recoil energy, the system can be treated discretized as the tight-binding model. Moreover, since V_2 is much smaller than the band gap of the first lattices, the second lattice can serve as a perturbation of the first lattice and one can restrict to the first band of the first lattice. Then, the single-particle Hamiltonian can be written as

$$\hat{H}_{\mathrm{AA}} = -J\sum_{\langle i,j\rangle}\left(\hat{a}_i^\dagger \hat{a}_j + \mathrm{H.c.}\right) + \Delta\sum_i \cos(2\pi r i + \varphi)\hat{a}_i^\dagger \hat{a}_i, \tag{4.4}$$

where $\hat{a}_i$ is the annihilation operator of a particle in the lattice site i (located at the position $x_i = a \times i$), J is the tunneling energy associated to lattice 1 and Δ is the quasi-periodic amplitude induced by lattice 2. The AA parameters J and Δ in Eq. (4.4) can be related to the parameters of the two lattices V_1 and V_2 by

$$J \simeq \frac{4E_r}{\sqrt{\pi}}\left(\frac{V_1}{E_r}\right)^{3/4}\exp\left(-2\sqrt{\frac{V_1}{E_r}}\right) \qquad \text{with} \qquad \Delta \simeq \frac{V_2}{2}\exp\left(-r^2\sqrt{\frac{E_r}{V_1}}\right). \tag{4.5}$$

The detailed derivation can be found in Refs. [164, 177].

In the AA model, it is well known that the phase transition happens at the critical potential $\Delta_c/2J = 1$. However, there is no ME existed. For $\Delta/2J > 1$, all states are localized while for $\Delta/2J < 1$ all states are extended. In the next section, we focus the localization phase transition of shallow quasiperiodic lattice, i.e.$V_1 \sim V_2 \sim E_r$ and study the critical behaviors.

4.2 Critical localization behavior in 1D shallow quasiperiodic lattices

In this section, we focus on the study of the critical localization behavior for single particles in 1D shallow quasiperiodic lattices. We mainly focus on three quantities, the critical potential V_c, the mobility edge ME, and critical exponents. We start with the balanced bichromatic lattice, and then generalize the study to the imbalanced bichromatic lattices as well as trichromatic lattices.

4.2.1 The localization properties of balanced bichromatic lattices

The single-particle wave functions $\psi(x)$ could be found by solving numerically the continuous-space, 1D Schrödinger equation:

$$E\psi(x) = -\frac{\hbar^2}{2m}\frac{d^2\psi}{dx^2} + V(x)\psi(x), \tag{4.6}$$

using exact diagonalization for Dirichlet absorbing boundary conditions, $\psi_n(0) = \psi_n(L) = 0$. Here, E and m are the particle energy and mass, respectively, L is the system size, and $\hbar$ is the reduced Planck constant. In this subsection, we consider the case of balanced bichromatice lattices. Thus, $V(x)$ takes the form of Eq. (4.2) with $V_1 = V_2$. We also take $r = (\sqrt{5}-1)/2$ the golden ratio, similar as the previous works based on the AA model. Here, one should notice that the choice of other incommensurate numbers shall give the same physics, except for Liouville numbers [185]. Moreover, the relative phase shift φ is essentially irrelevant, except for some values, which induce special symmetries. Thus, in the following, we always use $\varphi = 4$ which avoids such cases. One should note that the model we consider cannot be mapped onto the AA model, even for $V \gg E_r$, since none of the periodic components of $V(x)$ dominates the other.

The Mobility Edge

Figure 4.4(a) shows the IPR versus the particle energy E and the potential amplitude V for a large system, $L = 100a$ with $a = \pi/k_1$ the spatial period of the first periodic potential. The results indicate the onset of localization (corresponding to large values of the IPR) at a low particle energy and high potential amplitude, consistently with the

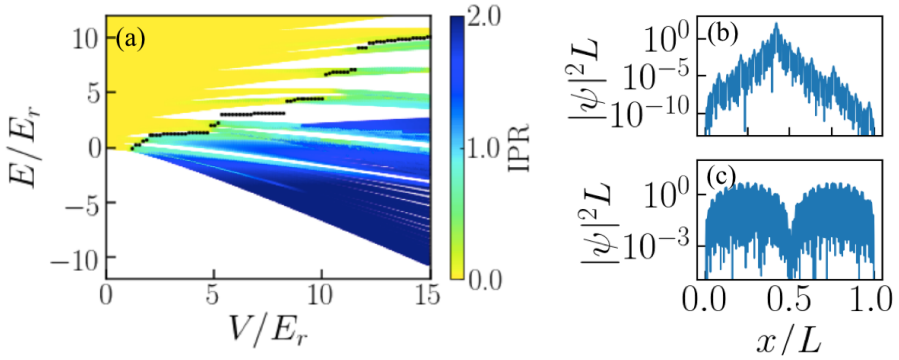

Figure 4.4: Localization transition for the balanced bichromatic potential, Eq. (4.2) with $V_1 = V_2 \equiv V$. (a) IPR versus the particle energy E and the lattice amplitude V for the system size $L = 100a$. Localized states correspond to large values of the IPR (blue) and extended to vanishingly small values (yellow). The ME, found from finite-L scaling analysis of the IPR, is shown as black points. (b) and (c) Density profiles of two eigenstates in the localized and extended regimes respectively. Here, the two states correspond to energies right below and right above the ME at $V = 2E_r$.

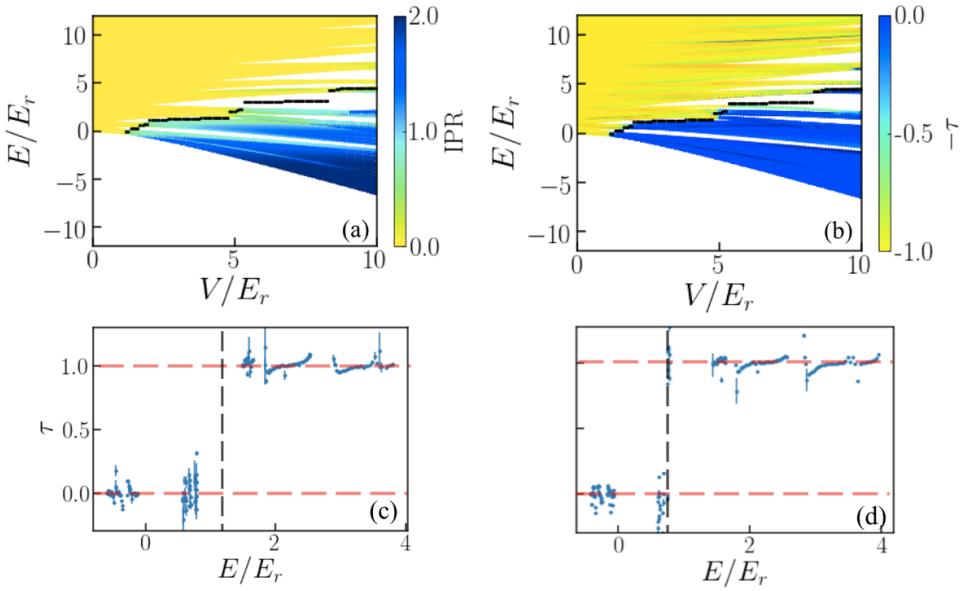

Figure 4.5: Accurate determination of the energy mobility edge E_c for the balanced bichromatic lattice. Panel (a) shows the IPR versus the particle energy E and the lattice amplitude V for the system size $L = 100a$ [reproduced from Fig. 4.4(a). Panel (b) shows the exponent τ versus E and V, as found from finite-size scaling analysis of data computed for various system sizes. Panels (c) and (d) are cuts of panel (b) at $V = 2E_r$ and $V = 1.7E_r$, respectively. The system size ranges from $L = 50a$ to $L = 800a$ for most of the points. When the ME lies in a very small gap, as for panel (d) for instance we use larger system sizes, typically up to $L = 1000a$.

existence of a V-dependent energy ME E_c. This is confirmed by the behavior of the wave functions, which turn from exponentially localized at low energy [Fig. 4.4(b)] to extended at high energy [Fig. 4.4(c)]. These results are characteristic of 1D quasiperiodic models that break the AA self-duality condition [176,180,181]. However, one should notice that the IPR varies smoothly with the particle energy, and is not sufficient to distinguish extended states from states localized on a large scale, see discussions in section 4.1.1.

To determine the ME precisely, we perform a systematic finite-size scaling analysis of the IPR and compute the quantity

$$\tau \equiv -\frac{d \log \mathrm{IPR}}{d \log L}. \tag{4.7}$$

For each value of the quasi-periodic amplitude V, we diagonalize the Hamiltonian for a series of system sizes L, typically ranging from $50a$ to $800a$. For any state, we find that the IPR scales as IPR $\sim L^{-\tau}$, with either $\tau = 0 \pm 0.2$ or $\tau = 1 \pm 0.2$. Therefore, in contrast to the IPR at a given system length, which varies smoothly (see the crossover of the color from blue to yellow via a green region in Fig. 4.4(a), also reproduced on Fig. 4.5(a)), the exponent τ shows a sharp transition from localized states (corresponding to $\tau \simeq 0$) to extended states (corresponding to $\tau \simeq 1$), see Fig. 4.5(b) as well as Fig. 4.5(c) and (d) for two typical cuts at fixed values of the quasi-periodic amplitude. The mobility edge (ME) E_c is then determined as the transition point between the values of τ, see black points on Fig. 4.5(b). More precisely, the ME is always in an energy gap (see detailed discussion of the dense gap structure and fractality for the energy spectrum) and we define E_c as the average energy of the last localized state and the first extended state, see dashed black lines on Figs. 4.5(c) and (d), corresponding to a large and small gap, respectively. For all the cases considered here, no intermediate behavior is found in the thermodynamic limit.

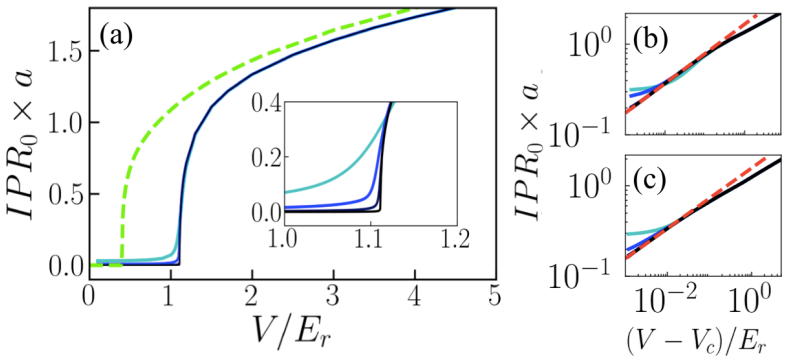

Figure 4.6: Critical localization behavior. (a) Ground-state IPR versus the quasiperiodic amplitude for the balanced bichromatic lattice (solid lines); Inset: Magnification in the vicinity of the critical point at V_c. Darker lines correspond to increasing system sizes, $L/a = 50$ (light blue), 200 (blue), 1000 (dark blue) and 10 000 (black). The dashed green line corresponds to the trichromatic lattice for $L/a = 10\,000$. (b), (c) Ground-state IPR versus $V - V_c$ in the log-log scale for the bichromatic and trichromatic lattices, respectively.

The critical potential

As shown in Fig. 4.4(a), a finite ME appears only for a potential amplitude V larger than some critical value V_c. This fits with the statement in Ref. [176]. In order to determine the critical potential, we plot the IPR of the ground state (IPR_0) versus V in Fig. 4.6(a). The darker color of the curves indicates the larger sizes of the systems, namely $L/a = 50$ (light blue), 200 (blue), 1000 (dark blue) and 10 000 (black). As usual, for a system with small size, the transition from the extended phase (vanishingly small IPR) to the localized phase (finite IPR) is a smooth crossover thanks to the finite size effect, see the cases $L/a = 50, 200$. It gets sharper when the system size increases and becomes critical in the thermodynamic limit, see the darker solid blue lines in the main figure of Fig. 4.6(a) and the inset).

The IPR scales as $\mathrm{IPR}_0 \sim 1/L$ in the extended phase and as $\mathrm{IPR}_0 \sim 1$ in the localized phase. Thus, the critical amplitude can be found with a high precision by plotting the quantity $\mathrm{IPR}_0 \times \sqrt{La}$ at various sizes, see Fig. 4.7. When increasing the system size L, its value increase as $\sqrt{L}$ for a localized state and decrease as $1/\sqrt{L}$ for an extended state.

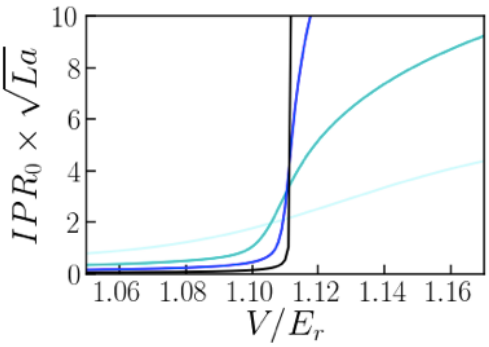

Figure 4.7: Plots of the quantity $\mathrm{IPR}_0 \times \sqrt{La}$ as a function of the potential amplitude V for the balanced bichromatic lattice and different system lengths. Darker lines correspond to increasing system sizes, $L/a = 200$ (light blue), 1000 (blue), 5000 (dark blue), 10000 (black).

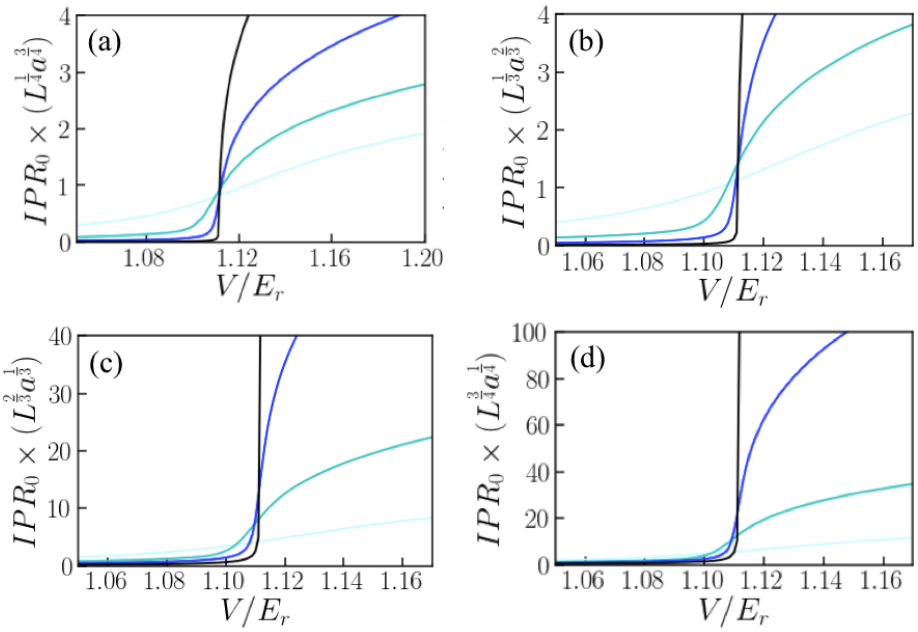

Figure 4.8: Plots of the quantity $\mathrm{IPR}_0 \times L^\alpha \times a^{1-\alpha}$ as a function of the potential amplitude V for the balanced bichromatic lattice and different system lengths. Darker lines correspond to increasing system sizes, $L/a = 200$ (light blue), 1000 (blue), 5000 (dark blue), 10000 (black).

Therefore, the fixed point of the curves indicates the transition point. It yields

$$V_\mathrm{c}/E_\mathrm{r} \simeq 1.112 \pm 0.002. \tag{4.8}$$

In fact, the critical potential amplitude V_c is determined by plotting the quantity $\mathrm{IPR}_0 \times L^\alpha a^{1-\alpha}$ versus V with any value of α between the range $0 < \alpha < 1$. However, we argue here that the choice $\alpha = 1/2$ gives the more accurate result. According to the L dependence of IPR, for a localized state, the quantity $\mathrm{IPR}_0 \times L^\alpha a^{1-\alpha}$ increases with L, while for an extended state it decreases with L. The turning point between these two opposite behaviours yields an accurate value of V_c. Figure 4.8 shows this approach for the balanced bichromatic lattice. For large enough systems and any of the considered values of α, the curves corresponding to different lengths cross each other at almost the same value of V/E_r. For the various values of α considered here, we find the following estimates:

α	1/4	1/3	1/2	2/3	3/4
$V_\mathrm{c}/E_\mathrm{r}$	1.113	1.111	1.112	1.111	1.110
accuracy	0.004	0.002	0.002	0.002	0.004

Table 4.1: The choice of α and the V_c found correspondlngly.

All the results agree within the errorbars. From the table, we find that the most accurate result is found for $\alpha = 1/2$, which maximally discriminates the localized and extended states. It yields the value in Eq. 4.8.

The critical exponent

The accurate value of V_c we obtained allows us to determine the critical exponent of the transition. Plotting IPR_0 versus $V - V_\mathrm{c}$ in log-log scale, we find a clear linear behavior for sufficiently large systems, consistent with the power-law scaling

$$\mathrm{IPR}_0 \sim (V - V_c)^\nu \tag{4.9}$$

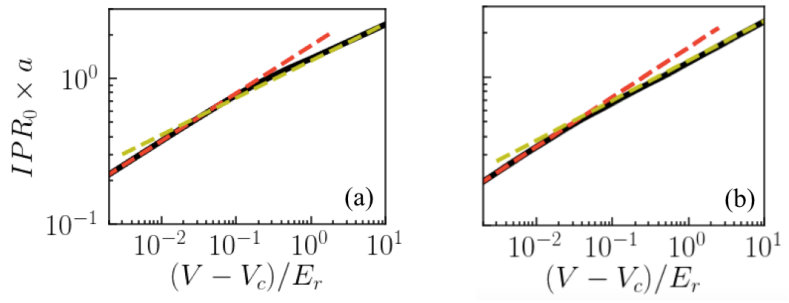

Figure 4.9: Crossover of ground-state IPR (solid black line) from the critical behaviour $\mathrm{IPR}_0 \sim (V - V_\mathrm{c})^\nu$ with $\nu \simeq 1/3$ (dashed red line) at criticality to the asymptotic behaviour $\mathrm{IPR}_0 \sim V^{\nu'}$ with $\nu' \simeq 1/4$ for $V \gg V_\mathrm{c}, E_\mathrm{r}$ (dashed yellow line). The panels (a) and (b) correspond to the bichromatic and trichromatic cases, respectively.

which can be seen from Fig. 4.6(b). Fitting the slope, we find the critical exponent $\nu \simeq 0.327 \pm 0.007$, see red dashed line in Fig. 4.9 (a). Note that for V far enough from V_c, the behavior of the IPR changes. It is normal that the behavior changes since the algebraic behavior is only expected near by the critical point. For instance, for the case $V \gg V_\mathrm{c}$, the local potential minima support bound states and, for the quasi-periodic potential, the tunnelling is suppressed. At the potential minima, we can perform Taylor expansion and find the harmonic approximation $V(x) \propto Vx^2 \sim \omega^2 x^2$. Thus, we find the frequency

$$\omega \propto \sqrt{VE_\mathrm{r}}/\hbar. \tag{4.10}$$

The lowest energy eigenstates of the quasi-periodic potential, which are the ground states of the local harmonic oscillators, are nearly Gaussian functions of width

$$\ell = \sqrt{\hbar/m\omega} \propto V^{1/4} \tag{4.11}$$

and centered at the bottom of different potential minima. Then, the IPR of the ground state scales as $\mathrm{IPR}_0 \sim 1/\ell$, i.e.

$$\mathrm{IPR}_0 \sim V^{\nu'} \qquad \text{with} \qquad \nu' = 1/4. \tag{4.12}$$

This exponent significantly differs from the critical exponent $\nu \simeq 1/3$ found at the critical point V_c. In Fig. 4.9 (a), we plot IPR as a function of $V - V_\mathrm{c}$ in a larger window, and find the scaling $\mathrm{IPR}_0 \sim V^{\nu'}$ with $\nu' \simeq 0.258 \pm 0.005$ in large V limit, see yellow dashed line This is consistent with the exponent $1/4$ expected in the tight-binding limit

4.2.2 Other quasi-periodic lattices and universality

In this subsection, we extend our study of the critical behavior to other quasiperiodic models and check the universality of the results. We start with the imbalanced bichromatic lattices, and then move to the trichromatic case.

The imbalanced bichromatic lattice

We first consider the imbalanced bichromatic lattice, Eq. (4.2) with $V_1 \neq V_2$. In Fig. 4.10, we plot the ME versus the quasiperiodic amplitudes V_1 and V_2. The dark region corresponds to cases where the ME is absent. Its boundary yields the critical line in the V_1-V_2 plane, thus it yields the pair of critical potential (V_{1c}, V_{2c}). Note that Fig 4.10 is not symmetric by exchange of V_1 and V_2 even upon rescaling the energies. This owes to the strong dependence of the model on the incommensurate ratio r. Since the two cosine

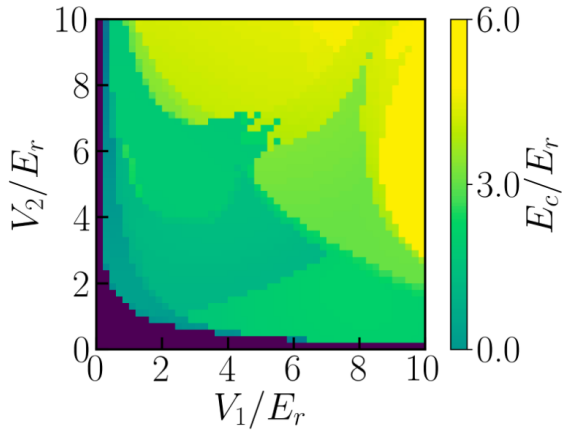

Figure 4.10: Mobility edge for the imbalanced bichromatic lattice, Eq. (4.2) versus the amplitudes V_1 and V_2. The dark region indicates the absence of a mobility edge, and its boundary the localization critical line.

functions in the potential have different frequencies, if one exchange the value of V_1 and V_2, the incommensurate ratio is also changed to the opposite and the critical localization potential changes.

We found that the localization transition is universal, and the critical and fractal properties discussed above for the balanced case apply irrespectively to the relative amplitudes of the two lattices, i.e. also for $V_1 \neq V_2$.

On the one hand, beyond the critical line, the ME still marks a sharp transition between exponentially localized and extended states, with no intermediate phase. For instance, we consider here the case with $V_1 = 8E_\mathrm{r}$ and scan the value of V_2 Here, the ME is found at $V_{2\mathrm{c}}/E_\mathrm{r} \simeq 0.140 \pm 0.005$, see Fig. 4.11(a). Using the same analysis as for the balanced lattice (see main text), we find the critical behaviour

$$\mathrm{IPR}_0 \sim (V_2 - V_{2\mathrm{c}})^\nu \qquad \text{with} \qquad \nu \simeq 0.33 \pm 0.01, \tag{4.13}$$

see inset of Fig. 4.11(a). This value of the critical exponent ν is very close to that found for the balanced case.

Now, we study the ME for a fixed potential amplitude $V_1 = 8E_\mathrm{r}, V_2 = 0.15E_\mathrm{r} > V_{2\mathrm{c}}$ and perform the finite-size analysis. We compute the IPR versus the energy E for various system sizes. For any E, we find the scaling $\mathrm{IPR} \sim 1/L^\tau$ with either $\tau \simeq 0$ or $\tau \simeq 1$ just as the balanced case, see Fig. 4.11 (b). A sharp jump from $\tau \simeq 0$ to $\tau \simeq 1$ marks the ME, here found at $E_\mathrm{c} \simeq 2.64$. As shown by Fig. 4.11(b), the ME is in a gap. It confirms that the transition is sharp, between a localized phase and an extended phase. The subfigure (c) indicates the fractal property for the energy spectrum which will be demonstrated in chapter 4.3.

On the other hand, for any value of V_1 up to values deep in the AA limit ($50E_\mathrm{r}$), we always found $\mathrm{IPR}_0 \sim (V_2 - V_{2\mathrm{c}})^\nu$ with $\nu \simeq 0.33 \pm 0.02$. The same applies to the discrete AA model, which we shall discuss in detail below.

The Aubry-André limit: critical potential and mobility edge

On Fig. 4.12(a), we plot the critical potential of the second lattice, $V_{2\mathrm{c}}$, versus the amplitude of the first lattice, V_1, for the imbalanced bichromatic lattice. It corresponds to the boundary between the colorful and dark region in Fig. 4.10. We find excellent agreement between the results founds for the continuous model (solid blue lines) and the prediction of the discrete AA model for $V_1 \gtrsim 8E_\mathrm{r}$, corresponding to $\Delta = 2J$ for Hamiltonian Eq. (4.4) [173] (dashed red lines),

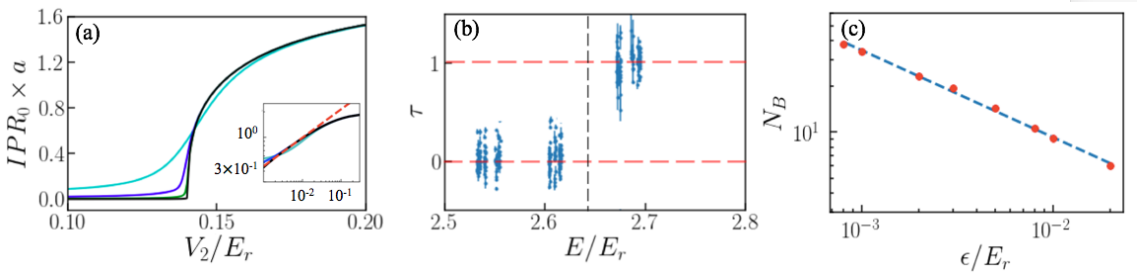

Figure 4.11: Critical and fractal behaviour for the imbalanced bichromatic lattice. Here we use $V_1 = 8.0E_\mathrm{r}$ and $r = (\sqrt{5}-1)/2$. (a) IPR of the ground state, IPR_0, versus the amplitude of the second lattice V_2. Darker lines correspond to increasing system sizes, $L/a = 50$ (light blue), 200 (blue), 1000 (dark blue), 10000 (black). Inset: Same data versus $V_2 - V_{2\mathrm{c}}$ in log-log scale, confirming the critical behaviour $\mathrm{IPR}_0 \sim (V_2 - V_{2\mathrm{c}})^\nu$, with $\nu \simeq 0.33 \pm 0.01$ (dashed red line). (b) Scaling exponent τ versus the energy E as found from fits as $\mathrm{IPR} \sim 1/L^\tau$, for the specific case $V_2 = 0.15E_\mathrm{r} > V_{2\mathrm{c}}$. The black dashed line marks the ME. (c) Energy box-counting number N_B as a function of the energy resolution ϵ, in the energy window corresponding to panel (b).

Figure 4.12(b) shows the same comparision in the opposite situation where lattice 2 is in the tight-binding regime and lattice 1 is weak. In this case, the AA parameters are changed from Eq. (4.5) by exchanging V_1 and V_2 and replacing E_r by r^2E_r. they write

$$J \simeq \frac{4E_\mathrm{r}r^{1/2}}{\sqrt{\pi}}\left(\frac{V_2}{E_\mathrm{r}}\right)^{3/4}\exp\left(-2r^{-1}\sqrt{\frac{V_2}{E_\mathrm{r}}}\right) \qquad \text{with} \qquad \Delta \simeq \frac{V_1}{2}\exp\left(-r^{-1}\sqrt{\frac{E_\mathrm{r}}{V_2}}\right). \tag{4.14}$$

Then, the critical potential $V_{1\mathrm{c}}$ found in the continuous model approaches the AA prediction for $V_2 \gtrsim 6E_\mathrm{r}$.

In the AA model, it is well known that there is no ME. However, in the AA limit of the continuous model, we find a finite ME. This is due to the fact that the ME is found above the lowest band, which is the only one described in the AA model. Thus, the two results are actually compatible. In Fig. 4.12(c), we show the lowest part of the energy spectrum in the AA limit of the continuous bichromatic model, $V_1 = 10E_\mathrm{r} \gg E_\mathrm{r}$, as a function of the amplitude of the second lattice, V_2. The structure of the spectrum is reminiscent of the band spectrum of the dominant lattice, and we refer to the visible states clusters as

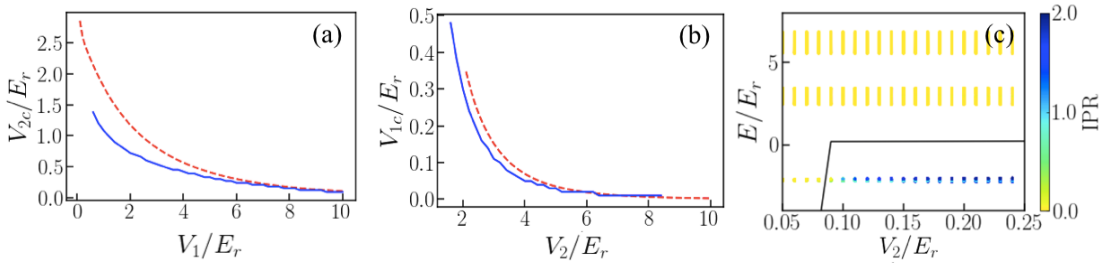

Figure 4.12: Comparison between the critical point found in the continuous bichromatic model (solid blue lines) and the discrete Aubry-André model (dashed red lines). Panel (a) corresponds to the tight-binding regime for lattice 1 and panel (b) to tight-binding regime for lattice 2, respectively. Panel (c) shows the lowest part of the energy spectrum for $V_1 = 10E_\mathrm{r}$, as a function of V_2. The color scale encodes the IPR, corresponding to localized (blue) and extended (yellow) states. The ME is shown as the solid black line.

the first bands of the main lattice. The color scale encodes the IPR, corresponding to localized (blue) and extended (yellow) states. The solid black line shows the mobility edge as found from a cut of Fig. 4.10 at the fixed value of $V_1 = 10E_r$. For vanishingly small values of V_2, there is no ME and all the states are extended. When increasing the value of V_2, the ME sharply jumps to a value in the first band gap of the main lattice. Then, all the states of the first band of the main lattice become localized. The critical point is found at $V_2 \simeq 0.09E_r$. Using the formulas in Eq. (4.5), we find that it corresponds to $\Delta/2J \simeq 1.04$, in excellent agreement with the prediction of the discrete AA model [173]. Note that the states of the second and third bands of the main lattice are still extended. They become localized at a higher value of V_2, see Fig. 4.10.

The Aubry-André limit: critical exponent

It is worth noting that the behavior of the IPR differs from that of the Lyapunov exponent (inverse localization length). The IPR is dominated by the core of the wave function and characterizes, for instance, the short-range interaction energy of two particles in a localized state [22]. In contrast, the Lyapunov exponent γ characterizes the exponential tails of the wave functions,

$$\psi(x) \sim \exp(-\gamma|x|), \tag{4.15}$$

and it is insensitive to the core. For nonpurely exponential wave functions, which appear in our model (see for instance Fig. 4.4(b)), these two quantities are not proportional. For instance, in the AA model, one has

$$\gamma \propto \ln(\Delta/2J). \tag{4.16}$$

At the critical point $\Delta = 2J$, we can perform the Taylor expansion of the ln function at $\Delta = 2J$ and find

$$\gamma \propto \frac{\Delta - \Delta_c}{2J}. \tag{4.17}$$

From Eq. (4.5), we find $\Delta \propto V_2$ and J is independent of V_2, thus we can write

$$\gamma \propto (V_2 - V_{2c})^{\beta}. \tag{4.18}$$

with the Lyapunov critical exponent $\beta = 1$. This value differs from the IPR critical exponent-$\nu \simeq 1/3$-found above.

In order to compare the two behaviors, we plot the ground-state wavefunction for the AA model slightly above the critical point, namely $\Delta/J = 2.05$, see Fig. 4.13. The wavefunction shows a clear exponential localization in the wings. The dahsed red lines

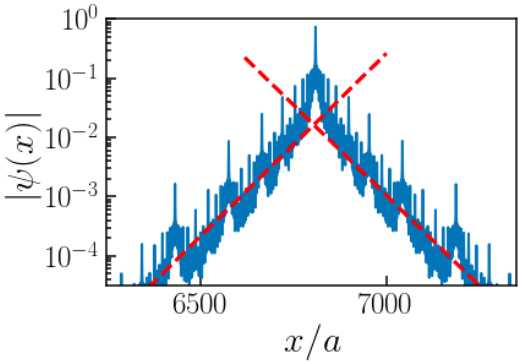

Figure 4.13: Ground-state wavefunction of the Aubry-André model for $\Delta/J = 2.05$ (solid blue line) together with exponential fits (dashed red lines) on the left-hand and right-hand sides of the localization center.

are the fitted exponential function $|\psi| \propto e^{-\gamma|x-x_0|}$ with the localization center x_0 and the Lyapunov exponent γ as fitting parameters. It yields $\gamma = 6.2 \times 10^{-3} \pm 6.85 \times 10^{-5}$. However, the wavefunction is not a pure exponential function. In particular, it shows a core about one order of magnitude larger than the exponential fit at the localization center x_0. This core dominates the IPR. For instance, restricting the wavefunction to the range $[x_1, x_2]$ such that $\psi(x_1) = \psi(x_2) = 0.01\psi(x_0)$, we find that the IPR is 99.5% of the value found for the full wavefunction. Here, we cut at $0.01\psi(x_0)$ since this is where the wavefunction starts to deviate from the exponential decay. Our result illustrated that the IPR is independent of the exponential behaviour of the tails, and the IPR and Lyapunov exponent yield different pieces of information about localization. Moreover, we perform the study of IPR and γ by scanning V_2 nearby V_{2c}, see Fig. 4.14. For both of the two parameters, we find a linear behavior in log-log scale. Fitting them by a linear function, we find the scalings

$$\mathrm{IPR}_0 \sim (V_2 - V_{2c})^{\nu} \qquad \text{and} \qquad \gamma \sim (V_2 - V_{2c})^{\beta}, \tag{4.19}$$

with $\nu \simeq 0.33 \pm 0.015$ and $\beta \simeq 0.96 \pm 0.04$.

The trichromatic lattice

Now, we consider the trichromatic lattice

$$V(x) = \frac{V}{2}\big[\cos(2k_1 x) + \cos(2k_2 x + \varphi) + \cos\big(2k_3 x + \varphi'\big)\big], \tag{4.20}$$

with $k_3/k_2 = k_2/k_1 = r$, so that the three lattice spacings are incommensurate to each other [note that $k_3/k_1 = r^2 = (3-\sqrt{5})/2$ is an irrational number]. Performing the same analysis as for the other models, we recover the same universal features. We find a finite critical amplitude V_c and the critical behavior $\mathrm{IPR}_0 \sim (V - V_c)^{\nu}$ with $\nu \simeq 0.327 \pm 0.007$; see Fig 4.6(c). The only significant difference is that the critical point for the trichromatic lattice, $V_c/E_r \simeq 0.400 \pm 0.005$, is smaller than for the bichromatic lattice, see green dashed line in Fig. 4.6(a). In particular, we study the standard deviation of the potential,

$$\Delta V = \sqrt{\langle V(x)^2\rangle - \langle V(x)\rangle^2} \tag{4.21}$$

which is the quantity that characterizes the amplitude of disorder in truly disordered system. For the quasiperiodic potentials we considered, the term $\langle V(x)\rangle^2$ in Eq. (4.21) is simply zero. Then, we have $\Delta V_2 \simeq \sqrt{1/4}V_2$ for the bichromatic case and $\Delta V_3 \simeq \sqrt{3/8}V_3$

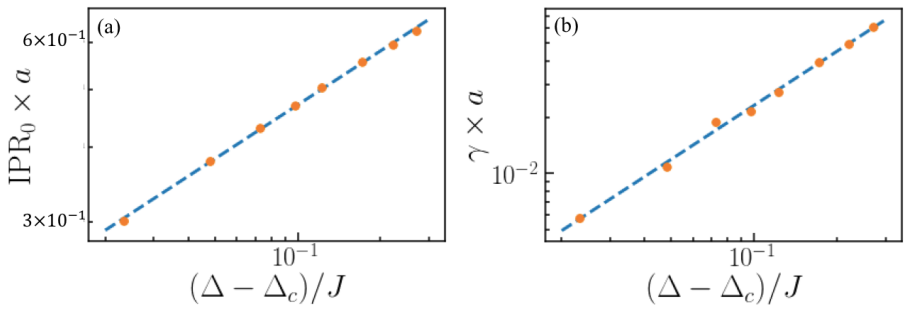

Figure 4.14: The ground state IPR and Lyapunov exponent γ for the AA model near the transition point Δ_c (data points plotted as yellow balls). Here, both of the two plots are in log-log scale. In both cases, with a linear fit (blue dashed line), we find the slopes $\nu \simeq 0.33 \pm 0.015$ for (a) and $\beta \simeq 0.96 \pm 0.04$ for (b).

for the trichromatic case. Taking the ratio of the two values at the critical point, we find

$$\frac{\Delta V_{2c}}{\Delta V_{3c}} = \sqrt{\frac{2}{3}}\frac{V_{2c}}{V_{3c}} = 2.27 \tag{4.22}$$

Comparing with the balanced bichromatic case, it is a factor about 2.27 smaller at the critical point for the trichromatic lattice. This is consistent with the intuitive expectation that it should vanish in the disordered case corresponding to an infinite series of cosine components with random phases [186, 187].

Up to now, we have checked the localization properties for imbalanced bichromatic lattices, continuous bichromatice lattices in AA limit, as well as trichromatic lattices. We find it's universal that there exists a finite critical potential and ME. Especially, in the AA limit of the continuous model, the ME exists and is above the band considered in the discrete AA model. Moreover, we find in all cases a critical exponent ν with the value around 1/3 which is quite remarkable. There is no explanation yet for this value and it will be worth understanding it. In the next subsection, we will focus on the fractal property of the energy spectrum and study the location of ME.

4.3 The fractality of the energy spectrum

In this section, we study in detail the fractal properties of the energy spectrum created by the quasiperiodic potential. It helps us understand better the structure of the bands and gaps and the position of the ME. Also, we will benefit from this result when studying the many-body phase diagram (see details in Chapter 5). Therefore, in this section, we first introduce the mathematical definition of the fractal as well as the Hausdorff dimension. Then, we perform the box-counting analysis to the energy spectrum of our quasiperiodic system and study its fractal dimension. It helps us reach the conclusion that the ME is always in a gap without any intermediate region thanks to the fractal-like spectrum. Finally, we study in detail the property of the fractal dimension, mainly about its dependence on the potential amplitude and spectrum range.

4.3.1 Fractals and fractal dimension

In mathematics, a fractal is a subset of an Euclidean space for which its dimension is smaller than the geometrical dimension. The main property of the fractal is the so called self-similarity: it exhibits similar pattern while going to increasingly smaller scale. In Fig. 4.15. (a) and (b), we show two typical examples of fractal structure. Figure 4.15.(a) shows the mathematic textbook example: Sierpinski triangle. The black and white regions stand for the set and empty space. When using a better and better resolution to observe the shape, small holes represented by the white triangles appear. The structure in smaller triangles are always a repetition of themselves in the larger ones. However, fractals exist much more widely on top of papers and textbooks. The world we live in is beautiful and there are plenty of approximate self-similar fractals in the nature. The Romanian broccoli presented in Fig. 4.15.(b) is one of them. There are also other good examples such as animal coloration patterns, DNA structure, rings of Saturn and etc.

On top of the fractal structure mentioned above, they also exist in the structure of physical quantities, for instance, the energy spectrum of the quasiperiod model. In Fig. 4.15.(c), we plot the first 500 eigenstate for the 1D balanced bichromatic lattice with $V = 2.0E_r$, with system size $L = 500a$. Zooming the first band, we clearly recover the same structure on a smaller scale, see inset plot. This process also applies for the "second and third bands", as well as higher level of zooming. Thus, it will be interesting to study further the fractal property for the spectrum of our system.

Figure 4.15: Three examples of fractal structures: (a). Sierpinski triangle. (b). Romanian broccoli. (c). Energy spectrum of the first 500 states for the 1D balanced bichromatic lattice with $V = 2.0E_{\mathrm{r}}$, with system size $L = 500a$.

Hausdorff dimension and box-counting analysis

An important property of a fractal structure is the fractal dimension. It depicts the shape scale when increasing the resolution in a predictable way. One of the most widely used method is the box-counting scaling. In this analysis, it defines a resolution box with linear size ϵ. Then, we count the minimal number of ϵ-size boxes needed to cover the full system, which is called the box-counting number N_{B}. In a perfect self-similar fractal structure, the scaling of $N_{\mathrm{B}}(\epsilon)$ versus the resolution ϵ is expected to be

$$N_{\mathrm{B}}(\epsilon) \sim \epsilon^{-D_{\mathrm{H}}}, \tag{4.23}$$

which defines the fractal dimension D_{H} of the energy spectrum. Thanks to the analysis, this quantity is also called box-counting dimension. In strict mathematical definition, it differs from the so-called Hausdorff dimension. However, for well-behaved structures, such as the Sierpinski triangle and the Cantor set, the two values are the same. This is also the case for all the models we considered in this thesis. Therefore, from now on, we may call it Hausdorff dimension D_{H} although the calculation is based on the box-counting analysis.

A natural way to calculate D_{H} in practice is to detect the scaling by changing the resolution. Decreasing the resolution by a factor of b, one should expect the box-counting number will increase with factor of B. It writes

$$N_{\mathrm{B}}(\frac{1}{b}\epsilon) = BN_{\mathrm{B}}(\epsilon). \tag{4.24}$$

Combing it with Eq. (4.23), one shall find

$$D_{\mathrm{H}} = \frac{\log\, B}{\log\, b}. \tag{4.25}$$

In Fig. 4.16, we show several typical examples of box-counting analysis. In each subplots, we show the resolution ϵ with the corresponding box-counting number N_{B}. In the upper row, for a one-dimensional line, we find $B = b$. Thus, the dimension is $D_{\mathrm{H}} = \log b/\log b = 1$. In the bottom row, similarly, we consider a filled parallelogram and find $B = b^2$. It leads to $D_{\mathrm{H}} = \log b^2/\log b = 2$. In the intermediate row, we show the analysis for the Sierpinski triangle. From the left to the right, each time we decrease the resolution by half and the number of necessary boxes increases by a factor of 3. It leads to $B = b^{\log_2 3}$. Thus, the Hausdorff dimension is

$$D_{\mathrm{H}} = \frac{\log 3}{\log 2} = 1.57. \tag{4.26}$$

Its value is fractional and smaller than the dimension of its Euclidean space (for a triangle, it is 2). This indicates that there exists a repeating self-similar hole structure when zooming on smaller and smaller resolutions.

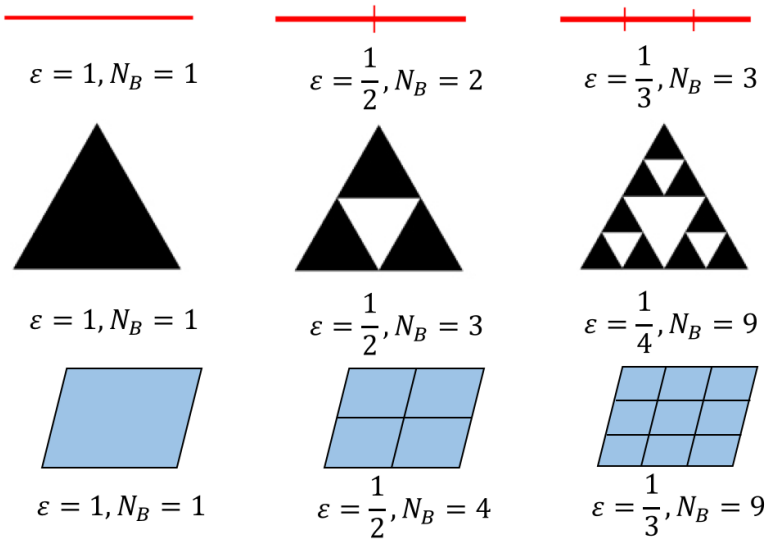

Figure 4.16: Three typical examples of box-counting analysis: Upper row: One dimensional line. Intermediate row: Sierpinski triangle with Hausdorff dimension $D_{\mathrm{H}} = 1.57$. Lower row: Two dimensional parallelogram.

Cantor set

The cantor set is another important example of fractals in mathematics. It is a set of points lying on a single line segment that has a bunch of gapped intervals which present in a self-similar structure. The construction of a Cantor set is shown in Fig. 4.17. On the 0-th level, we start with the interval $[0, 1]$. Then, for reaching the first level, we delete $1/3$ of the segment in the middle, $(\frac{1}{3}, \frac{2}{3})$, which leaves

$$C_1 = [0, \frac{1}{3}] \cup [\frac{2}{3}, 1]. \tag{4.27}$$

Next, for the two remaining segments, we delete the middle $1/3$ intervals for both of them, which leads to

$$C_2 = [0, \frac{1}{9}] \cup [\frac{2}{9}, \frac{1}{3}] \cup [\frac{2}{3}, \frac{7}{9}] \cup [\frac{8}{9}, 1]. \tag{4.28}$$

If we continue this process up to the level of infinity, we finally obtain the Cantor set C.

The process of deleting up to the n-th order can also be understood as observing the set with resolution $\epsilon = (1/3)^n$. Thus, we shall find $B = 2^n$ while $b = 3^n$. Therefore, we can calculate its Hausdorff dimension $D_{\mathrm{H}} = \log 2/\log 3 \simeq 0.631$. It is fractional and smaller than the dimension of the Euclidean space $D_{\mathrm{E}} = 1$. Thus, it has a fractal structure with

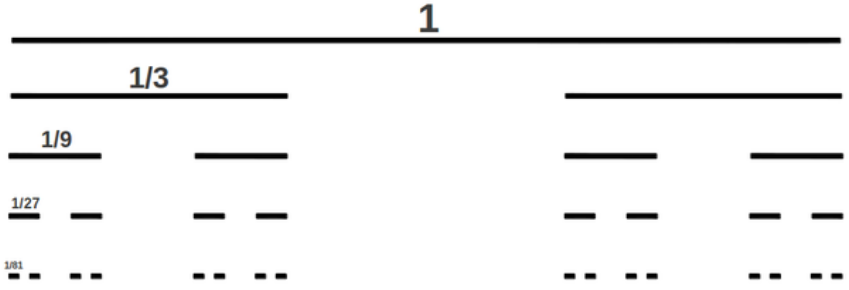

Figure 4.17: The construction process of the classical Cantor set.

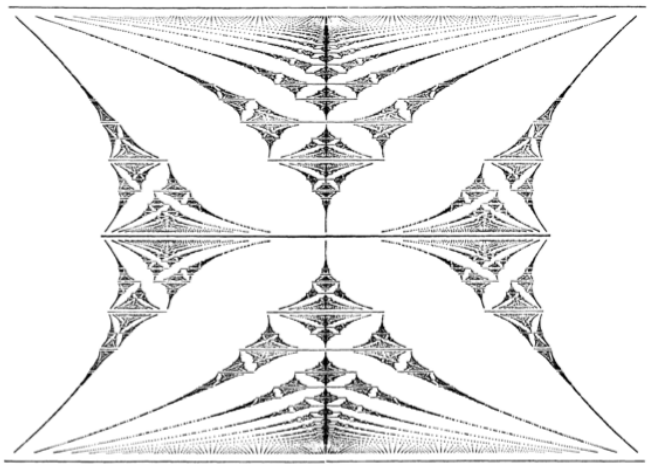

Figure 4.18: The original figure of the Hofstadter butterfly produced in Ref. [157],

infinite gaps open in a self-similar way. Moreover, one should notice that the Cantor set we introduced above is the so-called Cantor middle-1/3 set. The definition of a Cantor set can be much more general. During the process of construction, there does not have to be a single deleted interval and its position is also not necessarily the middle 1/3. This is also known as the so-called generalized Cantor set, which can be mapped to the energy spectrum of the quasiperiodic potentials [185, 188] (see details later).

AA model and Hofstader butterfly

The energy spectrum of the Aubry-André model has been studied in detail by Douglas R. Hofstadter in Ref. [157], known for the famous Hofstadter butterfly. Although its initial motivation was to study the Harper equation for 2D electrons in magnetic fields, the Schrödinger equation can be mapped onto the AA model as Eq. (4.4) with $J = 2\Delta$. The parameter r also stands for the magnetic flux per cell in the 2D problem. In Fig. 4.18, we show the original figure of the famous Hofstadter butterfly in Ref. [157]. It shows an interesting fractal structure. The horizontal axis is the eigenenergy, while the vertical axis is the ratio of the two lattice spacing r. When $r = p/q$ is rational, the spectrum contains q subbands. When r is irrational, the spectrum is fractal-like and it has a well-defined fractal dimension [189, 190].

In fact, when r is irrational, the spectrum is always a fractal, irrespective of the value for J/Δ. It is always homeomorphic to a Cantor set. This can be understood by the rational approximation for an irrational number. We take the golden ratio $r = (\sqrt{5}-1)/2$ as an example. It can always be approximated by the ratio of two neighbours in the Fibonacci series $\{F_n\}$, i.e. $r \simeq F_n/F_{n+1}$. On the n-th order of approximation, we find that the spectrum contains F_{n+1} subbands and $F_{n+1}-1$ gaps which opens by the beating of the two quasimomentums F_n and F_{n+1}. Increasing the approximation order n of the irrational number r, more gaps open and it similarly reproduces the construction of a Cantor set. For this choice of r, it has even been proved that the fractal dimension for the energy spectrum at $J = 2\Delta$ is $D_{\text{H}} = 0.5$ [189, 190]. For other incommensurate number which is not a Liouville number, one can always build the corresponding generalised Fibonacci series and perform the similar construction [185, 188].. Even for the continuous quasiperiodic system we studied, we argue that the statement still holds and we shall find the fractal-like structure in the energy spectrum.

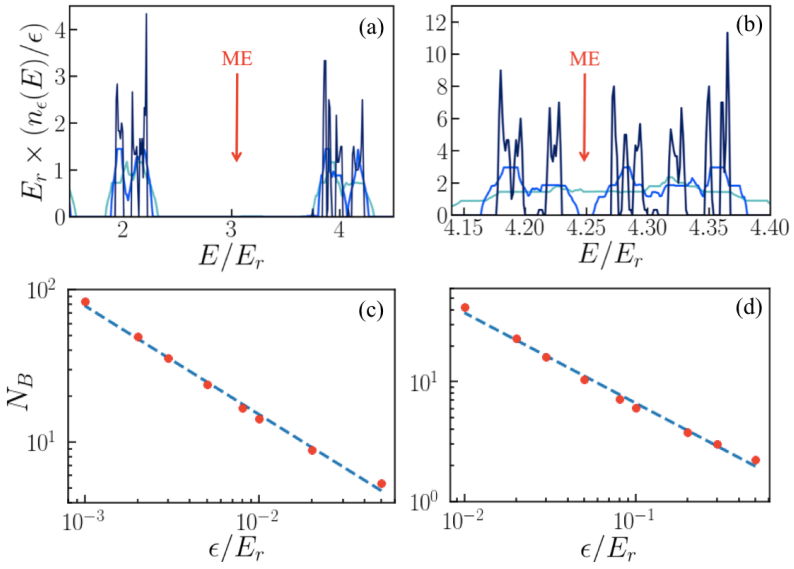

Figure 4.19: Fractal behavior of the energy spectrum. (a) shows $n_\epsilon(E)/\epsilon$ in the vicinity of the ME at $V = 6.0E_\mathrm{r}$ for $L = 600a$ and $\epsilon/E_\mathrm{r} = 0.1$ (light blue), 0.05 (blue), 0.01 (dark blue). (b) shows the same quantity for the ME at $V = 8.5E_\mathrm{r}$ for $L = 1000a$ and $\epsilon/Er = 0.1$ (light blue), 0.03 (blue), 0.003 (dark blue). (c) and (d) show the energy-box counting number N_B versus ϵ for the parameters of (a) and (b), respectively. The linear slopes in log-log scale are consistent with a fractal behavior, Eq. (4.23) with $D_H = 0.72 \pm 0.03$ and $D_H = 0.76 \pm 0.03$, respectively.

4.3.2 Fractality of the energy spectrum for 1D quasiperiodic systems

Now, we turn to the energy spectrum of 1D continuous quasiperiodic systems. From the integrated density of state (IDOS), we confirm the fractal structure of the spectrum. Then, we perform the box-counting analysis to calculate its fractal dimension, and conclude that the ME always lay in a gap.

The integrated density of states (IDOS)

To characterize the energy spectrum and understand better its fractal structure, we start by computing the IDOS per unit lattice spacing $n_\epsilon(E)$, i.e. the number of eigenstates in the energy range $[E - \epsilon/2, E + \epsilon/2]$, divided by L/a. Figures. 4.19(a) and (b) show the quantity $n_\epsilon(E)/\epsilon$ in the vicinity of the ME for two values of the quasiperiodic amplitude V and several energy resolutions ϵ. Here, one should notice that the quantity $n_\epsilon(E)/\epsilon$ may be interpreted as the density of states (DOS) for an energy resolution ϵ. Because of the fractality of the energy spectrum, the DOS- $\lim_{\epsilon\to 0_+} n_\epsilon(E)/\epsilon$- is, however, ill defined (see below). For any value of ϵ, the IDOS displays energy bands separated by gaps. However, when the resolution ϵ decreases (corresponding to increasingly dark lines on the plots), new gaps appear inside the bands, while the existing gaps are stable. It gives a first signal that the spectrum is nowhere dense while the gaps are dense in the thermodynamic limit. In particular, the density of states $\lim_{\epsilon\to 0_+} n_\epsilon(E)/\epsilon$ is singular. The limit of its value is zero since $D_\mathrm{H} < 1$. Moreover, the ME is always found in a gap for a sufficiently resolved spectrum, see the red arrow in Figs. 4.19(a) and 4.19(b).

Here, one should note that this is not a finite-size effect: For all the results shown here, we have used large enough systems so that each ϵ-resolved band contains at least 10 - 15 states. In addition, we have checked that the IDOS is stable against further increasing the system's length (see later discussion about the finite-size analysis). All these aspects confirm that the opening of an infinite series of minigaps is characteristic of a fractal

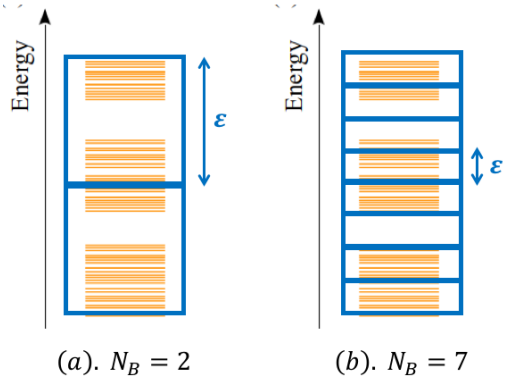

Figure 4.20: Two examples of the box-counting number N_{B} for the energy spectrum under different resolutions ϵ.

behavior.

Box-counting analysis for the energy spectrum

As we mentioned in the last subsection, the fractal character of the energy spectrum of 1D incommensurate systems has been studied for discrete models, such as the Fibonacci chain and the AA model [157, 161, 189–192]. In all of these cases, it was shown that the spectrum is homeomorphic to a Cantor set. To study fractality in our continuous model, we use the direct box-counting analysis similar as the mathematical one [193, 194]: We introduce the *energy-box counting number*,

$$N_{\mathrm{B}}(\epsilon) = \lim_{q\to 0_+} \int_{E_1}^{E_2} \frac{dE}{\epsilon} \left[n_\epsilon(E)\right]^q, \tag{4.29}$$

for some energy range $[E_1, E_2]$. In the limit $q \to 0_+$, the quantity $\left[n_\epsilon(E)\right]^q$ approaches 1 if $n_\epsilon(E) \neq 0$ and 0 if $n_\epsilon(E) = 0$. Therefore, the quantity $\lim_{q\to 0_+} \left[n_\epsilon(E)\right]^q$ contributes 1 in the boxes of width ϵ containing at least one state and vanishes in the empty boxes. The sum of these contributions, $N_{\mathrm{B}}(\epsilon)$, counts the minimal number of ϵ-wide boxes necessary to cover all the states within the energy range $[E_1, E_2]$. In Fig. 4.20, we show two typical examples of the box-counting number N_{B} under different observation resolution ϵ. In Fig. 4.20 (b), there are 8 boxes in the whole energy range but only $N_{\mathrm{B}} = 7$ filled box, since the third box from the bottom contains no eigenstate inside.

The scaling of $N_{\mathrm{B}}(\epsilon)$ versus the energy resolution ϵ will follow Eq. (4.23), which defines the Hausdorff dimension D_{H} of the energy spectrum. In all considered cases, we found a scaling consistent with Eq. (4.23) with $0 < D_{\mathrm{H}} < 1$. This is characteristic of a nontrivial fractal. For a continuous (respectively discrete) spectrum, one finds $D_{\mathrm{H}} = 1$ (respectively 0). Intermediate values of D_{H} are characteristic of a nontrivial self-similar behavior. For instance Figs. 4.19(c) and (d) show N_{B} versus ϵ in the vicinity of the MEs at $V = 6E_{\mathrm{r}}$ and $V = 8.5E_{\mathrm{r}}$ for the energy ranges corresponding to Figs. 4.19(a) and (b), respectively. We find a linear scaling in the log-log scale, consistent with Eq. (4.23) and the Hausdorff dimensions $D_{\mathrm{H}} = 0.72 \pm 0.03$ and $D_{\mathrm{H}} = 0.76 \pm 0.03$, respectively. Both values are significantly smaller than the geometrical dimension $d = 1$. Therefore, the Lebesgue measure of the energy support vanishes in the limit of an infinitely small resolution, and the spectrum is nowhere dense in the thermodynamic limit.

In the section 4.2.1, we have questioned whether the location of ME is a gap or a band. Thanks to the fractality of the spectrum, all the points in the spectrum are disconnected with each other. Therefore, there is even no connected band exists in the spectrum in the thermodynamic limit. And it confirms that the ME should always lie in a gap.

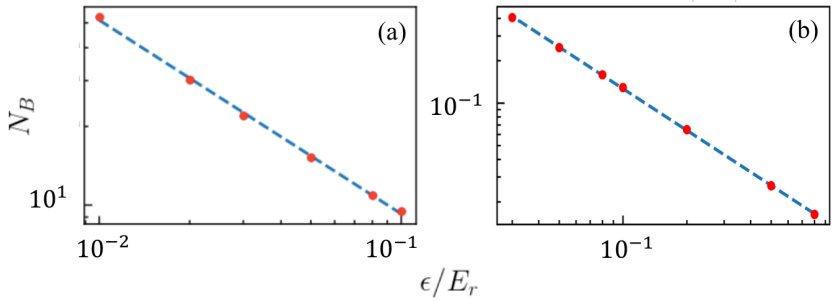

Figure 4.21: Two examples of the box-counting number N_{B} for the energy spectrum under different resolutions ϵ. (a). 1D trichromatic lattice with $V = 0.6E_{\mathrm{r}}$. (b) 2D quasicrystal structure with $V_0 = 5.5E_{\mathrm{r}}$.

Here, we should note that the Hausdorff dimension found above significantly differs from that found in previous work at the critical point of the AA model, $D_{\mathrm{H}} \simeq 0.5$ [189, 190]. We conclude that the spectral Hausdorff dimension is a nonuniversal quantity. This is confirmed by further calculations we performed. For instance, in the AA limit of our continuous model, $V_1 \gg V_2, E_{\mathrm{r}}$, we recover $D_{\mathrm{H}} = 0.507 \pm 0.005$ at the critical point. Conversely, we found $D_{\mathrm{H}} = 0.605 \pm 0.014$ at the critical point of the balanced lattice. However, we argue that the existence of the fractal spectrum structure and $D_{\mathrm{H}} < 1$ is universal. It holds for any 1D bichromatic lattices. We even confirm further that it holds for the spectrum of 1D trichromatic lattices and 2D quasiperiodic lattices. In Fig. 4.21, we show the box-counting number versus the resolution ϵ for the energy spectrums of two typical cases. In Fig. 4.21(a), we study the case of the 1D trichromatic lattice as Eq. (4.20) with $V = 0.6E_{\mathrm{r}}$. Here, we find a linear behavior in log-log scale with the fractal dimension $D_{\mathrm{H}} = 0.74 \pm 0.02$. Also, in Fig. 4.21(b), we treat the 2D quasicrystal structure considered in Refs. [19, 33, 195], which Hamiltonian writes

$$\hat{H} = \sum_j \left[-\frac{\hbar^2}{2m} \nabla_j^2 + V(\hat{\mathbf{r}}_j) \right] \tag{4.30}$$

where $\hat{\mathbf{r}}_j$ is the position of the j-th particle and $V(\mathbf{r})$ quasicrystal lattice potential. The quasicrystal potential is eightfold rotation symmetric,

$$V(\mathbf{r}) = V_0 \sum_{k=1}^{4} \cos^2 (\mathbf{G}_k \cdot \mathbf{r}) \tag{4.31}$$

where V_0 is the potential amplitude and the quantities $\mathbf{G}_k$ are the lattice vectors of four mutually incoherent standing waves oriented at the angles 0°, 45°, 90°, and 135°, respectively. We perform the similar exact diagonalization techniques as for the 1D case, for the potential $V_0 = 5.5E_{\mathrm{r}}$ to find the energy spectrum and perform the box-counting analysis to get Fig. 4.21(b). Even in this case, we find a linear behavior in log-log scale and a fractal dimension $D_{\mathrm{H}} = 0.83 \pm 0.03$.

Finite-size analysis and check of fidelity

Here, we want to show that the opening of mini gaps in the energy spectrum, i.e. the results shown in Figs. 4.19(a) and (b) are not due to finite-size effects. We have computed the integrated density of states (IDOS) for various system lengths. Figures 4.22(a) and (b) reproduce the IDOS shown on Fig. 4.19 for the smallest considered energy resolutions ϵ and various values of the length L. The results corresponding to the different system lengths are indistinguishiable. Moreover, we have computed the Hausdorff dimensions in

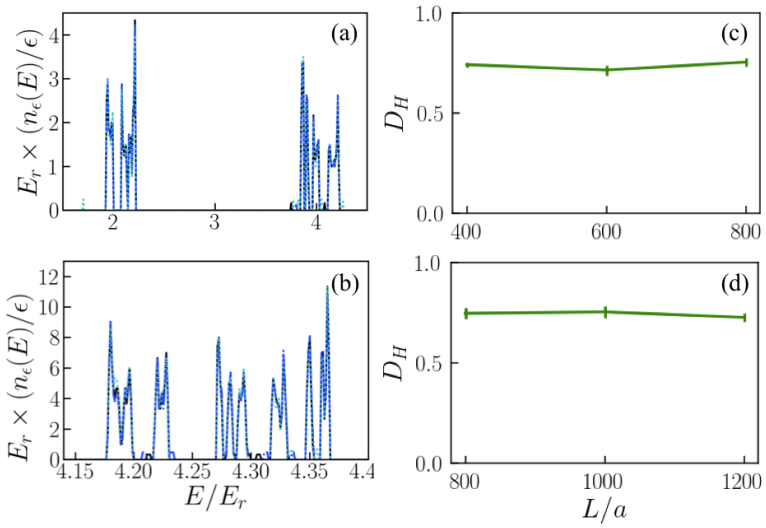

Figure 4.22: Finite-size scaling analysis for the IDOS. The panels (a) and (b) reproduce the IDOS divided by the energy resolution, $n_\epsilon(E)/\epsilon$, shown on Fig. 2 for the smallest considered energy resolutions ϵ but for various values of the length L. (a) IDOS in the vicinity of the ME at $V = 6E_\mathrm{r}$ for $\epsilon = 0.01E_\mathrm{r}$ and $L = 400a$ (dotted light blue line), $600a$ (dashed blue line), $800a$ (solid black line). (b) Same as panel (a) for $V = 8.5E_\mathrm{r}$, $\epsilon = 0.003E_\mathrm{r}$, and $L = 800a$ (dotted light blue line), $1000a$ (dashed blue line), $1200a$ (solid black line). (c) and (d) Hausdorff dimension D_H calculated for the various system sizes used for the panels (a) and (b).

both cases for the different lengths, see Figs. 4.22(c) and (d). The behaviours of D_H do not show significant variations with the system size. These results allow us to rule out finite-size effects.

Furthermore, we want to confirm the fidelity of our box-counting approach, we have performed two additional checks. On the one hand, we have computed the Hausdorff dimension of the first band of the first lattice for the continuous model in the Aubry-André limit ($V_1 \gg V_2, E_\mathrm{r}$). At the critical point, we find a clear fractal behaviour of the energy-box number, $N_\mathrm{B} \sim \epsilon^{-D_\mathrm{H}}$ with $D_\mathrm{H} = 0.51 \pm 0.01$, see Fig. 4.23(a). It is in excellent

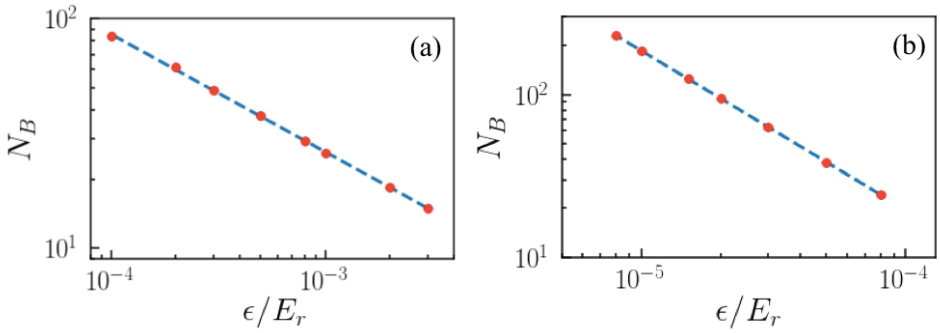

Figure 4.23: Energy-box counting number N_B versus ϵ for (a) the continuous bichromatic model in the Aubry-André limit, $V_1 = 10E_\mathrm{r}$ and $V_2 = 0.09E_\mathrm{r}$, at criticality and (b) the commensurate bichromatic lattice, $r = 2/3$ and $V_1 = V_2 = 6E_\mathrm{r}$.

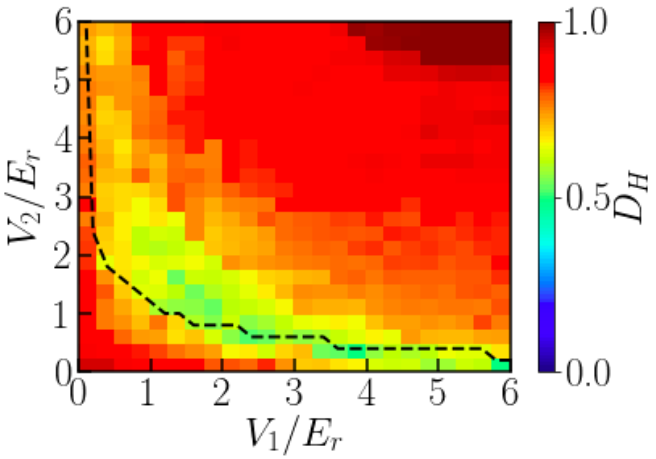

Figure 4.24: Fractal dimension of the energy spectrum for various values of V_1 and V_2. The black dashed line is the critical potential calculated in Ref. [86]

agreement with the Hausdorff dimension found by another method in the discrete Aubry-André model, $D_{\mathrm{H}} \simeq 0.5$ [189, 190]. On the other hand, we have reproduced the same calculations as for the case corresponding to Fig. 4.22(b), i.e. $V_1 = V_2 = 6E_{\mathrm{r}}$, but with the commensurate filling $r = 2/3$. It corresponds to a periodic system and a regular spectrum with $D_{\mathrm{H}} = 1$ is expected. The result is shown on Fig. 4.23(b) and we find $D_{\mathrm{H}} = 0.98 \pm 0.01$, in excellent agreement with this prediction. These results further validate our approach to determine the fractal dimension of the energy spectrum.

4.3.3 Properties of the spectrum fractal dimension

As we explained in the previous subsection, the existence of a spectrum fractal dimension smaller than unity is universal for quasiperiodic potentials with finite potential amplitudes. However, its value is not universal and will change with the potentials. In this subsection, we study in detail the property of the spectrum fractal dimension, i.e. its dependence on the quasiperiodic potentials.

We focus on the energy spectrum in the range $[E_0, E_N]$, where E_0 is the ground state energy and E_N is the energy of the N-th state with $N = L/a$. For the following calculations, we take $N = 500$. Here, we scan V_1 and V_2 and calculate the fractal dimension D_{H} of the energy spectrum. For both of the two values V_1 and V_2, we scan from $0E_{\mathrm{r}}$ to $6E_{\mathrm{r}}$, with resolution of $0.25E_{\mathrm{r}}$. The results are shown in Fig. 4.24. From the results, we find that when (V_1, V_2) is very small or large, D_{H} are going to unity. The physical interpretation is the following. In the zero potential limit, we find the spectrum of a free particle which is continuous parabola. In the large potential limit, the system is like isolated deep wells with different depth. The eigenenergies are simply the energy of each well. Thus, considering the thermodynamic limit $L \to \infty$, the eigenenergies go through all the values between, roughly, $[-V_1 - V_2, V_1 + V_2]$, and it should also be continuous and leads to $D_{\mathrm{H}} = 1$. In between, a non-monotonic behavior is presented. The minimum seems appearing at the critical potential (black dashed line).

To further check the position of the minimum fractal dimension, we plot two cuts of Fig. 4.24, for the two cases: (i) $V_1 = V_2 = V$, (ii) $V_2 = 10E_{\mathrm{r}}$ and scanning V_1, see Fig. 4.25 (a) and (b) correspondingly. In both cases, we find the fractal dimension tends to unity in the zero and large potential limits. Also, a minimum value of D_{H} is found approximately at the position of V_{c}. Especially, for the case (ii), we find the minimum value $D_{\mathrm{H}} = 0.51 \pm 0.02$, which recovers the prediction of the Aubry-André model in Refs. [189, 190]. Although the

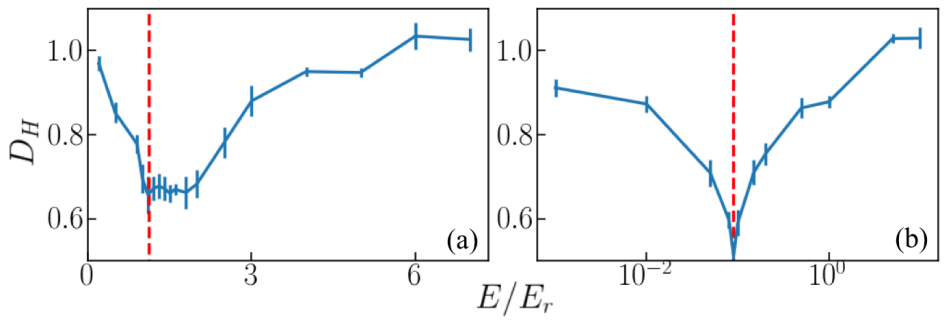

Figure 4.25: Fractal dimension of the energy spectrum for two cases: (i) $V_1 = V_2 = V$, (ii) $V_2 = 10E_\mathrm{r}$ and scanning V_1. The red dashed line is the critical potential calculated in Ref. [86]

physical explanation of the two potential limits is well understood, it is still open that why the minimum value of D_H appears at the critical potential. Also, another open question for this study is how should the fractal dimension varies with the range of spectrum we focus on. This calls for further work to understand it.

Conclusion

In this chapter, we have studied the critical and fractal behavior for single particles in quasiperiodic potentials. Our results shed light on models that have become pivotal for Anderson [181, 182] and many-body [16] localization. We found that the ME is always in a gap and separates localized and extended states, with no intermediate phase. We related this behavior to the fractality of the energy spectrum and found that the Hausdorff dimension is always smaller than unity but nonuniversal. In contrast, we calculated precisely the critical potential V_c and found the critical behaviour $\mathrm{IPR}_0 \sim (V - V_\mathrm{c})^\nu$ with the universal exponent $\nu \simeq 1/3$. These predictions may be confirmed in experiments similar to Ref. [182] using energy-resolved state selection [196–198]. In parallel to further theoretical studies, they may help answer questions our results call. For instance, it would be interesting to determine the physical origin of the critical exponent ν and extend our study to higher dimensions. Another important avenue would be to extend it to interacting models in connection to many-body localization.

Our results may also pave the way to the observation of the still elusive Bose-glass phase. So far ultracold-atom experiments have been performed in the AA limit, the energy scale of which is the tunneling energy J [23]. The latter is exponentially small in the main lattice amplitude and of the order of the temperature. It suppresses coherence, and significantly alters superfluid-insulator transitions [14, 24]. In shallow quasiperiodic potentials, the energy scale is, instead, the recoil energy E_r, which is much higher than the temperature. Temperature effects should thus be negligible. For strong interactions, the 1D Bose gas can be mapped onto an ideal Fermi gas and the Bose-glass transition is directly given by the ME we computed here. It would be interesting to determine how the transition evolves for weak interactions. Therefore, in the next chapter, we move further to the interacting atomic system in quasiperiodic potential at finite temperature, and study its phase transition.

Chapter 5

Lieb-Liniger bosons in a shallow quasiperiodic potential

Based on the study in the last chapter, we now turn to the Lieb-Liniger bosons in a shallow quasiperiodic lattices in presence of a finite interaction and a finite temperature. The main interest for investigating such kinds of systems is the interplay between interactions and disorder, which induces a rich physics. This is at the origin of many intriguing phenomena, including many-body localization [199–203], collective Anderson localization [41, 46–51, 149], and the emergence of new quantum phases. For instance, a compressible insulator, known as the Bose glass (BG) [52–54, 83, 204], may be stabilized against the superfluid (SF) and, in lattice models, against the Mott insulator (MI).

In one-dimensional (1D) systems, it is particularly fascinating for the SF may be destabilized by arbitrary weak perturbations, an example of which is the pinning transition in periodic potentials [3, 13, 15, 72, 205]. Similarly, above an interaction threshold, the BG transition can be induced by arbitrary weak disorder [52, 53]. The phase diagram of 1D disordered bosons has been extensively studied and is now well characterized theoretically [22, 83, 84, 204, 206, 207]. The experimental observation of the BG phase remains, however, elusive [20, 168, 208–211], despite recent progress using ultracold atoms in the tight-binding quasiperiodic potentials [14, 24].

Controlled quasiperiodic potentials, as realized in ultracold atom [153, 163, 212] and photonic [160,161,213,214] systems, have long been recognized as a promising alternative to observe the BG phase. So far, however, this problem has been considered only in the tight-binding limit, known as the Aubry-André model [23, 164, 165, 192, 215]. It sets the energy scale to the tunneling energy, which is exponentially small in the main lattice amplitude and of the order of magnitude of the temperature in typical experiments. The phase coherence is then strongly reduced, which significantly alters the phase diagram. Although such systems give some evidence of a Bose glass phase [14, 24], they require a heavy heuristic analysis of the data to factor out the very important effects of the temperature. Thus, we propose to overcome this issue by using shallow quasiperiodic potentials. The energy scale would then be the recoil energy, which is much larger than typical temperatures in ultracold-atom experiments [1, 212]. This, however, raises the fundamental question of whether a BG phase can be stabilized in this regime: In the hard-core limit, interacting bosons map onto free fermions [40] (see detail discussion in Chapter 1). A band of localized (resp. extended) single particles then maps onto the BG (resp. SF) phase while a band gap maps onto the MI phase. In the shallow bichromatic lattice, however, we have shown that band gaps, i.e. MI phases, are dense [86] and the BG would thus be singular, see detailed discussions about the fractality of the single-particle spectrum in Section 4.3. On the other hand, decreasing the interactions down to the meanfield regime favors the SF phase [22, 52, 53, 216]. Hence, a BG can only be stabilized, if at all, for intermediate

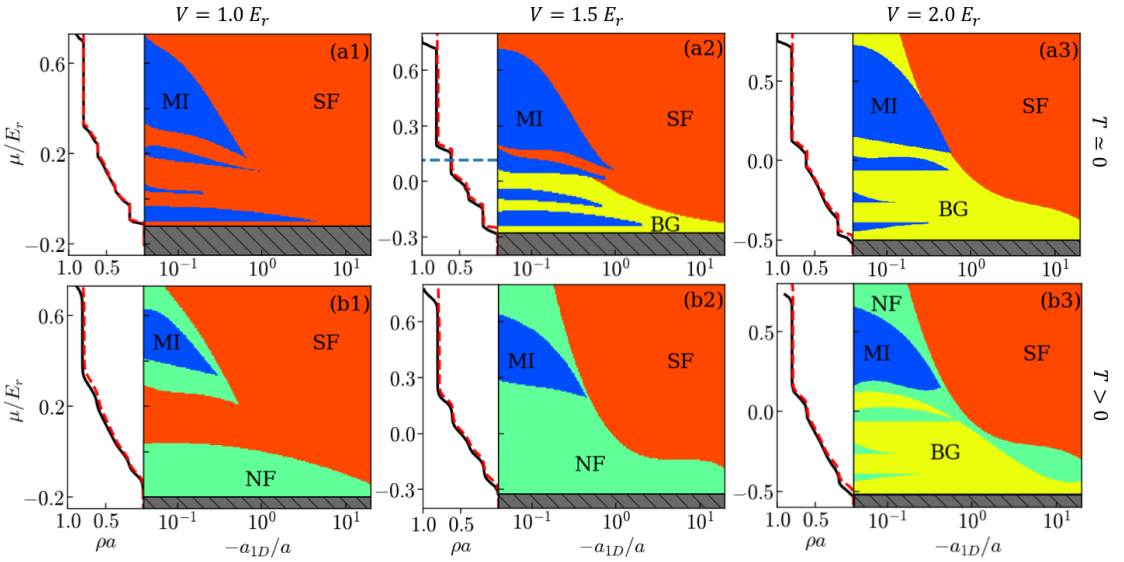

Figure 5.1: Phase diagrams of Lieb-Liniger bosons in a shallow quasiperiodic potential for increasing values of the potential ($V = E_\mathrm{r} < V_\mathrm{c}$, $V = 1.5E_\mathrm{r} \gtrsim V_\mathrm{c}$, and $V = 2E_\mathrm{r} > V_\mathrm{c}$ from left to right). Upper row: Quantum phase diagrams as found from QMC calculations at a vanishingly small temperature [$k_\mathrm{B}T = 10^{-3}E_\mathrm{r}$ for (a1) and $k_\mathrm{B}T = 2 \times 10^{-3}E_\mathrm{r}$ for (a2) and (a3)]. Lower row: Counterpart of the upper row at the finite temperature $k_\mathrm{B}T = 0.015E_\mathrm{r}$. There, the "SF", "MI", and "BG" regimes are defined as those that retain the zero-temperature properties of the corresponding phases. The normal fluid (NF) corresponds to points where significant temperature effects are found. On the left of each panel, we show the equation of state $\rho(\mu)$ at strong interactions, $-a_{1\mathrm{D}}/a = 0.05$ (solid black line) together with that of free fermions at the corresponding temperatures (dashed red line). Note that the smallest band gaps are smoothed out by the finite temperatures. The dotted blue line visible on panel (a2) shows the single-particle ME at $V = 1.5E_\mathrm{r}$, $E_\mathrm{c} \simeq 0.115E_\mathrm{r}$.

interactions.

In this chapter, we tackle this issue using exact quantum Monte Carlo calculations [217]. Firstly, we briefly review the previous studies of the BG transition in the disordered system as well as the Aubry-André model. Then, we move to the computation of the exact phase diagram of interacting bosons in a shallow 1D bichromatic lattice. Our main results are summarized on Fig. 5.1 and we will give detailed discussion for it in Section 5.2. We shall see that a BG phase can be stabilized at intermediate interaction for a quasiperiodic potential above a critical threshold. Finally, we will study the finite temperature effect and we shall show that the BG phase is robust to the thermal fluctuations up to temperatures accessible to present-day experiments.

5.1 The Bose glass phase

Before addressing the problem of the phase diagram for 1D shallow quasiperiodic systems, we briefly review previous work and basic knowledge about the Bose glass. We start with the first waves of demonstration for Bose glass phase in purely disordered systems [52–54]. Then, we talk about the Bose glass physics in the Aubry-André model [23,164,165,192,215], and its experimental achievements [14, 20, 24].

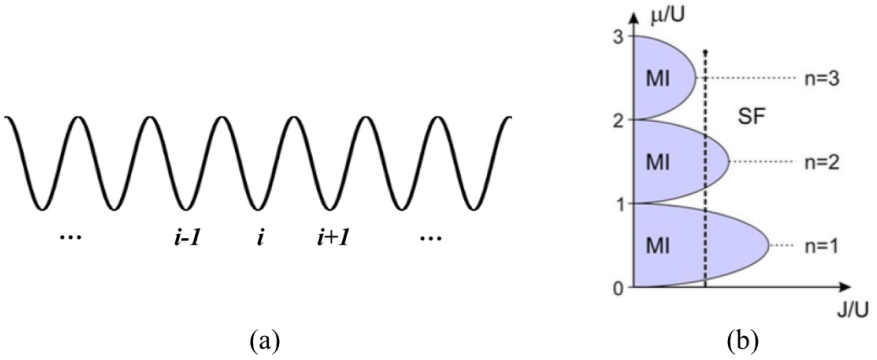

Figure 5.2: The Bose-Hubbard model. (a). The illustration of its potential. (b). The phase diagram.

5.1.1 Bose glass phase in random potentials

The first work on the Bose glass is in Refs. [52, 53]. It is specific to one dimensional continuous systems in the presence of disorder and use renormalization group analysis within Luttinger liquid approach. Then, in Ref. [54], M. P. A. Fisher et al consider the disordered Bose-Hubbard model. For 1D bosons in continuum, it is in superfluid phase at zero temperature. In presence of a disordered potential, however, a Bose glass phase may appear against the SF phase when the disorder is large enough. On the one hand, it is localized thanks to the disorder. On the other hand, adding one particle only cost a small amount of energy, i.e. it is compressible. Therefore, with the competition between disorder and interaction, the BG phase can be stabilized against SF in certain regimes. Moving to the lattice system, the argument is similar, except that the BG phase appears in between the Mott insultor and superfluid. In the following, we present the introduction of the Bose glass phase in disordered lattice model following the statement in Ref. [54], the main idea of which is the minimization of energy for Bose-Hubbard model. One may notice that an equivalent statement is illustrated in Ref. [53] from the renormalization group aspect.

The Bose-Hubbard model

We start with the Bose-Hubbard model which is created by an external periodic lattice potential, shown in Fig. 5.2.(a). In this case, we expect Mott insulator lobes in strongly-interacting regime which turns into superfluid phase while interaction decreases, as discussed in section 1.3. In this case, the Hamiltonian writes

$$\hat{H} = -J\sum_{i,j}\hat{a}_i^\dagger\hat{a}_j + \frac{U}{2}\sum_i \hat{n}_i(\hat{n}_i - 1) - \mu\sum_i \hat{n}_i \tag{5.1}$$

with J the tunneling, U the on-site interaction and μ the chemical potential. To obtain the quantum phase diagram at zero temperature, one should minimize the total energy. Equivalently, thanks to the periodicity, we simply minimize the on-site energy on each lattice sites. We first consider the atomic limit $J = 0$. Then, the on-site energy of lattice site i writes

$$e_i = \frac{1}{2}Un_i(n_i - 1) - \mu n_i, \tag{5.2}$$

which is a parabolic function of n_i. Thus, for a certain μ in the range $U(n-1) < \mu < Un$ with n a certain integer, taking $n_i = n$ will minimize the energy e_i. Equivalently, it means the system has a fixed integer fillings in each lattice sites, which forms the incompressible Mott-insulator phase.

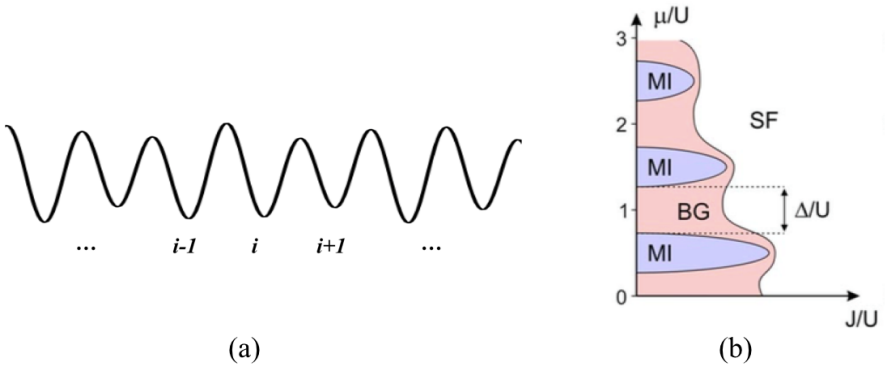

Figure 5.3: The Bose-Hubbard model with on-site disorder. (a). The illustration of its potential. (b). The phase diagram.

Now, we take a finite tunneling parameter $J > 0$. It is important to introduce two typical energies,

$$\delta E_p \sim (\frac{1}{2} - \alpha)U,\ \delta E_h \sim (\frac{1}{2} + \alpha)U \tag{5.3}$$

which are the energies required to add or remove one particle from the system. Let's consider starting from a point in the $\mu - J$ plane with n particle on each site. Allowing one particle to hop from one site to its neighbour will gain approximately J in kinetic energy with the expense of $\delta E_{ph} = \delta E_p + \delta E_h$ in the interaction energy. Thus, when J is small enough compared to the scale of δE_{ph}, the system will remain in the Mott insulator phase with filling n. For each fixed μ, when J is large enough compared to δE_{ph} and above a critical value $(J/U)_c$, the filling $n_i = n$ doesn't give the minimal energy any more. Each particle are delocalized on the full system and thus it forms a compressible and extended superfluid phase. Combining the above statements, we shall find the phase diagram in Fig. 5.2.(b).

Bose-Hubbard model with disorder

Now, we add the disorder on top of the Bose-Hubbard model, see Fig. 5.3.(a). With the presence of disorder, a localized but compressible Bose glass phase is expected to appear in between the MI and SF phase. Here, the Hamiltonian shall write

$$\hat{H} = -J\sum_{i,j}\hat{a}_i^\dagger\hat{a}_j + \frac{U}{2}\sum_i \hat{n}_i(\hat{n}_i - 1) - \sum_i(\mu_i + \delta\mu_i)\hat{n}_i \tag{5.4}$$

with $\delta\mu_i$ the on-site disorder. It's a random number following the uniform distribution between $[-\Delta, \Delta]$. Hence, in the atomic limit, the on-site energy of lattice site i should become

$$e_i = \frac{1}{2}Un_i(n_i - 1) - (\mu + \delta\mu_i)n_i. \tag{5.5}$$

We assume the disorder term Δ is smaller than the interaction term U. Starting with $J = 0$, for minimizing the on-site energy, there are three possibilities. They yield:

- For $n - 1 < \mu/U < n - 1 + \Delta$, the on-site energy might be minimized by either $n_i = n - 1$ or $n_i = n$.
- For $n - 1 + \Delta < \mu/U < n - \Delta$, the on-site energy will be minimized by $n_i = n$.
- For $n - \Delta < \mu/U < n$, the on-site energy might be minimized by either $n_i = n$ or $n_i = n + 1$.

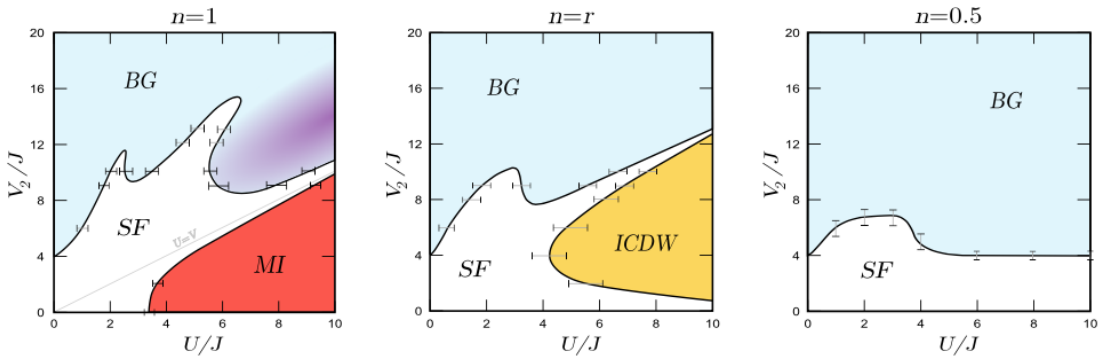

Figure 5.4: The phase diagram for bichromatic Bose-Hubbard model shown in Ref. [23]. The diagrams are shown as a function of the interaction U and quasiperiodic potential amplitude V_2, in the unit of the hopping J. The indicated phases are Bose glass (BG), superfluid (SF), Mott insulator (MI) and incommensurate charge density wave (ICDW). The three plots corresponds to three particle densities: (a). $n = 1$, (b). $n = r$, (c) $n = 0.5$. For the case $n = 1$, the darker region indicates there could be small gaps which cannot be resolved by the calculation.

For the second case above, all the lattice sites have the same integer filling $n_i = n$, and it thus forms a Mott insulator phase. The width of the Mott insulator lobe writes $\Delta\mu = U - 2\Delta$. However, for the first and third cases, different lattice sites might be minimized by different values of the filling. Thusr, the many-body state is localized globally and the average filling is not an integral. Thus, it is neither a Mott insulator nor a superfluid. It is a compressible insultator phase with fractional fillings, which we called Bose glass. Then, for $J > 0$, similar as the periodic system case, when $J \ll U$, it's insufficient to overcome the repulsive on-site potential and allow extra particles to hop in the system. Then, for each fixed μ, the system go through a transition to the superfluid phase when J is sufficiently large. Moreover, even for the BG phase, the finite tunneling enables the particles to hop between different sites and enhances the coherence of the system. Above a certain value $(J/U)_c$, the system becomes extended and it turns to the superfluid phase. Therefore, the phase diagram should look like Fig. 5.3.(b). Moreover, when the disorder is large enough $\Delta > 2U$, the Mott lobe are totally eliminated and there should only remain the BG and SF phases in the phase diagram.

5.1.2 Bose glass phase in quasiperiodic Bose-Hubbard model

In this part, we shall introduce the known work of Bose glass physics in quasiperiodic systems. All the following work is done in the tight-binding limit, i.e. the Aubry-André model, and it contains research both theoretically and experimentally.

Theoretical prediction of the phase diagram

The system we consider now is a Lieb-Liniger gas, i.e. a 1D N-bosons gas with repulsive contact interactions, subjected to a quasiperiodic potential $V(x)$. We recall the Hamiltonian writes

$$\mathcal{H} = \sum_{1\leq j\leq N} \Big[-\frac{\hbar^2}{2m}\frac{\partial^2}{\partial x_j^2} + V(x_j)\Big] + g\sum_{j<\ell}\delta(x_j - x_\ell), \tag{5.6}$$

where m is the particle mass, x is the space coordinate, and $g = -2\hbar^2/ma_{1D}$ is the interaction strength with $a_{1D} < 0$ the 1D scattering length. The quasiperiodic potential

writes

$$V(x) = V_1 \cos^2(k_1 x) + V_2 \cos^2(k_2 x + \varphi). \tag{5.7}$$

where the spatial frequencies k_1 and k_2 are incommensurate. The corresponding recoil energy is defined as $E_{rj} = \hbar^2 k_j^2/2m$ with $j = 1, 2$.

Now, we introduce the theoretical outcome from Ref. [23] for the tight-binding limit, which is named as bichromatic Bose-Hubbard model. The considered situation satisfies the condition

$$V_1 \gg V_2, E_{r1}, E_{r2}. \tag{5.8}$$

It is similar as the one for the non-interacting Aubry-André model. On the one hand, the potential V_1 is much larger than the recoil energy, the system is thus in the tight-binding limit and can be treated as discretized. On the other hand, the second lattice V_2 is much smaller than the first one, which can be treated as a pertubation. Following the derivation in Ref. [23], one can recover the discrete version of the tight-binding Hamiltonian, which yields

$$\mathcal{H} = -J \sum_j [b_{j+1}^\dagger b_j + \text{h.c.}] + U \sum_j n_j(n_j - 1)/2 + \frac{V_2}{2} \sum_j [1 + \cos(2r\pi j + 2\phi)] n_j \tag{5.9}$$

with $b_j^\dagger$ the creation operator of bosons and $n_j = b_j^\dagger b_j$ the local particle number operator. The hopping term J and interaction term U follows the same definition as in the non-interacting Aubry-André model, see section 4.1.

With Density Matrix Renormalization Group (DMRG) calculations, one can calculate the phase diagram at finite interactions and zero temperature. In Fig. 5.4, they show the phase diagrams of three typical cases. In each plot, they show the result for a fixed density n at different interaction U and disorder V_2, rescaled by the hopping J. For obtaining the phase, the numerics are performed to calculate five quantities, namely the one-body correlation length ξ (see detailed definition in later discussion), the one-particle gap Δ_c, the condensate fraction f_c, the superfluid density ρ_s and the Luttinger parameter K. The verification of the different phases are identified as follows.

Phase	ξ	Δ_c	f_c	ρ_s	K
SF	$\simeq L$	$= 0$	$\gg 0$	> 0	> 0
MI	$\ll L$	> 0	$\gtrsim 0$	$= 0$	$= 0$
BG	$\ll L$	$= 0$	$\gtrsim 0$	$= 0$	$= 0$
ICWD	$\ll L$	> 0	$\gtrsim 0$	$= 0$	$= 0$

Table 5.1: Identification of the quantum phases from the DMRG calculations.

Here, from the first two columns of Table. 5.1, we can see that the first three phases can be distinguished by the correlation length ξ and the one-particle gap Δ. The correlation function is algebraic decaying in the SF phase and ξ is thus infinite. For a finite size system of size L, we would thus have $\xi \sim L$, For the other phases, the correlation function decays exponentially and ξ is finite and smaller than L. Then, the MI and ICWD phase are gapped insulator with finite Δ while the SF and BG are gapless. For further distinguishing the MI and ICWD, one should look at the particle filling n. It's an integer for MI and fractional number for ICWD. The other three columns in Table. 5.1, give redundant information. On the one hand, they can be used as a double check for the different phases. On the other hand, they all have specific physical meanings which describes one aspect of features for the system.

In Fig. 5.5, we show the calculated results for these quantities for the case $n = 1$, with the quantity equals to zero (finite value) while the color of the region is black (non black

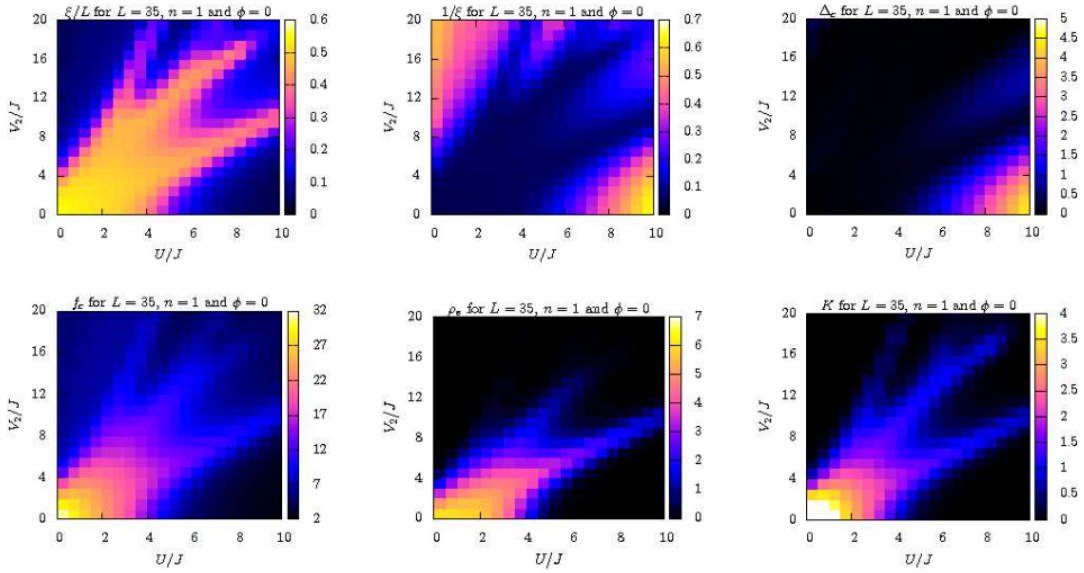

Figure 5.5: In the Bose-Hubbard-Aubry-André model, numerical results for the phase diagram $n = 1$ shown in Ref. [23]. The results come from the DMRG calculations with system size $L = 35$. They present the value of the correlation length ξ, the inverse of correlation length $1/\xi$, the one-particle gap Δ, the condensate fraction f_c, the superfluid density ρ_s and the Luttinger parameter K, correspondingly.

colors). With this result, one can recover the phase diagrams in Fig. 5.4 for $n = 1$. The other two cases are also obtained in the similar way.

Now, we turn to the discussion of the detailed phase diagram. For the case $n = 1$, three phases appear. At low enough interaction and disorder, the system is superfluid. Then, when the interaction becomes large enough, it starts to be Mott insulator with one particle on each sites. This phase transition comes from the fact that the interaction is competing with the hopping process. When the repulsive interaction is strong enough, it localizes the particles and the system becomes an insulator. On the other hand, when increasing the disorder amplitude, it also competes with the on-site interaction. When V_2 is large enough, the Bose glass phase, which is a gapless insulating phase, appears. The origin of the localization of the Bose glass phase comes from the external disorder potential, different from the Mott insulator which is localized due to the gapped spectrum formed by the repulsive interactions. Then, moving to the case $n = r$, we still find the SF and BG phases similarly. However, since the particle density is non integer but the lattice spacing ratio r, we find a Mott insulator phase with incommensurate fillings, which is named as incommensurate charge density wave by the authors. Finally, for the cases $n = 0.5$, because the density is neither an integer nor a linear combination of 1 and r, only the BG and SF phases appear in the phase diagram, at strong and weak disorder, correspondingly.

Another interesting result from the work Ref. [23] is the equation of state for hard-core bosons at different strength of disorder. First, one can calculate the single-particle spectrum with exact diagonalization similar as Chapter 4. Then, the equation of state in the hard-core limit can be computed using the Bose-Fermi mapping [40]. In Fig. 5.6, the authors show the equation of state for increasing values of V_2. As soon as the disorder V_2 is turned on, small gaps are open at relevant fillings of r, namely $n = r, 1 - r, 2r - 1...$, thanks to the beating of the two incommensurate lattices. By increasing the disorder, the plateaus increase and become more and more significant. Those mini-gaps corresponds

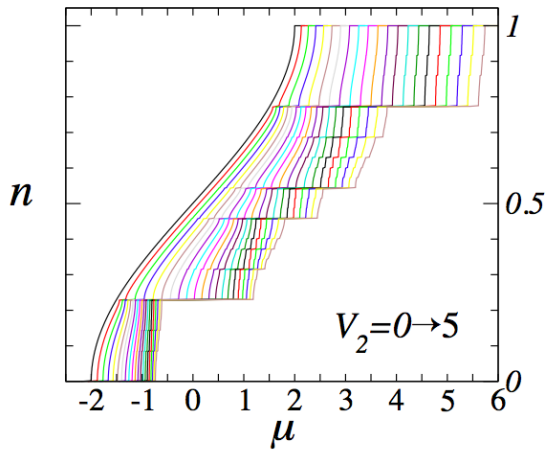

Figure 5.6: In the Bose-Hubbard-Aubry-André model, the equation of state $n(\mu)$ in the hard-core limit for increasing order of V_2 with step of $J/4$, from Ref. [23].

to the ICDW phases with incommensurate fillings. This also fits with the fractal energy spectrum for quasiperiodic systems as we described in Chapter 4.

The experimental observation

In Refs. [14], an experimental observation of the Bose glass phase transition is presented. For obtaining the Hamiltonian Eq. (5.6), C. D'Errico et al builds an experimental setup shown as Fig. 5.7. First of all, they prepare a 3D BEC with ^{39}K atoms. With the two laser pairs on the horizontal line, the system is cut into a 2D array of 1D tubes. Then, on the vertical line, a quasiperiodic potential is formed by superimposing two incommensurate optical lattices, with wave lengths $\lambda_1 = 1064nm$ and $\lambda_2 = 856nm$. Since $\lambda_1/\lambda_2 = 1.243...$ is far from a simple fraction, it mimics the potential with an incommensurate ratio of the two lattice spacings. The strength of the main lattice is $V_1/E_r = 9$ and the disorder parameter Δ is controlled by varying the amplitude of the second lattice. The degeneracy temperature of the system is $k_B T = 8J$. The typical experimental temperature is around $k_B T = 3J$, thus the gas reaches the quantum degeneracy.

By varying the amplitudes of the two lattices, one can control the two parameters of

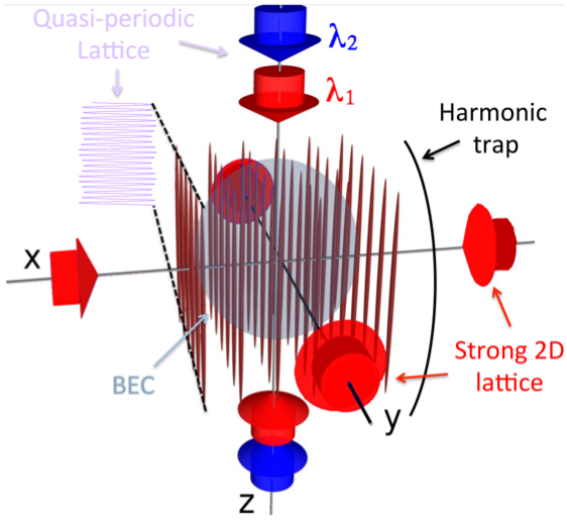

Figure 5.7: The experimental setup of Ref. [14] for producing the Hamiltonian Eq. 5.6.

the phase diagram, the interaction U/J and disorder Δ/J. By absorption imaging after a time-of-flight, one obtains the momentum distribution. A first indication of the phase can be captured by the root-mean-square width Γ of the momentum distribution $P(k)$, shown in Fig. 5.8. Here, we recall that in section 2.3.4, we have shown that the momentum distribution $P(k)$ is the Fourier transform of the one-body correlation function $g_1(x)$. It yields the relation between their widths $\Gamma \sim 1/\xi$. Therefore, for the insulating BG and MI phases, Γ is large since the correlation length is finite and small. On the contrary, there is no well-defined ξ in the SF phase since the g_1 function follows algebraic decay. Equivalently, it means the effective ξ is extremely large and Γ is extremely small.

To further distinguish the MI and BG phases, they take advantage of the lattice modulation spectroscopy [218]. In Fig. 5.9, they show the excitation spectra for fixed interaction $U = 26J$ and three different disorder strength from (a) to (c). When there is no disorder, we only find absorption peaks for the MI at $h\nu = jU$ with ν the modulation frequency and j some integers. Here, one may notice that U is the gap of the MI phase. When $h\nu = jU$, the system can be excited and an absorption of energy is shown in the spectroscopy. In Fig. 5.9.(a), we see the two MI peaks with $j = 1$ and $j = 2$. For $j = 1$, it corresponds to the excitations within the individual MI domains with fillings $n = 1, 2, 3$. For $j = 2$, it is due to the excitations between different MI domains [219]. By increasing the disorder, a BG phase suddenly appears and it creates another peak at $h\nu' \simeq \Delta < U$, see Fig. 5.9.(b) and (c). Here, the term Δ is the disorder amplitude with the similar definition as Eq. (4.5). This absorption peak cannot be correlated with the MI phase. In turn, it is the expected behavior of a strongly correlated BG phase which can be mapped onto a fermionic insulator, see detail discussions in Ref. [220]. Using the Bose-Fermi mapping, we can compute the absorption spectrum following the derivation of Ref. [220] and find the theoretical prediction for the BG behavior. In Fig. 5.9.(d), we zoom on the BG peak and find the data points fit well with the theoretical prediction(red solid line) calculated from the method in Ref. [220].

Later, in Ref. [24], L. Gori check the phases in Fig. 5.8. more carefully with numerics and study the diagram more in detail. They perform a DMRG calculation for the considered regimes in Fig. 5.8, taking into account the finite temperature effect and the presence of a harmonic trap. With the T=0 DMRG results, they manage to clarify the different

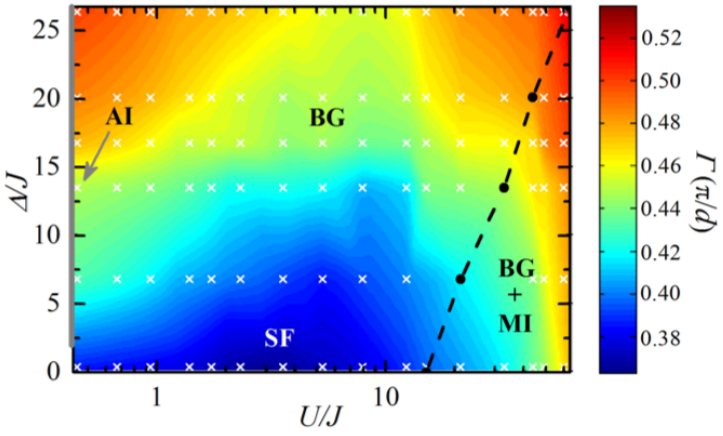

Figure 5.8: Measured root-mean-square width Γ of the momentum distribution $P(k)$ in the phase diagram of Fig. 5.7. There are mainly three phases: superfluid (SF), Mott insulator (MI) and Bose glass (BG). In the weakly-interacting limit, one also find the Anderson localization phase (AL). The plot is from Ref. [14].

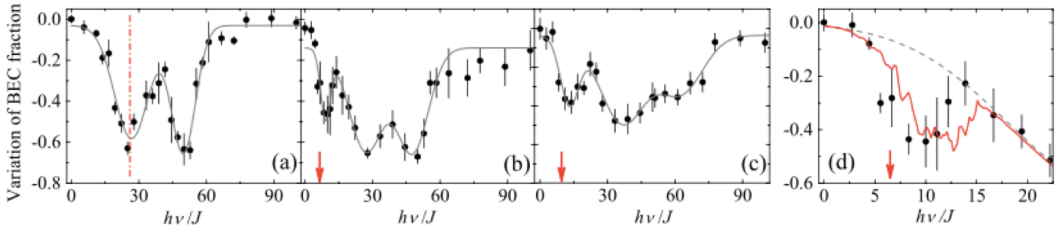

Figure 5.9: Excitation spectrum for three points of the phase diagram: the interaction strength $U = 26J$ and disorder (a). $\Delta = 0J$. (b). $\Delta = 6.5J$. (c). $\Delta = 9.5J$. The plot is from Ref. [14].

expected phases in Fig. 5.8, noted by the texted phase name. Along the zero interaction $U = 0$ line, one find the transition from SF phase to Anderson localization by increasing Δ. On the other limit $\Delta = 0$, we see the SF to MI transition by increasing the interaction U. For a fixed and not so strong interaction, one always finds the SF-BG transition by increasing Δ. Finally, at low disorder and strong interactions, one find a mixture of MI and BG phase, thanks to the presence of the harmonic trap.

Beyond the zero-temperature calculations, L. Gori et al perform further the finite-T phenomenological approaches based on $T = 0$DMRG calculations of the momentum distribution $P(k)$, see Fig. 5.10. For the aspect of the temperature effect, they calculate first $T = 0$ DMRG results of $P(k)$ and get its Fourrier transform, i.e. the one-body correlation length $g_{i,j}(T)$ at the distance $|i - j|$ and temperature T. Then, they propose a phenomenological ansatz where they introduce the modified correlations

$$\tilde{g}_{i,j}(T) = Ce^{-|i-j|/\xi_T} g_{i,j}(T = 0) \tag{5.10}$$

with $\tilde{g}_{i,j}(T)$ the finite temperature correlation function, ξ_T the effective thermal correlation length and C the normalization factor. Fitting the experimental data with Eq. (5.10), one can get the information for the thermal effect on the correlation length. Four typical examples of the momentum distribution $P(k)$ are shown as the small subplots on the left and right sides. The different curves are the zero-T DMRG results (black solid lines),

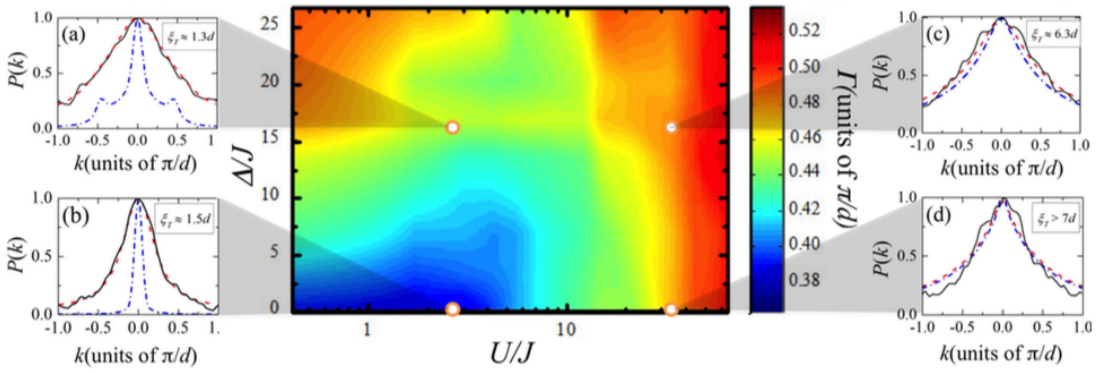

Figure 5.10: The $U - \Delta$ diagram for the momentum width Γ from finite-T DMRG calculations. The detailed plots of the momentum distribution $P(k)$ are shown for four typical points. The different curves are the zero-T DMRG results (black solid lines), experimental data (blue dash-dotted lines) and fit of finite-T phenomenological ansatz(red dashed lines). The plot is from Ref. [24].

finite-T phenomenological fit (red dashed lines) and experimental data (blue dash-dotted lines). Although the finite temperature results are similar as the zero-temperature case for the two points in the strongly-interacting regime, there is clearly a thermal broadening for the correlation length in the intermediate interaction regime. These results suggest that the measurements are strongly altered by the finite temperature effects. Therefore, in the next section, we will study the Bose glass phase transition in shallow quasiperiodic potentials, where the temperature effect is significantly reduced.

5.2 The phase diagram for the shallow quasiperiodic systems

Now, we turn to full continuous study of the phase diagram for shallow quasiperiodic systems. Instead of the deep lattice limit, now we turn to the shallow lattice case, i.e. we come back to the Hamiltonian Eq. (5.9). In particular, we are interested in the regime where the quasiperiodic potential is on the same scale of the recoil energy E_{r} and is bichromatic with equal amplitudes, i.e.

$$V(x) = \frac{V}{2}\big[\cos(2k_1 x) + \cos(2k_2 x + \varphi)\big]. \tag{5.11}$$

where the spatial frequencies k_1 and k_2 are incommensurate. In the following calculations, we will use the spatial period of the first lattice, $a = \pi/k_1$, and the corresponding recoil energy, $E_{\mathrm{r}} = \hbar^2 k_1^2/2m$, as the space and energy units, respectively.

We firstly start with the single-particle problem, i.e. $g = 0$ for Eq. (5.9). In Chapter 4, we have studied in detail the single-particle problem for the case $r = k_2/k_1 = (\sqrt{5}-1)/2$. As shown in Ref. [176], both the critical potential V_{c} and mobility edge E_{c} strongly depend on the incommensurate ratio r. In this chapter, we use the incommensurate ratio close to the experimental value of Refs. [14, 24], it yields

$$r = \frac{\lambda_1}{\lambda_2} = \frac{856\mathrm{nm}}{1064\mathrm{nm}} \simeq \frac{67}{83} \simeq 0.807. \tag{5.12}$$

Thus, we repeat the similar calculation for single-particle problem with a different value of $r = 0.807$ to provide a basis for the further study in this chapter.

Here, we recall that the main procedure is to determine the single-particle eigenstates by using exact diagonalization and computing the inverse participation ratio (IPR),

$$\mathrm{IPR}_n = \frac{\int dx\, |\Psi_n(x)|^4}{\left(\int dx\, |\Psi_n(x)|^2\right)^2}, \tag{5.13}$$

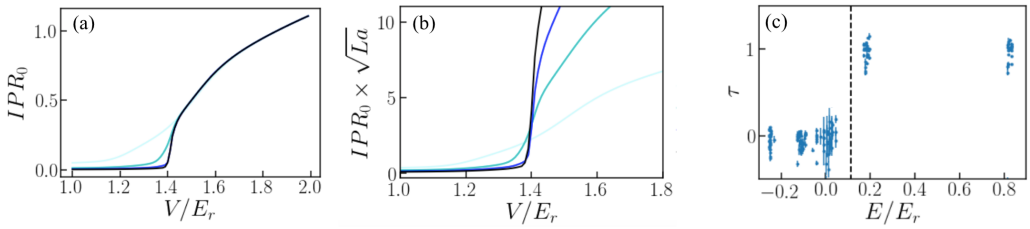

Figure 5.11: Critical potential and mobility edge for the single-particle problem in the shallow bichromatic lattice with $r \simeq 0.807$. (a) Ground-state IPR versus the quasiperiodic amplitude V for various system sizes. Darker lines correspond to increasing system sizes, $L/a = 50$ (light blue), 200 (blue), 500 (dark blue), and 1000 (black). (b) Rescaled IPR of the ground state, $\mathrm{IPR}_0 \times \sqrt{La}$ using the same data as in panel (a). (c) Scaling exponent τ of the IPR as a function of eigenenergy E for the quasiperiodic amplitude $V = 1.5E_{\mathrm{r}}$. It is computed for a system size varying from $L/a = 200$ to 2000.

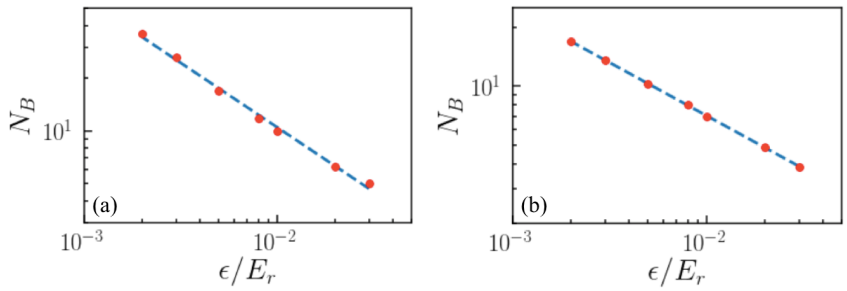

Figure 5.12: Fractal behaviour of the energy spectrum for single particles in the shallow bichromatic lattice. Shown are plots of the energy-box counting number $N_{\rm B}$ as a function of energy resolution ϵ, for two amplitudes of the bichromatic potential: (a) $V = 1E_{\rm r}$ and (b) $V = 1.5E_{\rm r}$. In both cases, the considered energy ranges $[E_1, E_2]$ are the same as those of the chemical potential μ on Fig. 5.1.

where Ψ_n is the n-th eigenstate. By computing the IPR of the ground state ($n = 0$) versus the quasiperiodic amplitude V for various system lengths L, we can determine the critical amplitude $V_{\rm c}$ for localization in the bichromatic lattice, see Fig. 5.11(a). As in section 4.2.1, we plot the rescaled IPR, $\mathrm{IPR}_0 \times \sqrt{La}$ for various system lengths L, see Fig. 5.11(b). Then, we can find the accurate value of the critical potential which yields

$$V_{\rm c}/E_{\rm r} \simeq 1.375 \pm 0.008. \tag{5.14}$$

Here, we should notice that we find a different value compared to that of Eq. (4.8) since we are using a different value of r. Based on this value, we choose three typical potential amplitudes in the later calculation of the many-body problem: $V = 1.0E_{\rm r} < V_{\rm c}$, $V = 1.5E_{\rm r} \gtrsim V_{\rm c}$ and $V = 2.0E_{\rm r} > V_{\rm c}$, see Fig. 5.1.

For the two cases $V > V_{\rm c}$ which are relevant to the many-body phase diagram in Fig. 5.1, i.e. $V = 1.5E_{\rm r} \gtrsim V_{\rm c}$ and $V = 2.0E_{\rm r} > V_{\rm c}$, we further compute the energy $E_{\rm c}$ of the ME in the single-particle spectrum. As in section 4.2.1, we fit the scaling IPR $\sim L^{-\tau}$ and plot τ as a function of the eigenenergy E. The case $V = 1.5E_{\rm r}$ is shown in Fig. 5.11(c), where we find the ME at the black dashed line. For $V = 1.5E_{\rm r}$ and $V = 2E_{\rm r}$, we find $E_{\rm c} \simeq 0.115E_{\rm r}$ and $E_{\rm c} \simeq 1.2E_{\rm r}$, respectively.

Also, we compute the fractal dimension for the single-particle spectrum for the case $V = 1.0E_{\rm r} < V_{\rm c}$ and $V = 1.5E_{\rm r} > V_{\rm c}$, which is relevant to the discussion in section 5.3. Here, we recall the definitions of the box counting number and the associated Hausdorff dimension introduced in Chapter 4. The energy-box counting number within the energy range $[E_1, E_2]$ is the quantity

$$N_{\rm B}(\epsilon) = \lim_{q \to 0_+} \int_{E_1}^{E_2} \frac{dE}{\epsilon} \left[n_\epsilon(E)\right]^q, \tag{5.15}$$

where $n_\epsilon(E)$ is the integrated density of states (IDOS) per unit lattice spacing. For a fractal spectrum, it scales as $N_{\rm B} \sim \epsilon^{-D_{\rm H}}$, where $D_{\rm H}$ the spectral Hausdorff dimension. In Fig. 5.12, we plot N_B versus ϵ for the two relevant values of the quasiperiodic amplitude, namely $V = E_{\rm r}$ and $V = 1.5E_{\rm r}$. The energy ranges considered here are the same as those of the chemical potential μ on the phase diagrams, see Fig. 5.1. Fitting the latter to the numerical data, we find $D_{\rm H} = 0.74 \pm 0.03$ for $V = E_{\rm r}$ and $D_{\rm H} = 0.54 \pm 0.01$ for $V = 1.5E_{\rm r}$.

5.2.1 Quantum Monte Carlo calculations for the determination of the phase

Now, we turn to the interacting Lieb-Liniger gas. At zero temperature, we expect three possible phases: the MI (incompressible insulator), the SF (compressible superfluid), and

the BG (compressible insulator). They can be identified through the values of only two quantities, namely the compressibility κ and the superfluid fraction f_{s}. Accurate values of both are found using large-scale, path-integral quantum Monte Carlo (QMC) calculations in continuous space using the worm algorithm implementation [58,59] as introduced in Chapter 2. The calculation is performed within the grand-canonical ensemble at the chemical potential μ and the temperature T. We span a large number of boson configurations within both the physical Z-sector (closed worldlines) and the unphysical G-sector (worms, i.e. worldlines with open ends). The average number of particles N is found from the statistics of worldlines within the Z-sector. It yields the particle density $\rho = N/L$, where L is the system size, and the compressibility $\kappa = \partial\rho/\partial\mu$. One can find details in the section 2.3.1. For the superfluid fraction $f_{\mathrm{s}} = \Upsilon_{\mathrm{s}}/\rho$, it can be found from the the superfluid stiffness Υ_{s} using the winding number estimator, as introduced in section 2.3.2. The calculation of these three quantities allows us to discriminate the 3 phases at zero temperature and most of them at finite temperature except BG and NF.

For distinguishing the BG and NF phases at finite temperature, we need to further calculate the one-body correlation function $g_1(x)$ at different temperatures. While ξ remains unchanged versus temperature for BG phase, it strongly depends on T for the thermal NF phase. Detailed discussion on this point can be found in section 5.3.1. We recall the definition of the one-body correlation function,

$$g_1(x) = \int \frac{dx'}{L} \langle \Psi(x'+x)^\dagger \Psi(x') \rangle, \tag{5.16}$$

where $\Psi(x)$ is the Bose field operator. In the QMC calculations, it is computed from the statistics of worms with open ends at x' and $x'+x$ within the G-sector, see section 2.3.4 for details. For insulating phases (i.e. MI, BG and NF phases), it behaves as

$$g_1(x) \sim \exp\left(-\frac{|x|}{\xi}\right) \tag{5.17}$$

where ξ is the correlation length. Fitting the function $g_1(x) \sim \exp(-|x|/\xi)$ and obtaining the parameter ξ, we can distinguish the BG from NF regimes via the temperature dependence (see details in Section 5.3.1). To make a short conclusion, the detailed properties of each phase can be found in Table 5.2.

Phase	SF fraction f_s	Compressibility κ	T-dep. of corr. length $\partial\xi/\partial T$
Superfluid (SF)	$\neq 0$	$\neq 0$	/
Mott-insulator (MI)	$= 0$	$= 0$	~ 0
Bose-glass (BG)	$= 0$	$\neq 0$	~ 0
Normal fluid (NF)	$= 0$	$\neq 0$	$\neq 0$

Table 5.2: Identification of the (zero-temperature) quantum phases and finite-temperature regimes from quantum Monte Carlo calculations. Note that the one-body correlation function $g_1(x)$ is algebraic in the superfluid regime and the correlation length $\xi(T)$ is not defined.

Figure 5.13 shows typical results for the particle density ρ, the compressibility κ, and the superfluid fraction f_{s}. The six panels correspond to cuts of the six diagrams of Fig. 5.1 at the interaction strength $-a_{1\mathrm{D}}/a = 0.1$.

Figure 5.13(a1): We consider first the case $V = E_{\mathrm{r}}$,i.e. below the critical potential and zero temperature $T = 0$. In this case, we find an alternation of compressible ($\kappa > 0$) and incompressible ($\kappa = 0$) phases, in exact correspondance with superfluidity: the compressible phases always have a finite superfluid fraction ($f_{\mathrm{s}} > 0$) while the incompressible phases are

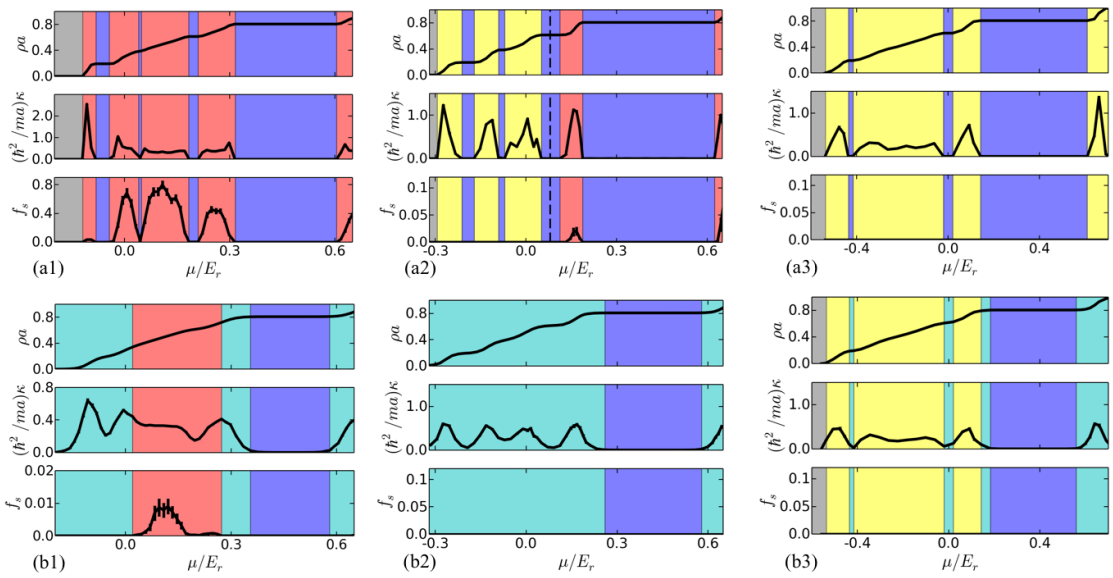

Figure 5.13: Typical QMC results for the density ρ, the superfluid fraction $f_{\rm s}$, and the compressibility κ as a function of the chemical potential μ. The various panels are cuts of the diagrams of Fig. 5.1 at the interaction strength $-a_{\rm 1D}/a = 0.1$: (a1) $V = E_{\rm r}$ and $k_{\rm B}T/E_{\rm r} = 0.001$, (a2) $V = 1.5E_{\rm r}$ and $k_{\rm B}T/E_{\rm r} = 0.002$ (a3) $V = 2E_{\rm r}$ and $k_{\rm B}T/E_{\rm r} = 0.002$, (b1)-(b3) Same as in panle (a) but at temperature $k_{\rm B}T/E_{\rm r} = 0.015$.

always non-superfluid ($f_{\rm s} = 0$). They correspond to SF (red areas) and MI phases (blue areas), respectively. There is no BG phase existed which is consistent with the fact that the potential amplitude is below the critical potential, $V < V_{\rm c} \simeq 1.38E_{\rm r}$.

Figure 5.13(a2): We consider then the case $V = 1.5E_{\rm r}$,i.e. slightly above the critical potential, and zero temperature $T = 0$. Here we find a similar behaviour for large enough chemical potential, $\mu \gtrsim 0.1E_{\rm r}$. For smaller chemical potentials, however, we find clear signatures of BG phases, corresponding to a compressible insulator ($\kappa > 0$ and $f_{\rm s} = 0$, yellow areas). Here, the BG phases are separated by MI phases ($\kappa = 0$ and $f_{\rm s} = 0$, blue areas). As expected, in the strongly-interacting limit, the BG phase appears only for $\mu < E_{\rm c} \simeq 0.115E_{\rm r}$, i.e. the single-particle mobility edge in Fig. 5.11.(c) (dashed black line).

Figure 5.13(a3) [$V = 2E_r$ even more above the critical potential; $T = 0$]: We consider then the case $V = 2.0E_{\rm r}$,i.e. even more above the critical potential, and zero temperature $T = 0$. In this case, the Bose gas is non-superfluid, $f_{\rm s} = 0$, in the whole range of the chemical potential considered here. It, however, shows an alternance of compressible and incompressible phases, corresponding to BG (yellow areas) and MI (blue areas) phases, respectively. Note that for $V = 2E_{\rm r}$ the single-particle mobility edge is $E_{\rm c} \simeq 1.2E_{\rm r}$, which is beyond the considered range of the chemical potential.

Figure 5.13(b1-b3): Finally, we consider the case of finite temperature $T = 0.015E_{\rm r}$. The lower panel shows the finite-temperature counterpart of the upper panel. The various regimes are characterized by the same criteria as for zero temperature. First, we find regimes with vanishingly small compressibility and superfluid fraction. They correspond to regimes where the zero-temperature MI is unaffected by the finite temperature effects (blue areas, all panels). Second, although superfluidity is absent in the thermodynamic limit, we find compressible regimes with a clear non-zero superfluid fraction in our system of size $L = 83a$ for weak enough quasiperiodic potential (red areas, left panel). We refer to such regimes as finite-size superfluids. We have checked that the one-body correlation

function is, consistently, algebraic over the full system size in these regimes (see below). Third, we find insulating, compressible regimes ($f_s = 0$ and $\kappa > 0$). At finite temperature, however, the values of f_s and κ are not sufficient to distinguish the BG and NF phases, which are thus discriminated via the temperature dependence of the correlation length $\xi(T)$: the absence of temperature dependence shows that the quantum phase is unaffected by the thermal fluctuations and the corresponding regimes are identified as the BG (yellow areas). Conversely, the regimes where the correlation length shows a sizable temperature dependence are identified as the NF (light blue areas).

5.2.2 Analysis of the phase diagram

Now, we come back to the results of the whole phase diagram. With the method mentioned above, we are able to identify the different phases of the system at varying interactions, chemical potentials, potential amplitudes and temperatures. The computed phase diagram is our main result of this chapter and plotted in Fig. 5.1. The upper row on Fig. 5.1 shows the quantum phase diagrams versus the inverse interaction strength and the chemical potential, for increasing amplitudes of the quasiperiodic potential. They are found from QMC calculations of κ and f_s at a vanishingly small temperature. In practice, we have used $k_B T \sim 0.001 - 0.002 E_r$, where k_B is the Boltzmann constant, and we have checked that there is no sizable temperature dependence at a lower temperature. The results thus fairly account for the zero-temperature phase diagram of the system. For $V < V_c$, no localization is expected and we only find SF and MI phases, see panel (a1). The SF dominates at large chemical potentials and weak interactions. Strong enough interactions destabilize the SF phase and Mott lobes open, with fractional occupation numbers ($\rho a = r$, $2r - 1$, $2 - 2r$, $1 - r$ from top to bottom). The number of lobes increases with the interaction strength and eventually become dense in the hard-core limit (see below). For $V > V_c$ and a finite interaction, a BG phase , reminiscent of single-particle localization, develops in between the MI lobes up to the single-particle ME at $\mu = E_c$, see panel (a2). There, the SF fraction is strictly zero and the compressibility has a sizable, non-zero value, within QMC accuracy. When the quasiperiodic amplitude V increases, the BG phase extends at the expense of both the MI and SF phases, see panel (a3).

The lower row on Fig. 5.1 shows the counterpart of the previous diagrams at the finite temperature $T = 0.015 E_r/k_B$, corresponding to the minimal temperature in Ref. [12]. While quantum phases may be destroyed by arbitrarily small thermal fluctuations, the finite-size systems we consider ($L = 83a$) retain characteristic properties, reminiscent of the zero-temperature phases. The SF, MI, and BG *regimes* shown on Figs. 5.1(b1)-(b3) are identified accordingly. While the former two are easily identified, special care should be taken for the BG, which cannot be distinguished from the normal fluid (NF), since both are compressible insulators ($\kappa > 0$ and $f_s = 0$). A key difference, however, is that correlations are suppressed by the disorder in the BG and by thermal fluctuations in the NF. To identify the BG regime, we thus further require that the suppression of correlations is dominated by the disorder, i.e. the correlation length is nearly independent of the temperature. The QMC results show that the NF develops at low density and strong interactions, see panel (b1). For a moderate quasiperiodic amplitude, it takes over the BG, which is completely destroyed, see panel (b2). For a strong enough quasiperiodic potential, however, the BG is robust against thermal fluctuations and competes favourably with the NF regime, see panel (b3). We hence find a sizable BG regime, which should thus be observable at temperatures accessible to current experiments using 1D quantum gases.

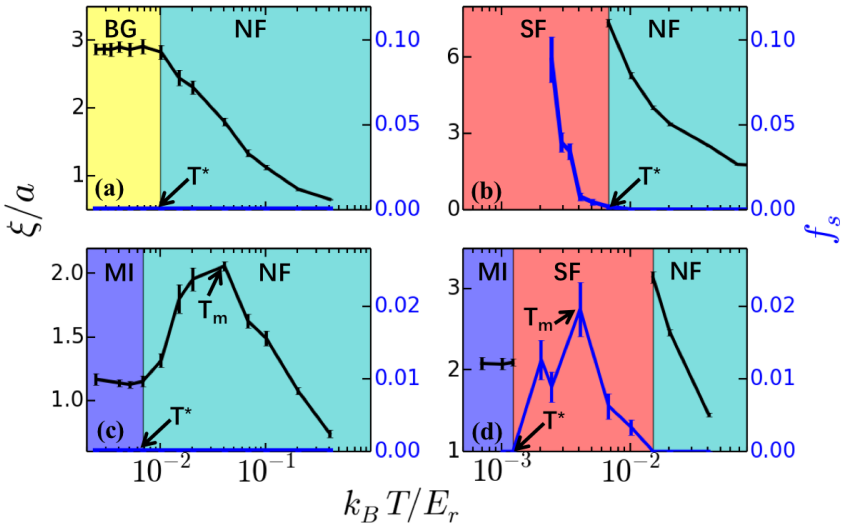

Figure 5.14: Temperature-induced melting of the quantum phases. The various panels show the coherence length ξ (black lines) and the superfluid fraction f_s (blue lines) as a function of temperature for four typical cases: (a) BG to NF crossover ($V = 2E_r$, $\mu = -0.28E_r$, and $-a_{1D}/a = 4.0$), (b) SF to NF crossover ($V = 2E_r$, $\mu = 0.53E_r$, and $-a_{1D}/a = 0.2$), (c) MI to NF crossover ($V = 2E_r$, $\mu = 0.47E_r$,and $-a_{1D}/a = 0.2$), (d) MI to NF, via SF, crossover ($V = E_r$, $\mu = 0.2E_r$, and $-a_{1D}/a = 0.05$). The colored areas correspond to the regimes identified as in Fig. 5.1.

5.3 Finite temperature effects

5.3.1 The melting of the quantum phases

Now, we turn to the quantitative study of the temperature effects. As we explained in the previous section, we compute the one-body correlation function and fit it to $g_1(x) \sim \exp(-|x|/\xi)$, and the quantity we focused on is the correlation length ξ. At low enough temperature, ξ remains constant while increasing temperature T, see for instance Fig. 5.14(a). Thus, although the temperature is not strictly zero, we argue that the phase in this situation is reminiscent of the zero temperature quantum phase, at the finite size we considered. This is the criteria we use to determine whether the observed regime is reminiscent of the zero-temperature quantum phase or not. Then, further increasing the temperature, ξ starts to show a strong dependence on T which presents the crossover to the thermal phase. In Fig. 5.14, we show four typical examples for such a finite temperature behavior. Now, we shall explain them in detail.

BG→NF transition

In Fig. 5.14(a), the typical behavior of $\xi(T)$ when increasing the temperature T from a point in the BG phase ($V = 2E_r$, $\mu = -0.28E_r$, and $-a_{1D}/a = 4.0$) is displayed by the black solid line. Here, one should notice that a key difference between the BG and NF phases is that correlations are suppressed by the disorder in the BG and by thermal fluctuations in the NF. To identify the BG regime, we thus further require that the suppression of correlations is dominated by the disorder, i.e. the correlation length is nearly independent of the temperature. In Fig. 5.14(a), it shows a plateau at low temperature, which is identified as the BG regime, reminiscent of the zero temperature quantum phase. Above some melting temperature T^*, the thermal fluctuations suppress phase coherence and ξ decreases with T, as expected for a NF. In both the BG and NF regimes, superfluidity is absent and we consistently find $f_s = 0$, also shown in the figure (blue line).

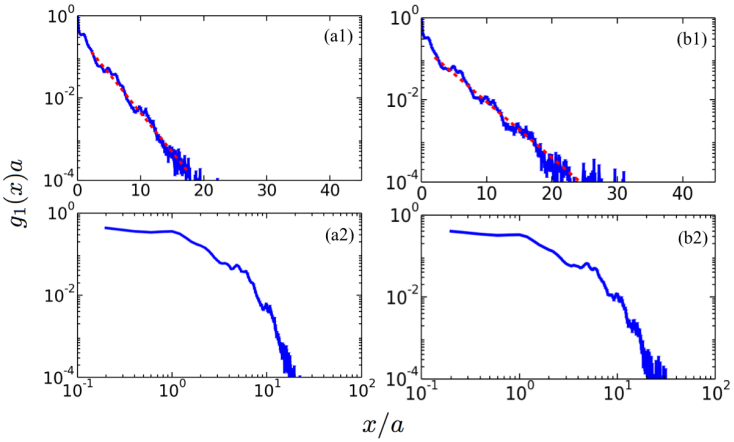

Figure 5.15: One-body correlation function $g_1(x)$ for the parameters $V = 2E_\mathrm{r}$, $\mu = -0.28E_\mathrm{r}$, and $-a_{1\mathrm{D}}/a = 4.0$. The calculations are for two different temperatures: (a) $T = 0.004E_\mathrm{r}/k_\mathrm{B}$ (BG regime) and (b) $T = 0.04E_\mathrm{r}/k_\mathrm{B}$ (NF regime). The upper and lower panels show plots of the same data in semi-log and log-log scales, respectively. The dashed red lines indicate linear fits to $g_1(x)$ in semi-log scale. It yields the coherence lengths (a) $\xi \simeq 2.86a$ and (b) $\xi = 1.81a$, respectively.

In Fig. 5.15, we show in detail the behaviour of $g_1(x)$ for a typical point of BG and NF in Fig. 5.14(a) respectively. The upper and lower panels show plots of the same data in semi-log and log-log scales, respectively. We find, in both cases, that $g_1(x)$ is better fitted by an exponential function, $g_1(x) \sim \exp(-|x|/\xi)$, rather than an algebraic function. This is consistent with the expected behaviour in insulating regimes. Fitting the linear slope in semi-log scale (dotted red line), we extract the correlation length $\xi(T)$. Here, the case in subplot (a) has the correlation length $\xi/a = 2.86$, which is the same value of the zero-temperature limit ξ_0. Thus, we identify it as finite temperature BG phase in the reminiscent of the zero temperature quantum phase. On the contrary. for the case in subplot (b), we find $\xi = 1.81a < \xi_0$, where a strong finite-temperature is observed. We conclude the system is in NF phase in this case.

SF→NF transition

Consider now increasing the temperature from a point in the SF phase at $T = 0$, see Fig. 5.14(b). For low enough T, we find a finite SF fraction f_s, which, however, strongly decreases with T. In this regime, the correlation function shows a characteristic algebraic decay over the full system of length $L = 83a$. The sharp decrease of f_s allows us to identify a rather well defined temperature T^* beyond which we find a NF regime, characterized by a vanishingly small f_s. In this regime, the correlation function consistently shows an exponential decay and the correlation length $\xi(T)$ decreases with T. This scenario is consistent with the expected suppression of coherence induced by thermal fluctuations.

In Fig. 5.16, we show examples of correlation functions for two typical points in the SF and NF regimes of Fig. 5.14(b). On the one hand, the left panel corresponds to the temperature $T = 2.4 \times 10^{-3} E_\mathrm{r}/k_\mathrm{B}$, where we find a finite-size SF. Consistently, the one-body correlation function is well fitted by an algebraic function (dotted red line), but not by an exponential function, over the full system size. On the other hand, the right panel corresponds to the temperature $T = 3 \times 10^{-2} E_\mathrm{r}/k_\mathrm{B}$, where we find a compressible insulator with a temperature-dependent correlation length. Consistently, the one-body correlation function is here better fitted by an exponential function (dotted red line) than by an algebraic function, over the full system size.

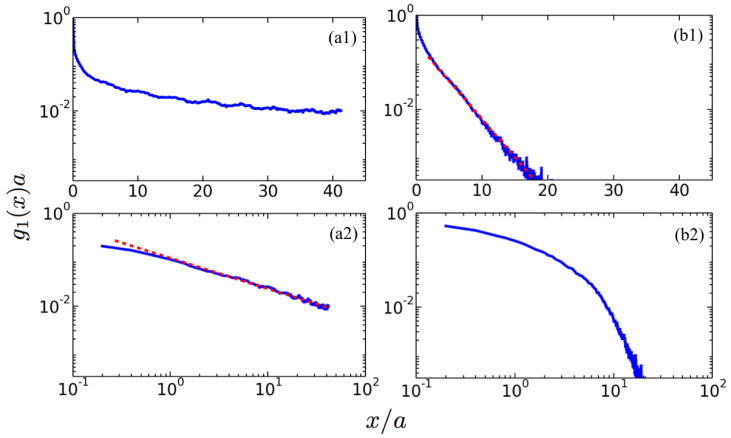

Figure 5.16: One-body correlation function $g_1(x)$ for the parameters $V = 2E_\mathrm{r}$, $\mu = 0.53E_\mathrm{r}$, and $-a_\mathrm{1D}/a = 0.2$. The calculations are for two different temperatures: (a) $T = 2.4 \times 10^{-3}E_\mathrm{r}/k_\mathrm{B}$ (finite-size SF regime) and (b) $T = 0.03E_\mathrm{r}/k_\mathrm{B}$ (NF regime). The upper and lower panels show plots of the same data in semi-log and log-log scales, respectively. The dashed red lines indicate linear fits to $g_1(x)$ in semi-log scale or log-log scale.

MI→NF transition

Consider now increasing the temperature from a point in a MI lobe at $T = 0$, a typical example is shown on Figs. 5.14(c). As expected, below a melting temperature T^*, the correlation length shows a plateau, identified as the MI regime. Quite counterintuitively, however, we find that above T^* the phase coherence is enhanced by thermal fluctuations, up to some temperature T_m, beyond which it is finally suppressed. This anomalous behavior is signaled by the nonmonotony of the correlation length $\xi(T)$, see Fig. 5.14(c). We interpret this behavior from the competition of two effects. On the one hand, a finite but small temperature permits the formation of particle-hole pair excitations, which are extended and support phase coherence. This effect, which is often negligible in strong lattices, is enhanced in shallow lattices owing to the smallness of the Mott gaps, particularly in the quasiperiodic lattice where Mott lobes with fractional fillings appear [86, 192]. This favours the onset of a finite-range coherence at finite temperature. On the other hand, when the temperature increases, a larger number of extended pairs, which are mutually incoherent, is created. This suppresses phase coherence on a smaller and smaller length scale, hence competing with the former process and leading to the nonmonotonic temperature dependence of the coherence length.

MI→SF→NF transition

In Fig. 5.14(d), we show the melting effect for another point which is MI at zero temperature and inside a MI lobe surrounded by a SF phase. In this case, the nonmonotonic temperature effect on the correlation length still exists. It is even strong enough to induce a finite superfluid fraction f_s, and correspondingly an algebraic correlation function in our finite-size system, see Fig. 5.14(d).

To further confirm the appearance of the SF region in this case, Fig. 5.17 shows the $g_1(x)$ functions, in both semi-log (upper panel) and log-log (lower panel) scales, for the parameters of Fig. 5.14(d) and three different temperatures: (a) $T = 8 \times 10^{-4}E_\mathrm{r}/k_\mathrm{B}$, corresponding to the MI regime, (b) $T = 4 \times 10^{-3}E_\mathrm{r}/k_\mathrm{B}$, corresponding to the finite-size SF regime, and (c) $T = 3 \times 10^{-2}E_\mathrm{r}/k_\mathrm{B}$, corresponding to the NF regime [see Fig. 5.14(d)]. Consistently, we find that $g_1(x)$ is better fitted by an exponential function in the insulating regimes [MI and NF, panels (a) and (c)] and by an algebraic function in the finite-size SF

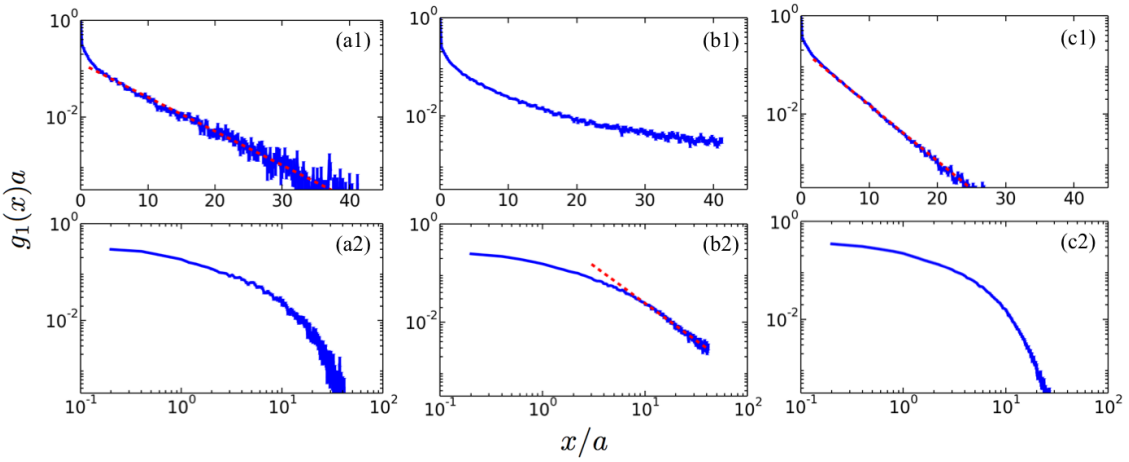

Figure 5.17: One-body correlation function $g_1(x)$ for the parameters $V = E_r$, $\mu = 0.2E_r$, and $-a_{1D}/a = 0.05$ at three different temperatures: (a) $T = 8 \times 10^{-4} E_r/k_B$ (MI regime), (b) $T = 4 \times 10^{-3} E_r/k_B$ (finite-size SF regime), and (c) $T = 3 \times 10^{-2} E_r/k_B$ (NF regime). The upper and lower panels show plots of the same data in semi-log and log-log scales, respectively. The dashed red lines indicate linear fits to $g_1(x)$ in semi-log or log-log scale.

regime [panel (b)]. This is further confirmed by the calculation of the Pearson correlation coefficients P for a linear fit of $g_1(x)$ in semi-log and log-log scales, see Fig. 5.18. The Pearson correlation coefficient P for a linear fit of data (X, Y) defines as

$$P(X,Y) = \frac{\mathrm{cov}(X,Y)}{\sigma_X \sigma_Y} \tag{5.18}$$

with $\mathrm{cov}(X, Y)$ the covariance of (X, Y) and σ_X is the variance of X. The closer P is to unity, the better the linear fit. Figure 5.18 confirms that the correlation function is closer to an exponential function in the MI (dark blue) and NF (light blue) regimes, and closer to an algebraic function in the superfluid regime (red).

Bose glass at higher temperatures in actual experiment

Results such as those shown on Fig. 5.14(a) provide us with the condition of experimental temperature for observing the BG phase. Here, we discuss further the observability in actual experiment based on our phase diagram. In the Fig 5.1, the diagrams of the

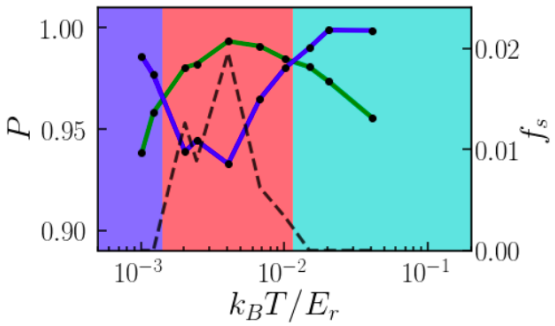

Figure 5.18: Pearson's correlation coefficient for linear fits of one-body correlation function $g_1(x)$ for the parameters $V = E_r$, $\mu = 0.2E_r$, and $-a_{1D}/a = 0.05$, in semi-log scale (solid blue line) and log-log scale (solid green line). The shaded areas correspond to the MI (dark blue), SF (red), and NF (light blue) regimes, determined as in Fig. 2(d).

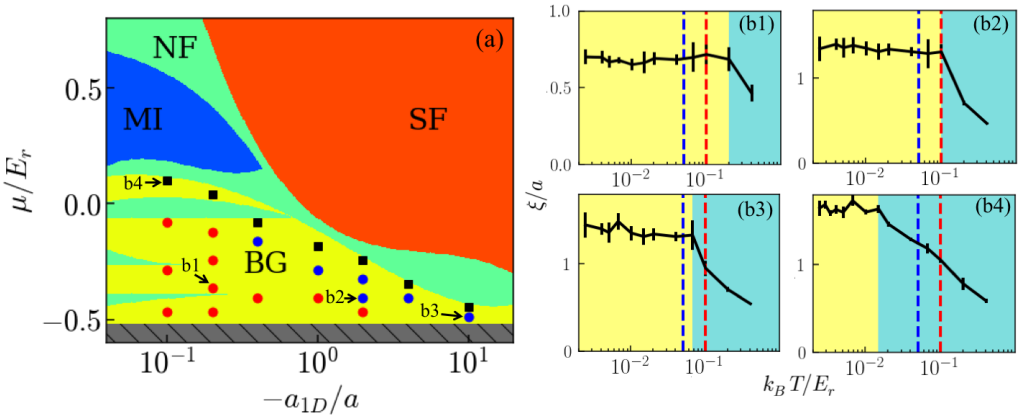

Figure 5.19: Existence of the BG regime for $V = 2E_\mathrm{r}$ at higher temperatures. (a) Reproduction of the Fig. 5.1(b3), indicating the MI (blue), SF (red), BG (yellow), and NF (green) regimes at the temperature $T = 0.05E_\mathrm{r}/k_\mathrm{B}$. The markers indicate points where the melting temperature T^* of the BG phase is $k_\mathrm{B}T^*/E_\mathrm{r} < 0.05$ (black squares), $0.05 < k_\mathrm{B}T^*/E_\mathrm{r} < 0.1$ (blue disks) or $k_\mathrm{B}T^*/E_\mathrm{r} > 0.1$ (red disks). (b) Temperature dependence of the correlation length ξ for the four points indicated on panel (a). The dashed blue and red lines indicate the temperatures $T = 0.05E_\mathrm{r}/k_\mathrm{B}$ and $T = 0.1E_\mathrm{r}/k_\mathrm{B}$, respectively. The background colors indicate the BG (yellow) and NF (light blue) regimes.

lower row are computed at the finite temperature $T = 0.015E_\mathrm{r}/k_\mathrm{B}$. It corresponds to the temperature $T = 1.5$nK for 1D ^{133}Cs atoms, corresponding approximately to the lowest temperatures reported in Ref. [12]. For the amplitude of the quasiperiodic potential $V = 2E_\mathrm{r}$, its shows a sizable BG regime, see red disks in Fig. 5.19(a), which reproduces the Fig. 5.1(b3). The BG should be observable in such an experiment.

Moreover, we have checked that a sizable BG regime survives up to higher temperatures. For instance the experiment of Ref. [12] reported temperatures in the range $1\mathrm{nK} \lesssim T \lesssim 10\mathrm{nK}$ for ^{133}Cs atoms, corresponding to $0.01 \lesssim k_\mathrm{B}T/E_\mathrm{r} \lesssim 0.1$. The experiment of Ref. [14] was operated at $T \simeq 15$nK for ^{39}K atoms, corresponding to $k_\mathrm{B}T/E_\mathrm{r} \simeq 0.07$. We have studied the temperature dependence of the correlation length ξ as determined from exponential fits to the one-body correlation function $g_1(x)$. Some examples are shown on Fig. 5.14 as well as in Figs. 5.19(b1)-(b4). The melting temperature T^* of the BG is the temperature where $\xi(T)$ starts to decrease. The points in the BG regime we have check are indicated by markers on Fig. 5.19(a): black squares correspond to cases where $k_\mathrm{B}T^*/E_\mathrm{r} < 0.05$ [see for instance Fig.5.19(b4)], blue disks to cases where $0.05 < k_\mathrm{B}T^*/E_\mathrm{r} < 0.1$ [see for instance Fig. 5.19(b3)], and red disks to cases where $k_\mathrm{B}T^*/E_\mathrm{r} > 0.1$ [see for instance Fig. 5.19(b1) and (b2)]. It shows that sizable BG regimes are still found at $T \simeq 0.05E_\mathrm{r}/k_\mathrm{B}$ and at $T \simeq 0.1E_\mathrm{r}/k_\mathrm{B}$, and should thus be observable in experiments such as those of Refs. [12, 14].

5.3.2 Fractal Mott lobes

According to the statement in Ref. [221], the typical scale of the melting temperature for the Mott lobe is given by

$$T^* \propto \Delta/k_\mathrm{B} \tag{5.19}$$

where Δ is the width of the lobe. More precisely, it normally appears typically at the temperature scale $T \sim 0.1\Delta/k_\mathrm{B}$. In the quasiperiodic lattice, however, there is no typical gap, owing to the fractal structure of the Mott lobes, inherited from that of the single-particle spectrum, see discussions in section 4.3 and Refs. [23, 86, 192]. In this subsection,

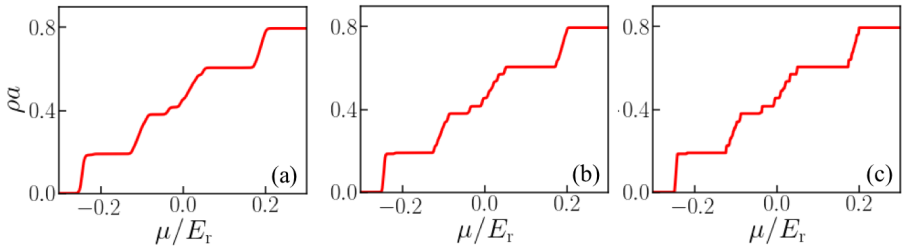

Figure 5.20: Equation of state $\rho(\mu)$ for free fermions, equivalent to hard-core bosons. (a) Same as Fig. 5.1(a2), $V = 1.5E_\mathrm{r}$, $r = 0.807$, $T = 2 \times 10^{-3} E_\mathrm{r}/k_\mathrm{B}$. (b) and (c) are same as panel (a) but with smaller temperatures, $T = 8 \times 10^{-4} E_\mathrm{r}/k_\mathrm{B}$ and $T = 1.6 \times 10^{-4} E_\mathrm{r}/k_\mathrm{B}$ correspondingly.

we will study in detail the finite temperature effect for the fractal Mott lobes and its link with the fractality of the energy spectrum.

Smoothing of the spectral gaps in the hard-core limit

First of all, we want to understand better the origin of the fractal Mott lobes. We start with the equation of state which is linked with the fractality of the single-particle spectrum. As discussed before, Bose-Fermi mapping in the hard-core limit allows us to write the equation of state

$$\rho(\mu) \simeq \frac{1}{L} \sum_j f_\mathrm{FD}(E_j - \mu) \tag{5.20}$$

with the Fermi-Dirac distribution

$$f_\mathrm{FD}(E) = \frac{1}{e^{E/k_\mathrm{B}T} + 1}, \tag{5.21}$$

where E_j is the energy of the j-th eigenstate of the single-particle Hamiltonian. At zero temperature, $f_\mathrm{FD}(E)$ is simply a Heaviside step function centred at $E = \mu$. Thus, it simply fills all the state below μ with one particle per state and leaves empty the states above μ. Therefore, with the single-particle energy spectrum, one can recover the equation of state in the hard-core limit. Owing to the fractality of the single-particle spectrum (see details in Sec. 4.3), at strictly zero temperature, $\rho(\mu)$ is a discontinuous step-like function at any scale.

Any finite temperature T smoothes out all the gaps smaller than the typical energy scale $k_\mathrm{B}T$. For instance, Fig. 5.20(a) reproduces the equation of state plotted on the left-hand side of the Fig. 5.1(a2), corresponding to the temperature $T = 2 \times 10^{-3} E_\mathrm{r}/k_\mathrm{B}$. One sees compressible regions between the plateaus. When the temperature decreases, however, new plateaus appear within these compressible regions. See for instance Fig. 5.20(b) and (c), which correspond to the temperatures $T = 8 \times 10^{-4} E_\mathrm{r}/k_\mathrm{B}$ and $T = 1.6 \times 10^{-4} E_\mathrm{r}/k_\mathrm{B}$. This is consistent with the pure step-like equation of state expected at strictly zero temperature. The new plateaus observed on Fig. 5.20(b) and (c) correspond to Mott gaps for interacting bosons. By taking a smaller value of T and larger values of g, we shall see these smaller gaps. They, however, appear at a stronger interaction strength than that considered in this study. They are thus irrelevant to our discussion.

The compressible fraction and spectrum fractal dimension

To get further insight into the description of the melting of the MI lobes, consider the *compressible phase fraction*, i.e. the complementary of the fraction of MI lobes,

$$\mathcal{K} = \lim_{q \to 0_+} \int_{\mu_1}^{\mu_2} \frac{d\mu}{\mu_2 - \mu_1} \left[\kappa(\mu)\right]^q, \tag{5.22}$$

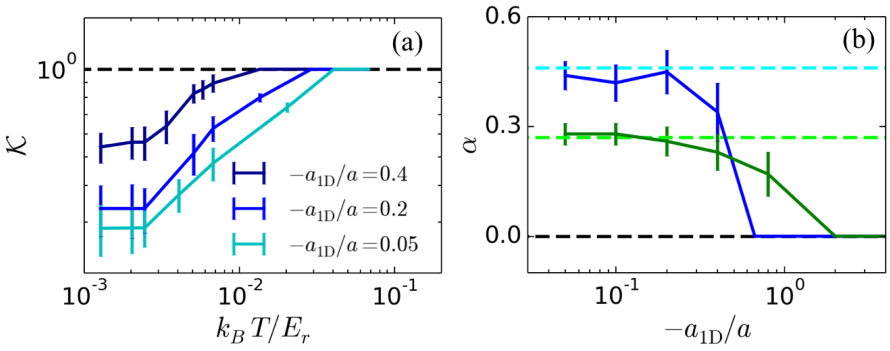

Figure 5.21: Melting of the Mott phase. (a) Compressible phase fraction versus temperature for $V = 1.5E_r$, $\mu/E_r \in [-0.4, 0.8]$, and various interaction strengths. (b) Exponent α versus the interaction strength for $V = E_r$ (green solid line) and $V = 1.5E_r$ (blue). The colored dashed lines indicate the corresponding values of $1 - D_H$.

in the chemical potential range $[\mu_1, \mu_2]$. Here, we may notice that the compressible phases contribute with $\kappa(\mu) = 1$ and the incompressible MI phase with $\kappa(\mu) = 0$. The behavior of $\mathcal{K}$ versus temperature is shown on Fig. 5.21(a) for various interaction strengths. Below the melting temperature of the smallest MI lobes, $T_1^\star$, $\mathcal{K}$ is insensitive to thermal fluctuations and we correspondingly find $\mathcal{K} = \text{cst}$. Above that of the largest one, $T_2^\star$, all MI lobes are melt and $\mathcal{K} = 1$. Here, one should note that the gap of the smallest lobes does not vary much with the interaction strength while that of the largest lobes do, see Fig. 5.1. It explains that only $T_2^\star$ varies significantly with the interaction strength on Fig. 5.21. In the intermediate regime, $T_1^\star \lesssim T \lesssim T_2^\star$, we find the algebraic scaling $\mathcal{K} \sim T^\alpha$, where the exponent α depends on both the interaction strength and the quasiperiodic amplitude V, see Fig. 5.21(b). This behavior is reminiscent of the fractal structure of the MI lobes.

To understand this, consider the Tonks-Girardeau limit, $a_{1D} \to 0$ where the Lieb-Liniger gas may be mapped onto free fermions [40]. We recall that in this limit, the particle density then reads as Eq. (5.20). This picture provides a very good approximation of our QMC results at large interaction, irrespective of T and V, see left panels of each plot on Fig. 5.1. The compressibility thus reads as

$$\kappa(\mu) \simeq \frac{1}{L} \sum_j \left(-\frac{\partial f_{FD}}{\partial E} \right) \Big|_{E=E_j-\mu} \tag{5.23}$$

Since $f'_{FD} = \partial f_{FD}/\partial E$ is a peaked function of typical width $k_B T$ around the origin, we find

$$\kappa(\mu) \sim n_{\epsilon=k_B T}(\mu), \tag{5.24}$$

where $n_\epsilon(E)$ is the integrated density of states (IDoS) per unit length of the free Hamiltonian in the energy range $[E - \epsilon/2, E + \epsilon/2]$. Hence, the compressibility maps onto the IDoS, $k_B T$ onto the energy resolution, and, up the factor $k_B T/(\mu_2 - \mu_1)$, the compressible phase fraction onto the spectral box-counting number $N_B(\epsilon)$ introduced in Ref. [86] as well as section 4.3 of this manuscript. We then find

$$\mathcal{K} \sim \frac{k_B T}{\mu_2 - \mu_1} N_B(\epsilon = k_B T) \sim T^{1-D_H}, \tag{5.25}$$

where D_H is the Hausdorff dimension of the free spectrum, and we recover the algebraic temperature dependence $\mathcal{K} \sim T^\alpha$, with $\alpha = 1 - D_H$.

To validate this picture, we have computed the exponent α by fitting curves as on Fig. 5.21(a) as a function of the interaction strength. The results are shown on Fig. 5.21(b)

for two values of the quasiperiodic amplitude (colored solid lines). As expected, we find $\alpha \to 1 - D_{\mathrm{H}}$ (colored dashed lines) in the Tonks-Girardeau limit, $a_{\mathrm{1D}} \to 0$. When the interaction strength decreases, the fermionization picture breaks down. The exponent α then decreases and vanishes when the last MI lobe shrinks.

Moreover, our results show that the compressible BG fraction is suppressed at low temperature ($\alpha > 0$) and strong interactions [see Fig. 5.21(a)]. This is consistent with the expected singularity of the BG phase in the hard-core limit, where the MI lobes become dense.

Conclusion

In summary, in this section, we have computed the quantum phase diagram of Lieb-Liniger bosons in a shallow quasiperiodic potential. Our main result is that a BG phase emerges above a critical potential and for finite interactions, surrounded by SF and MI phases. We have also studied the effect of a finite temperature. We have shown that the melting of the MI lobes is characteristic of their fractal structure and found regimes where the BG phase is robust against thermal fluctuations up to a range accessible to experiments. For instance, the temperature $T = 0.015 E_{\mathrm{r}}/k_{\mathrm{B}}$ used in Fig. 5.1 corresponds to $T \simeq 1.5$nK for ^{133}Cs ultracold atoms, which is about the minimal temperature achieved in Ref. [12]. Further, we have checked that a sizable BG regime is still observable at higher temperatures, for instance $T = 0.1 E_{\mathrm{r}}/k_{\mathrm{B}}$, which is higher than the temperatures reported in Refs. [12, 14]. This paves the way to the direct observation of the still elusive BG phase, as well as the fractality of the MI lobes, in ultracold quantum gases. We propose to characterize the phase diagram using the one-body correlation function, as obtained from Fourier transforms of time-of-flight images in ultracold atoms [14,24]. Discrimination of algebraic and exponential decays could benefit from box-shaped potentials [222–224]. Our results indicate that the variation of the correlation length $\xi(T)$ with the temperature characterizes the various regimes, see Fig. 5.14.

Further, our work questions the universality of the BG transition found here. On the one hand, in contrast to truly disordered [52, 53] or Fibonacci [225, 226] potentials, the shallow bichromatic lattice contains only two spatial frequencies of finite amplitudes. Hence, the emergence of a BG requires the growth of a dense set of density harmonics within the renormalization group flow, which may significantly affect the value of the critical Luttinger parameter. On the other hand, it will be interesting to investigate the Bose glass transition in higher dimension, such as two-dimensional quasicrystal structure.

Chapter 6

Conclusion and perspectives

In this manuscript, we have studied the properties of one dimensional (1D) Bosons in various contexts. We have mainly focused on the characterization of the quantum degeneracy regimes in the trapped gases at a finite temperature and on the effect of quasiperiodic potentials on correlated bosons. We have used a variety of approaches, from analytical (Bethe ansatz, Yang-Yang thermodynamics) to advanced quantum Monte Carlo (QMC) techniques, as well as exact diagonalization. The combination of all these methods have been crucial to obtain the various results presented in this thesis. Beyond its interest from the theoretical point of view, those results are also particularly relevant for nowadays experiments, in particular for ultracold atom systems but potentially also in other quantum simulator platforms such as quantum photonics for instance.

Main results presented in the thesis

We first studied the Tan contact for 1D Lieb-Liniger bosons in the presence of a harmonic trap in Chapter 3. This quantity, which characterizes the amplitude of the long momentum tails as well as spectroscopic signals, can be accurately measured in ultracold atom experiments. We have shown that it provides a useful characteristics of the degenerate quantum regimes. Our most important results is that the contact exhibits a maximum as a function of temperature. In the strongly-interacting regime, it provides a signature of the crossover to fermionization at finite temperature, while usual quantities vary smoothly and monotonously from low to high temperature. Also, we analysed the conditions for experimental observation and this work can trigger fruitful physics to be detected in experiment.

Then, we moved to the study of 1D bosons in the presence of a quasiperiodic potential.

In Chapter 4, we discussed the localization properties of single particles in a 1D quasiperiodic potential. On the one hand, we studied the fractal structure of the energy spectrum and proposed a box-counting analysis to calculate the fractal dimension. It confirms the spectrums are fractal-like. We have shown that the fractal dimension is nonuniversal and depends on the model as well as the potential amplitude. As a byproduct, we have shown that the spectrum is nowhere dense (since the fractal dimension is smaller than unity). It shows that the mobility edge is always in a gap, hence invalidating previous assertions. On the other hand, we found a finite critical potential for the IPR and finite ME in balanced bichromatic systems, which is totally different from the tight-binding AA model or the 1D purely disordered system. We also found the IPR critical exponent $\nu = 1/3$ which is universal. And we also extend this study to more general cases, such as imbalanced bichromatic systems and trichromatic systems. This extends the previous study about the localization problem in the 1D tight-binding quasiperiodic system (AA model) into the shallow lattice case. It also provides a steady basis for the study of the interacting system.

Then, in Chapter 5, we moved to the study of the many-body problem and determined the phase diagram for 1D Lieb-Liniger bosons in a shallow quasiperiodic potential where the potential amplitude is around the recoil energy $V \sim E_{\mathrm{r}}$. As argued in this thesis, this case is important because it significantly lowers the energy scale to a regime where temperature effects are negligible. The existence of a Bose glass was, however, not guaranteed owing to the fact that the Mott lobes are dense in the Tonks-Girardeau limit. Using QMC, we have been able to show that the Bose glass phase can be stabilized at intermediate interactions. At zero temperature, we found that a clear compressible insulting Bose glass phase appears on top of the superfluid and Mott insulator phases, for a chemical potential above the single-particle mobility edge. Also, we studied the finite-temperature effects on all phases. Most importantly, we found that the Bose glass phase can be robust to thermal fluctuations up to the range which is accessible by experiments. Moreover, we have shown that the melting effect of the Mott lobes is a signature of its fractal structure and can be linked, in the Tonks-Girardeau limit, to the fractal dimension of the single-particle spectrum.

Perspectives

This work paves the way for the further research, both experimentally and theoretically.

Experimental perspectives—

From the experimental perspective, this works provides predictions that can be detected in the present-day experiments.

In the case of 1D bosons in a harmonic trap (chapter 3), the measurement of the Tan contact is direct via momentum distribution. By changing the level of cooling and fixing the number of particles, one can scan the temperature effect on the contact. Especially at large interactions, one expects to observe the maximum contact which is the signature of the crossover to fermionized regime. The experimetal setup in Ref. [12] can realize 1D strongly-interacting systems with at least up to $\xi_\gamma \simeq 7.5$ and the measurement technique in Ref. [125] allows one to detect the momentum distribution with high accuracy with 6 orders of magnitudes. These kinds of setups are extremely suitable for the experimental observation of our predictions. Also, for most of the experiments, instead of generating a single tube, they create 2D arrays of 1D tubes by 2D optical lattices, see for instance Ref. [12]. Therefore, it will be useful to study how the 2D tube distribution influences the detected contact and the existence of the maximum.

In the case of 1D bosons in the quasiperiodic potential (chapter 4 and 5), generally speaking, the most interesting thing to be detected is the phase diagram. So far, no experiments provide direct observation of a Bose glass phase, although careful analysis has allowed to show observations compatible with a Bose glass phase [14, 24]. Also, the temperature effects blur the phase diagram. Here, we propose an approach to overcome these issues. It is realizeable in present-day experiment and would represent the first direct determination of the phase diagram and observation of the Bose glass phase. Moreover, we have found that the Mott lobes has an interesting fractal behavior. We have shown that the temperature-induced melting of the latter is characteristic of their fractality, which also offers stimulating experimental perspectives.

Theoritical perspectives—

From the theoretical aspect, there are also several possible extensions based on our work.

For the Tan contact of 1D bosons (Chapter 3), there are two main directions of possible future research. On the one hand, one can further perform the analysis of the Tan contact for the excited states. On the other hand, it will be interesting to extend the study to

other type of systems, such as systems in higher dimension, fermionic systems and multi-component (Bose, Fermi or Bose-Fermi) systems.

For the single-particle problem of the quasiperiodic system (Chapter 4), several points deserve further investigation. First, it's not clear what is the explanation of the universal critical exponent $\nu \simeq 1/3$ for the IPR. This value is universal for 1D bichromatic lattice with balanced and imbalanced amplitude, as well as 1D trichromatic lattice. However, a proper interpretation for this number is still lacking. Second, it's important to study the properties of the fractal dimension, for instance it's dependence on the potential amplitude and energy spectrum range. This can help us understand better several related and important properties, such as the fractality of the Mott lobes and other physical consequences of the spectral fractality of quasiperiodic systems. Thirdly, it's also important to check the universality of our results in higher dimensions, for instance in 2D quasiperiodic potentials.

For the many-body systems in the presence of a quasiperiodic potentials (Chapter 5), one can identify three main lines of perspectives. First, it will be interesting to study the Luttinger parameters and its critical value at the transition point. In Ref. [226], the authors show that the critical Luttinger parameter for fermions in the Fibonacci chain is different from the one in disordered potentials. It's interesting to study the case of 1D bosons in quasiperiodic potentials compared with the these two known results. Second, although the initial motivation for studying the quasiperiodic potential is to simplify the realization of disordered potentials in early experiments, here we show that the quasiperiodic potentials are interesting in their own right. One major point is the fractality and we have shown that the melting of certain quantum phases is characteristic of such a fractal behavior. So far, this aspect has been loosing studied and would deserve further work to explore other consequences. Finally, one can also generalize the study of the phase diagram to other types of quasiperiodic systems. On the one hand, one can extend the study to 1D trichromatic lattices. This is rather a technical point but it is potentially important for experiments. We shall expect that the physics is similar but one can benefit from a lower value of the critical potential. On the other hand, it would be interesting to investigate higher dimensional quasicrystal structures. This line of research is fully open. We have just started to study this for 2D quasicrystal structures and a publication is under preparation while completing this thesis.

Beyond all these points about physics, there is also an outlook for the QMC code we have discussed in Chapter 2 and used in the whole thesis. There are two possible extensions for this code. On the one hand, the interactions can be changed into long-range type and it can simulate the Rydberg gases. The difficulty for this update is to find the proper analytical forms for the interaction propagator by the scattering theory. On the other hand, one can extend the code into higher dimensions. As mentioned above, I've collaborated with an internship student Ronan Gautier and we extend this code to 2D. We've checked that the code is working well in 2D quasiperiodic potentials and find the quantum phase diagram ranging from weak to strong interactions [227]. In the future, one can adapt the code into other 2D structures and even 3D systems.

Appendix: Derivation for the virial expansion equation of the Tan contact

Here, we present the details about solving Eq. (3.52) and obtain the analytical formula for the Tan contact, Eq. (3.53), which is the equation for the contact in the regime of high temperature ($k_{\rm B}T \gg N\hbar\omega$) and large interactions $|a_{\rm 1D}|/a_{\rm ho} \ll 1$. This derivation was proposed by Prof. Patrizia Vignolo. Here, we recall the first step which is already presented in section 3.2.2 and it yields the virial expansion we find for the contact [18]

$$C = \frac{4m\omega}{\hbar\lambda_T} N^2\, c_2 \tag{6.1}$$

where $c_2 = \lambda_T \dfrac{\partial b_2}{\partial |a_{\rm 1D}|}$ and $b_2 = \sum_\nu e^{-\beta\hbar\omega(\nu+1/2)}$. The ν's are the solutions of the transcendental equation

$$f(\nu) = \frac{\Gamma(-\nu/2)}{\Gamma(-\nu/2+1/2)} = \sqrt{2}\frac{a_{\rm 1D}}{a_{\rm ho}}. \tag{6.2}$$

First, we start with using the Euler reflection formula of the Γ function, which yields,

$$\Gamma(z)\Gamma(1-z) = \frac{\pi}{\sin(\pi z)}. \tag{6.3}$$

With Eq. (6.3), one can re-write Eq. (6.2) under the form

$$f(\nu) = -\cot(\pi\nu/2)\frac{\Gamma(\nu/2+1/2)}{\Gamma(\nu/2+1)}. \tag{6.4}$$

Now, we remind the asympotic series for the Γ function

$$\Gamma(z) \simeq \sqrt{2\pi}\, z^{z-1/2}\, e^{-z}\, (1 + O(1/z))\,. \tag{6.5}$$

Inserting Eq. (6.5) into Eq. (6.4), in the limit $\nu \gg 1$, we obtain the asymptotic expression for $f(\nu)$

$$f(\nu) \simeq -\cot(\pi\nu/2)\frac{1}{\sqrt{\nu/2+1/2}} \simeq -\sqrt{\frac{2}{\nu}}\cot(\pi\nu/2). \tag{6.6}$$

In the Tonks-Girardeau regime ($a_{\rm 1D} = 0$) , one has $\nu = 2n+1$, with $n \in \mathbb{N}$. Thus, in the regime $|a_{\rm 1D}|/a_{\rm ho} \ll 1$, we obtain an explicit expression for ν, by writing

$$\sqrt{\frac{2}{2n+1}}\cot(\pi\nu/2) \simeq \sqrt{2}\frac{|a_{\rm 1D}|}{a_{\rm ho}} \tag{6.7}$$

namely

$$\nu_n = \frac{2}{\pi}\mathrm{arccot}(\sqrt{2n+1}|a_{\rm 1D}|/a_{\rm ho}) + 2n, \qquad n \in \mathbb{N}. \tag{6.8}$$

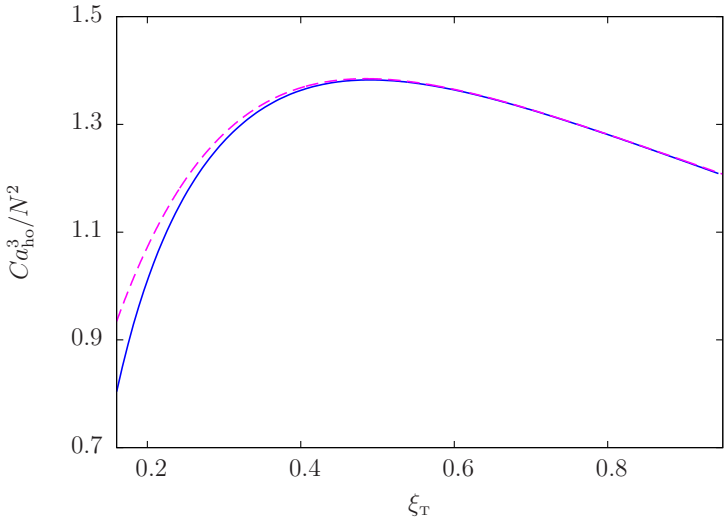

Figure 6.1: $Ca_{\rm ho}^3/N^2$ calculated using the numerical solution of Eq. (6.2) (blue continuous line) and using the analytical expression (3.54) (magenta dashed line). We have considered $|a_{\rm 1D}|/a_{\rm ho} = 0.4$.

This yields the following explicit expression for c_2:

$$\begin{aligned} c_2 &= \lambda_T \sum_{\nu} (-\beta\hbar\omega) \frac{\partial \nu}{\partial |a_{\rm 1D}|} e^{-\beta\hbar\omega(\nu_n+1/2)} \\ &= \lambda_T \sum_{n} (-\beta\hbar\omega) \frac{2}{\pi} \frac{\sqrt{2n+1}}{a_{\rm ho}} \frac{-1}{1+(2n+1)\frac{a_{\rm 1D}^2}{a_{\rm ho}^2}} e^{-\beta\hbar\omega(\nu_n+1/2)} \\ &= \frac{2\lambda_T \beta\hbar\omega}{\pi a_{\rm ho}} \sum_{n} \frac{\sqrt{2n+1}}{1+(2n+1)\frac{a_{\rm 1D}^2}{a_{\rm ho}^2}} e^{-\beta\hbar\omega(\nu_n+1/2)}. \end{aligned} \tag{6.9}$$

In order to evaluate analytically the sum in Eq. (6.9), we replace ν with $2n+1$ in the exponential. Indeed, the first-order correction in $|a_{\rm 1D}|$ gives a negligible contribution in the limit $\beta\hbar\omega \to 0$ and $|a_{\rm 1D}|/a_{\rm ho} \to 0$. Also, we recall the property of the complementary error function $\mathrm{Erfc}(x)$,

$$\mathrm{Erfc}(az) = \frac{2z}{\pi} e^{-a^2z^2} \int_0^{+\infty} \frac{e^{-a^2t^2}}{t^2+z^2}\, dt. \tag{6.10}$$

Taking $a^2 = \beta\hbar\omega$ and $z = a_{\rm ho}/a_{\rm 1D}$, combined with Eq. (6.9), we finally get

$$c_2 = \sqrt{2}\left(\frac{1}{2\pi\xi_{\rm T}^2} - \frac{e^{1/2\pi\xi_{\rm T}^2}}{2^{3/2}\pi\xi_{\rm T}^3} \mathrm{Erfc}(1/\sqrt{2\pi}\xi_{\rm T}) \right). \tag{6.11}$$

with $\xi_{\rm T} = -a_{\rm 1D}/\lambda_T$ defined in section 3.1.1. Combined with Eq. (6.1), the contact at large temperatures and large interactions can be approximated by

$$\begin{aligned} C =& \frac{4\sqrt{2}N^2\xi_{\rm T}}{|a_{\rm 1D}|a_{\rm ho}^2} \left(\frac{1}{2\pi\xi_{\rm T}^2} - \frac{1}{2^{3/2}\pi\xi_{\rm T}^3} e^{1/2\pi\xi_{\rm T}^2} \mathrm{Erfc}(1/\sqrt{2\pi}\xi_{\rm T}) \right) \\ =& \frac{2N^{5/2}}{\pi a_{\rm ho}^3} \frac{\xi_\gamma}{\xi_{\rm T}} \left(\sqrt{2} - \frac{\mathrm{e}^{1/2\pi\xi_{\rm T}^2}}{\xi_{\rm T}} \mathrm{Erfc}(1/\sqrt{2\pi}\xi_{\rm T}) \right). \end{aligned} \tag{6.12}$$

In Fig. 6.1, we plot Eq. (6.1) (magenta dashed line) and compare it with the results calculated by the numerical solution of Eq. (6.2) (blue continuouus line). From the plot, we can see that these two curves fit well with each other when $\xi_{\rm T} \gtrsim 0.3$.

List of publications

1. **H. Yao**, D. Clément, A. Minguzzi, P. Vignolo and L. Sanchez-Palencia. "Tan's contact for trapped Lieb-Liniger bosons at finite temperature", *Phys. Rev. Lett.* **121**,220402 (2018).

2. **H. Yao**, H. Khoudli, L. Bresque and L. Sanchez-Palencia. "Critical behavior and fractality in shallow one-dimensional quasiperiodic potentials", *Phys. Rev. Lett.* **123**, 070405 (2019).

3 **H. Yao**, T. Giamarchi, and L. Sanchez-Palencia, "Lieb-Liniger bosons in a shallow quasiperiodic potential: Bose glass phase and fractal Mott lobes", *Phys. Rev. Lett.* **125**, 060401 (2020).

4. R. Gautier, **H. Yao** and L. Sanchez-Palencia. "Strongly-Interacting bosons in a two-dimensional quasicrystal lattice", *arXiv*: 2010.07590 (2020)

Bibliography

[1] I. Bloch, J. Dalibard, and W. Zwerger, *Many-body physics with ultracold gases*, Rev. Mod. Phys. **80**, 885 (2008).

[2] T. Giamarchi, *Quantum Physics in One Dimension* (Carendon press, Oxford, 2004).

[3] M. A. Cazalilla, R. Citro, T. Giamarchi, E. Orignac, and M. Rigol, *One dimensional bosons: From condensed matter systems to ultracold gases*, Rev. Mod. Phys. **83**, 1405 (2011).

[4] S. Chu, L. Hollberg, J. E. Bjorkholm, A. Cable, and A. Ashkin, *Three-dimensional viscous confinement and cooling of atoms by resonance radiation pressure*, Phys. Rev. Lett. **55**, 48 (1985).

[5] J. Reichel, F. Bardou, M. Ben-Dahan, E. Peik, S. Rand, C. Salomon, and C.-T. C., *Raman cooling of cesium below 3nK: New approach inspired by Lévy flight statistics*, Phys. Rev. Lett. **75**, 4575 (1995).

[6] E. Raab, M. Prentiss, A. Cable, S. Chu, and D. Pritchard, *Trapping of neutral sodium atoms with radiation pressure*, Phys. Rev. Lett. **59**, 2631 (1987).

[7] E. A. Cornell and C. E. Wieman, *Nobel lecture: Bose-Einstein condensation in a dilute gas, the first 70 years and some recent experiments*, Rev. Mod. Phys. **74**(3), 875 (2002).

[8] G. Roati, F. Riboli, G. Modugno, and M. Inguscio, *Fermi-Bose quantum degenerate ^{40}K-^{87}Rb mixture with attractive interaction*, Phys. Rev. Lett. **89**, 150403 (2002).

[9] B. Paredes, A. Widera, V. Murg, O. Mandel, S. Fölling, I. Cirac, G. V. Shlyapnikov, T. W. Hänsch, and I. Bloch, *Tonks-Girardeau gas of ultracold atoms in an optical lattice.*, Nature (London) **429**, 277 (2004).

[10] T. Kinoshita, T. Wenger, and D. S. Weiss, *Observation of a one-dimensional Tonks-Girardeau gas*, Science **305**, 1125 (2004).

[11] I. Bouchoule, N. J. van Druten, and C. I. Westbrook, *Atom Chips. J. Reichel and V. Vuletic eds* (Wiley-Blackwell, 2011), chap. "Atom chips and one-dimensional Bose gases", pp. 331–363.

[12] F. Meinert, M. Panfil, M. J. Mark, K. Lauber, J.-S. Caux, and H.-C. Nägerl, *Probing the excitations of a Lieb-Liniger gas from weak to strong coupling*, Phys. Rev. Lett. **115**, 085301 (2015).

[13] E. Haller, R. Hart, M. J. Mark, J. G. Danzl, L. Reichsöllner, M. Gustavsson, M. Dalmonte, G. Pupillo, and H.-C. Nägerl, *Pinning quantum phase transition for a Luttinger liquid of strongly interacting bosons*, Nature (London) **466**, 597 (2010).

[14] C. D'Errico, E. Lucioni, L. Tanzi, L. Gori, G. Roux, I. P. McCulloch, T. Giamarchi, M. Inguscio, and G. Modugno, *Observation of a disordered bosonic insulator from weak to strong interactions*, Phys. Rev. Lett. **113**, 095301 (2014).

[15] G. Boéris, L. Gori, M. D. Hoogerland, A. Kumar, E. Lucioni, L. Tanzi, M. Inguscio, T. Giamarchi, C. D'Errico, G. Carleo, *et al.*, *Mott transition for strongly interacting one-dimensional bosons in a shallow periodic potential*, Phys. Rev. A **93**, 011601(R) (2016).

[16] T. Kohlert, S. Scherg, X. Li, H. P. Lüschen, S. Das Sarma, I. Bloch, and M. Aidelsburger, *Observation of many-body localization in a one-dimensional system with a single-particle mobility edge*, Phys. Rev. Lett. **122**, 170403 (2019).

[17] A. Minguzzi, P. Vignolo, and M. Tosi, *High momentum tail in the Tonks gas under harmonic confinement*, J. Phys. Lett. A **294**, 222 (2002).

[18] P. Vignolo and A. Minguzzi, *Universal contact for a Tonks-Girardeau gas at finite temperature*, Phys. Rev. Lett. **110**, 020403 (2013).

[19] K. Viebahn, M. Sbroscia, E. Carter, J.-C. Yu, and U. Schneider, *Matter-wave diffraction from a quasicrystalline optical lattice*, Phys. Rev. Lett. **122**, 110404 (2019).

[20] L. Fallani, J. E. Lye, V. Guarrera, C. Fort, and M. Inguscio, *Ultracold atoms in a disordered crystal of light: Towards a Bose glass*, Phys. Rev. Lett. **98**, 130404 (2007).

[21] L. Tanzi, E. Lucioni, S. Chaudhuri, L. Gori, A. Kumar, C. D'Errico, M. Inguscio, and G. Modugno, *Transport of a Bose gas in 1D disordered lattices at the fluid-insulator transition*, Phys. Rev. Lett. **111**, 115301 (2013).

[22] P. Lugan, D. Clément, P. Bouyer, A. Aspect, M. Lewenstein, and L. Sanchez-Palencia, *Ultracold Bose gases in 1D disorder: From Lifshits glass to Bose-Einstein condensate*, Phys. Rev. Lett. **98**, 170403 (2007).

[23] G. Roux, T. Barthel, I. P. McCulloch, C. Kollath, U. Schollwöck, and T. Giamarchi, *Quasiperiodic Bose-hubbard model and localization in one-dimensional cold atomic gases*, Phys. Rev. A **78**(2), 023628 (2008).

[24] L. Gori, T. Barthel, A. Kumar, E. Lucioni, L. Tanzi, M. Inguscio, G. Modugno, T. Giamarchi, C. D'Errico, and G. Roux, *Finite-temperature effects on interacting bosonic one-dimensional systems in disordered lattices*, Phys. Rev. A **93**, 033650 (2016).

[25] L. Pricoupenko and M. Olshanii, *Stability of two-dimensional Bose gases in the resonant regime*, J. Phys. B: At. Mol. Opt. Phys. **40**, 2065 (2007).

[26] C. Mora and Y. Castin, *Extension of bogoliubov theory to quasicondensates*, Phys. Rev. A **67**(5), 053615 (2003).

[27] Z. Hadzibabic and J. Dalibard, *Two-dimensional Bose fluids: An atomic physics perspective*, Rivista del Nuovo Cimento **34**, 389 (2011).

[28] G. Carleo, G. Boéris, M. Holzmann, and L. Sanchez-Palencia, *Universal superfluid transition and transport properties of two-dimensional dirty bosons*, Phys. Rev. Lett. **111**, 050406 (2013).

[29] L.-C. Ha, C.-L. Hung, X. Zhang, U. Eismann, S.-K. Tung, and C. Chin, *Strongly interacting two-dimensional bose gases*, Phys. Rev. Lett. **110**(14), 145302 (2013).

[30] C. De Rossi, R. Dubessy, K. Merloti, M. d. G. de Herve, T. Badr, A. Perrin, L. Longchambon, and H. Perrin, *Probing superfluidity in a quasi two-dimensional bose gas through its local dynamics*, New J. Phys. **18**(6), 062001 (2016).

[31] A. Szabó and U. Schneider, *Non-power-law universality in one-dimensional quasicrystals*, Phys. Rev. B **98**, 134201 (2018).

[32] A. Szabó and U. Schneider, *Mixed spectra and partially extended states in a two-dimensional quasiperiodic model*, Phys. Rev. B **101**(1), 014205 (2020).

[33] M. Sbroscia, K. Viebahn, E. Carter, J.-C. Yu, A. Gaunt, and U. Schneider, *Observing localisation in a 2D quasicrystalline optical lattice*, arXiv preprint arXiv:2001.10912 (2020).

[34] F. Meinert, M. Knap, E. Kirilov, K. Jag-Lauber, M. B. Zvonarev, E. Demler, and H.-C. Nägerl, *Bloch oscillations in the absence of a lattice*, Science **356**(6341), 945 (2017).

[35] G. Lang, F. Hekking, and A. Minguzzi, *Ground-state energy and excitation spectrum of the lieb-liniger model: accurate analytical results and conjectures about the exact solution*, SciPost Physics **3**(1), 003 (2017).

[36] J. Despres, L. Villa, and L. Sanchez-Palencia, *Twofold correlation spreading in a strongly correlated lattice Bose gas*, Sci. Rep. **9**, 4135 (2019).

[37] L. Villa, J. Despres, and L. Sanchez-Palencia, *Unraveling the excitation spectrum of many-body systems from quantum quenches*, Phys. Rev. A **100**, 063632 (2019).

[38] L. Villa, J. Despres, S. Thomson, and L. Sanchez-Palencia, *Local quench spectroscopy of many-body quantum systems*, arXiv preprint arXiv:2007.08381 (2020).

[39] Y. Guo, R. Dubessy, M. d. G. de Herve, A. Kumar, T. Badr, A. Perrin, L. Longchambon, and H. Perrin, *Supersonic rotation of a superfluid: a long-lived dynamical ring*, Phys. Rev. Lett. **124**(2), 025301 (2020).

[40] M. Girardeau, *Relationship between systems of impenetrable bosons and fermions in one dimension*, J. Math. Phys. **1**, 516 (1960).

[41] S. Lellouch and L. Sanchez-Palencia, *Localization transition in weakly-interacting Bose superfluids in one-dimensional quasiperdiodic lattices*, Phys. Rev. A **90**, 061602(R) (2014).

[42] D. Jaksch, C. Bruder, J. I. Cirac, C. W. Gardiner, and P. Zoller, *Cold bosonic atoms in optical lattices*, Phys. Rev. Lett. **81**(15), 3108 (1998).

[43] M. Greiner, O. Mandel, T. Esslinger, T. W. Hänsch, and I. Bloch, *Quantum phase transition from a superfluid to a Mott insulator in a gas of ultracold atoms*, Nature (London) **415**(6867), 39 (2002).

[44] S. Inouye, M. R. Andrews, J. Stenger, H. J. Miesner, D. M. Stamper-Kurn, and W. Ketterle, *Observation of Feshbach resonances in a Bose-Einstein condensate*, Nature (London) **392**(6672), 151 (1998).

[45] S. L. Cornish, N. R. Claussen, J. L. Roberts, E. A. Cornell, and C. E. Wieman, *Stable ^{85}Rb Bose-Einstein condensates with widely tunable interactions*, Phys. Rev. Lett. **85**(9), 1795 (2000).

[46] V. Gurarie and J. T. Chalker, *Some generic aspects of bosonic excitations in disordered systems*, Phys. Rev. Lett. **89**, 136801 (2002).

[47] V. Gurarie, G. Refael, and J. T. Chalker, *Excitations of one-dimensional Bose-Einstein condensates in a random potential*, Phys. Rev. Lett. **101**(17), 170407 (2008).

[48] N. Bilas and N. Pavloff, *Anderson localization of elementary excitations in a one-dimensional Bose-Einstein condensate*, Eur. Phys. J. D **40**(3), 387 (2006).

[49] P. Lugan, D. Clément, P. Bouyer, A. Aspect, and L. Sanchez-Palencia, *Anderson localization of Bogolyubov quasiparticles in interacting Bose-Einstein condensates*, Phys. Rev. Lett. **99**(18), 180402 (2007).

[50] P. Lugan and L. Sanchez-Palencia, *Localization of Bogoliubov quasiparticles in interacting Bose gases with correlated disorder*, Phys. Rev. A **84**(1), 013612 (2011).

[51] S. Lellouch, L.-K. Lim, and L. Sanchez-Palencia, *Propagation of collective pair excitations in disordered Bose superfluids*, Phys. Rev. A **92**, 043611 (2015).

[52] T. Giamarchi and H. J. Schulz, *Localization and interactions in one-dimensional quantum fluids*, Europhys. Lett. **3**, 1287 (1987).

[53] T. Giamarchi and H. J. Schulz, *Anderson localization and interactions in one-dimensional metals*, Phys. Rev. B **37**(1), 325 (1988).

[54] M. P. A. Fisher, P. B. Weichman, G. Grinstein, and D. S. Fisher, *Boson localization and the superfluid-insulator transition*, Phys. Rev. B **40**(1), 546 (1989).

[55] E. H. Lieb and W. Liniger, *Exact analysis of an interacting Bose gas. I. The general solution and the ground state*, Phys. Rev. **130**, 1605 (1963).

[56] E. H. Lieb, *Exact analysis of an interacting Bose gas. II. The excitation spectrum*, Phys. Rev. **130**, 1616 (1963).

[57] C. N. Yang and C. P. Yang, *Thermodynamics of a one-dimensional system of bosons with repulsive δ-function interaction*, J. Math. Phys. **10**, 1115 (1969).

[58] M. Boninsegni, N. Prokof'ev, and B. Svistunov, *Worm algorithm for continuous-space path integral Monte Carlo simulations*, Phys. Rev. Lett. **96**, 070601 (2006).

[59] M. Boninsegni, N. V. Prokof'ev, and B. V. Svistunov, *Worm algorithm and diagrammatic Monte Carlo: A new approach to continuous-space path integral Monte Carlo simulations*, Phys. Rev. E **74**, 036701 (2006).

[60] V. Gurarie, *One-dimensional gas of bosons with Feshbach-resonant interactions*, Phys. Rev. A **73**(3), 033612 (2006).

[61] N. Fabbri, M. Panfil, D. Clément, L. Fallani, M. Inguscio, C. Fort, and J.-S. Caux, *Dynamical structure factor of one-dimensional Bose gases: Experimental signatures of beyond-Luttinger-liquid physics*, Phys. Rev. A **91**, 043617 (2015).

[62] M. Olshanii, *Atomic scattering in the presence of an external confinement and a gas of impenetrable bosons*, Phys. Rev. Lett. **81**(5), 938 (1998).

[63] V. Flambaum, G. Gribakin, and C. Harabati, *Analytical calculation of cold-atom scattering*, Phys. Rev. A **59**(3), 1998 (1999).

[64] S. Dettmer, D. Hellweg, P. Ryytty, J. J. Arlt, W. Ertmer, K. Sengstock, D. S. Petrov, G. V. Shlyapnikov, H. Kreutzmann, L. Santos, *et al.*, *Observation of phase fluctuations in elongated Bose-Einstein condensates*, Phys. Rev. Lett. **87**, 160406 (2001).

[65] F. Gerbier, J. H. Thywissen, S. Richard, M. Hugbart, P. Bouyer, and A. Aspect, *Momentum distribution and correlation function of quasicondensates in elongated traps*, Phys. Rev. A **67**, 051602 (2003).

[66] J. Estève, J.-B. Trebbia, T. Schumm, A. Aspect, C. I. Westbrook, and I. Bouchoule, *Observations of density fluctuations in an elongated Bose gas: Ideal gas and quasicondensate regimes*, Phys. Rev. Lett. **96**, 130403 (2006).

[67] J. Decamp, M. Albert, and P. Vignolo, *Tan's contact in a cigar-shaped dilute bose gas*, Phys. Rev. A **97**(3), 033611 (2018).

[68] T. NAGAMIYA, *Statistical mechanics of one-dimensional substances i*, Proceedings of the Physico-Mathematical Society of Japan. 3rd Series **22**(8-9), 705 (1940).

[69] G. De Rosi, P. Massignan, M. Lewenstein, and G. E. Astrakharchik, *Beyond-Luttinger-liquid thermodynamics of a one-dimensional bose gas with repulsive contact interactions*, Phys. Rev. R **1**(3), 033083 (2019).

[70] D. S. Petrov, G. V. Shlyapnikov, and J. T. M. Walraven, *Regimes of quantum degeneracy in trapped 1D gases*, Phys. Rev. Lett. **85**, 3745 (2000).

[71] A. O. gogolin, A. A. Nersesyan, and A. M. Tsvelik, *Bosonization and strongly correlated systems* (Cambridge university press, 2004).

[72] F. D. M. Haldane, *Effective harmonic-fluid approach to low-energy properties of one-dimensional quantum fluids*, Phys. Rev. Lett. **47**, 1840 (1981).

[73] G. G. Batrouni, R. T. Scalettar, and G. T. Zimanyi, *Quantum critical phenomena in one-dimensional Bose systems*, Phys. Rev. Lett. **65**, 1765 (1990).

[74] V. A. Kashurnikov, A. V. Krasavin, and B. V. Svistunov, *Mott-insulator-superfluid-liquid transition in a one-dimensional bosonic hubbard model: Quantum monte carlo method*, JETP Lett. **64**(2), 99 (1996).

[75] T. D. Kühner and H. Monien, *Phases of the one-dimensional Bose-Hubbard model*, Phys. Rev. B **58**, R14741 (1998).

[76] T. D. Kühner, S. R. White, and H. Monien, *One-dimensional Bose-Hubbard model with nearest-neighbor interaction*, Phys. Rev. B **61**, 12474 (2000).

[77] N. Elstner and H. Monien, *Dynamics and thermodynamics of the bose-hubbard model*, Phys. Rev. B **59**(19), 12184 (1999).

[78] V. Pokrovsky and A. Talapov, *Ground state, spectrum, and phase diagram of two-dimensional incommensurate crystals*, Phys. Rev. Lett. **42**(1), 65 (1979).

[79] H. J. Schulz, *Critical behavior of commensurate-incommensurate phase transitions in two dimensions*, Phys. Rev. B **22**, 5274 (1980).

[80] T. Giamarchi, *Resistivity of a one-dimensional interacting quantum fluid*, Phys. Rev. B **46**, 342 (1992).

[81] E. B. Kolomeisky, *Universal jumps of conductance at the metal-insulator transition in one dimension*, Phys. Rev. B **47**, 6193 (1993).

[82] H.-P. Büchler, G. Blatter, and W. Zwerger, *Commensurate-incommensurate transition of cold atoms in an optical lattice*, Phys. Rev. Lett. **90**(13), 130401 (2003).

[83] S. Rapsch, U. Schollwöck, and W. Zwerger, *Density matrix renormalization group for disordered bosons in one dimension*, Europhys. Lett. **46**, 559 (1999).

[84] L. Fontanesi, M. Wouters, and V. Savona, *Superfluid to Bose-glass transition in a 1d weakly interacting Bose gas*, Phys. Rev. Lett. **103**(3), 030403 (2009).

[85] L. Pollet, N. V. Prokof'ev, B. V. Svistunov, and M. Troyer, *Absence of a direct superfluid to Mott insulator transition in disordered Bose systems*, Phys. Rev. Lett. **103**(14), 140402 (2009).

[86] H. Yao, H. Khoudli, L. Bresque, and L. Sanchez-Palencia, *Critical behavior and fractality in shallow one-dimensional quasiperiodic potentials*, Phys. Rev. Lett. **123**, 070405 (2019).

[87] A. Lüscher and A. M. Läuchli, *Exact diagonalization study of the antiferromagnetic spin-1/2 heisenberg model on the square lattice in a magnetic field*, Phys. Rev. B **79**(19), 195102 (2009).

[88] A. M. Läuchli, J. Sudan, and E. S. Sørensen, *Ground-state energy and spin gap of spin-1/2 kagomé-heisenberg antiferromagnetic clusters: Large-scale exact diagonalization results*, Phys. Rev. B **83**(21), 212401 (2011).

[89] E. P. Gross, *Structure of a quantized vortex in boson systems*, Il Nuovo Cimento (1955-1965) **20**(3), 454 (1961).

[90] L. P. Pitaevskii, *Vortex lines in an imperfect bose gas*, Sov. Phys. JETP **13**(2), 451 (1961).

[91] N. Bogoliubov, *On the theory of superfluidity*, J. Phys **11**(1), 23 (1947).

[92] L. Pollet, *Recent developments in quantum monte carlo simulations with applications for cold gases*, Reports on progress in physics **75**(9), 094501 (2012).

[93] W. L. McMillan, *Ground state of liquid he 4*, Phys. Rev. **138**(2A), A442 (1965).

[94] D. Ceperley, G. Chester, and M. Kalos, *Monte carlo simulation of a many-fermion study*, Phys. Rev. B **16**(7), 3081 (1977).

[95] J. W. Moskowitz, K. Schmidt, M. A. Lee, and M. H. Kalos, *A new look at correlation energy in atomic and molecular systems. ii. the application of the green's function monte carlo method to LiH*, The Journal of chemical physics **77**(1), 349 (1982).

[96] P. J. Reynolds, D. M. Ceperley, B. J. Alder, and W. A. Lester Jr, *Fixed-node quantum monte carlo for molecules*, The Journal of Chemical Physics **77**(11), 5593 (1982).

[97] E. Pollock and D. M. Ceperley, *Simulation of quantum many-body systems by path-integral methods*, Phys. Rev. B **30**(5), 2555 (1984).

[98] E. Pollock and D. M. Ceperley, *Path-integral computation of superfluid densities*, Phys. Rev. B **36**(16), 8343 (1987).

[99] D. M. Ceperley, *Path integrals in the theory of condensed helium*, Rev. Mod. Phys. **67**, 279 (1995).

[100] N. Prokof'ev and B. Svistunov, *Bold diagrammatic Monte Carlo technique: when the sign problem is welcome*, Phys. Rev. Lett. **99**, 250201 (2007).

[101] G. Carleo, F. Becca, M. Schiró, and M. Fabrizio, *Localization and glassy dynamics of many-body quantum systems*, Sci. Rep. **2**, 243 (2012).

[102] G. Carleo, L. Cevolani, L. Sanchez-Palencia, and M. Holzmann, *Unitary dynamics of strongly interacting Bose gases with the time-dependent variational Monte Carlo method in continuous space*, Phys. Rev. X **7**, 031026 (2017).

[103] N. Wiener, *The average of an analytic functional*, Proceedings of the National Academy of Sciences of the United States of America **7**(9), 253 (1921).

[104] N. Wiener, *Differential-space*, Journal of Mathematics and Physics **2**(1-4), 131 (1923).

[105] P. DIRAC, *The lagrangian in quantum mechanics*, Physikalische Zeitschirift der Sowjetunion **3**, 312 (1933).

[106] R. P. Feynman, *Space-time approach to nonrelativistic quantum mechanics*, Rev. Mod. Phys. **20**, 367 (1948).

[107] M. Kac, *On distributions of certain wiener functionals*, Transactions of the American Mathematical Society **65**(1), 1 (1949).

[108] H. F. Trotter, *On the product of semi-groups of operators*, Proceedings of the American Mathematical Society **10**(4), 545 (1959).

[109] M. Suzuki, *Generalized trotter's formula and systematic approximants of exponential operators and inner derivations with applications to many-body problems*, Communications in Mathematical Physics **51**(2), 183 (1976).

[110] J. Barker, *A quantum-statistical monte carlo method; path integrals with boundary conditions*, The Journal of Chemical Physics **70**(6), 2914 (1979).

[111] Y. Yan and D. Blume, *Incorporating exact two-body propagators for zero-range interactions into n-body monte carlo simulations*, Phys. Rev. A **91**(4), 043607 (2015).

[112] W. Krauth, *Statistical mechanics: algorithms and computations*, vol. 13 (OUP Oxford, 2006).

[113] M. Pierce and E. Manousakis, *Path-integral monte carlo simulation of the second layer of 4 he adsorbed on graphite*, Physical Review B **59**(5), 3802 (1999).

[114] N. Metropolis, A. W. Rosenbluth, M. N. Rosenbluth, A. H. Teller, and E. Teller, *Equation of state calculations by fast computing machines*, The journal of chemical physics **21**(6), 1087 (1953).

[115] W. HASTINGS, *Monte carlo sampling methods using marcov chains and their applications*, Biometrika **57**, 97 (1970).

[116] V. Ambegaokar and M. Troyer, *Estimating errors reliably in monte carlo simulations of the ehrenfest model*, American Journal of Physics **78**(2), 150 (2010).

[117] B. Bauer, L. Carr, H. G. Evertz, A. Feiguin, J. Freire, S. Fuchs, L. Gamper, J. Gukelberger, E. Gull, S. Guertler, *et al.*, *The alps project release 2.0: open source software for strongly correlated systems*, Journal of Statistical Mechanics: Theory and Experiment **2011**(05), P05001 (2011).

[118] M. Troyer, B. Ammon, and E. Heeb, in *International Symposium on Computing in Object-Oriented Parallel Environments*, Springer (1998), pp. 191–198.

[119] W. Krauth, *Quantum monte carlo calculations for a large number of bosons in a harmonic trap*, Phys. Rev. Lett. **77**(18), 3695 (1996).

[120] M. Holzmann and W. Krauth, *Kosterlitz-thouless transition of the quasi-two-dimensional trapped bose gas*, Phys. Rev. Lett. **100**(19), 190402 (2008).

[121] M. Olshanii and V. Dunjko, *Short-distance correlation properties of the Lieb-Liniger system and momentum distributions of trapped one-dimensional atomic gases*, Phys. Rev. Lett. **91**, 090401 (2003).

[122] S. Tan, *Large momentum part of fermions with large scattering length*, Ann. Phys. (NY) **323**, 2971 (2008).

[123] S. Tan, *Generalized virial theorem and pressure relation for a strongly correlated Fermi gas*, Ann. Phys. (NY) **323**, 2987 (2008).

[124] S. Tan, *Energetics of a strongly correlated Fermi gas*, Ann. Phys. (NY) **323**, 2952 (2008).

[125] R. Chang, Q. Bouton, H. Cayla, C. Qu, A. Aspect, C. I. Westbrook, and D. Clément, *Momentum-resolved observation of thermal and quantum depletion in a Bose gas*, Phys. Rev. Lett. **117**, 235303 (2016).

[126] R. J. Wild, P. Makotyn, J. M. Pino, E. A. Cornell, and D. S. Jin, *Measurements of Tan's contact in an atomic Bose-Einstein condensate*, Phys. Rev. Lett. **108**, 145305 (2012).

[127] J. T. Stewart, J. P. Gaebler, T. E. Drake, and D. S. Jin, *Verification of universal relations in a strongly interacting Fermi gas*, Phys. Rev. Lett. **104**, 235301 (2010).

[128] Y. Sagi, T. E. Drake, R. Paudel, and D. S. Jin, *Measurement of the homogeneous contact of a unitary Fermi gas*, Phys. Rev. Lett. **109**, 220402 (2012).

[129] S. Hoinka, M. Lingham, K. Fenech, H. Hu, C. J. Vale, J. E. Drut, and S. Gandolfi, *Precise determination of the structure factor and contact in a unitary Fermi gas*, Phys. Rev. Lett. **110**, 055305 (2013).

[130] C. Luciuk, S. Trotzky, S. Smale, Z. Yu, S. Zhang, and J. H. Thywissen, *Evidence for universal relations describing a gas with p-wave interactions*, Nat. Phys. **12**, 599 (2016).

[131] R. J. Fletcher, R. Lopes, J. Man, N. Navon, R. P. Smith, M. W. Zwierlein, and Z. Hadzibabic, *Two- and three-body contacts in the unitary Bose gas*, Science **355**, 377 (2017).

[132] S. Laurent, M. Pierce, M. Delehaye, T. Yefsah, F. Chevy, and C. Salomon, *Connecting few-body inelastic decay to quantum correlations in a many-body system: A weakly coupled impurity in a resonant Fermi gas*, Phys. Rev. Lett. **118**, 103403 (2017).

[133] A. Johnson, S. S. Szigeti, M. Schemmer, and I. Bouchoule, *Long-lived nonthermal states realized by atom losses in one-dimensional quasicondensates*, Phys. Rev. A **96**, 013623 (2017).

[134] K. V. Kheruntsyan, D. M. Gangardt, P. D. Drummond, and G. V. Shlyapnikov, *Pair correlations in a finite-temperature 1D Bose gas*, Phys. Rev. Lett. **91**, 040403 (2003).

[135] M. Kormos, G. Mussardo, and A. Trombettoni, *Expectation values in the Lieb-Liniger Bose gas*, Phys. Rev. Lett. **103**, 210404 (2009).

[136] W. Xu and M. Rigol, *Universal scaling of density and momentum distributions in Lieb-Liniger gases*, Phys. Rev. A **92**, 063623 (2015).

[137] H. Yao, D. Clément, A. Minguzzi, P. Vignolo, and L. Sanchez-Palencia, *Tan's contact for trapped Lieb-Liniger bosons at finite temperature*, Phys. Rev. Lett. **121**, 220402 (2018).

[138] M. Barth and W. Zwerger, *Tan relations in one dimension*, Ann. Phys. (NY) **326**, 2544 (2011).

[139] M. A. Cazalilla, *One-dimensional optical lattices and impenetrable bosons*, Phys. Rev. A **67**, 053606 (2003).

[140] H. Hu, X.-J. Liu, and P. D. Drummond, *Universal contact of strongly interacting fermions at finite temperatures*, New J. Phys. **13**(3), 035007 (2011).

[141] X.-J. Liu, H. Hu, and P. D. Drummond, *Virial expansion for a strongly correlated Fermi gas*, Phys. Rev. Lett. **102**(16), 160401 (2009).

[142] T. Busch, B.-G. Englert, K. Rzażewski, and M. Wilkens, *Two cold atoms in a harmonic trap*, Foundations of Physics **28**(4), 549 (1998).

[143] P. W. Anderson, *Absence of diffusion in certain random lattices*, Phys. Rev. **109**, 1492 (1958).

[144] E. Abrahams, *50 years of Anderson Localization* (World Scientific, Singapore, 2010).

[145] P. A. Lee and T. V. Ramakrishnan, *Disordered electronic systems*, Rev. Mod. Phys. **57**(2), 287 (1985).

[146] D. S. Wiersma, P. Bartolini, A. Lagendijk, and R. Righini, *Localization of light in a disordered medium*, Nature (London) **390**, 671 (1997).

[147] M. Störzer, P. Gross, C. M. Aegerter, and G. Maret, *Observation of the critical regime near Anderson localization of light*, Phys. Rev. Lett. **96**(6), 063904 (2006).

[148] T. Schwartz, G. Bartal, S. Fishman, and M. Segev, *Transport and Anderson localization in disordered two-dimensional photonic lattices*, Nature (London) **446**, 52 (2007).

[149] V. Gurarie and J. T. Chalker, *Bosonic excitations in random media*, Phys. Rev. B **68**(13), 134207 (2003).

[150] P. W. Anderson, *Theory of dirty superconductors*, J. Phys. Chem. Sol. **11**, 26 (1959).

[151] G. Orso, *BCS-BEC crossover in a random external potential*, Phys. Rev. Lett. **99**(25), 250402 (2007).

[152] L. Han and C. A. R. Sá de Melo, *Evolution from Bardeen-Cooper-Schrieffer to Bose-Einstein condensate superfluidity in the presence of disorder*, New J. Phys. **13**(5), 055012 (2011).

[153] L. Sanchez-Palencia and M. Lewenstein, *Disordered quantum gases under control*, Nat. Phys. **6**, 87 (2010).

[154] D. Shechtman, I. Blech, D. Gratias, and J. W. Cahn, *Metallic phase with long-range orientational order and no translational symmetry*, Phys. Rev. Lett. **53**, 1951 (1984).

[155] R. Peierls, *Theory of the diamagnetism of conduction electrons*, Z. Phys. **80**, 763 (1933).

[156] P. G. Harper, *Single band motion of conduction electrons in a uniform magnetic field*, Proc. Phys. Soc. London **A 68**, 874 (1955).

[157] D. R. Hofstadter, *Energy levels and wave functions of Bloch electrons in rational and irrational magnetic fields*, Phys. Rev. B **14**, 2239 (1976).

[158] J. Wilson, F. Di Salvo, and S. Mahajan, *Charge-density waves and superlattices in the metallic layered transition metal dichalcogenides*, Adv. Phys. **24**, 117 (1975).

[159] R. Merlin, K. Bajema, R. Clarke, F. Y. Juang, and P. K. Bhattacharya, *Quasiperiodic GaAs-AlAs heterostructures*, Phys. Rev. Lett. **55**, 1768 (1985).

[160] Y. Lahini, R. Pugatch, F. Pozzi, M. Sorel, R. Morandotti, N. Davidson, and Y. Silberberg, *Observation of a localization transition in quasiperiodic photonic lattices*, Phys. Rev. Lett. **103**, 013901 (2009).

[161] D. Tanese, E. Gurevich, F. Baboux, T. Jacqmin, A. Lemaître, E. Galopin, I. Sagnes, A. Amo, J. Bloch, and E. Akkermans, *Fractal energy spectrum of a polariton gas in a Fibonacci quasiperiodic potential*, Phys. Rev. Lett. **112**, 146404 (2014).

[162] A. Aspect and M. Inguscio, *Anderson localization of ultracold atoms*, Phys. Today **62**, 30 (2009).

[163] G. Modugno, *Anderson localization in Bose-Einstein condensates*, Rep. Prog. Phys. **73**, 102401 (2010).

[164] B. Damski, J. Zakrzewski, L. Santos, P. Zoller, and M. Lewenstein, *Atomic Bose and Anderson glasses in optical lattices*, Phys. Rev. Lett. **91**, 080403 (2003).

[165] R. Roth and K. Burnett, *Phase diagram of bosonic atoms in two-color superlattices*, Phys. Rev. A **68**, 023604 (2003).

[166] L. Sanchez-Palencia and L. Santos, *Bose-Einstein condensates in optical quasicrystal lattices*, Phys. Rev. A **72**, 053607 (2005).

[167] N. Macé, A. Jagannathan, and M. Duneau, *Quantum simulation of a 2D quasicrystal with cold atoms*, Crystals **6**, 124 (2016).

[168] B. Gadway, D. Pertot, J. Reeves, M. Vogt, and D. Schneble, *Glassy behavior in a binary atomic mixture*, Phys. Rev. Lett. **107**, 145306 (2011).

[169] S. Iyer, V. Oganesyan, G. Refael, and D. A. Huse, *Many-body localization in a quasiperiodic system*, Phys. Rev. B **87**, 134202 (2013).

[170] A. Lukin, M. Rispoli, R. Schittko, M. E. Tai, A. M. Kaufman, S. Choi, V. Khemani, J. Léonard, and M. Greiner, *Probing entanglement in a many-body-localized system*, arXiv:1805.09819 (2018).

[171] R. Matthew, L. Alexander, S. Robert, K. Sooshin, T. M. Eric, L. Julian, and G. Markus, *Quantum critical behavior at the many-body-localization transition*, arXiv:1812.06959 (2018).

[172] E. Abrahams, P. W. Anderson, D. C. Licciardello, and T. V. Ramakrishnan, *Scaling theory of localization: Absence of quantum diffusion in two dimensions*, Phys. Rev. Lett. **42**, 673 (1979).

[173] S. Aubry and G. André, *Analyticity breaking and Anderson localization in incommensurate lattices*, Ann. Israel Phys. Soc. **3**, 133 (1980).

[174] C. Soukoulis and E. Economou, *Localization in one-dimensional lattices in the presence of incommensurate potentials*, Phys. Rev. Lett. **48**, 1043 (1982).

[175] S. Das Sarma, A. Kobayashi, and R. E. Prange, *Proposed experimental realization of Anderson localization in random and incommensurate artificially layered systems*, Phys. Rev. Lett. **56**, 1280 (1986).

[176] J. Biddle, B. Wang, D. J. Priour Jr, and S. Das Sarma, *Localization in one-dimensional incommensurate lattices beyond the Aubry-André model*, Phys. Rev. A **80**, 021603 (2009).

[177] J. Biddle and S. Das Sarma, *Predicted mobility edges in one-dimensional incommensurate optical lattices: An exactly solvable model of Anderson localization*, Phys. Rev. Lett. **104**, 070601 (2010).

[178] J. Biddle, D. J. Priour Jr, B. Wang, and S. D. Sarma, *Localization in one-dimensional lattices with non-nearest-neighbor hopping : Generalized Anderson and Aubry-André models*, Phys. Rev. B **83**, 075105 (2011).

[179] S. Ganeshan, J. Pixley, and S. Das Sarma, *Nearest neighbor tight binding models with an exact mobility edge in one dimension*, Phys. Rev. Lett. **114**, 146601 (2015).

[180] D. J. Boers, B. Goedeke, D. Hinrichs, and M. Holthaus, *Mobility edges in bichromatic optical lattices*, Phys. Rev. A **75**, 063404 (2007).

[181] X. Li, X. Li, and S. Das Sarma, *Mobility edges in one-dimensional bichromatic incommensurate potentials*, Phys. Rev. B **96**, 085119 (2017).

[182] H. P. Lüschen, S. Scherg, T. Kohlert, M. Schreiber, P. Bordia, X. Li, S. Das Sarma, and I. Bloch, *Single-particle mobility edge in a one-dimensional quasiperiodic optical lattice*, Phys. Rev. Lett. **120**, 160404 (2018).

[183] F. Evers and A. D. Mirlin, *Anderson transitions*, Rev. Mod. Phys. **80**, 1355 (2008).

[184] R. B. Diener, G. A. Georgakis, J. Zhong, M. Raizen, and Q. Niu, *Transition between extended and localized states in a one-dimensional incommensurate optical lattice*, Phys. Rev. A **64**(3), 033416 (2001).

[185] A. Avila and S. Jitomirskaya, *The ten martini problem*, Annals of Mathematics pp. 303–342 (2009).

[186] I. M. Lifshits, S. Gredeskul, and L. Pastur, *Introduction to the Theory of Disordered Systems* (Wiley, New York, 1988).

[187] C. W. J. Beenakker, *Random-matrix theory of quantum transport*, Rev. Mod. Phys. **69**, 731 (1997).

[188] B. Simon, *Almost periodic schrödinger operators: a review*, Advances in Applied Mathematics **3**(4), 463 (1982).

[189] C. Tang and M. Kohmoto, *Global scaling properties of the spectrum for a quasiperiodic Schrödinger equation*, Phys. Rev. B **34**, 2041 (1986).

[190] M. Kohmoto, B. Sutherland, and C. Tang, *Critical wave functions and a Cantor-set spectrum of a one-dimensional quasicrystal model*, Phys. Rev. B **35**, 1020 (1987).

[191] M. Kohmoto, *Metal-insulator transition and scaling for incommensurate systems*, Phys. Rev. Lett. **51**, 1198 (1983).

[192] T. Roscilde, *Bosons in one-dimensional incommensurate superlattices*, Phys. Rev. A **77**, 063605 (2008).

[193] B. B. Mandelbrot, *The Fractal Geometry of Nature*, vol. 2 (WH freeman New York, 1982).

[194] J. Theiler, *Estimating fractal dimension*, JOSA A **7**, 1055 (1990).

[195] A. Jagannathan and M. Duneau, *An eightfold optical quasicrystal with cold atoms*, Europhys. Lett. **104**(6), 66003 (2014).

[196] L. Pezzé and L. Sanchez-Palencia, *Localized and extended states in a disordered trap*, Phys. Rev. Lett. **106**, 040601 (2011).

[197] V. V. Volchkov, M. Pasek, V. Denechaud, M. Mukhtar, A. Aspect, D. Delande, and V. Josse, *Measurement of spectral functions of ultracold atoms in disordered potentials*, Phys. Rev. Lett. **120**, 060404 (2018).

[198] J. Richard, L.-K. Lim, V. Denechaud, V. V. Volchkov, B. Lecoutre, M. Mukhtar, F. Jendrzejewski, A. Aspect, A. Signoles, L. Sanchez-Palencia, *et al.*, *Elastic scattering time of matter waves in disordered potentials*, Phys. Rev. Lett. **122**, 100403 (2019).

[199] D. M. Basko, I. L. Aleiner, and B. L. Altshuler, *Metal-insulator transition in a weakly interacting many-electron system with localized single-particle states*, Ann. Phys. (NY) **321**(5), 1126 (2006).

[200] V. Oganesyan and D. A. Huse, *Localization of interacting fermions at high temperature*, Phys. Rev. B **75**, 155111 (2007).

[201] R. Nandkishore and D. A. Huse, *Many-body localization and thermalization in quantum statistical mechanics*, Annual Rev. Cond. Mat. Phys. **6**, 15 (2015).

[202] E. Altman and R. Vosk, *Universal dynamics and renormalization in many-body-localized systems*, Annual Rev. Cond. Mat. Phys. **6**, 383 (2015).

[203] D. A. Abanin, E. Altman, I. Bloch, and M. Serbyn, *Colloquium: Many-body localization, thermalization, and entanglement*, Rev. Mod. Phys. **91**, 021001 (2019).

[204] W. Krauth, N. Trivedi, and D. Ceperley, *Superfluid-insulator transition in disordered boson systems*, Phys. Rev. Lett. **67**(17), 2307 (1991).

[205] F. D. M. Haldane, *Solidification in a soluble model of bosons on a one-dimensional lattice: The Boson-Hubbard chain*, J. Phys. Lett. A **80**, 281 (1980).

[206] R. T. Scalettar, G. G. Batrouni, and G. T. Zimanyi, *Localization in interacting, disordered, Bose systems*, Phys. Rev. Lett. **66**(24), 3144 (1991).

[207] R. Vosk and E. Altman, *Superfluid-insulator transition of ultracold bosons in disordered one-dimensional traps*, Phys. Rev. B **85**, 024531 (2012).

[208] Y. Lahini, A. Avidan, F. Pozzi, M. Sorel, R. Morandotti, D. N. Christodoulides, and Y. Silberberg, *Anderson localization and nonlinearity in one-dimensional disordered photonic lattices*, Phys. Rev. Lett. **100**(1), 013906 (2008).

[209] M. Pasienski, D. McKay, M. White, and B. DeMarco, *A disordered insulator in an optical lattice*, Nat. Phys. **6**, 677 (2010).

[210] B. Deissler, M. Zaccanti, G. Roati, C. D'Errico, M. Fattori, M. Modugno, G. Modugno, and M. Inguscio, *Delocalization of a disordered bosonic system by repulsive interactions*, Nat. Phys. **6**, 354 (2010).

[211] R. Yu, L. Yin, N. S. Sullivan, J. S. Xia, C. Huan, A. Paduan-Filho, N. F. O. Jr, S. Haas, A. Steppke, C. F. Miclea, *et al.*, *Bose glass and Mott glass of quasiparticles in a doped quantum magnet*, Nature (London) **489**, 379 (2012).

[212] M. Lewenstein, A. Sanpera, V. Ahufinger, B. Damski, A. Sen, and U. Sen, *Ultracold atomic gases in optical lattices: Mimicking condensed matter physics and beyond*, Adv. Phys. **56**, 243 (2007).

[213] M. Verbin, O. Zilberberg, Y. Lahini, Y. E. Kraus, and Y. Silberberg, *Topological pumping over a photonic Fibonacci quasicrystal*, Phys. Rev. B **91**, 064201 (2015).

[214] F. Baboux, E. Levy, A. Lemaître, C. Gómez, E. Galopin, L. Le Gratiet, I. Sagnes, A. Amo, J. Bloch, and E. Akkermans, *Measuring topological invariants from generalized edge states in polaritonic quasicrystals*, Phys. Rev. B **95**, 161114 (2017).

[215] X. Deng, R. Citro, A. Minguzzi, and E. Orignac, *Phase diagram and momentum distribution of an interacting Bose gas in a bichromatic lattice*, Phys. Rev. A **78**, 013625 (2008).

[216] L. Sanchez-Palencia, *Smoothing effect and delocalization of interacting Bose-Einstein condensates in random potentials*, Phys. Rev. A **74**(5), 053625 (2006).

[217] H. Yao, T. Giamarchi, and L. Sanchez-Palencia, *Lieb-Liniger bosons in a shallow quasiperiodic potential: Bose glass phase and fractal Mott lobes*, Phys. Rev. Lett. **125**, 060401 (2020).

[218] T. Stöferle, H. Moritz, C. Schori, M. Köhl, and T. Esslinger, *Transition from a strongly interacting 1d superfluid to a mott insulator*, Physical review letters **92**(13), 130403 (2004).

[219] C. Kollath, A. Iucci, T. Giamarchi, W. Hofstetter, and U. Schollwöck, *Spectroscopy of ultracold atoms by periodic lattice modulations*, Phys. Rev. Lett. **97**(5), 050402 (2006).

[220] G. Orso, A. Iucci, M. Cazalilla, and T. Giamarchi, *Lattice modulation spectroscopy of strongly interacting bosons in disordered and quasiperiodic optical lattices*, Phys. Rev. A **80**(3), 033625 (2009).

[221] F. Gerbier, *Boson Mott insulators at finite temperatures*, Phys. Rev. Lett. **99**, 120405 (2007).

[222] T. P. Meyrath, F. Schreck, J. L. Hanssen, C.-S. Chuu, and M. G. Raizen, *Bose-Einstein condensate in a box*, Phys. Rev. A **71**, 041604 (2005).

[223] A. L. Gaunt, T. F. Schmidutz, I. Gotlibovych, R. P. Smith, and Z. Hadzibabic, *Bose-Einstein condensation of atoms in a uniform potential*, Phys. Rev. Lett. **110**, 200406 (2013).

[224] L. Chomaz, L. Corman, T. Bienaimé, R. Desbuquois, C. Weitenberg, S. Nascimbène, J. Beugnon, and J. Dalibard, *Emergence of coherence via transverse condensation in a uniform quasi-two-dimensional Bose gas*, Nat. Comm. **6**, 6162 (2015).

[225] J. Vidal, D. Mouhanna, and T. Giamarchi, *Correlated fermions in a one-dimensional quasiperiodic potential*, Phys. Rev. Lett. **83**, 3908 (1999).

[226] J. Vidal, D. Mouhanna, and T. Giamarchi, *Interacting fermions in self-similar potentials*, Phys. Rev. B **65**, 014201 (2001).

[227] R. Gautier, H. Yao, and L. Sanchez-Palencia, *Strongly-interacting bosons in a two-dimensional quasicrystal lattice*, arXiv preprint arXiv:2010.07590 (2020).

ECOLE DOCTORALE

Titre : Bosons fortement corrélés unidimensionnels dans des potentiels continus et quasi-périodiques

Mots clés : Monte Carlo quantique ; thermodynamique de Yang-Yang ; contact de Tan ; potentiel quasi-périodique ; verre de Bose ; fractale

Résumé : Dans cette thèse, nous étudions les propriétés des bosons unidimensionnels dans divers types de systèmes, en nous concentrant sur les transitions de phase ou les croisements entre différents régimes de dégénérescence quantique. En combinant la méthode de Monte Carlo quantique avec d'autres techniques standard telles que la diagonalisation exacte et l'ansatz de Bethe thermique, nous pouvons calculer le comportement des bosons à une dimension dans différents cas où les résultats font encore défaut. Tout d'abord, dans le cas de bosons continus piégés de manière harmonique, nous fournissons une caractérisation complète d'une quantité appelée contact de Tan. En calculant la fonction d'échelle universelle de cette quantité, nous identifions le comportement du contact dans différents régimes de dégénérescence pour les bosons 1D. Nous montrons que le contact présente un maximum en fonction de la température et qu'il s'agit d'une signature de la fermionisation du gaz dans le régime de forte interaction. Ensuite, nous étudions la localisation et les propriétés fractales des gaz idéaux 1D dans des potentiels quasi-périodiques peu profonds. Le système quasi-périodique constitue un intermédiaire intéressant entre les systèmes ordonnés à longue distance et les véritables systèmes désordonnés aux propriétés critiques inhabituelles. Alors que le modèle d'Aubry-André (AA) à liaison étroite a été largement étudié, le cas du réseau peu profond se comporte différemment. Nous déterminons les propriétés critiques de localisation du système, le potentiel critique, les bords de mobilité et les exposants critiques qui sont universels. De plus, nous calculons la dimension fractale du spectre d'énergie et nous constatons qu'elle est non universelle mais toujours inférieure à l'unité, ce qui montre que le spectre n'est dense nulle part. Enfin, nous passons à l'étude avec les interactions. Avec les calculs quantiques de Monte Carlo, nous calculons le diagramme de phase des bosons de Lieb-Liniger en potentiels quasi-périodiques peu profonds. On trouve un verre de Bose, entouré de phases superfluides et de Mott. À température finie, nous montrons que la fusion des lobes de Mott est caractéristique d'une structure fractale et constatons que le verre de Bose est robuste contre les fluctuations thermiques jusqu'à des températures accessibles dans les expériences.

Title : Strongly-correlated one-dimensional bosons in continuous and quasiperiodic potentials

Keywords : quantum Monte Carlo ; Yang-Yang thermodynamics ; Tan contact ; quasiperiodic potential ; Bose glass ; fractal

Abstract : In this thesis, we investigate the properties of one-dimensional bosons in various types of systems, focusing on the phase transitions or crossovers between different quantum degeneracy regimes. Combining quantum Monte Carlo with other standard techniques such as exact diagonalization and thermal Bethe ansatz, we can compute the behavior of 1D bosons in different cases where the results are still lacking. First, in the case of harmonically trapped continuous bosons, we provide a full characterization of a quantity called Tan's contact. By computing the universal scaling function of it, we identify the behavior of the contact in various regimes of degeneracy for 1D bosons. We show that the contact exhibits a maximum versus temperature and that it is a signature of the crossover to fermionization in the strongly-interacting regime. Secondly, we study the localization and fractal properties of 1D ideal gases in shallow quasiperiodic potentials. The quasiperiodic system provides an appealing intermediate between long-range ordered and genuine disordered systems with unusual critical properties. While the tight-binding Aubry-André (AA) model has been widely studied, the shallow lattice case behaves differently. We determine the critical localization properties of the system, the critical potential, mobility edges and critical exponents which are universal. Moreover, we calculate the fractal dimension of the energy spectrum and find it is non-universal but always smaller than unity, which shows the spectrum is nowhere dense. Finally, we move to the study of the interacting case. With the quantum Monte Carlo calculations, we compute the phase diagram of Lieb-Liniger bosons in shallow quasiperiodic potentials. A Bose glass, surrounded by superfluid and Mott phases, is found. At finite temperature, we show that the melting of the Mott lobes is characteristic of a fractal structure and find that the Bose glass is robust against thermal fluctuations up to temperatures accessible in experiments.

Institut Polytechnique de Paris
91120 Palaiseau, France